ADVANCES IN MULTI-SCALE MULTI-PHYSICS GEOPHYSICAL MODELLING AND FLUID TRANSPORT IN UNCONVENTIONAL OIL AND GAS RESERVOIR

EDITED BY: Wenhui Song, Zheng Sun, Yu Pang, Yanyong Wang and Jianlin Zhao

PUBLISHED IN: Frontiers in Earth Science

frontiers Research Topics

frontiers

ISSN 1664-8714
ISBN 978-2-88976-775-5
DOI 10.3389/978-2-88976-775-5

About Frontiers

Frontiers is more than just an open-access publisher of scholarly articles: it is a pioneering approach to the world of academia, radically improving the way scholarly research is managed. The grand vision of Frontiers is a world where all people have an equal opportunity to seek, share and generate knowledge. Frontiers provides immediate and permanent online open access to all its publications, but this alone is not enough to realize our grand goals.

Frontiers Journal Series

The Frontiers Journal Series is a multi-tier and interdisciplinary set of open-access, online journals, promising a paradigm shift from the current review, selection and dissemination processes in academic publishing. All Frontiers journals are driven by researchers for researchers; therefore, they constitute a service to the scholarly community. At the same time, the Frontiers Journal Series operates on a revolutionary invention, the tiered publishing system, initially addressing specific communities of scholars, and gradually climbing up to broader public understanding, thus serving the interests of the lay society, too.

Dedication to Quality

Each Frontiers article is a landmark of the highest quality, thanks to genuinely collaborative interactions between authors and review editors, who include some of the world's best academicians. Research must be certified by peers before entering a stream of knowledge that may eventually reach the public - and shape society; therefore, Frontiers only applies the most rigorous and unbiased reviews.
Frontiers revolutionizes research publishing by freely delivering the most outstanding research, evaluated with no bias from both the academic and social point of view. By applying the most advanced information technologies, Frontiers is catapulting scholarly publishing into a new generation.

What are Frontiers Research Topics?

Frontiers Research Topics are very popular trademarks of the Frontiers Journals Series: they are collections of at least ten articles, all centered on a particular subject. With their unique mix of varied contributions from Original Research to Review Articles, Frontiers Research Topics unify the most influential researchers, the latest key findings and historical advances in a hot research area! Find out more on how to host your own Frontiers Research Topic or contribute to one as an author by contacting the Frontiers Editorial Office: frontiersin.org/about/contact

ADVANCES IN MULTI-SCALE MULTI-PHYSICS GEOPHYSICAL MODELLING AND FLUID TRANSPORT IN UNCONVENTIONAL OIL AND GAS RESERVOIR

Topic Editors:
Wenhui Song, China University of Petroleum, Huadong, China
Zheng Sun, China University of Mining and Technology, China
Yu Pang, University of Calgary, Canada
Yanyong Wang, Chengdu University of Technology, China
Jianlin Zhao, ETH Zürich, Switzerland

Citation: Song, W., Sun, Z., Pang, Y., Wang, Y., Zhao, J., eds. (2022). Advances in Multi-scale Multi-physics Geophysical Modelling and Fluid Transport in Unconventional Oil and Gas Reservoir. Lausanne: Frontiers Media SA.
doi: 10.3389/978-2-88976-775-5

Table of Contents

frontiers in Earth Science

BRIEF RESEARCH REPORT
published: 13 September 2021
doi: 10.3389/feart.2021.738545

Pore Network Modeling of Oil–Water Flow in Jimsar Shale Oil Reservoir

Xiukun Wang[1,2], Zheng Zhang[3], Rundong Gong[1] and Sen Wang[2]*

[1]Unconventional Petroleum Institute, China University of Petroleum (Beijing), Beijing, China, [2]Key Laboratory of Unconventional Oil and Gas Development (China University of Petroleum (East China)), Ministry of Education, Qingdao, China, [3]China National Oil and Gas Exploration and Development Company Ltd., Beijing, China

The oil–water two-phase flow mechanism is the critical issue for producing shale oil reservoirs after huge-volume hydraulic fracturing treatment. Due to the extremely low permeability of the shale matrix, the two-phase experimental measurement is impossible for shale samples. In this work, a pore network model is proposed to simulate steady-state oil–water flow with mixed wettability under consideration. The model is first applied in Berea sandstone, and the calculated relative permeabilities are validated with experimental studies for different wettability scenarios. Then, the three-dimensional FIB-SEM imaging of the Jimsar shale sample is used to extract a representative shale pore network with 13,419 pores and 31,393 throats. The mean values of pores and throats are 29.75 and 19.13 nm, and the calculated absolute permeability is 0.005 mD. With our proposed model, the calculated relative permeability curves show a high residual oil saturation for all the wettability conditions. Specifically, the oil-wet and mixed-wet conditions yield lower residual oil compared with the water-wet condition. For 50–50 mixed-wet conditions, the water phase relative permeability is much higher for smaller pores being oil-wet than the larger pores being oil-wet.

Keywords: shale oil, pore network modeling, two-phase flow, relative permeability, mixed-wettability

OPEN ACCESS

Edited by:
Yu Pang,
University of Calgary, Canada

Reviewed by:
Guanglong Sheng,
Yangtze University, China
Ping Yue,
Southwest Petroleum University, China

****Correspondence:***
Xiukun Wang
xiukunwang@cup.edu.cn

Specialty section:
This article was submitted to Economic Geology, a section of the journal Frontiers in Earth Science

Received: *09 July 2021*
Accepted: *30 July 2021*
Published: *13 September 2021*

Citation:
Wang X, Zhang Z, Gong R and Wang S (2021) Pore Network Modeling of Oil–Water Flow in Jimsar Shale Oil Reservoir. Front. Earth Sci. 9:738545. doi: 10.3389/feart.2021.738545

INTRODUCTION

Worldwide, the shale oil and gas reservoirs are important supplementary unconventional resources for the petroleum industry. The shale boom helps the United States to regain status as the top oil-producing country and changes the political and energetical situations for the whole world. In China, the Jimsar shale oil in Xinjiang province is one of the most high-potential shale pay zones (Yang et al., 2018). Because almost all the multifractured horizontal wells are commonly used to develop shale oil reservoirs, the oil–water two-phase flow becomes vital after a huge amount of fracturing water injection. Due to the extremely low permeability of the shale matrix, the two-phase experimental measurement is impossible for shale samples. The digital rock physics and pore-scale modeling methods are believed to be a substitute for laboratory multiphase flow experimental studies. Conventionally, the digital rock data set is obtained by a micro-CT scanner with a resolution of around 1 μm; however, the pore and throat sizes of the shale matrix are much smaller, and most pore diameters are less than 100 nm. Recently, the focused ion beam scanning electron microscope (FIB-SEM) imaging technique is introduced to reconstruct shale digital rock data (Kelly et al., 2016). This approach works by creating an image of the surface layer of a sample, which is then stripped away using a beam of charged particles to reveal the layer beneath. The new surface can then be imaged, and so on, through the whole sample.

As for pore-scale modeling methods, there are mainly two types: direct numerical simulation and pore network modeling. The former method consists of conventional grid-based CFD methods, e.g.,

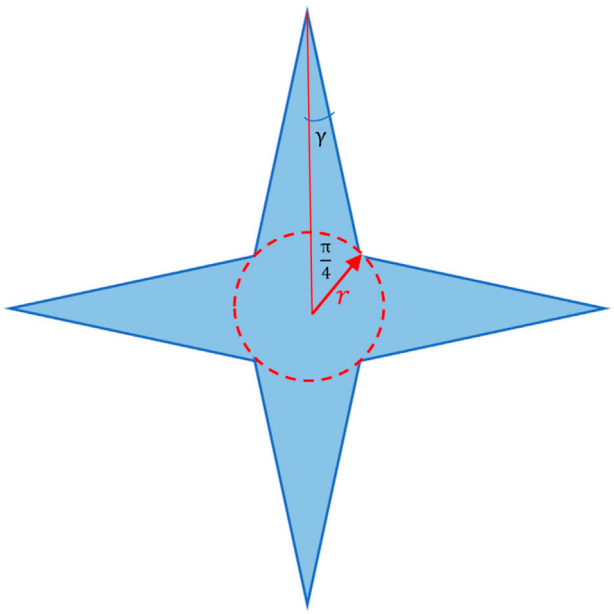

FIGURE 1 | Four-pointed, star-shaped, cross-section area of pores and throats.

VOF (Raeini et al., 2014), and the lattice Boltzmann method (Ramstad et al., 2010). As for the huge amount of the digital rock data, direct numerical simulation is almost impossible for multiphase flow simulation because of the high computational demand. The pore network modeling method relieves the computational effort by representing the detailed pore space *via* interconnected pores and throats. The pore network extraction algorithms include central axis extraction, maximum sphere filtration, watershed segmentation, etc. (Dong and Blunt, 2009; Rabbani et al., 2014). With the irregular, cross-sectional, triangular-shaped pores and throats, multiphase could coexist in a capillary balance, which leads to the birth of quasi-static pore network models (Øren et al., 1998; Valvatne and Blunt, 2004). To the best of our knowledge, the previous pore-scale modeling studies of fluids flow in shale mainly focus on single-phase flow and synthetic networks (Guo et al., 2018; Wang and Sheng, 2018).

In this work, a pore network model is proposed to simulate steady-state oil–water flow with mixed wettability under consideration. The model is first applied in Berea sandstone, and the calculated relative permeabilities are validated with experimental studies for different wettability scenarios. Then, three-dimensional FIB-SEM imaging of the Jimsar shale sample is used to extract a representative shale pore network used within our proposed model to investigate the oil–water flow mechanisms.

METHODOLOGY AND VALIDATION

Following the work by Ryazanov et al. (2009), the four-pointed, star-shaped, cross-sectional area is used to improve the representative accuracy of irregular triangles. The geometrical diagram is shown in **Figure 1**. Then, the crossing area A, perimeter P, and shape factor G of a pore or throat are given in **Eqs 1–3**.

$$A = 2r^2\left(1 + cot\gamma\right), \tag{1}$$

$$G = \frac{1}{16} sin\gamma\left(sin\gamma + cos\gamma\right), \tag{2}$$

$$P = \frac{4\sqrt{2}r}{sin\gamma}. \tag{3}$$

The crude oil within shale formations is supposed to be accumulated by primary drainage, where the initial water coexists and the corresponding water saturation can be calculated by the maximum drainage capillary pressure p_c^{max} in **Eq. 4**. The p_c^{max} is defined as the threshold pressure for the smallest throat being invaded.

$$S_w = \frac{4\left(\frac{\sigma}{p_c^{max}}\right)^2\left(\theta_r + \gamma - \frac{\pi}{2} + \frac{cos\,\theta_r\, cos\left(\theta_r+\gamma\right)}{sin\,\gamma}\right)}{A}, \tag{4}$$

where θ_r and σ are the receding contact angle and oil–water interfacial tension, respectively.

As for oil–water flow encountered in field practice, the steady-state water injection is used for pore scale simulating shale oil–water flow processes, in which the capillary pressure decreases from maximum value to zero and then to the negative maximum. Because the shale oil formations are believed to be mixed-wet, the displacement mechanisms are divided into water-wet and oil-wet pores.

First, for water-wet throats, spontaneous snap-off and piston-like filling are considered, and the corresponding threshold capillary pressures are given in **Eq. 5** and **Eq. 6**.

$$p_c^{sf} = \frac{\sqrt{2}\sigma\cos\left(\theta_a + \gamma\right)}{r}, \tag{5}$$

$$p_c^{pl} = \frac{2\sigma\cos\theta_a}{r}, \tag{6}$$

where θ_a is the advancing contact angle. Note that the snap-off will not happen if $\theta_a \geq \frac{\pi}{2} - \gamma$ and that piston-like filling is more favorable over snap-off if the throat is accessible by a filled pore body.

For water-wet pore bodies, cooperative pore filling is also considered, and the corresponding threshold capillary pressure is formulated in **Eq. 7**.

$$p_c^{In} = \frac{2\sigma cos\theta_a}{r} - \sigma\sum_{i=1}^{n} a_i x_i, \tag{7}$$

where $a_1 = 0$, $a_{i\geq 2} = \frac{0.03}{\sqrt{k_{abs}}}$, x is a random number within 0–1, and n is the number of oil-filled throats connecting to the pore body.

After inlet capillary pressure reduces to negative, the oil-wet pores and throats are filled by forced water injection, which is similar to the process of primary drainage except for the existence of sandwiched oil film. When $\theta_a < \frac{\pi}{2} + \gamma$, water invades and fulfills the oil-wet pores and throats, in which the corresponding threshold capillary pressure is the same as in **Eq. 6** except the value is negative. When $\theta_a \geq \frac{\pi}{2} + \gamma$, sandwiched oil film formed after forced water intrusion, and the threshold capillary pressure is given by

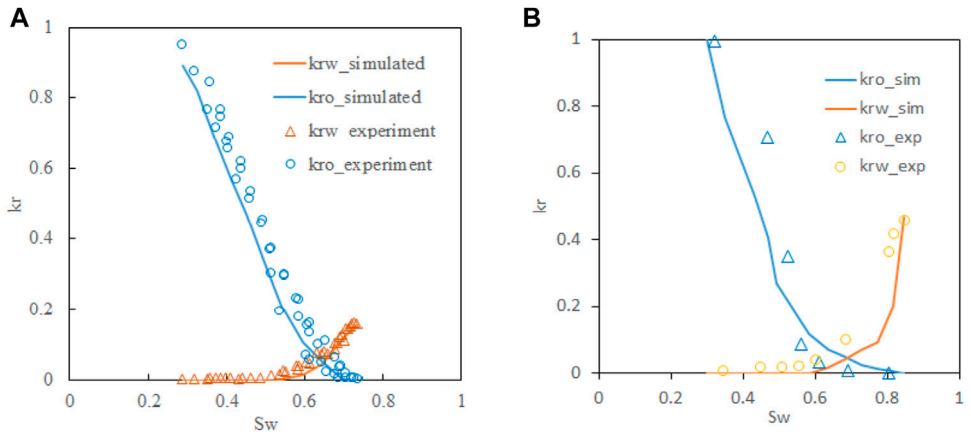

FIGURE 2 | Pore network model–calculated relative permeability curves of Berea sandstone validated by experimental data (Valvatne and Blunt, 2004) **(A)** for water-wet, **(B)** for 50–50 mixed-wet.

$$P_c^{pl} = \frac{\sigma}{2PG}\left(cos\theta_a - \sqrt{cos^2\theta_a - 16A_{\alpha 2}G}\right), \quad (8)$$

where $A_{\alpha 2} = \frac{\pi}{2} - \theta_a + \gamma + \frac{cos\,\theta_a \cos(\theta_a - \gamma)}{sin\,\gamma}$.

As for oil-wet throat forced snap-off, due to the minimum value of corresponding threshold pressure, the happening probability is quite low (Blunt, 2017), which is not considered in this work.

During the water injection process, the oil and water saturation are updated by the microdisplacement mechanisms as shown. The efficient graph-based NetworkX (Hagberg et al., 2008) package is used to recheck the trapped oil clusters. For every capillary pressure decreasing step, the phase conductance of every pore and throat are updated by their balanced water saturation. Then, an adjacent matrix is established by putting the conductance values on the corresponding positions. Given an arbitrary pressure drop between the inlet and outlet, the pressure of every pore and throat are calculated. Then, the outlet face flow rate is obtained. Finally, we apply Darcy's equation, and the absolute and phase effective permeability are computed.

Applying the proposed pore network model to the Berea sandstone pore network data extracted using Dong and Blunt's software, the absolute permeability yields 1.78 mD, which is close to the experimental value of 2.45 mD. The error is caused by the micro-heterogeneity. The relative permeability curves for water-wet and 50–50 mixed-wet scenarios are shown in **Figure 2**, in which the contact angle of water-wet and oil-wet pores are set as 60° and 120°, respectively. The experimental measured data matches the pore network calculated curves, which validates our model to predict oil–water flow mechanisms within a 3-D digitalized rock.

PORE NETWORK MODELING OF OIL–WATER FLOW IN JIMSAR SHALE

The Jimsar shale sample is used in this study to digitalize the pore space in three dimensions. The FIB-SEM experiment is implemented, in which the resolution is 20 nm*20 nm*20 nm and the data size is 500*500*500. Applying the fast Fourier transformation, the noisy artifacts are removed from the 3-D image. The pore space is segmented by setting a threshold grayscale value, and the maximum sphere algorithm is used to extract the pore network. The 3-D pore space and pore network are visualized in Paraview (Ahrens et al., 2015) as shown in **Figure 3**.

There are 13,419 pores and 31,393 throats for the Jimsar shale pore network, and the connected porosity is 16.35%, which is close to the experimentally measured 19%. The loss of porosity is due to the unresolvable voxel for pores and throats less than 20 nm. Applying statistics of the pore network properties, the mean radius of pores and throats are 29.75 and 19.13 nm. The average pore–throat aspect ratio is 2.29 although we have several bigger pores and throats as shown in **Figure 3**.

Applying our proposed pore network model, the absolute Darcy permeability is calculated as 0.004–0.006 mD for x, y, and z flowing directions, which is also a reasonable value for the shale oil reservoir in the formation conditions. Note that the gas slippage and formation deformation (Sheng et al., 2019; Sheng et al., 2020; Pang et al., 2020; Pang et al., 2021) are not considered. With the 50–50 mixed-wet scenario, i.e., half of the pores and throats are water-wet and the other half are oil-wet. The contact angle of water-wet and oil-wet pores are set as 60° and 120°, respectively. Setting the larger or smaller half pores and throats to be oil-wet, the simulated relative permeability curves are shown in **Figure 4**.

According to the figure, both wettability scenarios indicate a high residual oil saturation (i.e., close to 40%) and a narrow two-phase flow region, which means that the oil recovery of shale oil is much lower than conventional highly permeable reservoirs. For larger pores being oil-wet, the water phase relative permeability is extremely low, and the endpoint value is less than 0.01, which means water within the shale matrix almost will not flow, which is quite similar to the phenomenon of permeability jail (Shanley et al., 2004). For the oil-wet smaller pore scenario, the water phase relative permeability increases much faster with the increase of water saturation, and the endpoint is around 0.3. The differences suggest that the larger pores contribute the most flow ability. When larger pores are oil-wet, water first fills the water-wet smaller pores, and then, the oil-filled larger pores are trapped with no escape channels. However, when larger pores are water-wet, water first fills them and then extends to smaller

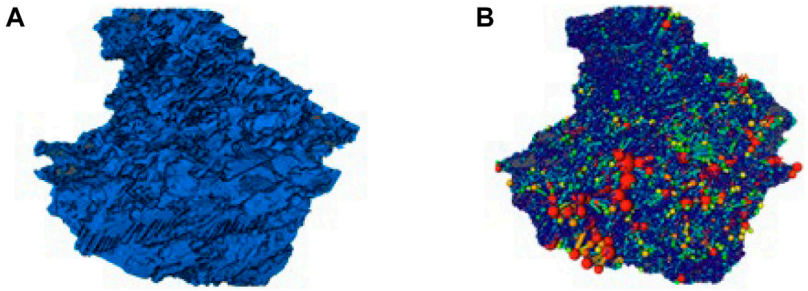

FIGURE 3 | Jimsar shale pore space and pore network visualization in Paraview; **(A)** pore space distribution, **(B)** pore network visualization.

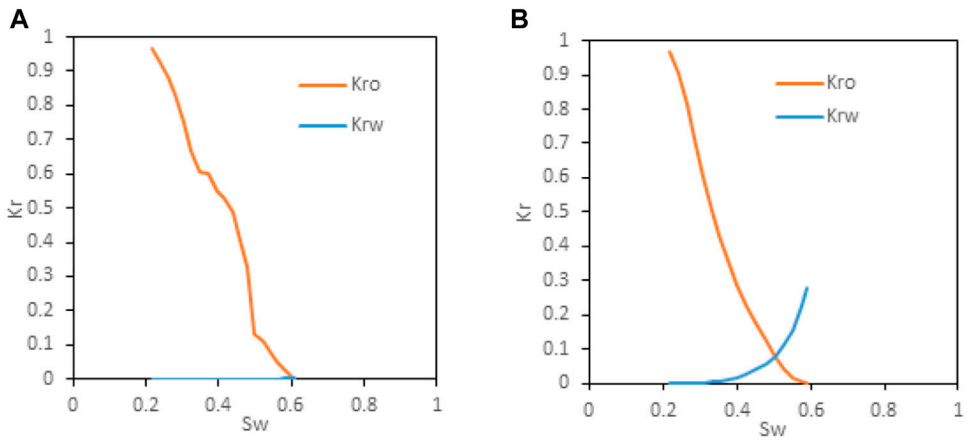

FIGURE 4 | Oil–water relative permeability of Jimsar shale with 50–50 mixed-wet conditions, **(A)** larger pores being oil-wet, **(B)** smaller pores being oil-wet.

oil-wet pores. The distribution of oil-wet pores plays a significant role in the oil-water flow mechanisms even though the overall wettability of both conditions is 50–50 mixed-wet. The future studies need to enlarge the pore network model to be more representative of the shale formations, which induces two challenges: experimental requirements and computational demand. The first one can be relieved by generating topological effective pore networks. The second challenge needs a more efficient pore network simulator, which is under the development of our future work.

CONCLUSION

A pore network model is proposed to simulate oil–water flow with mixed wettability scenarios. The model is applied in Berea sandstone, and the calculated relative permeabilities are validated with experimental studies for different wettability scenarios. Then the three-dimensional FIB-SEM imaging of the Jimsar shale sample is used to extract a representative shale pore network and our proposed model is used to investigating the oil–water flow mechanisms. The mean values of pores and throats are 29.75 and 19.13 nm, and the calculated absolute permeability is 0.005 mD. The calculated relative permeability curves show a high residual oil saturation for all the wettability conditions. The distribution of oil-wet pores plays a significant role in the oil-water flow mechanisms even though the overall wettability of both conditions is 50–50 mixed-wet.

DATA AVAILABILITY STATEMENT

The raw data supporting the conclusion of this article will be made available by the authors, without undue reservation.

AUTHOR CONTRIBUTIONS

All authors listed have made a substantial, direct, and intellectual contribution to the work and approved it for publication.

FUNDING

This work is supported by Beijing Municipal Natural Science Foundation (No. 2214077) and the Opening Fund of Key Laboratory of Unconventional Oil and Gas Development (China University of Petroleum (East China)), Ministry of Education (No. 19CX05005A-3).

REFERENCES

Ahrens, J., Geveci, B., and Law, C. (2005). Paraview: An End-User Tool for Large Data Visualization. *The visualization handbook*. 717 (8), 717–731. doi:10.1016/b978-012387582-2/50038-1

Blunt, M. J. (2017). *Multiphase Flow in Permeable media: A Pore-Scale Perspective*. Cambridge: Cambridge University Press.

Dong, H., and Blunt, M. J. (2009). Pore-Network Extraction From Micro-Computerized-Tomography Images. *Phys. Rev. E Stat. Nonlin Soft Matter Phys.* 80 (3), 036307. doi:10.1103/PhysRevE.80.036307

Guo, B., Ma, L., and Tchelepi, H. A. (2018). Image-Based Micro-Continuum Model for Gas Flow in Organic-Rich Shale Rock. *Adv. Water Resour.* 122, 70–84. doi:10.1016/j.advwatres.2018.10.004

Hagberg, A., Swart, P., and S Chult, D. (2008). *Exploring Network Structure, Dynamics, and Function Using NetworkX (No. LA-UR-08-05495; LA-UR-08-5495)*. Los Alamos, NM (United States): Los Alamos National Lab.(LANL).

Kelly, S., El-Sobky, H., Torres-Verdín, C., and Balhoff, M. T. (2016). Assessing the Utility of FIB-SEM Images for Shale Digital Rock Physics. *Adv. Water Resour.* 95, 302–316. doi:10.1016/j.advwatres.2015.06.010

Øren, P.-E., Bakke, S., and Arntzen, O. J. (1998). Extending Predictive Capabilities to Network Models. *SPE J.* 3 (04), 324–336. doi:10.2118/52052-pa

Pang, Y., Fan, D., and Chen, S. (2021). A Novel Approach to Predict Gas Flow in Entire Knudsen Number Regime Through Nanochannels With Various Geometries. *SPE J.*, 1–20. doi:10.2118/205506-pa

Pang, Y., Hu, X., Wang, S., Chen, S., Soliman, M. Y., and Deng, H. (2020). Characterization of Adsorption Isotherm and Density Profile in Cylindrical Nanopores: Modeling and Measurement. *Chem. Eng. J.* 396, 125212. doi:10.1016/j.cej.2020.125212

Rabbani, A., Jamshidi, S., and Salehi, S. (2014). An Automated Simple Algorithm for Realistic Pore Network Extraction from Micro-Tomography Images. *J. Pet. Sci. Eng.* 123, 164–171. doi:10.1016/j.petrol.2014.08.020

Raeini, A. Q., Blunt, M. J., and Bijeljic, B. (2014). Direct Simulations of Two-Phase Flow on Micro-CT Images of Porous Media and Upscaling of Pore-Scale Forces. *Adv. Water Resour.* 74, 116–126. doi:10.1016/j.advwatres.2014.08.012

Ramstad, T., Øren, P.-E., and Bakke, S. (2010). Simulation of Two-Phase Flow in Reservoir Rocks Using a Lattice Boltzmann Method. *Spe J.* 15 (04), 917–927. doi:10.2118/124617-pa

Ryazanov, A. V., Van Dijke, M. I. J., and Sorbie, K. S. (2009). Two-Phase Pore-Network Modelling: Existence of Oil Layers During Water Invasion. *Transp Porous Med.* 80 (1), 79–99. doi:10.1007/s11242-009-9345-x

Shanley, K. W., Cluff, R. M., and Robinson, J. W. (2004). Factors Controlling Prolific Gas Production From Low-Permeability Sandstone Reservoirs: Implications for Resource Assessment, Prospect Development, and Risk Analysis. *Bulletin.* 88 (8), 1083–1121. doi:10.1306/03250403051

Sheng, G., Su, Y., and Wang, W. (2019). A New Fractal Approach for Describing Induced-Fracture Porosity/Permeability/Compressibility in Stimulated Unconventional Reservoirs. *J. Pet. Sci. Eng.* 179, 855–866. doi:10.1016/j.petrol.2019.04.104

Sheng, G., Zhao, H., Su, Y., Javadpour, F., Wang, C., Zhou, Y., et al. (2020). An Analytical Model to Couple Gas Storage and Transport Capacity in Organic Matter With Noncircular Pores. *Fuel.* 268, 117288. doi:10.1016/j.fuel.2020.117288

Valvatne, P. H., and Blunt, M. J. (2004). Predictive Pore-Scale Modeling of Two-Phase Flow in Mixed Wet Media. *Water Resour. Res.* 40 (7), W07406. doi:10.1029/2003wr002627

Wang, X., and Sheng, J. J. (2018). Pore Network Modeling of the Non-Darcy Flows in Shale and Tight Formations. *J. Pet. Sci. Eng.* 163, 511–518. doi:10.1016/j.petrol.2018.01.021

Yang, Z., Hou, L., Lin, S., Luo, X., Zhang, L., Wu, S., et al. (2018). Geologic Characteristics and Exploration Potential of Tight Oil and Shale Oil in Lucaogou Formation in Jimsar Sag. *China Pet. Exploration.* 23 (4), 76–85. doi:10.3969/j.issn.1672-7703.2018.04.009

Conflict of Interest: Author ZZ is employed by China National Oil and Gas Exploration and Development Company Ltd.

The remaining authors declare that the research was conducted in the absence of any commercial or financial relationships that could be construed as a potential conflict of interest.

Publisher's Note: All claims expressed in this article are solely those of the authors and do not necessarily represent those of their affiliated organizations, or those of the publisher, the editors and the reviewers. Any product that may be evaluated in this article, or claim that may be made by its manufacturer, is not guaranteed or endorsed by the publisher.

frontiers in Earth Science

ORIGINAL RESEARCH
published: 22 September 2021
doi: 10.3389/feart.2021.751626

Numerical Investigation of the Fracturing Effect Induced by Disturbing Stress of Hydrofracturing

Xinglong Zhao[1,2], *Bingxiang Huang*[1]* *and Giovanni Grasselli*[2]

[1]State Key Laboratory of Coal Resources and Safe Mining, China University of Mining and Technology, Xuzhou, China, [2]Department of Civil and Mineral Engineering, University of Toronto, Toronto, ON, Canada

Fracturing induced by disturbing stress of hydraulic fracturing is the frontier common core scientific problem of reservoir stimulation of coal bed methane and shale gas. The finite-discrete element method, numerical calculation method, is used to analyze the basic law of shear failure and tension failure of natural fractures induced by the disturbing stress of the hydraulic fracture. The simulation results show that when natural fractures and other weak structures exist on the front or both sides of hydraulic fracture, the shear stress acting on the surface of natural fracture will increase until the natural fracture failure, which is caused by the disturbing stress of hydraulic fracturing. The seepage area on the front and both sides of the hydraulic fracture did not extend to the natural fracture while the natural fracture failure occurred. It indicates that the shear failure of natural fractures is induced by the disturbing stress of hydraulic fracturing. When the hydraulic fracture propagates to the natural fracture, the hydraulic tension fracture and disturbed shear fractures are connected and penetrated. As the fluid pressure within the natural fracture surface increases, the hydraulic fracture will continue to propagate through the natural fracture. Meanwhile, due to the action of fluid pressure, a tensile stress concentration will occur at the tip of the natural fracture, which will induce the airfoil tension failure of the natural fracture. With the increase of the principal stress difference, the range of the disturbing stress area and the peak value of the disturbing stress at the front of the hydraulic fracture tip increase, as well as the shear stress acting on the natural fracture surface. During the process of hydraulic fracture approaching natural fracture, the disturbing stress is easier to induce shear failure of natural fracture. With the increase of the cohesive force of natural fracture, the ability of natural fractures to resist shear failure increases. As the hydraulic fracture approaches natural fractures, the disturbing stress is more difficult to induce shear failure of natural fracture. This study will help to reveal the formation mechanism of the fracture network during hydraulic fracturing in the natural fractures developed reservoir.

Keywords: hydraulic fracturing, stress disturbance, disturbing stress, natural fracture, tension fracturing, shear fracturing

OPEN ACCESS

Edited by:
Yu Pang,
University of Calgary, Canada

Reviewed by:
Chun Yang,
McGill University, Canada
Xingwang Shi,
China Coal Research Institute, China

***Correspondence:**
Bingxiang Huang
huangbingxiang@cumt.edu.cn

Specialty section:
This article was submitted to Economic Geology, a section of the journal Frontiers in Earth Science

Received: *01 August 2021*
Accepted: *01 September 2021*
Published: *22 September 2021*

Citation:
Zhao X, Huang B and Grasselli G (2021) Numerical Investigation of the Fracturing Effect Induced by Disturbing Stress of Hydrofracturing. Front. Earth Sci. 9:751626. doi: 10.3389/feart.2021.751626

INTRODUCTION

Hydraulic fracturing technology was first applied to the development of oil and gas wells to improve the flow capacity of fluids in oil and gas reservoirs. It is a key measure for increasing the production of oil and gas wells with broad application prospects. At present, it is also the main reservoir stimulation technology for oil and natural gas exploitation (Burrows et al., 2020; Liu et al., 2020; Zhang et al., 2020). In order to achieve sufficient gas flow rates in shale gas, tight gas, tight oil, and coalbed methane wells, it is usually necessary to perform hydraulic fracturing to improve the permeability of the reservoir. In recent years, it has been widely used in the coal industry. Significant results have been achieved in the use of hydraulic fracturing technology for hard roof control, hard top coal weakening, coal seam permeability improvement, coal and gas outburst prevention, and rock burst prevention (Huang et al., 2015; Huang et al., 2016; Huang et al., 2017).

In the process of hydraulic fracturing, with the initiation and propagation of hydraulic fractures, the magnitude and distribution of stress around the hydraulic fractures also change. It is called the "stress disturbance" effect of hydraulic fracturing, which is known as the "stress shadow" effect in the oil industry (Roegiers and Bennaceur, 1990; Cheng, 2007). The stress caused by the stress disturbance effect of hydraulic fracturing is called disturbing stress.

There are complex natural fractures in the coal seam, including joints, bedding, and cleats. These naturally developed weak structural planes together form the natural fracture network structure of the coal seam. When hydraulic fracturing is performed in the coal seam with developed natural fractures, the disturbing stress of hydraulic fracturing will induce the natural fractures breaking around the hydraulic fractures, that is, the fracturing effect induced by disturbing stress of hydraulic fracturing. The practice of hydraulic fracturing in underground coal seams with shock tendency shows that the process of hydraulic fracturing weakens the coal strength to prevent shock which may be accompanied by "coal cannon." The position of the coal cannon is not necessarily exactly the same as the position of the hydraulic crack (Zhao, 2019) (**Figure 1**). It shows that the fractures formed during the hydraulic fracturing process not only include the fractures generated under the action of water pressure but also include the ruptures of natural fractures induced by the disturbing stress of hydraulic fracturing.

Many studies have been done on the interaction between natural cracks and artificial cracks. Related experimental research results show that the propagation of hydraulic fractures becomes very irregular due to the interference of natural fractures. The existence of natural fracture media causes a large amount of fluid loss, which induce the main hydraulic fracture to propagate along the natural fractures (Chen et al., 2008; Yang et al., 2012; Chen et al., 2013; Hu and Ghassemi, 2021). These studies are all aimed at the object that high-pressure water drives the natural fractures to open and extend after the hydraulic fractures propagate to natural fractures and high-pressure water enters the natural fractures. There is no research involving the break of the natural fractures induced by the disturbing stress of hydraulic fracturing.

Based on the author's previous study of the stress disturbance of hydraulic fracturing, this paper focuses on the disturbing stress of hydraulic fracturing inducing the break of natural fractures around the hydraulic fracture. The combined finite-discrete element method (FDEM) numerical calculation is utilized to analyze the basic law of shear failure and tension failure of natural fractures induced by the disturbing stress on the front and both sides of hydraulic fractures during the hydraulic fracturing process.

The fracturing induced by disturbing stress of hydraulic fracturing is a common and core scientific problem in the

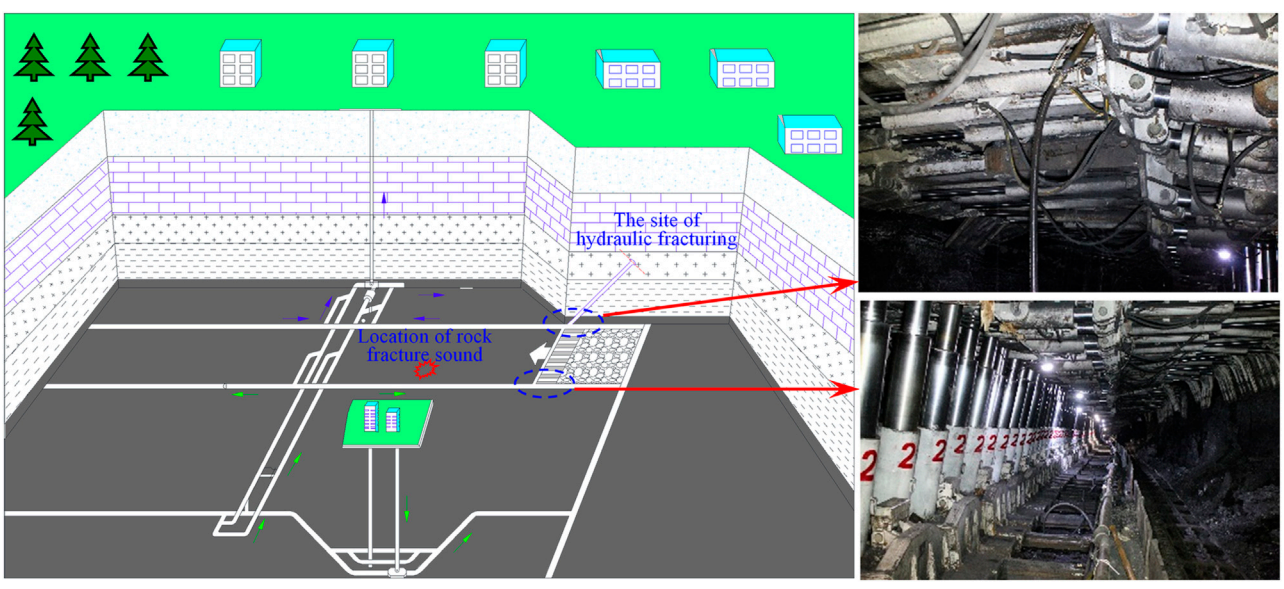

FIGURE 1 | Position of "coal cannon" during hydraulic fracturing in underground coal mines.

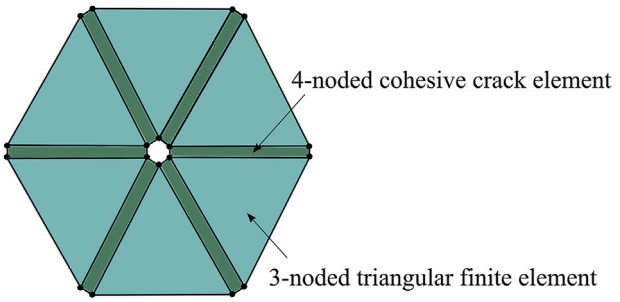

FIGURE 2 | The continuum was discretized using cohesive elements interspersed throughout a mesh of triangular elements.

fracturing of coalbed methane, shale gas, and dry hot rock. The fractures caused by the disturbing stress are a component of the fracture network during fracturing in the natural fractures developed reservoir. The fractures induced by the disturbing stress and the hydraulic fractures together form a fracture network structure. Studying the fracturing effect induced by disturbing stress of hydraulic fracturing will help to reveal the formation mechanism of the fracture network during hydraulic fracturing in the natural fractures developed reservoir. The research result will provide a more comprehensive theoretical basis for determining the fracturing technology and parameters of coalbed methane and shale gas reservoirs.

FDEM NUMERICAL CALCULATION PRINCIPLE

FDEM is a numerical method originally developed by Munjiza et al. It allows dynamic simulation of the interaction between multiple objects. The simulated object can be a single complete domain or a complete domain composed of a group of discrete bodies. During the simulation process, these objects can undergo elastic deformation, translation, rotation, interaction, and fracture when the rupture criterion is met, thereby generating new discrete bodies. Then, the newly created object can move further, interact, deform, and fracture. FDEM can well simulate the transition from continuous to discontinuous behavior in rock masses. It combines the advantages of finite element method (FEM) in describing elastic deformation and the ability of discrete element method (DEM) to capture discontinuities. Finite element method (FEM) is used to deal with material deformation and the process of evaluating material failure. Discrete element method (DEM) is used to detect new contacts and deal with the translation, rotation, and interaction of discrete bodies (Munjiza et al., 1995; Munjiza and Andrews, 1998; Munjiza et al., 1999; Munjiza and Andrews, 2000; Munjiza and John, 2002). Therefore, the FDEM method can effectively realize the hydraulic fracturing simulation of coal and rock mass.

The Basic Principle of FDEM

In FDEM, the continuum is discretized into three-node triangular elements and four-node cohesive elements with no thickness initially embedded on the common side of adjacent triangular elements (**Figure 2**). The constant strain linear elastic triangle element is used to capture the elastic deformation of the material. The failure of the inelastic crack element is used to simulate the initiation and propagation of fractures in the continuum (Munjiza, 2004).

Control Equation

The triangular element updates the displacement and velocity of the node according to the unbalanced force of the node according to Newton's second law. The generalized motion control equation can be expressed as follows (Lisjak and Grasselli, 2014):

$$\mathrm{M}\frac{\partial^2 x}{\partial t^2} + C\frac{\partial x}{\partial t} + F_{\mathrm{int}}(x) + F_{ext}(x) - F_c(x) = 0, \qquad (1)$$

where M and C are the system mass and damping matrix, respectively; x is the nodal displacement vector; and F_{int}, F_{ext}, and F_c are the internal force, external load, and contact force, respectively. The internal force includes the elastic reaction force and the cohesive force between elements. The external nodal force is the boundary condition of the model. In order to simulate quasi-static phenomena through dynamic relaxation or nonlinear behavior, numerical damping C is used in the control equation to consider the energy dissipation of the system.

Material Damage and Failure Modes

Nonlinear fracture mechanics is used to simulate the failure process of materials. When the stress in the front area of the fracture tip reaches the tensile strength of the material, a fracture process zone is formed at the front of the fracture tip (FPZ) (**Figure 3A**). The material force in this region exhibits nonlinear behavior. Although the material in the fracture process zone FPZ has been damaged, it can still transmit the load to the fracture wall (Lisjak et al., 2017). In FDEM, assuming that the fracture surface coincides with the edge of the triangular element, the fracture process zone is characterized by the four-node bond fracture element (**Figure 3B**).

According to the local stress and deformation fields, the fracture unit will yield and fail. There are three failure modes, namely, Mode I tensile failure, Mode II shear failure, and mixed Mode I-II composite failure (Geomechanica Inc, 2018; Liu et al., 2018) (**Figure 4**).

(1) Mode I tensile failure: before the fracture initiates, the stress at the fracture tip has a linear relationship with the opening between the two triangular elements. When the opening O between the two triangular elements reaches the critical value O_P, the Mode I fracture initiates and begins to propagate. The opening O_P when the Mode I fracture opens and initiates is related to the inherent tensile strength of the unit. After the fracture initiates, the normal cohesive force between the triangular elements will not disappear immediately, but will gradually decrease with the increase of the fracture opening. When the opening reaches the residual value O_r, the normal cohesive force between the elements drops to zero, resulting in a stress-free surface, which is the real fracture surface (**Figure 4A**).

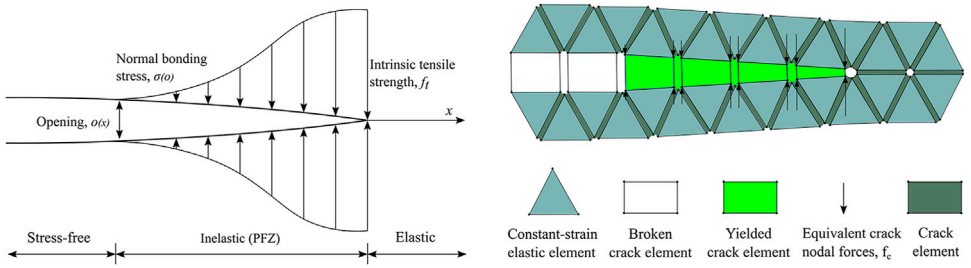

FIGURE 3 | (A) Fracture process zone (FPZ) and **(B)** Numerical characterization in FDEM.

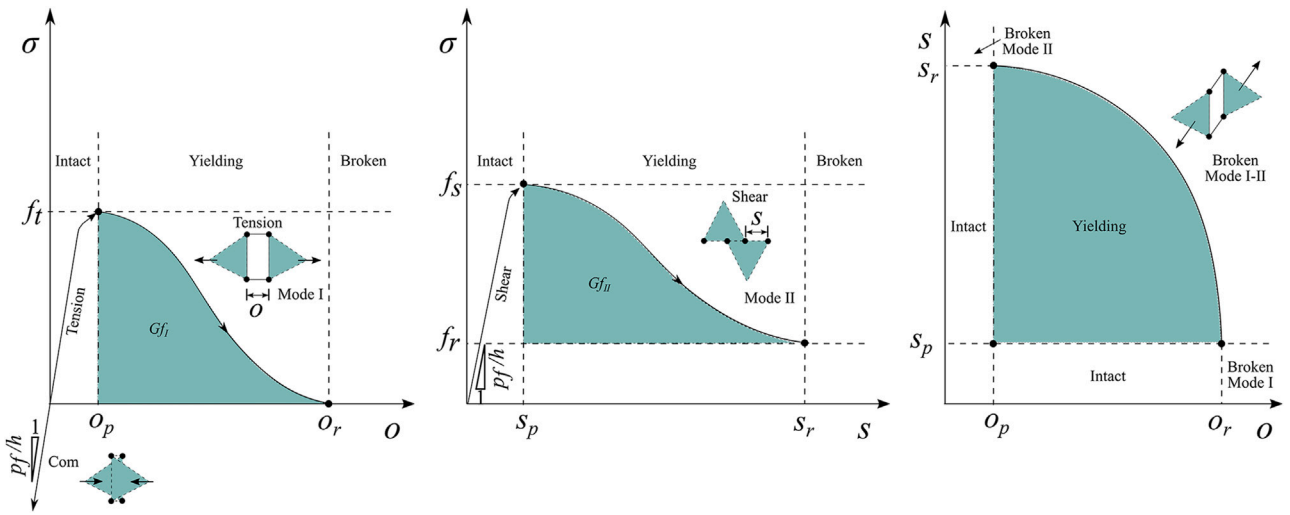

FIGURE 4 | The failure modes in FDEM. **(A)** Mode I tensile failure; **(B)** Mode II shear failure; **(C)** mixed Mode I-II failure.

(2) Mode II shear failure: the tangential cohesive force between triangular elements is a function of slip distance and normal stress (**Figure 4B**). When the tangential slip distance S between the fracture units reaches the critical value S_P, the Mode II fracture initiates and begins to propagate. The slip distance S_P when the Mode II fracture slips and initiates is related to the inherent tensile strength f_s of the element:

$$f_s = c + \sigma_n \tan\phi, \tag{2}$$

where c is the cohesive force; ϕ is the friction angle; and σ_n is the normal stress acting on the fracture element.

When the fracture slip distance is greater than the critical slip distance S_P, the tangential stress between the triangular elements gradually decreases to the residual value f_r. At this time, the shear fracture surface is formed, and the shear stress is equal to the net frictional resistance:

$$f_r = \sigma_n \tan\phi_r, \tag{3}$$

where ϕ is the residual friction angle.

(3) Mixed Mode I-II failure: in addition to pure tension failure and pure shear failure, the fracture unit will also have a mixed failure of two failure modes. Therefore, the coupling failure criterion of Mode I tensile failure and Mode II shear failure is defined (**Figure 4C**):

$$\left(\frac{O - O_P}{O_r - O_P}\right)^2 + \left(\frac{S - S_P}{S_r - S_P}\right)^2 \geq 1, \tag{4}$$

where O is the opening distance and S is the slipping distance.

The residual opening distance O_r and the residual sliding distance S_r depend on the Mode I energy release rate Gf_{I} and the Mode II energy release rate Gf_{II}:

$$Gf_{\mathrm{I}} = \int_{o_p}^{o_r} \sigma(o)do, \tag{5}$$

$$Gf_{\mathrm{II}} = \int_{s_p}^{s_r} |\tau_s - f_r| ds. \tag{6}$$

The Hydraulic-Mechanical Coupling Principle in FDEM

When FDEM is used to simulate hydraulic fracturing, fluid pressure is applied at the injection node. The nodal force as

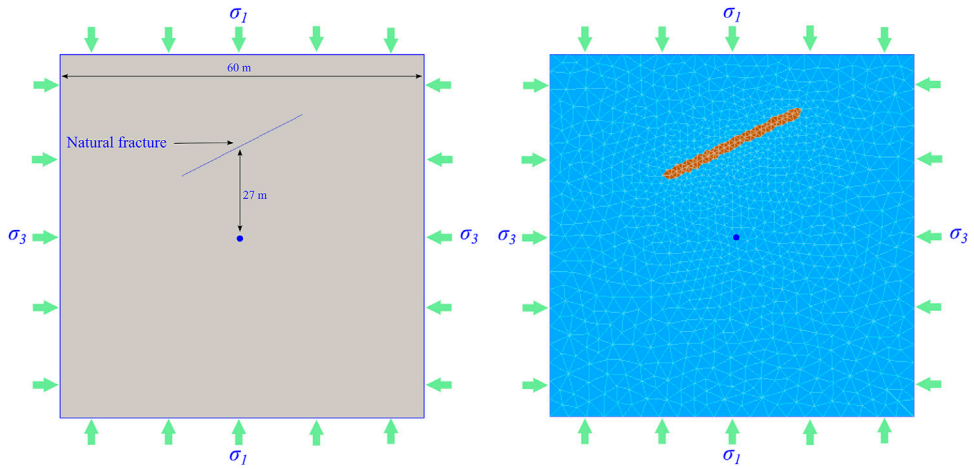

FIGURE 5 | Numerical model for case 1. **(A)** Geometry model; **(B)** meshing.

TABLE 1 | Numerical simulation program for case 1.

No.	Stress field		Stress difference/MPa	Cohesion, C/MPa
	σ_1/MPa	σ_3/MPa		
1	12.5	5.0	7.5	1.0
2	12.5	7.5	5.0	1.0
3	12.5	10.0	2.5	1.0
4	12.5	5.0	7.5	1.5
5	12.5	5.0	7.5	2.0

the external load is calculated by **Eq. 1**. After hydraulic fracturing, a fluid flow channel is created through the interface between adjacent triangular finite elements. The Darcy's law and parallel plate cube law are utilized to calculate the fluid flow process in the flow channel. The fluid pressure at the nodes of the fracture network is updated to drive the continuous propagation of the fractures (Labuz et al., 1985; Liu et al., 2018).

The hydraulic-mechanical coupling analysis in FDEM adopts a two-way explicit coupling analysis method. Iterative sequential solution is performed through data exchange between the mechanical solver and the hydraulic solver. The calculation of the mechanical field is affected by the fluid pressure between the internal cells. Meanwhile, due to the deformation and destruction of the solid, the calculation of the fluid field is affected by the opening between the finite elements.

FDEM NUMERICAL MODEL DESIGN

The disturbing stress concentration areas in the process of hydraulic fracture propagation are mainly distributed in the front of the fracture tip and on both sides of the main fracture. Therefore, two situations will be analyzed by two cases. Case 1 is the opening and propagation of natural fractures in front of the hydraulic fractures tip induced by disturbing stress. Case 2 is the opening and propagation of natural fractures on both sides of the hydraulic fractures induced by disturbing stress. The size of the numerical model is 60 m × 60 m.

Case 1: Disturbing Stress at the Front of Hydraulic Fractures Induces Natural Fractures to Open and Propagate

Numerical Model

An inclined natural fracture is set up in the direction of hydraulic fracture propagation in case 1. The length of the natural fracture is 23 m, and the distance from the hydraulic fracturing injection point is 27 m. When the hydraulic fractures are approaching natural fractures, the failure process of natural fractures induced by the disturbing stress at the front of the hydraulic fracture tip will be analyzed (**Figure 5**).

Simulation Scheme and Parameter Setting

The numerical simulation scheme of case 1 is shown in **Table 1**. The influence of principal stress difference and natural fracture cohesion on the failure of natural fractures in the process of hydraulic fracture approaching natural fracture will be mainly studied. The fluid bulk modulus is 5×10^7 Pa, and the kinematic viscosity is 1.004 × 10–6 m^2/s. The pump rate is 0.3 L/s. The input parameters of the model are shown in **Table 2**.

Case 2: Disturbing Stress on Both Sides of Hydraulic Fractures Induces Natural Fractures to Open and Propagate

Numerical Model

Two inclined natural fractures are set up on both sides of the hydraulic fracture propagation direction, respectively, in case 2. The length of the natural fracture is 5.6 m, and the distance from the hydraulic fracturing injection point is 6 m (**Figure 6**). The failure laws of natural fractures under the action of the disturbing stress on both sides of the hydraulic fractures will be analyzed.

TABLE 2 | The input parameter for FDEM model for case 1.

Parameter	Triangular finite element	Natural fracture element
Density/g/cm^3	1.40	—
Young's modulus/GPa	6.00	—
Poisson' ratio	0.25	—
Friction coefficient	0.58	0.45
Cohesion/MPa	5.00	0.25
Tensile strength/MPa	1.20	0.12
Mode I fracture energy/N/m	10	1
Mode II fracture energy/N/m	100	5

Simulation Scheme and Parameter Setting

The stress field loading of case 2 is σ_1 = 12.5 MPa and σ_3 = 5.0 MPa, respectively. The fluid bulk modulus is 5×10^7 Pa. The kinematic viscosity is 1.004×10^{-6} m^2/s. The pump rate is 0.5 L/s. The input parameters of the model are the same as in case 1 (**Table 2**).

DISTURBING STRESS AT THE FRONT OF HYDRAULIC FRACTURES INDUCES NATURAL FRACTURES TO OPEN AND PROPAGATE

The Failure Law of Natural Fractures in the Process of Hydraulic Fractures Approaching

The fracture shape and the distribution of fluid pressure, vertical stress, and shear stress in the process of hydraulic fracture approaching natural fracture are shown in **Figure 7**. When the injection time is 0.387 s, the peak water pressure in the hydraulic fracture is 8.1 MPa, the propagation length of the hydraulic fracture is 10.32 m, and the distance between the hydraulic fracture tip and the natural fracture is 10.05 m. At this time, the maximum vertical stress acting on the surface of the natural fracture is 14.2953 MPa, and the maximum shear stress is 1.05 MPa, both of which are located at the tip of the natural fracture (**Figure 7A**).

With the approach of hydraulic fractures, the shear stress acting on the natural fracture surface gradually increases. When the injection time is 0.430 s, the peak water pressure in the hydraulic fracture is 7.3 MPa, the propagation length of the hydraulic fracture is 11.18 m, and the distance between the hydraulic fracture tip and the natural fracture is 8.31 m. At this time, shear failure appears at the natural fracture. The maximum vertical stress acting on the natural fracture surface is 14.2967 MPa, and the maximum shear stress is 1.08 MPa, both of which are located at the shear fracturing (**Figure 7B**).

When shear failure appears at the natural fracture, the hydraulic fracture tip and frontier water seepage area have not propagated to the natural fractures, which indicates that the shear failure of natural fractures is not induced by water pressure, but the disturbing stress induced by the propagation of hydraulic fractures. That is, the disturbing stress at the front of the hydraulic fracture tip induces shear failure of the natural fracture.

With the hydraulic fracture tip gradually approaching the natural fracture, the shear stress on the natural fracture surface further increases and shear failure continues to occur. When the injection time is 0.882 s, the tip of the hydraulic fracture propagates to the natural fracture and connects with the natural fracture. Shear failure occurred at the junction of natural fractures and hydraulic fractures. At this time, the peak water pressure in the fracture is 7.1 MPa; the maximum vertical stress on the natural fracture surface is 14.50 MPa. The maximum shear stress is 1.74 MPa (**Figure 7C**).

After the hydraulic fracture is connected with the natural fracture, the water pressure gradually fills the natural fracture, which causes the water pressure acting on the surface of the natural fracture to gradually rise. When the injection time is

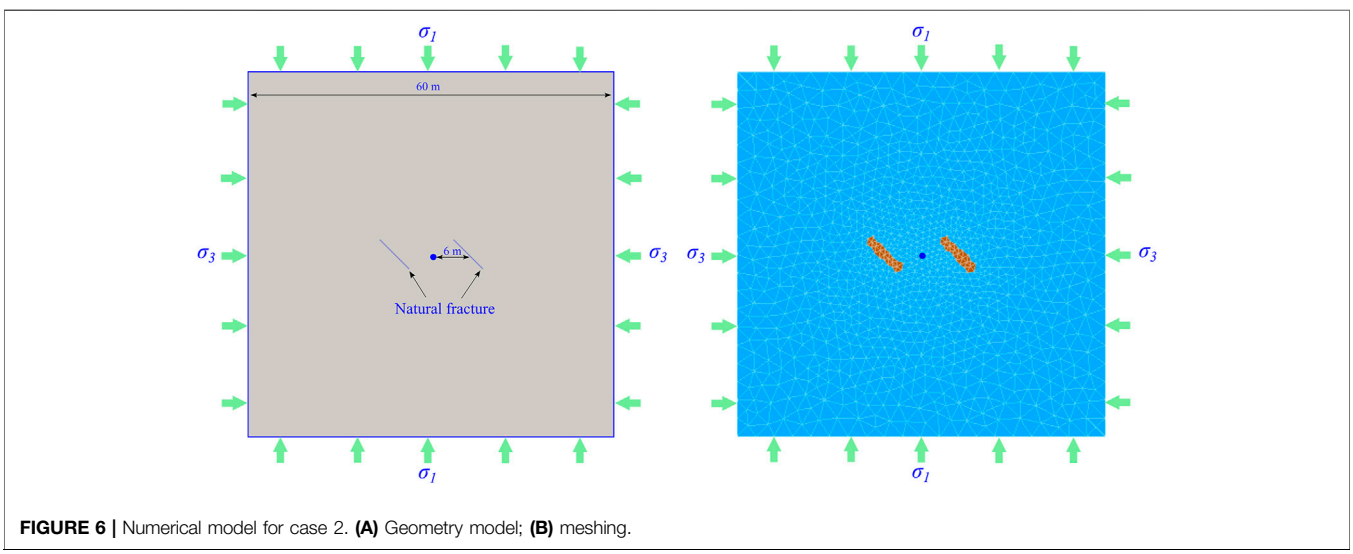

FIGURE 6 | Numerical model for case 2. **(A)** Geometry model; **(B)** meshing.

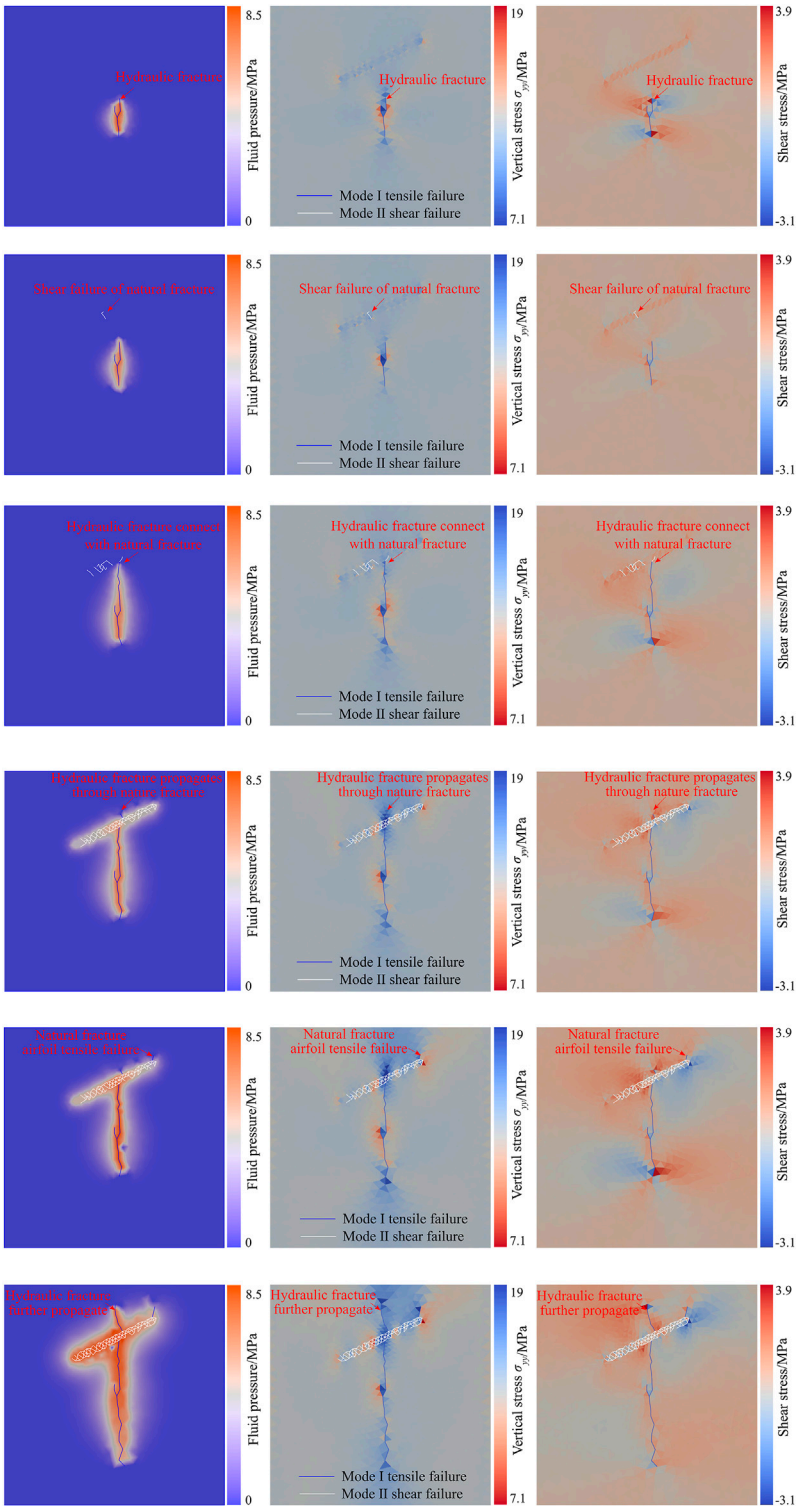

FIGURE 7 | The distribution of fluid pressure, vertical stress, and shearing stress during hydraulic fractures propagation. **(A)** t = 0.387 s; **(B)** t = 0.430 s; **(C)** t = 0.882 s; **(D)** t = 1.462 s; **(E)** t = 1.634 s; **(F)** t = 3.354 s.

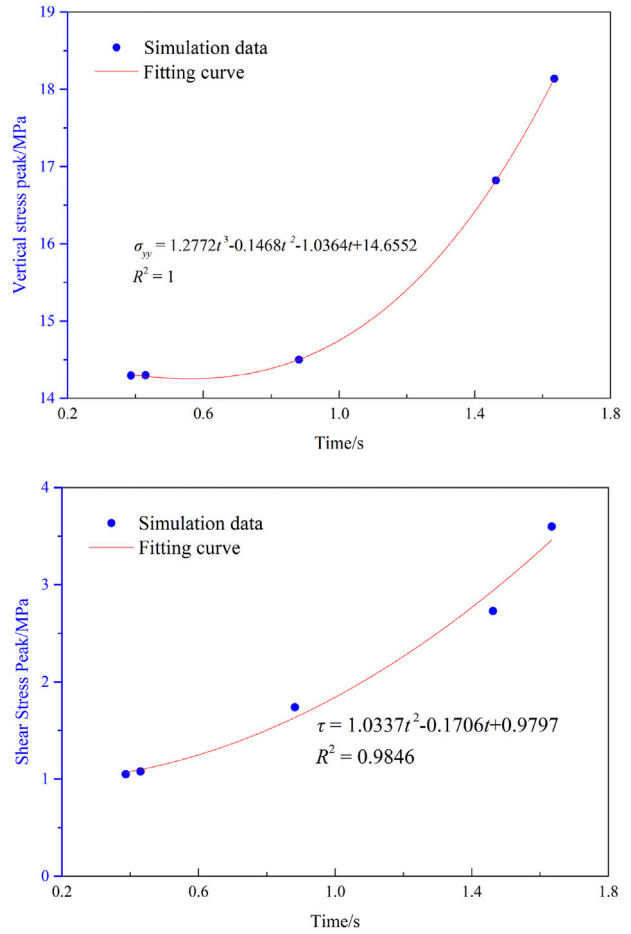

FIGURE 8 | The stress peaks of natural fracture during hydraulic fracturing. **(A)** Vertical stress peak; **(B)** shear stress peak.

1.462 s, the hydraulic fracture propagates through the natural fracture. At this time, the peak water pressure in the fracture is 7.2 MPa, the maximum vertical stress on the natural fracture surface is 16.82 MPa, and the maximum shear stress is 2.73 MPa (**Figure 7D**).

When the injection time is 1.634 s, the airfoil tension failure occurs in the natural fracture. At this time, the peak water pressure in the fracture is 8.5 MPa, the maximum vertical stress on the natural fracture surface is 18.14 MPa, and the maximum shear stress is 3.60 MPa. After the hydraulic fracture propagates through the natural fracture, as the water pressure in the natural fracture increases, tensile stress concentration tends to occur at the tip of natural fracture. When the tensile stress reaches the tensile strength, the natural fracture will undergo airfoil tension failure (**Figure 7E**). As the pumping injection continues, hydraulic fracture and airfoil fractures of natural fracture alternately propagate (**Figure 7F**).

During the hydraulic fractures propagation, the front area of the hydraulic fracture tip is squeezed along the fracture propagation direction, resulting in a compressive stress concentration zone, that is, a disturbing stress area. When there are weak structures such as natural fractures in the propagation direction of hydraulic fractures, the disturbing stress generated by hydraulic fracturing will increase the shear stress of the natural fracture surface. It will induce shear failure of the natural fractures, that is, the fracturing effect induced by disturbing stress of hydraulic fracturing. With the propagation of hydraulic fractures, the disturbing stress on natural fractures gradually increases (**Figure 8A**). The shear stress also gradually increases (**Figure 8B**), and the range of shear failure of natural fractures increases accordingly. When the hydraulic fracture propagates to a natural fracture, the hydraulic tension fracture and the disturbed shear fracture will be connected.

In the process of hydraulic fractures approaching natural fractures, the failure mode of natural fractures includes both shear failure and tensile failure. Because the disturbance range of matrix stress during hydraulic fracturing is larger than the range of water seepage (disturbance range of pore pressure), the shear failure of natural fractures occurs before hydraulic fractures and pressure water seepage area propagates to natural fractures. Therefore, the reason for the shear failure of natural fractures is that the disturbing stress of hydraulic fracturing causes the shear stress acting on the natural fractures to increase. When the hydraulic fractures propagate to natural fractures, the water pressure gradually fills up the natural fractures. With the increase of water pressure in natural fractures, due to the existence of water wedge effect, tensile stress concentration is generated at the tip of natural fracture, which eventually induces the airfoil tensile failure and propagation of natural fracture. Therefore, the tensile failure of natural fractures is caused by the action of fluid pressure. As the natural fractures are filled with water pressure, the failure mode of natural fractures changes from shear failure to tensile failure.

Influencing Factors

The Influence of Principal Stress Difference

The hydraulic fracture propagation process and the distribution of fluid pressure, vertical stress, and shear stress under different principal stress differences are shown in **Figure 9**. When the principal stress difference is 7.5 MPa, shear failure of the natural fracture appears at t = 0.387 s. When the natural fracture occurs for the first time, the hydraulic fracture has not yet propagated to the natural fracture. At this time, the peak water pressure in the fracture is 7.3 MPa. The propagation length of the hydraulic fracture is 11.18 m. The distance between the hydraulic fracture tip and the natural fracture is 8.31 m. The maximum vertical stress on the natural fracture surface is 14.2967 MPa, and the maximum shear stress is 1.08 MPa, both of which are located at the shear fracturing (**Figure 9A**). Afterward, with the increase of water pressure in the fracture, the hydraulic fracture first passes through the natural fracture and continues to propagate. Then, airfoil failure occurs at the natural fracture. When airfoil propagation occurs in the natural fracture, the peak water pressure in the fracture is 8.5 MPa. The maximum vertical stress on the natural fracture surface is 18.14 MPa, and the maximum shear stress is 3.60 MPa (**Figure 9B**).

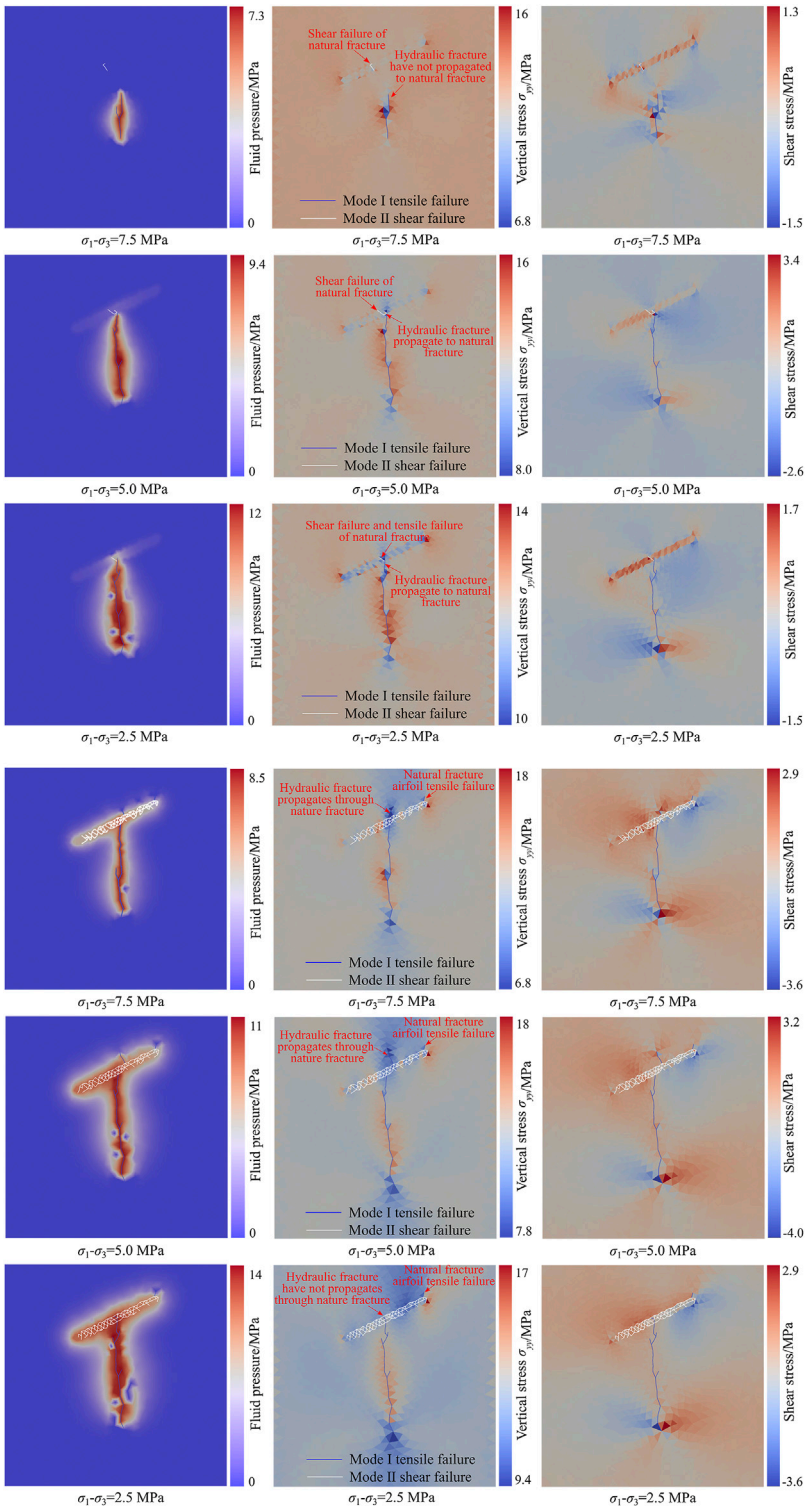

FIGURE 9 | The distribution of fluid pressure, vertical stress, and shearing stress during hydraulic fractures propagation under different principal stress differences. **(A)** First failure of natural fractures; **(B)** airfoil propagation of natural fractures.

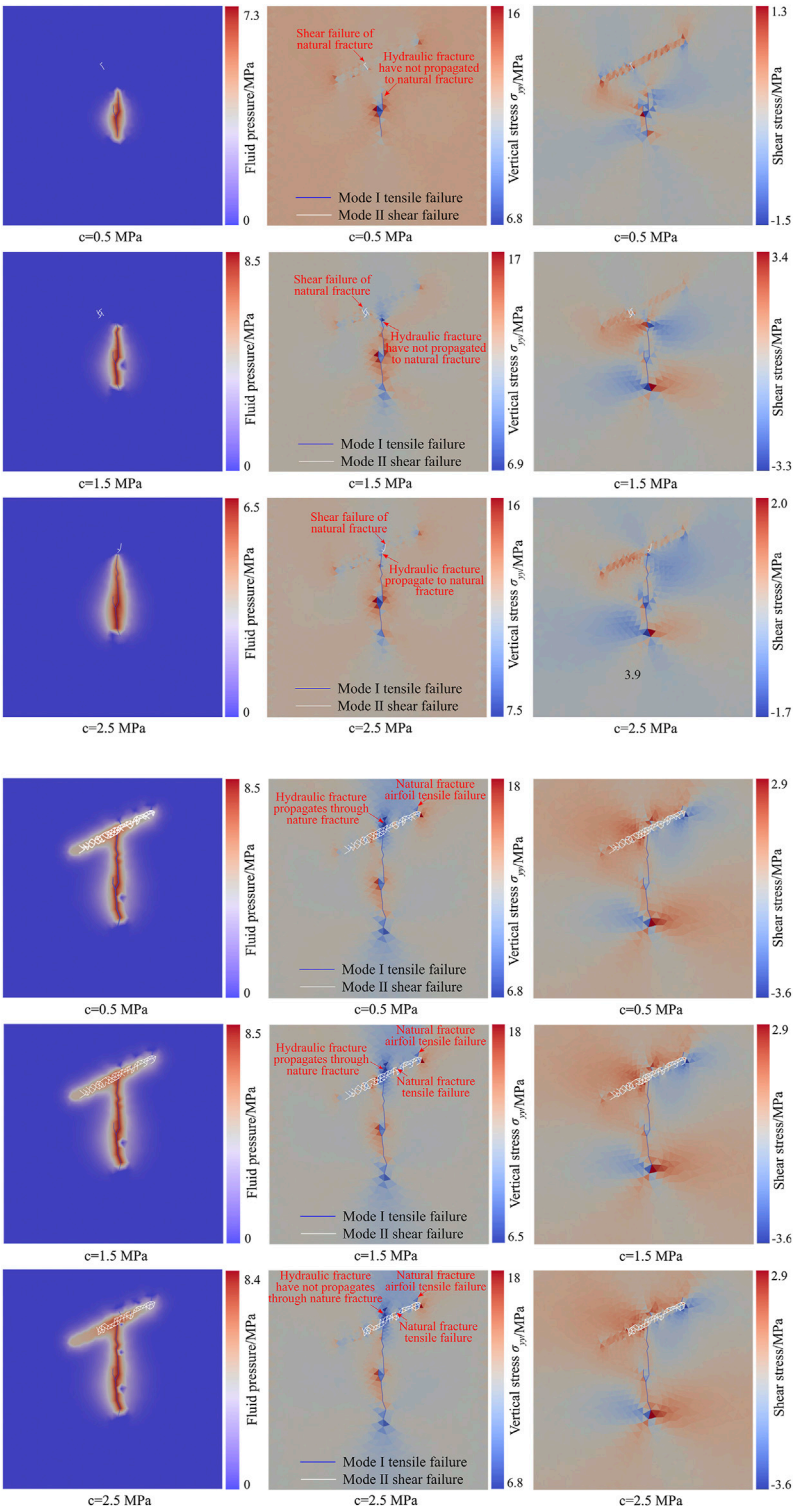

FIGURE 10 | The relationship between the vertical stress peak of natural fracture and the difference of principal stress during hydraulic fracturing. **(A)** Vertical stress peak; **(B)** shear stress peak.

When the principal stress difference is 5.0 MPa, shear failure occurs at the natural fracture after the hydraulic fracture propagates to the natural fracture. At this time, the peak water pressure in the fracture is 9.4 MPa. The maximum vertical stress on the natural fracture surface is 14.32 MPa, and the maximum shear stress is 1.58 MPa (**Figure 9A**). Since then, as the pumping injection continues, the hydraulic fractures first pass through the natural fractures and continue to propagate, and then airfoil failure occurs at the natural fractures. When the airfoil propagation of the natural fracture occurs, the peak water pressure in the fracture is 11.0 MPa. The maximum vertical stress on the natural fracture surface is 17.97 MPa, and the maximum shear stress is 3.49 MPa (**Figure 9B**).

When the principal stress difference is 2.5 MPa, both shear and tensile failures occurs at the natural fracture after the hydraulic fracture propagates to the natural fracture. At this time, the peak water pressure in the fracture is 12.0 MPa, the maximum vertical stress on the natural fracture surface is 14.10 MPa, and the maximum shear stress is 1.41 MPa (**Figure 9A**). When the hydraulic fracture is connected to the natural fracture, due to the high water pressure in the fracture, the tensile stress at the fracture tip is relatively large so that the tensile failure and shear failure occur at natural fracture simultaneously. After that, as the pumping injection continued, airfoil failure occurs at the natural fractures. The hydraulic fractures did not propagate through the natural fractures. When airfoil crack propagates, the peak water pressure in the fracture is 14.0 MPa. The maximum vertical stress on the natural fracture surface is 17.00 MPa, and the maximum shear stress is 2.90 MPa (**Figure 9B**).

With the increase of the principal stress difference, the range and peak value of the disturbing stress in the front of the hydraulic fracture tip increase (**Figure 10A**), and the shear stress on the natural fracture surface also increases accordingly (**Figure 10B**). In the process of hydraulic fractures approaching natural fractures, the more easily the disturbing stress induces shear failure of natural fractures. On the other hand, as the principal stress difference decreases, the water pressure in the fracture rises accordingly. The tensile stress at the tip of the hydraulic fracture becomes larger. When the hydraulic fracture and the natural fracture are connected, natural cracks will also undergo tensile failure while shearing failure occurs. At the same time, the reduction of the principal stress difference leads to an increase in the ability of coal and rock mass to resist tensile failure during the hydraulic fracturing. After the hydraulic fracture propagates to the natural fracture, the ability to pass through the natural fracture is reduced. When the principal stress difference increases to a certain degree, after the hydraulic fracture propagates to the natural fracture, it will not pass through the natural fracture, but will undergo airfoil propagation along the natural fracture.

The Influence of Natural Fracture Cohesion

The hydraulic fracture propagation process and the distribution of fluid pressure, vertical stress, and shear stress under different natural fracture cohesions are shown in **Figure 11**. When the cohesion of a natural fracture is 1.0 MPa, shear failure of the

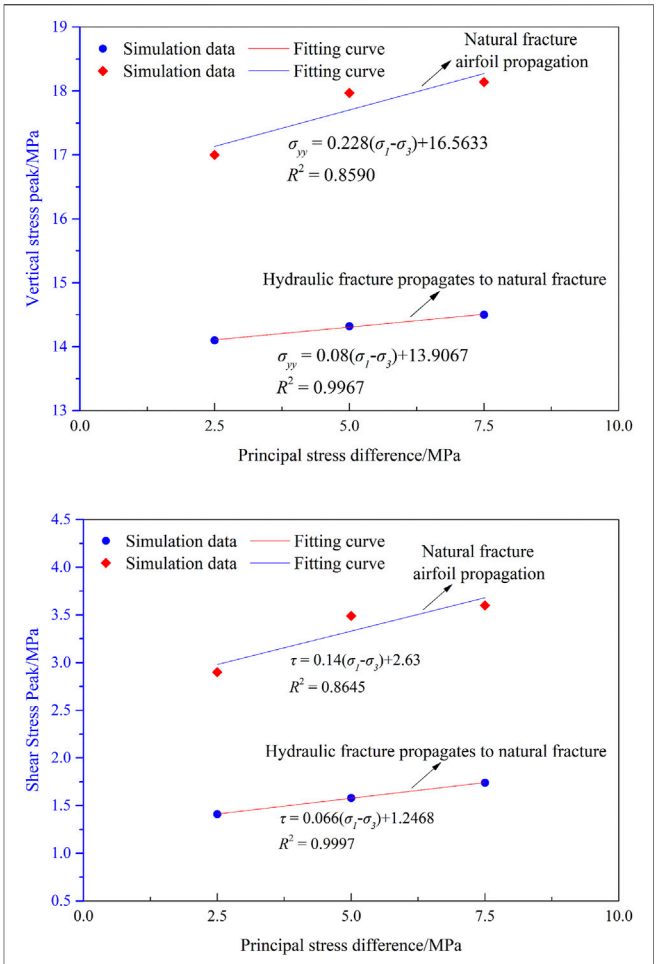

FIGURE 11 | The distribution of fluid pressure, vertical stress, and shearing stress during hydraulic fractures propagation under different cohesive of natural fracture. **(A)** First failure of natural fractures; **(B)** airfoil propagation of natural fractures.

natural fracture occurs at t = 0.387 s. When the natural fracture occurs for the first time, the hydraulic fracture has not yet propagated to the natural fracture. At this time, the peak water pressure in the fracture is 7.3 MPa. The propagation length of the hydraulic fracture is 11.18 m, and the distance between the hydraulic fracture tip and the natural fracture is 8.31 m. The maximum vertical stress on the natural fracture surface is 14.2967 MPa, and the maximum shear stress is 1.08 MPa, both of which are located at the shear fracturing (**Figure 11A**). Afterward, with the increase of water pressure in the fracture, the hydraulic fracture first passes through the natural fracture and continues to propagate, and then the airfoil failure occurs at natural fracture. When the airfoil propagation of the natural fracture occurs, the peak water pressure in the fracture is 8.5 MPa. The maximum vertical stress on the natural fracture surface is 18.14 MPa, and the maximum shear stress is 3.60 MPa (**Figure 11B**).

When the cohesion of the natural fracture is 1.5 MPa, the shear failure of natural fracture occurs at t = 0.667 s. When the

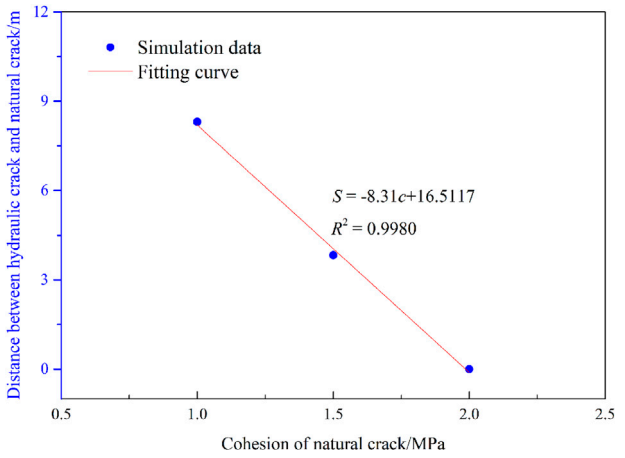

FIGURE 12 | The relationship between the distance from the HF tip to NF and the cohesive of NF during the NF initiation.

natural fracture occurs for the first time, the hydraulic fracture has not yet propagated to the natural fracture. At this time, the peak water pressure in the fracture is 8.5 MPa. The propagation length of hydraulic fracture is 18.72 m, and the distance between the tip of hydraulic fracture and the natural fracture is 3.83 m. The maximum vertical stress on the natural fracture surface is 14.54 MPa, and the maximum shear stress is 1.59 MPa, both of which are located at the shear fracturing (**Figure 11A**). As the cohesion of natural fractures increases, the ability of natural fractures resisting shear failure increases accordingly. After the hydraulic fracture is connected with the natural fracture, with the increase of the water pressure in the fracture, there will be both shear failure and tension failure in the natural fracture, and shear fracture dominates. After that, the hydraulic fractures first pass through the natural fractures and continue to propagate, and then airfoil failure occurs at natural fracture. When the airfoil propagation of the natural fracture occurs, the peak water pressure in the fracture is 8.5 MPa. The maximum vertical stress on the natural fracture surface is 18.48 MPa, and the maximum shear stress is 3.60 MPa (**Figure 11B**).

When the cohesion of natural fractures is 2.0 MPa, the shear failure of natural fracture occurs at 0.925 s. When the natural fracture occurs for the first time, the hydraulic fracture has not yet propagated to the natural fracture. At this time, the peak water pressure in the fracture is 6.5 MPa, the maximum vertical stress on the natural fracture surface is 14.48 MPa, and the maximum shear stress is 1.28 MPa (**Figure 11A**). With the increase of water pressure in natural fractures, the hydraulic fracture propagates through the natural fractures, and then the natural fractures develop airfoil propagation. When airfoil propagation of natural fractures occurs, the peak water pressure in the fracture is 8.4 MPa. The maximum vertical stress on the natural fracture surface is 18.38 MPa, and the maximum shear stress is 3.60 MPa (**Figure 11B**).

As the cohesion of natural fractures increases, the ability of natural fractures to resist shear failure increases. In the process of hydraulic fractures approaching natural fractures, the less likely it is for disturbing stress to induce shear failure of natural fractures. With the increase of cohesion of natural fractures, when the disturbing stress of hydraulic fracturing induces the initial shear failure of natural fractures, the distance between the hydraulic fracture tip and the natural fracture is smaller (**Figure 12**). When the hydraulic fracture is connected with the natural fracture, the water pressure enters the natural fracture. Tension failure occurs at the same time as shear failure of natural fractures occurs. Besides, the area of natural fractures where shear failure occurs gradually decreases.

In addition, the pumping rate, the shear angle of the natural fracture, the approach angle of the hydraulic fracture, and the natural fracture will also affect the process of natural fracture failure induced by the disturbing stress of hydraulic fracturing. Therefore, when hydraulic fracturing is performed in the reservoir with natural fractures developed, whether the natural fractures in front of hydraulic fractures occurs shear failure under the action of the disturbing stress of hydraulic fracturing is mainly determined by the disturbing stress field of the hydraulic fracturing and the shear strength parameters of the natural fracture.

DISTURBING STRESS ON BOTH SIDES OF HYDRAULIC FRACTURE INDUCES SHEAR FAILURE OF NATURAL FRACTURE

The failure process of natural fractures on both sides of hydraulic fracture and the distribution of fluid pressure, vertical stress, and shear stress are shown in **Figure 13**. At the pumping injection time of 0.645 s, the peak water pressure in the fracture is 7.0 MPa, and a compressive stress concentration occurs at the tip of the natural fracture. The peak horizontal stress in the tip area of the natural fracture on the left side of the hydraulic fracture is 8.77 MPa, the peak vertical stress is 25.73 MPa, and the peak shear stress is 5.75 MPa. The peak horizontal stress at the tip of the natural fracture on the right side of the hydraulic fracture is 8.80 MPa, the peak vertical stress is 26.85 MPa, and the peak shear stress is 6.28 MPa. The natural fracture surface is the compressive stress reduction zone (**Figure 13A**).

With the propagation of hydraulic fractures, the shear stress on the natural fracture surface gradually increases. At the pumping injection time of 1.075 s, shear failure occurs at the natural fracture on the left side of the hydraulic fracture. At this time, the peak water pressure in the fracture is 8.3 MPa, the peak horizontal stress at the tip of the natural fracture on the left side of the hydraulic fracture is 11.94 MPa, the peak vertical stress is 26.70 MPa, and the peak shear stress is 7.26 MPa. The peak horizontal stress at the tip of the natural fracture on the right side of the hydraulic fracture is 12.47 MPa, the peak vertical stress is 27.63 MPa, and the peak shear stress is 6.06 MPa. The shear stress at the shear failure area of the natural fracture on the left is 2.49 MPa (**Figure 13B**).

With the further propagation of hydraulic fractures, shear failure occurs at the natural fractures on the right side of the

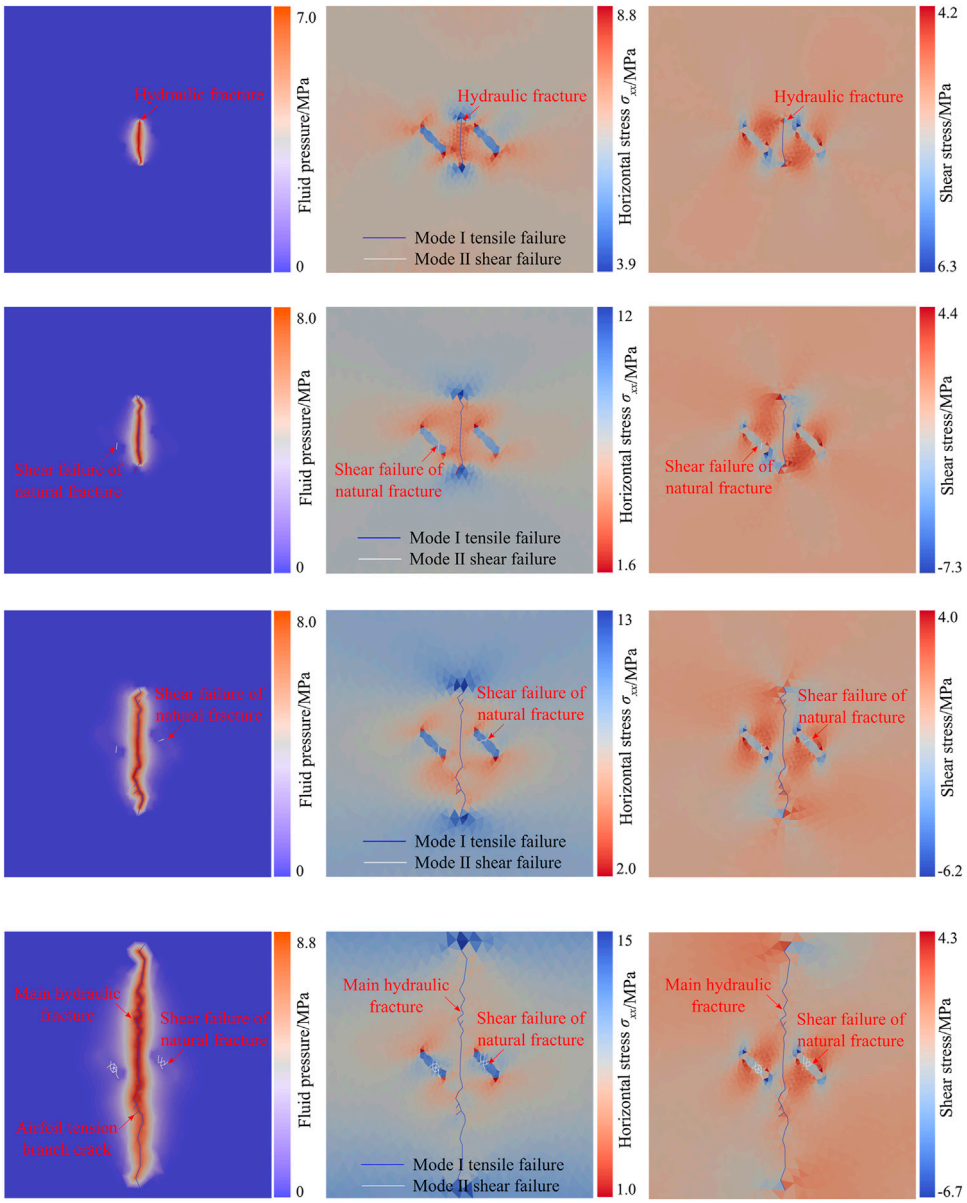

FIGURE 13 | The fracturing process of natural fracture and distribution of fluid pressure, horizontal stress, and shearing stress during hydraulic fractures propagation. **(A)** t = 0.645 s; **(B)** t = 1.075 s; **(C)** t = 1.892 s; **(D)** t = 3.591 s.

hydraulic fractures at the pumping injection time of 1.892 s. At this time, the peak water pressure in the fracture is 8.0 MPa, the peak horizontal stress at the tip of the natural fracture on the left side of the hydraulic fracture is 12.15 MPa, the peak vertical stress is 27.71 MPa, and the peak shear stress is 5.98 MPa. The peak horizontal stress at the tip of the natural fracture on the right side of the hydraulic fracture is 13.34 MPa, the peak vertical stress is 28.64 MPa, and the peak shear stress is 6.22 MPa. The shear stress at the shear failure area of the natural fracture on the right is 2.58 MPa (**Figure 13C**). After shear failure occurs at the natural fractures on both sides of the hydraulic fracture, as the hydraulic fractures propagate, the shear failure area of the natural fractures on both sides will further expand (**Figure 13D**).

During the shear failure of natural fractures, the seepage area on both sides of hydraulic fractures did not propagate to the natural fractures. It indicates that the shear failure of natural fractures is induced by the disturbing stress of hydraulic fracturing. During the propagation of hydraulic fractures, there will be compressive stress concentration areas on both sides of the hydraulic fractures, that is, disturbing stress area. When natural fractures exist on both sides of hydraulic fractures, the disturbing stress generated by hydraulic fracturing will increase the shear stress of the natural fracture surface. When the shear stress reaches the shear strength of the

natural fracture, the disturbing stress of hydraulic fracturing induces shear failure of the natural fracture.

CONCLUSION

(1) When natural fractures and other weak structures exist on the front or both sides of hydraulic fracture, the shear stress acting on the surface of natural fracture will increase until the natural fracture failure, which is caused by the disturbing stress of hydraulic fracturing.
(2) The seepage area on the front and both sides of hydraulic fracture did not extend to the natural fracture while the natural fracture failure occurred. It indicates that the shear failure of natural fractures is induced by the disturbing stress of hydraulic fracturing.
(3) When the hydraulic fracture propagates to the natural fracture, the hydraulic tension fracture and disturbed shear fractures are connected and penetrated. As the fluid pressure within the natural fracture surface increases, the hydraulic fracture will continue to propagate through the natural fracture. Meanwhile, due to the action of fluid pressure, a tensile stress concentration will occur at the tip of the natural fracture, which will induce the airfoil tension failure of the natural fracture.
(4) With the increase of the principal stress difference, the range of the disturbing stress area and the peak value of the disturbing stress at the front of the hydraulic fracture tip increase, as well as the shear stress acting on the natural fracture surface. During the process of hydraulic fracture approaching natural fracture, the disturbing stress is easier to induce shear failure of natural fracture.
(5) With the increase of the cohesive force of natural fracture, the ability of natural fractures to resist shear failure increases. As the hydraulic fracture approaches natural fractures, the disturbing stress is more difficult to induce shear failure of natural fracture.

DATA AVAILABILITY STATEMENT

The original contributions presented in the study are included in the article/Supplementary Material; further inquiries can be directed to the corresponding author.

AUTHOR CONTRIBUTIONS

XZ and BH conceived the research. XZ wrote the manuscript and prepared the figures. BH reviewed and supervised the manuscript. GG involved in the modeling. All authors finally approved the manuscript and thus agreed to be accountable for this work.

FUNDING

This work was supported by the National Natural Science Foundation of China (No. 52004269) and the Fundamental Research Funds for the Central Universities (No. 2020QN39).

ACKNOWLEDGMENTS

The authors would like to thank the Geomechanics Group at the University of Toronto for their assistance in numerical simulation.

REFERENCES

Burrows, L. C., Haeri, F., Cvetic, P., Sanguinito, S., Shi, F., Tapriyal, D., et al. (2020). A Literature Review of CO2, Natural Gas, and Water-Based Fluids for Enhanced Oil Recovery in Unconventional Reservoirs. *Energy Fuels* 34, 5331–5380. doi:10.1021/acs.energyfuels.9b03658

Chen, M., Zhou, J., Jin, Y., and Zhang, G. Q. (2008). Experimental Study on Fracturing Features in Naturally Fractured Reservoir. *Acta Petrol. Sin.* 29, 431–434. doi:10.7623/syxb200803023

Chen, T., Wang, Z. M., and Yang, G. (2013). Experiments of Fracturing and Pressure Curve Analysis of T-Shape Fractures of Coal Bed. *Spec. Oil Gas Reservoirs* 20, 123–126. doi:10.3969/j.issn.1006-6535.2013.03.030

Cheng, Y. (2007). "Boundary Element Analysis of the Stress Distribution Around Multiple Fractures: Implications for the Spacing of Perforation Clusters of Hydraulically Fractured Horizontal Wells," in SPE125769, Charleston, WV, September 2009.

Geomechanica Inc (2018). Irazu 2D Geomechanical Simulation Software. Theory Manual.

Hu, L., and Ghassemi, A. (2021). Laboratory-Scale Investigation of the Slippage of a Natural Fracture Resulting from an Approaching Hydraulic Fracture. *Rock. Mech. Rock. Eng.* 54, 2547–2558. doi:10.1007/S00603-021-02398-Y

Huang, B., Wang, Y., and Cao, S. (2015). Cavability Control by Hydraulic Fracturing for Top Coal Caving in Hard Thick Coal Seams. *Int. J. Rock Mech. Mining Sci.* 74, 45–57. doi:10.1016/j.ijrmms.2014.10.011

Huang, B. X., Chen, S. L., and Cheng, Q. Y. (2016). Basic Problems of Hydraulic Fracturing for Mining and Control Zone Gas in Coal Seams. *J. China Coal Soc.* 41, 128–137. doi:10.13225/j.cnki.jccs.2015.9024

Huang, B. X., Zhao, X. L., Chen, S. L., and Liu, J. W. (2017). Theory and Technology of Controlling Hard Roof with Hydraulic Fracturing in Underground Mining. *Chin. J. Rock Mech. Eng.* 36, 1–17. doi:10.13722/j.cnki.jrme.2017.0078

Labuz, J. F., Shah, S. P., and Dowding, C. H. (1985). Experimental Analysis of Crack Propagation in Granite. *Int. J. Rock Mech. Mining Sci. Geomech. Abstr.* 22, 85–98. doi:10.1016/0148-9062(85)92330-7

Lisjak, A., and Grasselli, G. (2014). A Review of Discrete Modeling Techniques for Fracturing Processes in Discontinuous Rock Masses. *J. Rock Mech. Geotechn. Eng.* 6, 301–314. doi:10.1016/j.jrmge.2013.12.007

Lisjak, A., Kaifosh, P., He, L., Tatone, B. S. A., Mahabadi, O. K., and Grasselli, G. (2017). A 2D, Fully-Coupled, Hydro-Mechanical, FDEM Formulation for Modelling Fracturing Processes in Discontinuous, Porous Rock Masses. *Comput. Geotech.* 81, 1–18. doi:10.1016/j.compgeo.2016.07.009

Liu, Q., Sun, L., Liu, P., Chen, L., and Wu, W. (2018). Modeling Simultaneous Multiple Fracturing Using the Combined Finite-Discrete Element Method. *Geofluids* 2018, 1–20. doi:10.1155/2018/4252904

Liu, Z., Tang, X., Tao, S., Zhang, G., and Chen, M. (2020). Mechanism of Connecting Natural Caves and wells through Hydraulic Fracturing in Fracture-Cavity Reservoirs. *Rock. Mech. Rock. Eng.* 53, 5511–5530. doi:10.1007/s00603-020-02225-w

Munjiza, A., and Andrews, K. R. F. (1998). NBS Contact Detection Algorithm for Bodies of Similar Size. *Int. J. Numer. Meth. Eng.* 43, 131–149. doi:10.1002/(SICI)1097-0207(19980915)43:1<131::AID-NME447>3.0.CO;2-S

Munjiza, A., and Andrews, K. R. F. (2000). Penalty Function Method for Combined Finite-Discrete Element Systems Comprising Large Number of Separate Bodies. *Int. J. Numer. Meth. Engng.* 49, 1377–1396. doi:10.1002/1097-0207(20001220)49:11<1377::AID-NME6>3.0.CO;2-B

Munjiza, A., Andrews, K. R. F., and White, J. K. (1999). Combined Single and Smeared Crack Model in Combined Finite-Discrete Element Analysis. *Int. J. Numer. Meth. Engng.* 44, 41–57. doi:10.1002/(SICI)1097-0207(19990110)44:1<41::AID-NME487>3.0.CO;2-A

Munjiza, A., and John, N. W. M. (2002). Mesh Size Sensitivity of the Combined FEM/DEM Fracture and Fragmentation Algorithms. *Eng. Fracture Mech.* 69, 281–295. doi:10.1016/S0013-7944(01)00090-X

Munjiza, A., Owen, D. R. J., and Bicanic, N. (1995). A Combined Finite-discrete Element Method in Transient Dynamics of Fracturing Solids. *Eng. Comput.* 12, 145–174. doi:10.1108/02644409510799532

Munjiza, A. (2004). *The Combined Finite-Discrete Element Method*. Chichester, UK: John Wiley & Sons. doi:10.1002/0470020180

Roegiers, J. C., and Bennaceur, K. (1990). "Stress Relief by Hydraulic Fracturing - Dream or Reality?," in Proc ISRM International Symposium on Static and Dynamic Considerations in Rock Engineering, Mbabane, Swaziland, September 1990 (Publ Rotterdam: A A Balkema), 257–263.

Yang, J. S., Wang, Y. B., Li, A. Q., Chen, Z. H., Chen, Y. P., and Zou, Y. S. (2012). Experimental Study on Propagation Mechanism of Complex Hydraulic Fracture in Coal-Bed. *J. China Coal Soc.* 37, 73–77. doi:10.3844/ajassp.2012.1055.1062

Zhang, R., Hou, B., Tan, P., Muhadasi, Y., Fu, W., Dong, X., et al. (2020). Hydraulic Fracture Propagation Behavior and Diversion Characteristic in Shale Formation by Temporary Plugging Fracturing. *J. Pet. Sci. Eng.* 190, 107063. doi:10.1016/j.petrol.2020.107063

Zhao, X. L. (2019). The Mechanism of Pore Pressure Gradient Effect and the Fracturing Effect Induced by Disturbing Stress during Hydrofracturing. Master's Thesis. Xuzhou (Jiangsu): China University of Mining and Technology.

Conflict of Interest: The authors declare that the research was conducted in the absence of any commercial or financial relationships that could be construed as a potential conflict of interest.

Publisher's Note: All claims expressed in this article are solely those of the authors and do not necessarily represent those of their affiliated organizations, or those of the publisher, the editors, and the reviewers. Any product that may be evaluated in this article, or claim that may be made by its manufacturer, is not guaranteed or endorsed by the publisher.

frontiers in Earth Science

ORIGINAL RESEARCH
published: 28 September 2021
doi: 10.3389/feart.2021.743157

Deformation Bands and Associated FIP Characteristics From High-Porous Triassic Reservoirs in the Tarim Basin, NW China: A Multiscale Analysis

Wenyuan Yan, Ming Zha, Jiangxiu Qu, Xiujian Ding and Qinglan Zhang*

School of Geosciences, China University of Petroleum (East China), Qingdao, China

Deformation bands are widely formed and distributed in Triassic high-porous rocks as a result of multistage tectonic movement. In this research, core observation, the rock thin section (fluorescence and casting thin section), FIB-SEM, X-ray diffraction, Raman laser, and thermometry of fluid inclusions were employed to describe the macro- and micro characteristics of deformation bands and their associated relationship with microfractures. Results indicate that the main types of deformation bands formed in the Lunnan Triassic high-porosity sandstone during the Yanshanian and Himalayan periods under different temperature and pressure conditions are compaction shear bands, and their quantity increases evidently with the distance of thrust faults. The density of deformation bands near the fault is about 15/m; porosity and permeability decrease sharply compared with those of the host rock. Microscopically, two obtained fluid-inclusion planes (FIPs) can be distinguished as 51 samples collected from 12 wells by the cutting relationship and mechanical characteristics. The homogenization temperature of associated aqueous inclusion is generally characterized by two peaks, mainly 70–80°C and 110–120°C, which were formed in the Late Yanshanian and Late Himalayan periods. The formation period of deformation bands induced by the intragranular microfractures improved the reservoir seepage capacity. In the later stage, as the interlayer and barrier with low porosity and low permeability affects the distribution of oil and gas, which is an important factor in this study of the local fluid dynamic field and high-quality reservoir evolution distribution.

Keywords: deformation band, FIP, homogenization temperature, fault seal, reservoir characteristics, Tarim basin

OPEN ACCESS

Edited by:
Zheng Sun,
China University of Mining and Technology, China

Reviewed by:
Yisheng Liu,
Chengdu University of Technology, China
Ke Wang,
Guizhou University, China
Yanan Miao,
Shandong University of Science and Technology, China

****Correspondence:***
Wenyuan Yan
156727991@qq.com

Specialty section:
This article was submitted to Economic Geology, a section of the journal Frontiers in Earth Science

Received: *17 July 2021*
Accepted: *09 August 2021*
Published: *28 September 2021*

Citation:
Yan W, Zha M, Qu J, Ding X and Zhang Q (2021) Deformation Bands and Associated FIP Characteristics From High-Porous Triassic Reservoirs in the Tarim Basin, NW China: A Multiscale Analysis. Front. Earth Sci. 9:743157. doi: 10.3389/feart.2021.743157

INTRODUCTION

In general, fault zone structures with different lithology properties caused by various tectonic movements are significantly different (Fossen et al., 2007; Fossen et al., 2018). High-porous rocks fail to develop fractures during the deformation process; instead, the mineral particles are rolled, rearranged, and even broken by tectonic stress, and then the fault zone was formed (Fossen and Bale, 2007; Schultz and Fossen, 2008; Ballas et al., 2014; Pei et al., 2015; Philit et al., 2018). Deformation band is a kind of brittle-ductile sub-seismic deformation structure that develops particularly in consolidated or semi-consolidated high-porosity rocks, which is the intuitive response of the host rock to the velocities and displacements imposed by tectonic movements, and the direction, distribution, and types of deformation bands developed by specific boundary conditions and tectonic structures have certain regularity (Fossen et al., 2007; Philit et al., 2018). Factors

affecting the deformation mechanism and the resulting type of the deformation zone include not only the rock composition, grain size, shape, sorting, and initial porosity of the host rock but also the atmospheric conditions of temperature and pressure. Fossen classified deformation bands into disaggregation band, phyllosilicate band, cataclastic band, and solution-cementation band according to the combining mineralogical characteristics, cementation degree, porosity, and stress state of deformation bands (Exner et al., 2013; Soliva et al., 2013; Pei et al., 2015; Bossennec et al., 2018; Fossen et al., 2018). It can also be divided into dilatation band, shear band, and compaction band according to the type of stress; the most common type is the compaction shear band (CSB) formed by both shear and compaction (Fossen et al., 2018). Deformation band reduces permeability by up to 6 orders of magnitude compared to that of the host rock (Fisher and Knipe, 2001). The deformation band cluster is effective in sealing approximately the 140 m height of the oil column under experimental conditions (Torabi and Fossen, 2009; TorabiBraathen et al., 2013). The variability of its inherent physical properties affects the migration and preservation of hydrocarbons to a certain extent, and its distribution rules and relevant characteristics are influential scientific issues for reservoir inhomogeneity and exploration prediction in petroliferous basins.

The fluid-inclusion plane (FIP) is an assemblage of fluid inclusions capturing paleo-fluids during the healing process which are linearly arranged in the microfractures of mineral grains caused by tectonic movement (Onasch, 1990; Anders and Wiltschko, 1994; Boullier, 1999; Anders et al., 2014). Although the solubility of silica is low, rehearing of microfractures is probably rapid because surface areas for silica dissolution and precipitation are large, and bridging of microfracture walls should occur readily (Parnell et al., 2001; Laubach et al., 2010; Lander and Laubach, 2014). Notably, the mechanical direction and feature of the tectonic motion can be preserved as the quartz grains have anisotropic homogeneous mechanical properties, and the homogeneous temperature of fluid inclusions in the healing microfracture can reflect the formulation time. Thus, FIP can be used as an indicator of paleo stress direction, paleo temperature, and geochemistry in various tectonic contexts, revealing the composition and migration of paleo fluids, which is significantly necessary for the research of tectonic motion (Anders and Wiltschko, 1994; Boullier, 1999; Anders et al., 2013; Hooker et al., 2018; Miao et al., 2020).

The development of deformation bands in the study area has not been reported in previous studies. Mesozoic Triassic located at the Lunnan uplift is an important petroliferous horizon in the northeast of the Tarim Basin, characterized by large burial depths and high-quality reservoir properties, as well as multiple periods of strong tectonic movements controlling the migration and preservation of hydrocarbons. Thus, the Triassic sandstone of the Lunnan uplift provides a typical case for the developmental characteristics of deformation bands in a deep burial environment and investigation of the influence on fluid flow.

The objectives of our study include 1) investigation of the characteristics of different deformation bands formed in deep burial environments through cores 2) and determination of the formation time and geological significance of the FIP characteristics simultaneously formed with different deformation bands.

GEOLOGICAL SETTING

Location and Structural Evolution of the Lunnan Uplift

The Tarim Basin is the largest petroliferous onshore basin in China, with an area of 560,000 km^2 (Yang et al., 2007; Miao et al., 2018). The Lunnan uplift is located at the central east of the Tabei uplift in the Tarim Basin, and it belongs to a secondary-order sub-tectonic unit of the Tabei uplift. The northern side is bounded by the Luntai fault, and the southern edges, by the Manjiaer depression, with an area of 4,420 km^2 (**Figure 1**). During the evolution process from marine to onshore facies, the tectonic stress field undergoes multiple tension-extrusion transitions and led to the formation of the present large nose structure of the Lunnan uplift, which is the highest part located at the north side of the Lunan fault horst belt and dips to the southwest (Zhang et al., 2011; Zhang et al., 2012; Su et al., 2013).

The evolution of the Lunnan uplift can be divided into the Late Caledonian–Early Hercynian initial formation phase, the Late Hercynian–Indosinian definitive period with strong extrusion and lifting, the tectonic inversion period of the Late Yanshan–Early Himalayan, and the ultimately definitive period of the Himalayan (Yang et al., 2007; Zhang et al., 2011; Zhang et al., 2012).

A total of four major fault systems have developed in the Triassic (Zhang et al., 2011; Zhao et al., 2012; Su et al., 2013): the Late Caledonian NNE–SSW–oriented left strike-slip faults, in which two groups of faults in the east and west of the Lunnan area are formed; the Late Hercynian left-slip shear conjugate faults, which are mainly distributed in the south and east of Lunnan; the Indosinian–Yanshanian growth faults, which are formed in the Lunnan and Sangtamu fault horst belt; and the Late Himalayan left-slip en-echelon faults, which are mainly distributed in the south of the study area (**Figure 2**).

Characteristics of Petroleum Geology

The Lunnan uplift of the Triassic is related to Jurassic, Carboniferous, and Ordovician regional unconformity. Sedimentary was affected by the Luntai fault growth due to the large difference of elevation between the hanging wall and the footwall (Yang et al., 2007). Several sets of fan-braided deltaic sandstones are characterized by the decreasing percent of conglomerates and water-flow energy, which are developed from the north to south along the footwall. The profile suggests three sets of fining-upward positive cycles. These sandstones are deeply buried to a depth of 4.2–5.4 km and divided into three oil groups by a development program; total thickness approaches 80~200 m (**Figure 1B**). The II oil group is not developed in the southern part of the study area; the planar distribution and vertical variation of the I and III oil groups are stabilized.

The Lunnan Triassic is the most important oil and gas development layer in the Mesozoic. The early formed faults were reactivated by the late tectonic effects, and the Paleozoic oil and gas migrated through the faults and accumulated in the structural culmination of the Lunnan and Sangtamu fault horst belt and formed Mesozoic secondary oil and gas reservoirs subsequently (Sun and Li, 2004; Yang et al., 2007; Zhang

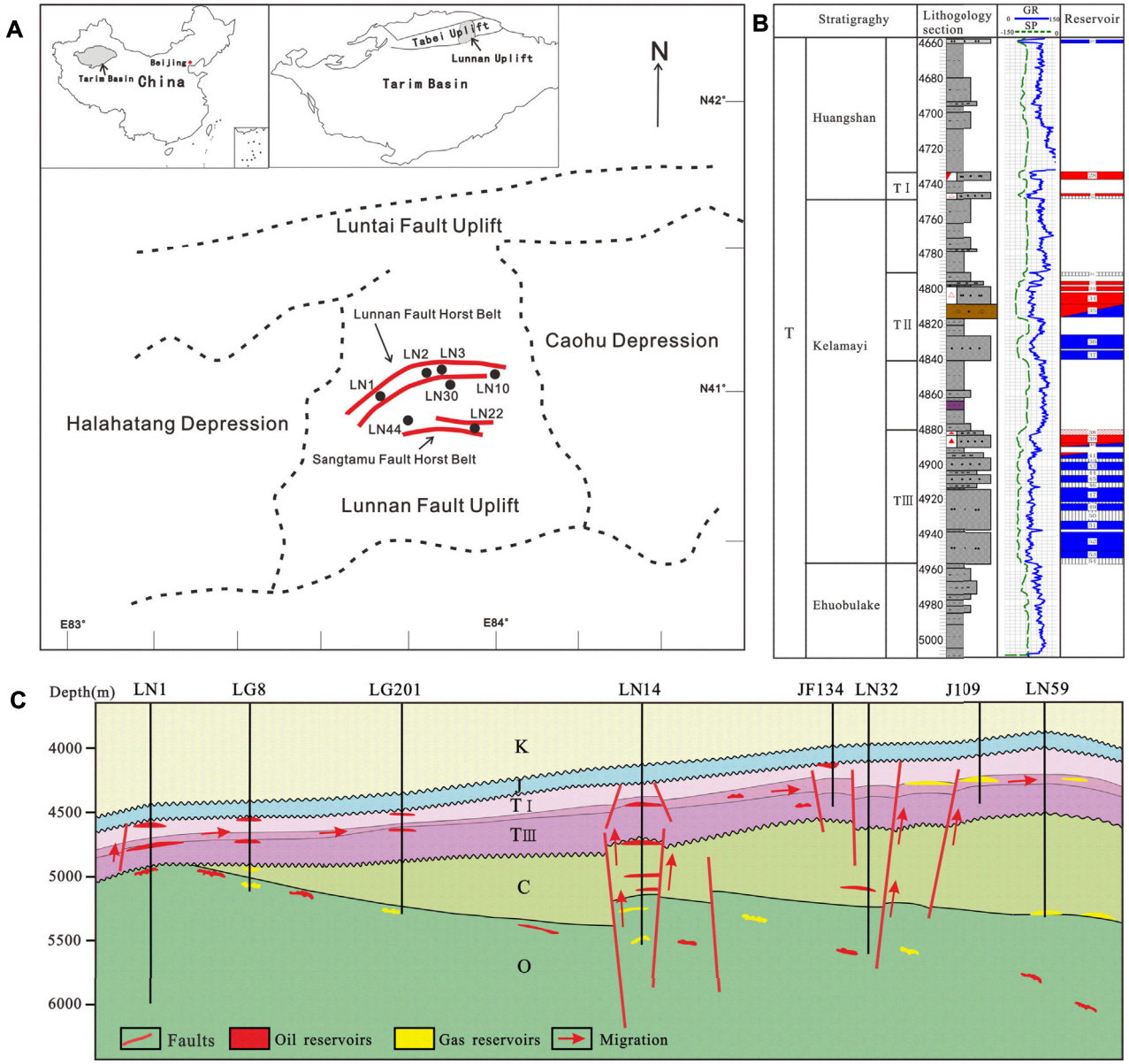

FIGURE 1 | (A) Simplified structural map of the Lunnan uplift and the study area. The study area has two fault horst belts and the intermediate areas. The location of the study area is colored in gray. The regional boundary is shown as a dotted line. **(B)** Stratigraphy and lithology sections of LN3 well located at the Lunnan fault horst belt. **(C)** The oil and gas accumulation model in the study area from the northeast to southwest (Yang et al., 2007). O, Ordovician; C, Carboniferous; T, Triassic; J, Jurassic; K, Cretaceous.

et al., 2012; Sun et al., 2018). And most of the traps are anticlines with oil and gas–water boundaries and area controlled by tectonic lines, with typical features of high abundance and wide range (**Figure 1C**).

METHODS

A total of 51 samples collected from 15 wells are investigated in this study, which are taken from a depth ranging from 4,369 m to 4,824 m located at different tectonic units and large-scale fault systems. Core physical data and the distribution of the Triassic fault in the Lunnan uplift were obtained from the China National Petroleum Tarim Oilfield E&P Research Institute. All experiments involved in this study were carried out at the Key laboratory of deep oil and gas, China University of Petroleum (East China), China.

Petrology Analysis

A total of 37 samples were prepared and processed as standard 30-μm-thick thin sections filled with blue resin from representative deformation bands and host rocks. With the

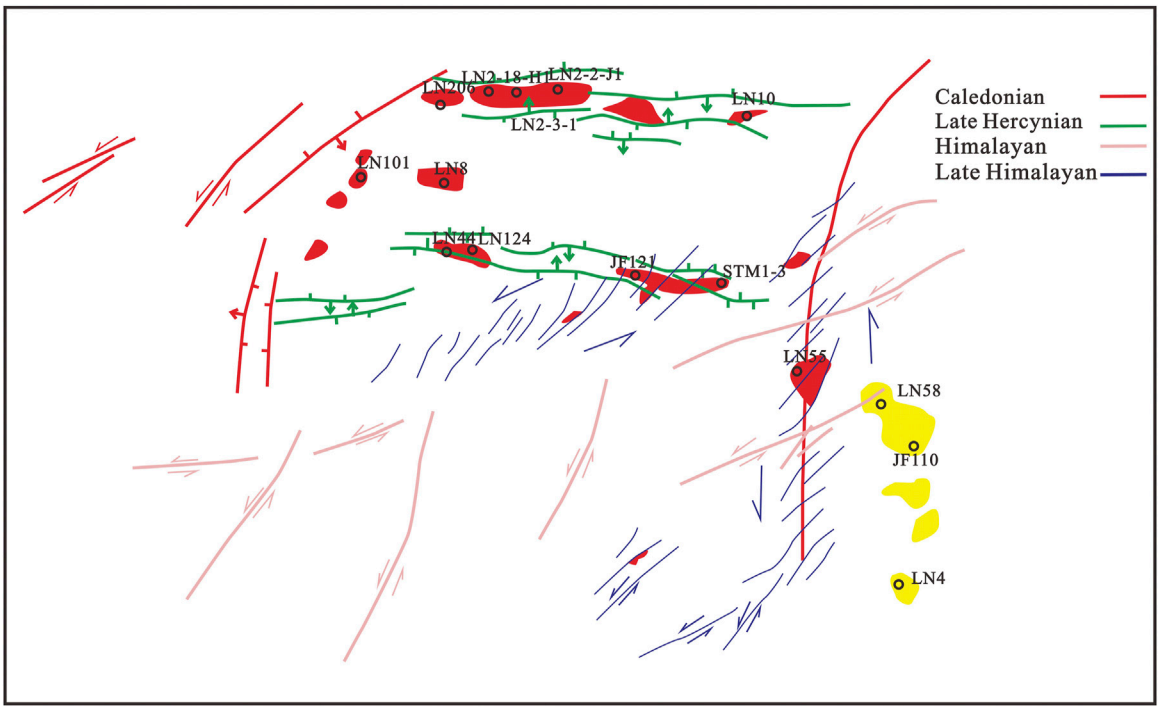

FIGURE 2 | Sketch of the fault system of the Triassic strata in the study area. The principal faults formed in different periods are highlighted by different colors. The wells marked in the figure are the selected sampling wells in this research.

utilization of the polarizing microscope, textures, rock and mineral composition, diagenesis, pore types, and visual porosity can be analyzed.

X-ray diffraction (XRD) analysis of whole-rock samples and quantitative clay minerals was performed on 45 core samples to identify species and contents of major minerals and relative contents of different clay minerals.

Microstructural Analysis

In order to observe the characteristics of grain crushing and authigenic minerals developed in deformation bands, 37 representative core samples (from the main reservoir sandstone of key wells with hydrocarbon) were coated with gold and examined with a Hitachi S-4800 scanning electron microscope (SEM) equipped with a Bruker Quantax 100 energy-dispersive X-ray spectroscope (EDX). Cathodoluminescence (CL) analyses of 20 typical core samples, in which physical properties and oil-bearing properties significantly decreased compared with that of host rocks, were completed using an Olympus microscope equipped with a CL8200-MKS CL instrument.

Fluid Inclusion Analysis

As for fluid inclusions (FI), 51 core samples were selected to record the petrographic characteristics including distribution, size, shape, phase, number, and color in transmitted and ultraviolet light. Petrographic studies were carried out using a Nikon 80I dual-channel fluorescence microscope equipped with transmitted and reflected light. Fluorescence quantification of hydrocarbon inclusions during UV excitation was performed using a Maya 2000 Pro spectrometer.

The composition of fluid inclusions from 9 samples of deformation bands and host rocks on the perimeter was detected using a Renishaw RM2000 laser Raman spectrometer, and the experimental results were analyzed by Labspec5 software. A source power of 5 mW and an argon ion laser with the wavelength of 514 nm are used for the detection. The charge-coupled device area is 20 μm^2, and the accumulation time is 30 s for each scan. The spectral range falls between 100 and 4,000 cm^{-1} for the analysis of the vapor and liquid phases.

Microthermal measurements of fluid inclusions were performed using a calibrated Linkam THMS600 cooling-heating stage. A thermal cycling method was used to determine the homogenization temperature (Th) of the fluid inclusions (Goldstein and Reynolds, 1994). When the initial heating rate was set as 15°C/min, switching to 5°C/min when the two-phase liquid vapor was homogenized to a single-phase liquid or gas, the measurement accuracy was estimated to be ±0.1°C.

RESULTS

Host Rock

The Triassic reservoirs consist of conglomerates and coarse sandstones in the Lunnan uplift, both are mainly fan-braided deltaic deposits (**Figure 3B**). Detrital quartz, feldspar with

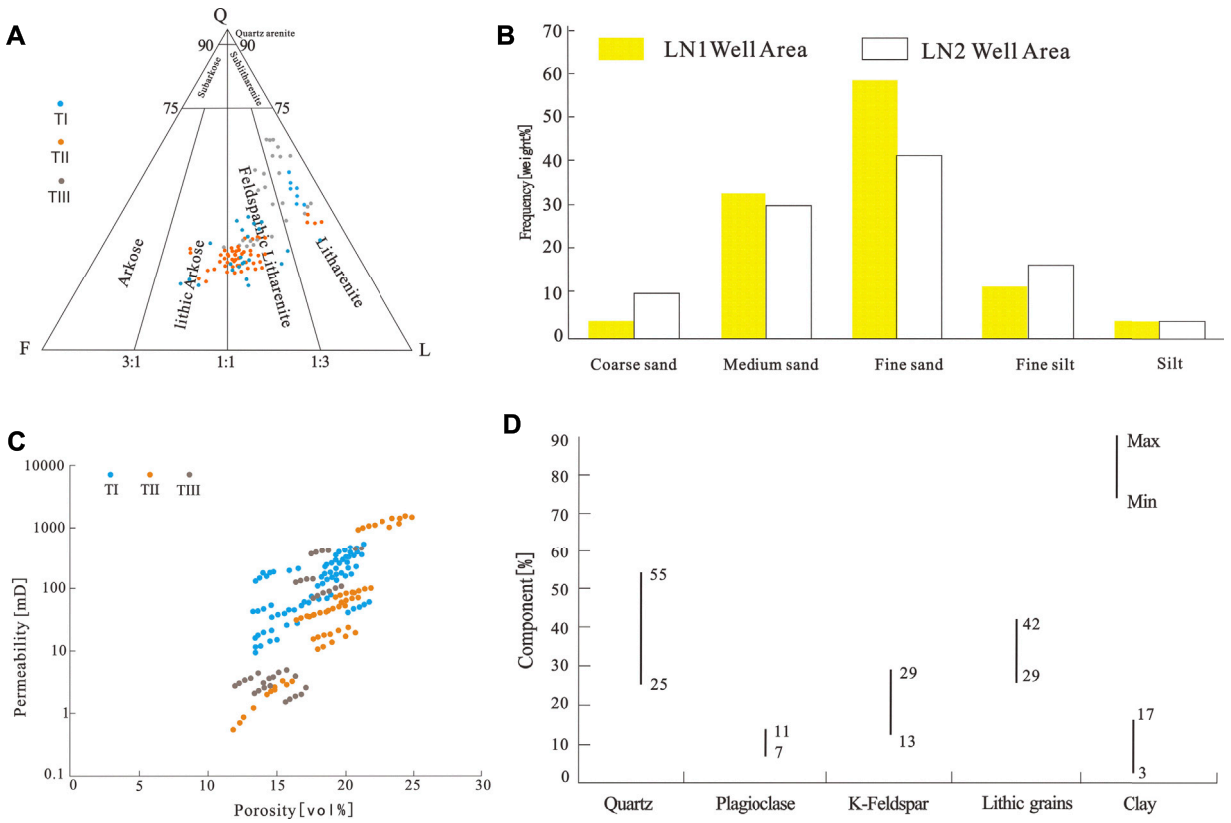

FIGURE 3 | (A) Ternary diagram showing the framework grain composition of the study area sandstones, plotted on the Folk (1968) diagram (Folk and Ward, 1957). F, feldspar; L, lithic grains; Q, quartz. **(B)** Grain size distributions of sandstones in the Lunnan area. **(C)** Core-measured porosity versus core permeability cross-plots at 56 mPa (8,145 psi) net confining stress for sandstones in the Lunnan area. **(D)** X-ray diffraction data of sandstones in the Lunnan area.

plagioclase, and K-feldspar are the major types of rock grains, clay, and cement in the pores, accounting for 30–45 vol%, 15–29 vol%, 29–42 vol%, less than 5 vol%, and less than 7 vol%, respectively (**Figure 3D**). Sandstones are of relatively low compositional maturity and low textural maturity, controlled by the provenance and sedimentary facies. The feldspar content shows an increasing trend with the increasing grain size. The grain shape ranges from angular to sub-angular. The primary intragranular pore is the main pore type. The types of grain contacts are dominated by point-contact and line-contact. According to the division standard of the diagenetic phase, the Triassic falls in the B stage of the early phase (Zhang et al., 2012).

The rock porosity and permeability under net overburden pressure in line with conventional reservoir conditions indicate that porosity ranges from 12 to 26 vol%, and permeability ranges from 0.6 to 1,000 mD (**Figure 3C**). The high permeability is mainly attributed to the primary intragranular pore dominating the pore systems, observed by petrography and SEM studies.

Core Observations

The Triassic was continuously subjected to regional intensive compression and associated shearing at different directions during the Late Hercynian, Indosinian–Yanshanian, and Himalayan Periods (Zhang et al., 2011), which acts as a prominent role in controlling the distribution of deformation bands around the tectonic setting and large-scale fault systems. Based on the core observation, deformation bands can be visually recognized in the sandstone cores of several wells, and combination patterns such as parallel and crossover can be identified. And the internal oil content is much lower than that of the host rock on either side, which in some cores shows the bands as an interbedded layer or barrier restricting oil flow and distribution in sandstone reservoirs (**Figure 4B**). The extension length of the deformation bands is not visible in the core observation. The width of a single band visible to the naked eye is mostly 0.15~3 cm, and the width of a cluster of deformation bands can reach a maximum of about 5 cm. The dip angle varies from 70° to horizontal, and small faults that are formed by the inherited development of the cluster deformation band can be identified (**Figure 4C**). The density of the deformation bands in the reservoir near the Himalayan fault is greater than or equal to 30 bands/m, and it gradually decreases and stabilizes as the distance from the fault increases. Moreover, the vertical distribution has the greatest density on both sides of the fault damage zone, which is inversely proportional to the distance of the fault damage zone (Ballas et al., 2013; Schueller et al., 2013).

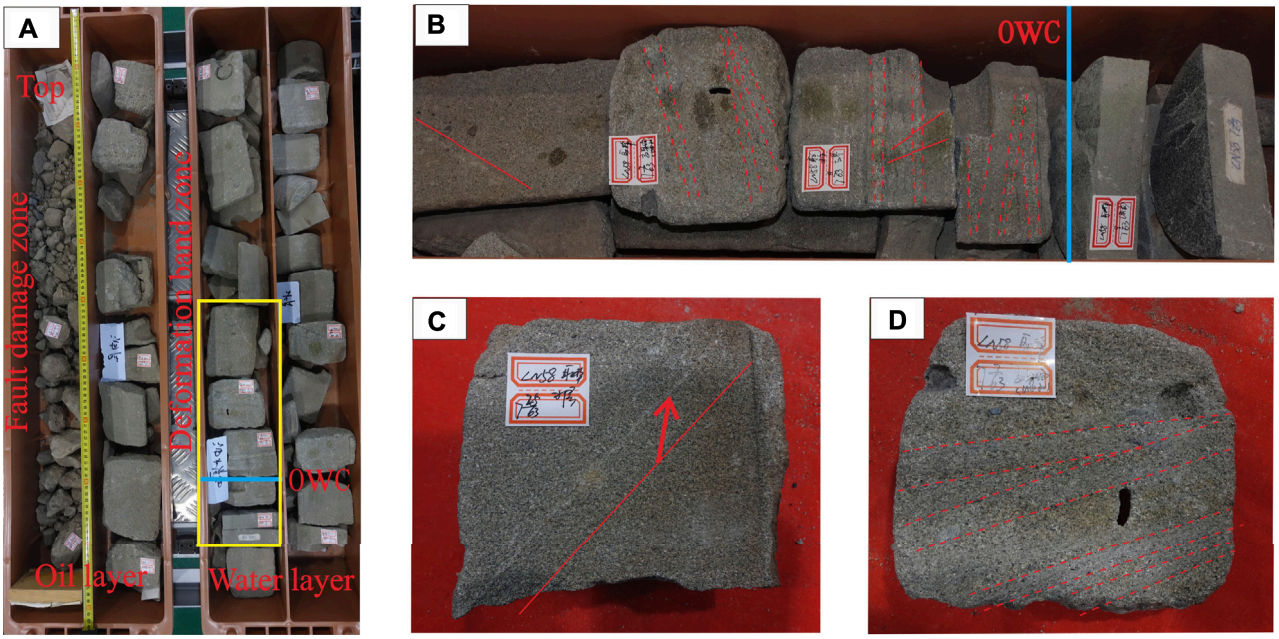

FIGURE 4 | (A) Core samples collected from the T2 oil group, LN58 well (depth: 4,369–4,373 m). **(B)** Abundant deformation bands near the fault zone; its density increases while approaching the fault zone. The single band is indicated using a red line, and the cluster band boundary is indicated using a red dotted line. **(C)** Characteristic of the single band. **(D)** Characteristic of the cluster band.

Microstructures

Few disaggregation bands (**Figure 5A**) formed in the poorly lithified stage can be identified from a small series of thin sections, which were formed in an environment with low stress and temperature conditions, and the dominant deformation mechanism is the granular flow (Fossen et al., 2007). The internal brittle grain rotational displacement compared to the host rock has the characteristic of long axis isotropic arrangement, and the spatial distribution rule fails to be recognized.

The major types of the deformation band that can be macroscopically recognized in the core are compactional shear bands (CSBs) (**Figure 5B**) caused by grain reorganization and cataclasis (Fossen et al., 2018). Cathodoluminescence (CL) and X-ray diffraction patterns show minimal differences in the mineralogical composition between the deformation bands and the host rock (**Figure 5D**). The host rock without deformation has high porosity, excellent pore–throat connectivity, intact grains, and few microfractures. Microscopic analysis of thin sections revealed that the composition of CSB contains fractured grains (intragranular microfractures), smaller grain fragments, and clay. CL revealed that the brittle grains such as quartz and feldspar within the deformation bands are highly fragmented, having diameters lower than 10% of the grain diameter of the host rock in the bands. The preferential fracture of feldspar grains relative to quartz grains can be observed (Radjai et al., 1998; Torabi and Fossen, 2009; Lommatzsch et al., 2015; Beke et al., 2019), and grain contacts are dominated by planar and concave–convex surfaces with poor sorting. Plastic grains such as biotite are deformed by extrusion stress and squeezed into the primary pore. The brittle grains on both sides adjacent to the host rock are tightly packed, with no significant change in size compared to the host rock. And the number of microfractures and quartz-filled microfractures (FIP) formed in the quartz grains during the same generation has increased significantly (Hooker et al., 2018), mainly that formed in single grains and rarely seen through multiple grain fractures (**Figure 5E**). The FIP type is dominated by conjugate microfractures caused by compressive shear stress. Scanning electron microscopy shows that the conjugate microfractures developed by quartz grains are flat and highly closed, and the inner walls of the microfracture are smooth and sharp (**Figure 5F**).

Inclusion Petrography

In sedimentary basins, secondary inclusions trapped by microfractures related to the tectonic action can reveal the specific tectonic stress field characteristics. The composition, temperature, and pressure information of the corresponding paleo-fluids as the microfractures sealing can be an extremely rapid process (Lander and Laubach, 2014). Microscopic observations show that microfractures of various sizes and combinations are generated within the quartz grains during the formation of the deformation bands, and they exhibit a strong preferred orientation (**Figure 6**). Focusing on whether the fluid inclusions contain hydrocarbons, the inclusions of secondary fluids captured by microfractures are first classified into three categories: hydrocarbon inclusions, hydrocarbon-containing inclusions, and non-hydrocarbon inclusions, and then they are subdivided according to the mineralogical sequence, cutting relationship, inclusions composition, and

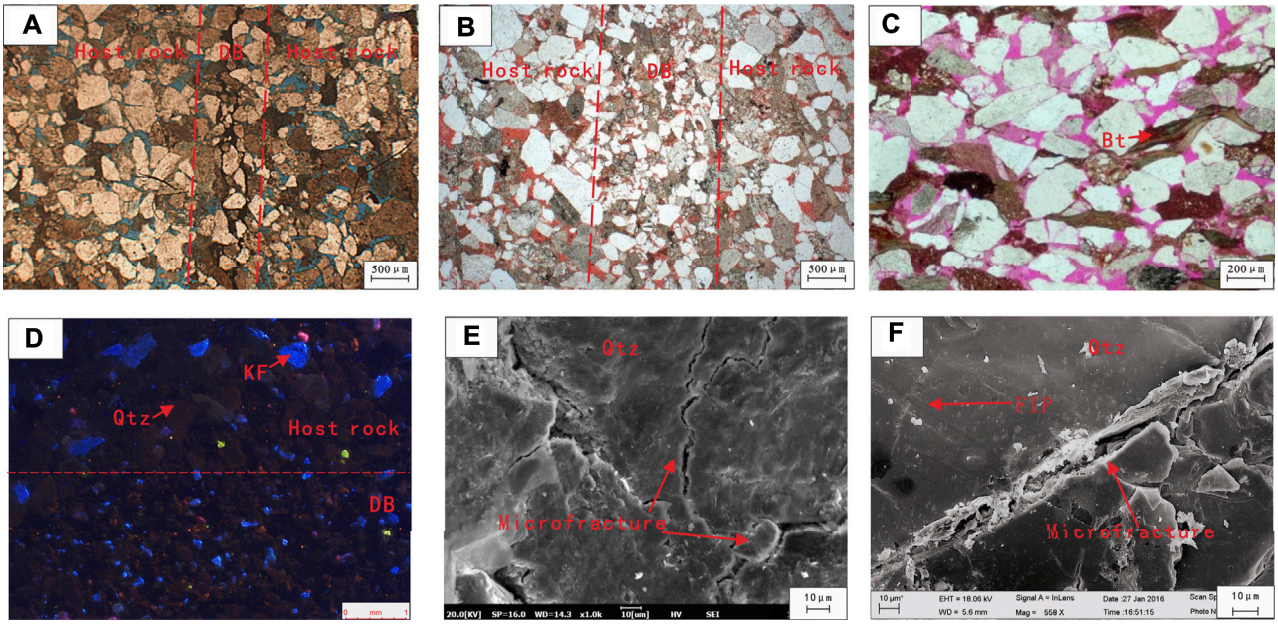

FIGURE 5 | (A) The microscopic characteristics of the disaggregation band, LN2-3-1, 4,871 m, porosity is shown in blue, plane-polarized light (PPL). **(B)** The microscopic characteristics of the CSB, feldspar, and quartz grains in the CSB are fragmented as crush micro-breccia and block the primary pore throats, LN31, 4,745 m, PPL. **(C)** Deformed biotite squeezed into the primary pore, LN30, 4,714 m, PPL. **(D)** Comparison of the composition and grain size of the host rock and deformation band; feldspar (blue luminescent) has a higher level of fragmentation compared to quartz (non-luminescent), LN44, 4,971 m, CL. **(E)** "Hertzian" contact points, which is a singular contact between two grains, formed preferred orientation of fractures through grains, SEM. **(F)** Microfractures and quartz-filled microfractures (FIP) formed in the quartz grains, LN44, 4,971 m, SEM. Qtz, quartz, KF, K-feldspar, Bt, biotite, DB, deformation band, red dotted lines is the band boundary.

homogeneous temperature (Th) into two generations of conjugate FIP. Several individual fluid inclusions were measured in each FIP to assure the reliability of homogenization temperatures from each microfracture. The Th variation was generally less than 3°C.

After serious analysis, the first-generation FIP is developed by compression-shear tectonic stress under brittle tectonic conditions, approximately 20–30% of the total number. Few detrital quartz grains can observe overgrowths. The longest intragranular microfractures cut across the single detrital quartz grain and stop at the dust lines of grain overgrowths, indicating that the FIP preceded the formation of the quartz grains overgrowths. The most common microfractures have straight traces marked by arrays of fluid inclusions. At room temperature, FIs trapped in microfractures contain coexisting two-phase inclusions, liquid-rich aqueous inclusions, and single-phase liquid inclusions, ranging from spherical to angular. The single-phase liquid inclusions are less than 1–3 μm in size. The two-phase liquid-rich aqueous inclusions contain 7–12 vol% vapor and are less than 4–7 μm in size. Final ice-melting temperatures were recorded in the range of approximately −2.5 to −5°C, using the experimental phase diagram to determine the salinity of the fluid, corresponding to salinities of 4–8 wt% NaCl equivalent (Bodnar, 1993), with a dominant range at approximately 5 wt% NaCl. The laser Raman spectrum indicates that the vapors of two-phase liquid-rich aqueous inclusions are mainly carbon dioxide.

The second-generation FIP is formed by compression-shear tectonic stress under brittle tectonic conditions, and the abundance is much greater than the above generation 1. The longest intragranular microfractures cut across the single detrital quartz grain and the dust lines of grain overgrowths (Anders et al., 2013) (**Figure 6D**). The most common microfractures show slightly curved traces marked by arrays of fluid inclusions (**Figure 6E**). At room temperature, microfracture-trapped FIs contain hydrocarbon inclusions and aqueous inclusions, which can be further divided into two-phase inclusions and single-phase inclusions, ranging from spherical to angular, with the fluorescence colors of near-green and green-yellow. Most of the hydrocarbon FIs have experienced oil and gas cracking and bitumen, which can be observed. The single-phase liquid inclusions are less than 1.5–3 μm in size. The two-phase inclusions contain 10 to 15 vol% vapor and less than 4–9 μm in size. Final ice-melting temperatures of aqueous inclusions were recorded in the range of approximately −5.2 to −17°C, corresponding to salinities of 8.1–20.2 wt% NaCl equivalent, with a dominant range at approximately 12 wt% NaCl. The laser Raman spectrum shows that the vapors of two-phase liquid-rich aqueous inclusions are mainly carbon dioxide, and a few inclusions contain ethane.

Fluid Inclusion Microthermometry

As most of the hydrocarbon FIs have experienced oil and gas cracking and bitumen, it can be demonstrated that its homogeneous temperature cannot represent the real formation temperature. When hydrocarbon and aqueous inclusions were captured simultaneously, the homogenous temperature of the

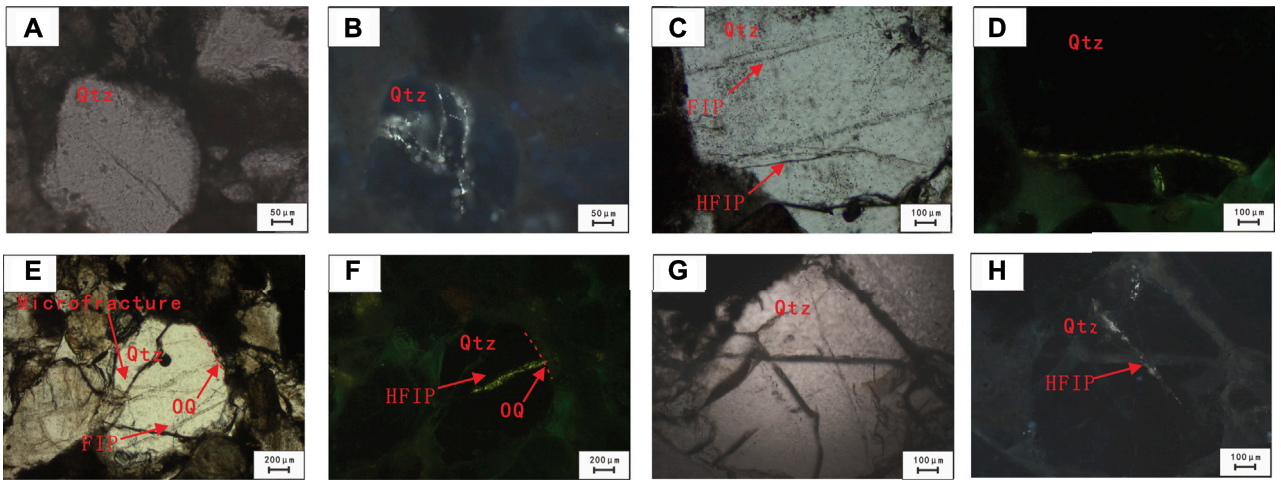

FIGURE 6 | Thin section images of samples in plane-polarized light **(A, C, E, G)** and ultra-violet light images of the same areas **(B, D, F, H)**. **(B)** X-shaped conjugated HFIP in quartz grains. **(E)** "Hertzian" contact points formed preferred orientation of microfractures and FIPs through the grain and quartz overgrowth which is indicated using a red dotted line. **(G)** Different generation microfractures and HFIP in crosscutting.

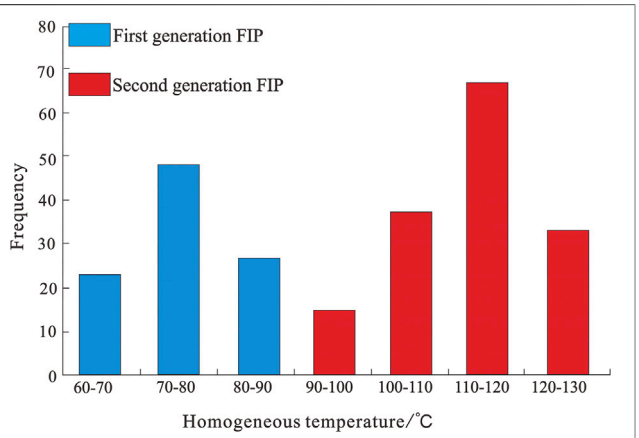

FIGURE 7 | Homogenization temperature data from 12 wells, with the main peak distributed in the range of 70–80°C and 110–120°C.

aqueous inclusions can typically represent the capture temperature of both types of inclusions without pressure correction (Nedkvitne et al., 1993). Considering that the quartz grains in the host rock may contain inherited FIPs if tectonic movements are experienced in the source region, the FIPs can be formed during the burial compaction process of the strata (Hooker et al., 2018; O'Kane et al., 2007). However, the Triassic reservoirs experienced a complicated burial history due to the compressional uplift, and fluid inclusions with the same homogenization temperature may be trapped more than once. Hence, in this study, only the aqueous FIPs of quartz grains are consistent with the mechanical characteristics of the deformation bands.

Fluid inclusion was trapped in quartz microfractures from 51 Triassic reservoir sandstone samples. As depicted in **Figure 7**, the distribution of the homogenous temperatures of the coexisting oil and aqueous inclusions in all samples is analyzed and presented. In detail, microthermometric analyses indicate that all the selected fluid inclusions can homogenize to a single liquid phase. The homogenous temperature of inclusions in samples from wells LN2-3-1, LN206, and LN2-2-J1, located at the circumference of the fault horst belt, is mainly distributed in the range of 70–140°C, with the main peak range distributed in the range of 70–80°C and 110–120°C. It can be divided into two intervals, and the main peak of aqueous inclusions associated with hydrocarbon inclusions is 110–120°C and has the highest abundance. The FIP abundance in samples from well LN101 well located at the middle of the two-fault horst belt is significantly lower than that in samples in the fault horst belt circumference wells, especially the FIP abundance with the homogenous temperature of 70–80°C.

DISCUSSION

Associated Relationship Between Deformation Bands and the FIP

The macroscopic tectonic fault features of the highly porous sandstone formation under compression-shear tectonic stress are triggered by the microscopic grain failure. And the deformation structures evolve in the direction of the maximum principal stress with the strength and nature of the tectonic movement influencing the number and distribution of the deformation bands. The evolution process from the microscopic deformation structure to the macroscopic fault structure can be revealed through multi-scale observation and investigation (Fossen and Hesthammer, 2000; Parnell et al., 2004; Parry et al., 2004; Mitchell and Faulkner, 2009; Solum et al., 2010). As cleavage cracks within brittle minerals such as feldspar and calcite are formed by external stress according to the crystallographic nature (Fossen and Hesthammer, 2000; Sun

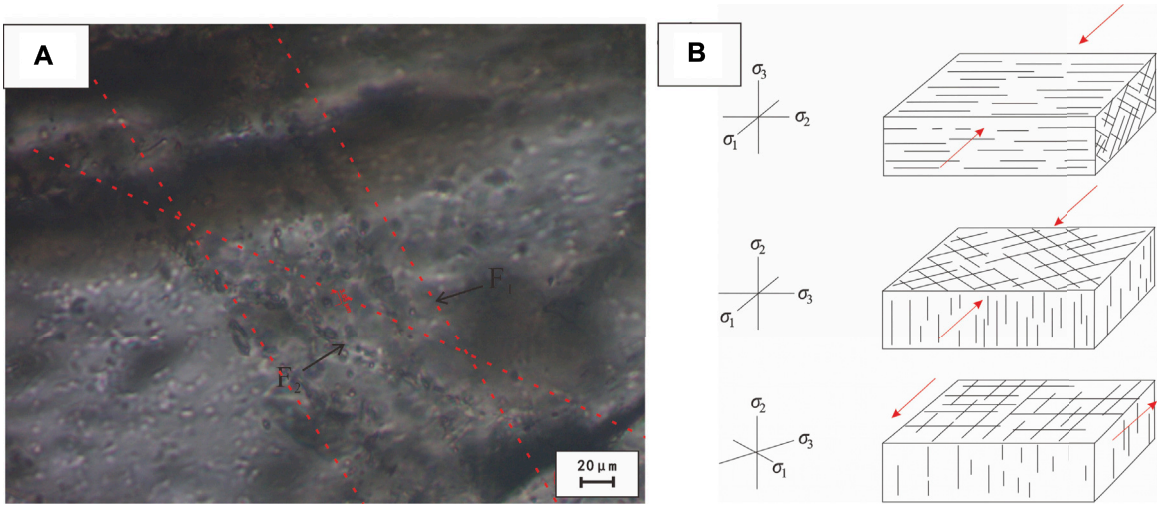

FIGURE 8 | (A) Thin-section photomicrograph of the X-shaped conjugated FIP which is indicated using a red dotted line, LN2-3-1, 4,870.7 m. **(B)** The relation between the maximum principal stress direction and X-shaped conjugated FIP.

et al., 2019a), the research on microstructural petrography needs to consider not only the strength and nature of tectonic movements but also the selection of mineral grain types, microfracture characteristics, and the generation relationship of fluid inclusions.

As the host mineral, quartz grains subjected to regional stress cracking develop microfractures that are independent of mineral crystallographic properties and can be easily healed to trap fluids as fluid inclusions (Onasch, 1990; Boullier, 1999; Parnell et al., 2001). The conjugate shear FIP is composed of two crossing rupture surfaces, which are formed as a result of shear stress acting on the mineral grains exceeding the shear strength of the grains (**Figure 8A**) (Anders et al., 2013), and the fractured rupture surface angle is restricted by the properties of the grains and the external temperature and pressure conditions during formation. Under the brittle tectonic conditions, the direction of the acute angle bisector of the two crushing surfaces points to the direction of the maximum principal stress σ_1. Under the brittle domain deformation condition, the direction of the acute angle bisector of the two crushing surfaces points to the direction of the maximum principal stress σ_1 (**Figure 8B**) (Soliva et al., 2013; Anders et al., 2014). The microfracture abundance is proportional to the intensity of large-scale tectonic movements, and the FIP assemblages formed by more than one tectonic movement exhibit cutting relationships with each other in space.

Microscopic analysis of thin sections revealed fragmented grains occur along the boundary between the host rock and deformation band subjected to contact stresses which have "Hertzian" contact points (**Figure 9**) (Radjai et al., 1998) with magnitudes much greater than the average stress. The force chains are recognized by obliquely intersecting the deformation band (**Figure 9B**). We interpret the preferred orientation of the microfracture and FIP is parallel to the maximum compression direction at the time of deformation

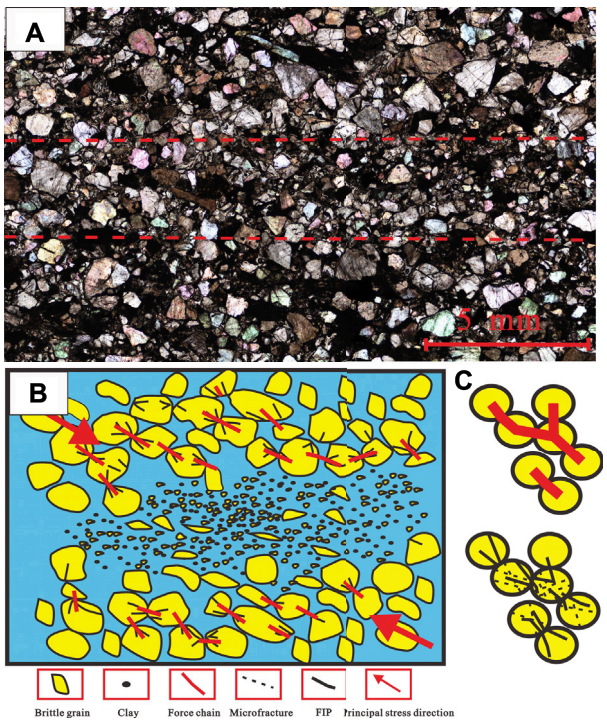

FIGURE 9 | (A) Thin-section photomicrograph of microstructures from the host rock and deformation bands; the boundary is indicated using red dotted lines. **(B)** Illustration of the relation between maximum principal stress direction, microstructures, and the force chains. **(C)** The geometry of the "Hertzian" contact, FIP, and geometry of force chains as inferred from grain contact points, modified from Soliva et al. (2013).

(**Figure 9C**) (Ballas et al., 2013; Soliva et al., 2013). Permeability and porosity transient increasing during the shear-induced dilatant phase of failure may result in hydrocarbon flow into sandstone

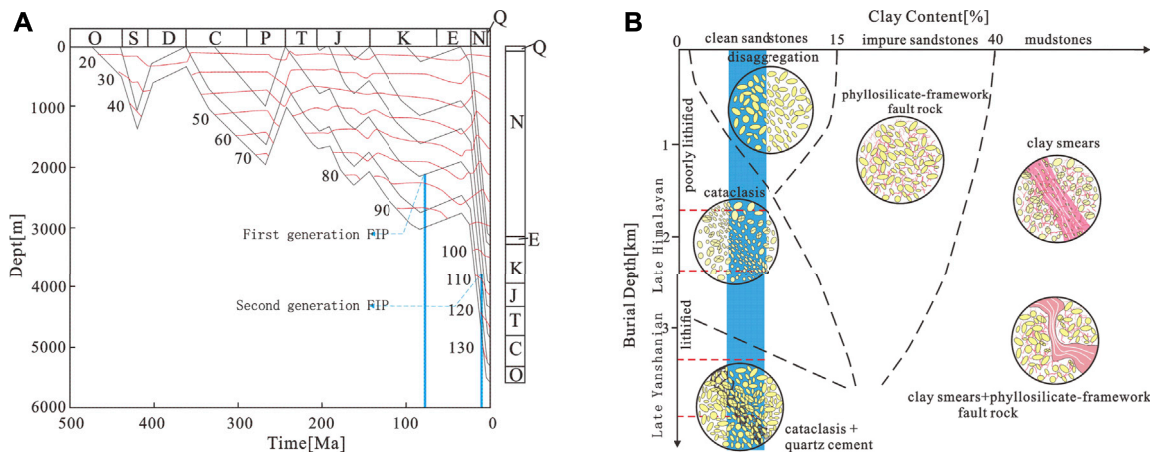

FIGURE 10 | (A) Burial and thermal history and deformation band formed time for well LN10. **(B)** Characteristic patterns of deformation band evolution in the Lunnan uplift, modified from Fossen et al. (2007), Pei et al. (2015).

reservoirs. FIP-trapped hydrocarbon fluid inclusions crosscutting quartz grain overgrowths occur in the damage zone of the deformation band, which show that oil charging postdated the deformation band formation or performed at the same time (Parnell et al., 2004; Sun et al., 2020).

Formation Time of the Deformation Band

Based on petrography and microthermometry, it is suggested that there were two generations of deformation bands formed because of the presence of two-generation conjugate FIPs observed in the CSB damage zone. The latter generation is closely related to oil and gas charging. By the integration temperature data from aqueous inclusions trapped in two generations conjugate FIPs of 51 samples collected from 12 wells with the burial plot, we can predict the time and depth of the deformation band formed.

Generally, the Triassic reservoirs are shallowly buried (0–2,000 m) within a long period and then become rapidly buried into a deeper depth (>4,500 m) in the Late Himalayan period. Integration of the minimum Th of two generation aqueous fluid inclusions in the conjugate FIPs of 51 samples, collected from 15 wells by coeval with the thermal history plot for selected wells, inferred that two-generation deformation bands are formed, respectively, in the Late Yanshan period (75~57 Ma) and the Late Himalayan period (14~4 Ma), coinciding with the regional uplift and extrusion.

Implication for Hydrocarbon Exploration

Deformation bands in sandstone reservoirs can act as fluid pathways or barriers for fluid flow, depending on the timing relationship between the hydrocarbon charge and deformation. The mechanism of fluid sealing can be divided into the formation of cis-layer cement at the early stage (Baron et al., 2008; Exner et al., 2013; Sun et al., 2019b) and the significant decrease of physical properties compared with the host rock at the late-generation stage under the compression and torsion (Fossen et al., 2007; Solum et al., 2010). Also, the decrease of permeability by three orders of magnitude compared with that of the host rock is the threshold value for influencing fluids (Solum et al., 2010); therefore, the investigations on the influence of deformation bands on fluids not only include the present-day physical characteristics but also need to restore their dynamic evolution process, which makes them important to investigate the associated relationship between hydrocarbon charging and deformation band formation.

Two generations of shear compaction bands can be observed and identified in the Triassic reservoir by FIP characteristics and homogeneous temperature (**Figure 10B**). And the early-formed shear deformation bands mainly show that extrusion and crushing of brittle grains, deformation of plastic grains, and intragranular microfractures emanating from contact points are common. The microscopic conductive properties of the sandstone layer were improved, and the physical properties showed little variation compared to those of the host rock. As the extrusion intensity of the tectonic movement and the temperature of the buried environment increase, the later formed deformation bands turn into an interlayer with regular spatial combination, which can be regarded as densely spread deformation bands separating oil and water layers. Some of the deformation bands with internal quartz grains trapped hydrocarbon inclusions, implying that the oil charge would have not been affected by the deformation-related structure. In summary, the deformation bands in the research area mainly affect the physical adjustment of the hydrocarbon distribution in the later stage and the present flow properties of the reservoir and have a slight influence on the hydrocarbon migration and the charge of Triassic reservoirs.

CONCLUSION

Comprehensive characteristics of deformation bands from Triassic high-porous reservoirs in the Lunnan uplift, Tarim Basin, are reported for the first time. The dominant deformation mechanisms are controlled by the strength and nature of

tectonic movements. Experimental observations in terms of core samples indicate that the deformation bands can act as interbedded layers or barriers restricting the oil flow capacity. Integrated studies of fluid inclusions demonstrate the time and depth of the two-generation deformation band formed during the Yanshanian and Himalayan periods. In particular, the hydrocarbon charge has not been affected by deformation band formation because the oil-trapping quartz microfracture is cut by deformation bands. The deformation bands in the research area mainly affect hydrocarbon distribution and the present seepage flow properties of reservoirs, which may promote reservoir compartmentalization.

DATA AVAILABILITY STATEMENT

The raw data supporting the conclusion of this article will be made available by the authors, without undue reservation.

AUTHOR CONTRIBUTIONS

WY: investigation and supervision; MZ: funding acquisition and methodology; JQ: investigation; XD: draft writing and experiments; and QZ: data analysis.

REFERENCES

Anders, M. H., Laubach, S. E., and Scholz, C. H. (2014). Microfractures: A Review. *Journal Structural Geology.* 69, 377–394. doi:10.1016/j.jsg.2014.05.011

Anders, M. H., Schneider, J. R., Scholz, C. H., and Losh, S. (2013). Mode I Microfracturing and Fluid Flow in Damage Zones: The Key to Distinguishing Faults from Slides. *Journal Structural Geology.* 48, 113–125. doi:10.1016/j.jsg.2012.11.010

Anders, M. H., and Wiltschko, D. V. (1994). Microfracturing, Paleostress and the Growth of Faults. *Journal Structural Geology.* 16 (6), 795–815. doi:10.1016/0191-8141(94)90146-5

Ballas, G., Soliva, R., Benedicto, A., and Sizun, J.-P. (2014). Control of Tectonic Setting and Large-Scale Faults on the Basin-Scale Distribution of Deformation Bands in Porous Sandstone (Provence, France). *Journal Structural Geology.* 55, 142–159. doi:10.1016/j.marpetgeo.2013.12.020

Ballas, G., Soliva, R., Sizun, J.-P., Fossen, H., Benedicto, A., and Skurtveit, E. (2013). Shear-Enhanced Compaction Bands Formed at Shallow Burial Conditions; Implications for Fluid Flow (Provence, France). *Journal Structural Geology.* 47, 3–15. doi:10.1016/j.jsg.2012.11.008

Baron, M., Parnell, J., Mark, D., Carr, A., Przyjalgowski, M., and Feely, M. (2008). Evolution of Hydrocarbon Migration Style in a Fractured Reservoir Deduced from Fluid Inclusion Data, Clair Field, West of Shetland, UK. *Marine Petroleum Geology.* 25 (2), 153–172. doi:10.1016/j.marpetgeo.2007.05.010

Beke, B., Fodor, L., Millar, L., and Petrik, A. (2019). Deformation Band Formation as a Function of Progressive Burial: Depth Calibration and Mechanism Change in the Pannonian Basin (Hungary). *Marine Petroleum Geology.* 105, 1–16. doi:10.1016/j.marpetgeo.2019.04.006

Bodnar, R. J. (1993). Revised Equation and Table for Determining the Freezing Point Depression of H2O-Nacl Solutions. *Geochim. Cosmochim. Acta* 53. doi:10.1016/0016-7037(93)90378-A

Bossennec, C., Géraud, Y., Moretti, I., Mattioni, L., and Stemmelen, D. (2018). Pore Network Properties of Sandstones in a Fault Damage Zone. *Journal Structural Geology.* 110, 24–44. doi:10.1016/j.jsg.2018.02.003

Boullier, A-M. (1999). Fluid Inclusions: Tectonic Indicators. *Journal Structural Geology.* 21 (8-9), 1229–1235. doi:10.1016/s0191-8141(99)00039-5

Exner, U., Kaiser, J., and Gier, S. (2013). Deformation Bands Evolving from Dilation to Cementation Bands in a Hydrocarbon Reservoir (Vienna Basin, Austria). *Marine Petroleum Geology.* 43, 504–515. doi:10.1016/j.marpetgeo.2012.10.001

Fisher, Q. J., and Knipe, R. J. (2001). The Permeability of Faults within Siliciclastic Petroleum Reservoirs of the North Sea and Norwegian Continental Shelf. *Mar. Pet. Geology.* 18 (10), 1063–1081. doi:10.1016/s0264-8172(01)00042-3

Folk, R. L., and Ward, W. C. (1957). Brazos River Bar [Texas]; a Study in the Significance of Grain Size Parameters. *Journal Sedimentary Research.* 27 (1), 3–26. doi:10.1306/74d70646-2b21-11d7-8648000102c1865d

Fossen, H., and Bale, A. (2007). Deformation Bands and Their Influence on Fluid Flow. *Bulletin* 91 (12), 1685–1700. doi:10.1306/07300706146

Fossen, H., and Hesthammer, J. (2000). Possible Absence of Small Faults in the Gullfaks Field, Northern North Sea: Implications for Downscaling of Faults in Some Porous Sandstones. *Journal Structural Geology.* 22 (7), 851–863. doi:10.1016/s0191-8141(00)00013-4

Fossen, H., Schultz, R. A., Shipton, Z. K., and Mair, K. (2007). Deformation Bands in Sandstone: A Review. *Journal Geological Society.* 164 (4), 755–769. doi:10.1144/0016-76492006-036

Fossen, H., Soliva, R., Ballas, G., Trzaskos, B., Cavalcante, C., and Schultz, R. A. (2018). A Review of Deformation Bands in Reservoir Sandstones: Geometries, Mechanisms and Distribution. *Geol. Soc. Lond. Spec. Publications* 459 (1), 9–33. doi:10.1144/sp459.4

Goldstein, R. H., and Reynolds, T. J. (1994). Systematics Of Fluid Inclusions In Diagenetic Minerals. SEPM Short Course*: Systematics of Fluid Inclusions in Diagenetic Minerals*. Tulsa, OK: SEPM Short Course.

Hooker, J. N., Laubach, S. E., and Marrett, R. (2018). Microfracture Spacing Distributions and the Evolution of Fracture Patterns in Sandstones. *Journal Structural Geology.* 108, 66–79. doi:10.1016/j.jsg.2017.04.001

Lander, R. H., and Laubach, S. E. (2014). Insights into Rates of Fracture Growth and Sealing from a Model for Quartz Cementation in Fractured Sandstones. *GSA Bulletin.* 127 (3-4), 516–538. doi:10.1130/b31092.1

Laubach, S. E., Eichhubl, P., Hilgers, C., and Lander, R. H. (2010). Structural Diagenesis. *Journal Structural Geology.* 32 (12), 1866–1872. doi:10.1016/j.jsg.2010.10.001

Lommatzsch, M., Exner, U., Gier, S., and Grasemann, B. (2015). Structural and Chemical Controls of Deformation Bands on Fluid Flow: Interplay between Cataclasis and Diagenetic Alteration. *Bulletin* 99 (04), 689–710. doi:10.1306/10081413162

Miao, Y., Li, X., Zhou, Y., Wu, K., Chang, Y., Xiao, Z., et al. (2018). A Dynamic Predictive Permeability Model in Coal Reservoirs: Effects of Shrinkage Behavior Caused by Water Desorption. *J. Pet. Sci. Eng.* 168, 533–541. doi:10.1016/j.petrol.2018.05.028

Miao, Y., Zhao, C., and Zhou, G. (2020). New Rate-Decline Forecast Approach for Low-Permeability Gas Reservoirs with Hydraulic Fracturing Treatments. *J. Pet. Sci. Eng.* 190, 107112. doi:10.1016/j.petrol.2020.107112

Mitchell, T. M., and Faulkner, D. R. (2009). The Nature and Origin of Off-Fault Damage Surrounding Strike-Slip Fault Zones with a Wide Range of Displacements: A Field Study from the Atacama Fault System, Northern Chile. *Journal Structural Geology.* 31 (8), 802–816. doi:10.1016/j.jsg.2009.05.002

Nedkvitne, T., Karlsen, D. A., Bjørlykke, K., and Larter, S. R. (1993). Relationship between Reservoir Diagenetic Evolution and Petroleum Emplacement in the Ula Field, North Sea. *Marine Petroleum Geology.* 10 (3), 255–270. doi:10.1016/0264-8172(93)90108-5

O'Kane, A., Onasch, C. M., and Farver, J. R. (2007). The Role of Fluids in Low Temperature, Fault-Related Deformation of Quartz Arenite. *Journal Structural Geology.* 29 (5), 819–836. doi:10.1016/j.jsg.2007.01.003

Onasch, C. M. (1990). Microfractures and Their Role in Deformation of a Quartz Arenite from the Central Appalachian Foreland. *Journal Structural Geology.* 12 (7), 883–894. doi:10.1016/0191-8141(90)90061-3

Parnell, J., Middleton, D., Honghan, C., and Hall, D. (2001). The Use of Integrated Fluid Inclusion Studies in Constraining Oil Charge History and Reservoir Compartmentation: Examples from the Jeanne d'Arc Basin, Offshore Newfoundland. *Marine Petroleum Geology.* 18 (5), 535–549. doi:10.1016/s0264-8172(01)00018-6

Parnell, J., Watt, G. R., Middleton, D., Kelly, J., and Baron, M. (2004). Deformation Band Control on Hydrocarbon Migration. *Journal Sedimentary Research.* 74 (4), 552–560. doi:10.1306/121703740552

Parry, W. T., Chan, M. A., and Beitler., B. (2004). Chemical Bleaching Indicates Episodes of Fluid Flow in Deformation Bands in Sandstone. *Bulletin* 88 (2), 175–191. doi:10.1306/09090303034

Pei, Y., Paton, D. A., Knipe, R. J., and Wu, K. (2015). A Review of Fault Sealing Behaviour and its Evaluation in Siliciclastic Rocks. *Earth-Science Reviews* 150, 121–138. doi:10.1016/j.earscirev.2015.07.011

Philit, S., Soliva, R., Castilla, R., Ballas, G., and Taillefer, A. (2018). Clusters of Cataclastic Deformation Bands in Porous Sandstones. *Journal Structural Geology.* 114, 235–250. doi:10.1016/j.jsg.2018.04.013

Radjai, F., Wolf, D. E., Jean, M., and Moreau, J.-J. (1998). Bimodal Character of Stress Transmission in Granular Packings. *Phys. Rev. Lett.* 80 (1), 61–64. doi:10.1103/physrevlett.80.61

Schueller, S., Braathen, A., Fossen, H., and Tveranger, J. (2013). Spatial Distribution of Deformation Bands in Damage Zones of Extensional Faults in Porous Sandstones: Statistical Analysis of Field Data. *Journal Structural Geology.* 52, 148–162. doi:10.1016/j.jsg.2013.03.013

Schultz, R. A., and Fossen, H. (2008). Terminology for Structural Discontinuities. *Bulletin* 92 (7), 853–867. doi:10.1306/02200807065

Soliva, R., Schultz, R. A., Ballas, G., Taboada, A., Wibberley, C., Saillet, E., et al. (2013). A Model of Strain Localization in Porous Sandstone as a Function of Tectonic Setting, Burial and Material Properties; New Insight from Provence (Southern France). *Journal Structural Geology.* 49, 50–63. doi:10.1016/j.jsg.2012.11.011

Solum, J. G., Brandenburg, J. P., KostenkoBrandenburg, O. V., Wilkins, S. J., and Schultz, R. A. (2010). Characterization of Deformation Bands Associated with Normal and Reverse Stress States in the Navajo Sandstone, Utah. *Bulletin* 94 (9), 1453–1475. doi:10.1306/01051009137

Su, J., Zhu, G., Yang, H., Dang, X., Wang, Y., Zhang, B., et al. (2013). The Research of Types and Formation Mechanism of Physical Adjustment Reservoirs: Applying the Three-Dimensional Fluorescence Quantitative to Study on the Adjustment Mechanism of Triassic Oil and Gas Reservoirs in the Lunnan Area, Tarim Basin[J]. *Acta Petrologica Sinica, 2013* 29 (9), 32513262.

Sun, L., and Li, Y. (2004). The Lunnan Lower Uplift:a Multiple Oil-Gas Accumulation Play in the Tarim Basin, NW China[J]. *Chin. J. Geology.* (02), 296–304.

Sun, Z., Li, X., Liu, W., Zhang, T., He, M., and Nasrabadi, H. (2020). Molecular Dynamics of Methane Flow Behavior through Realistic Organic Nanopores under Geologic Shale Condition: Pore Size and Kerogen Types. *Chem. Eng. J.* 398, 124341. doi:10.1016/j.cej.2020.124341

Sun, Z., Li, X., Shi, J., Zhang, T., Feng, D., Sun, F., et al. (2018). A Semi-analytical Model for the Relationship between Pressure and Saturation in the CBM Reservoirs. *J. Nat. Gas Sci. Eng.* 49, 365–375. doi:10.1016/j.jngse.2017.11.022

Sun, Z., Shi, J., Wu, K., Zhang, T., Feng, D., and Li, X. (2019). Effect of Pressure-Propagation Behavior on Production Performance: Implication for Advancing Low-Permeability Coalbed-Methane Recovery. *SPE J.* 24 (02), 681–697. doi:10.2118/194021-pa

Sun, Z., Wu, K., Shi, J., Zhang, T., Feng, D., Wang, S., et al. (2019). Effect of Pore Geometry on Nanoconfined Water Transport Behavior. *AIChE J.* 65 (8), e16613. doi:10.1002/aic.16613

Torabi, A., and Fossen, H. (2009). Spatial Variation of Microstructure and Petrophysical Properties along Deformation Bands in Reservoir Sandstones. *Bulletin* 93 (7), 919–938. doi:10.1306/03270908161

TorabiBraathen, A., Fossen, H., and Braathen, A. (2013). Insight into Petrophysical Properties of Deformed Sandstone Reservoirs. *Bulletin* 97, 619–637. doi:10.1306/10031212040

Yang, H., Hao, F., Han, J., Cai, Z., Gu, Q., et al. (2007). Fault Systems and Multiple Oil-Gas Accumulation Play of the Lunnan Lower Uplift, Tarim Basin[J]. *Chin. J. Geology.* (04), 795–811.

Zhang, S., Zhang, B., Yang, H., Zhu, G., Su, J., and Wang, X. (2012). Adjustment and Alteration of Hydrocarbon Reservoirs during the Late Himalayan Period, Tarim Basin, NW China[J]. *Pet. Exploration Develop.* 39 (06), 668–680. doi:10.1016/s1876-3804(12)60096-2

Zhang, Y., Ren, J., Yang, H., Hu, D., and L, P. (2011). Structure Features and its Evolution of Lunnan Low Uplift, the Tarim Basin[J]. *Oil Gas Geology.* 32 (03), 440–447.

Zhao, Y., Li, Y., Sun, L. D., Zheng, D., Liu, Y., and Wang, D. (2012). Mesozoic-Cenozoic Extensional Structure in North Uplift of Tarim basin and its Genetic Discussion[J]. *Acta Petrologica Sinica* 28 (08), 2557–2568.

Conflict of Interest: The authors declare that the research was conducted in the absence of any commercial or financial relationships that could be construed as a potential conflict of interest.

Publisher's Note: All claims expressed in this article are solely those of the authors and do not necessarily represent those of their affiliated organizations, or those of the publisher, the editors, and the reviewers. Any product that may be evaluated in this article, or claim that may be made by its manufacturer, is not guaranteed or endorsed by the publisher.

frontiers in Earth Science

ORIGINAL RESEARCH
published: 30 September 2021
doi: 10.3389/feart.2021.755050

Composite Strike-Slip Deformation Belts and Their Control on Oil and Gas Reservoirs: A Case Study of the Northern Part of the Shunbei 5 Strike-Slip Deformation Belt in Tarim Basin, Northwestern China

Haowei Yuan[1,2]*, *Shuping Chen*[1,2]*, *Yuan Neng*[3], *Huaibo Zhao*[1,2], *Shidong Xu*[1,2], *Xinpeng Wang*[1,2] and *Guimin Feng*[1,2]

[1]State Key Laboratory of Petroleum Resources and Prospecting, China University of Petroleum, Beijing, China, [2]College of Geosciences, China University of Petroleum, Beijing, China, [3]China University of Petroleum-Beijing at Karamay, Karamay, China

Strike-slip deformation belts are interesting structures in the crust and are of significance in petroleum exploration. The Shunbei 5 fault belt (SB5), a long strike-slip deformation belt in the Tarim Basin, played an important role in the formation of a recently discovered major oilfield known as the Shunbei oilfield. In this study, models of plan view and vertical profile were established to interpret SB5 with multi-cycled tectonic activities. To this end, its structural framework, tectonic evolution, and associated plate tectonics were investigated using 2D and 3D seismic data. SB5 was formed as a dextral simple shear belt at the end of the Middle Ordovician. In the plan view, R-shears and P-shears with local transpressional and transtensional structures were observed. Along the vertical profiles, various structural styles occurred at various depths and strata in response to various stratigraphy mechanisms. Although these structures show clear boundaries between them, they correspond to the same formation time, indicating that they underwent deformation simultaneously. The second activity of SB5 occurred at the end of the late Ordovician, during which it was a dextral transtensional strike-slip deformation belt consisting of left-stepping en echelon R-shears. The R-shears were transtensional during the progressive deformation. Subsequently, SB5 underwent several strike slips of weak strength. Notably, SB5 cut through a deep Middle Cambrian gypsum salt layer and connected the deep Lower Cambrian source rock with deep Lower and Middle Ordovician carbonates to form the oil and gas reservoirs. The established models are of reference value in the interpretation of other subsurface strike-slip deformation belts.

Keywords: strike-slip deformation belt, structural style, interpretation model, oil and gas reservoir, Tarim Basin

OPEN ACCESS

Edited by:
Wenhui Song,
China University of Petroleum (Huadong), China

Reviewed by:
Jia Lu,
China University of Geosciences, China
Mianmo Meng,
China University of Petroleum (Huadong), China

***Correspondence:**
Haowei Yuan
yuanatcugb@163.com
Shuping Chen
csp21c@163.com

Specialty section:
This article was submitted to Economic Geology, a section of the journal Frontiers in Earth Science

Received: *07 August 2021*
Accepted: *17 September 2021*
Published: *30 September 2021*

Citation:
Yuan H, Chen S, Neng Y, Zhao H, Xu S, Wang X and Feng G (2021) Composite Strike-Slip Deformation Belts and Their Control on Oil and Gas Reservoirs: A Case Study of the Northern Part of the Shunbei 5 Strike-Slip Deformation Belt in Tarim Basin, Northwestern China. Front. Earth Sci. 9:755050. doi: 10.3389/feart.2021.755050

INTRODUCTION

Strike-slip faults are an important tectonic feature in nature. A strike-slip deformation belt commonly consists of various structures with different mechanics, such as normal faults, shear faults, and reverse faults or folds (Riedel, 1929; Chinnery, 1963; Wilcox et al., 1973; Sylvester, 1988). These structures can form petroleum traps in a basin. Moreover, strike-slip faults may cut deep below the surface to form petroleum migration pathways. Therefore, strike-slipping structures are of important significance in petroleum exploration (Lowell, 1985; Allen and Allen, 2013; Chen et al., 2018; El Ghamry et al., 2020).

In recent years, the China Petroleum and Chemical Corporation (Sinopec) discovered a major oilfield known as the Shunbei oilfield around the Shunbei 5 well in the middle west of the Tarim basin (**Figure 1**). The oil and gas reservoirs exist in Lower and Middle Ordovician carbonates, unevenly distributed along faults at depths exceeding 7,000 m (Cao et al., 2020). Its total resource is estimated at 17×10^8 t, of which oil and gas account for 12×10^8 t and $5{,}000 \times 10^8$ m^3, respectively (Jiao, 2018). The reservoirs are fractures and caves and are characterized by ultra-depth, and ultra-high pressure and temperature.

The formation of the Shunbei oilfield is related to the Shunbei 5 strike-slip deformation belt (SB5). The strike-slip faults in this belt connected the deep Lower Cambrian source rock with the Ordovician carbonates. The complex structural framework of SB5 determined the uneven distribution of oil and gas along the fault (Cao et al., 2020). However, the interpretation of the structural framework of SB5 is debatable (Deng et al., 2018; Li et al., 2019; Liu, 2020; Wang et al., 2020). The active time of SB5 is difficult to determine and its formation mechanism is not clear. U-Pb isotopic dating of calcite in fractures in Ordovician Carbonate rocks indicated that the formation of SB5 began at the end of the Middle Ordovician (Wu et al., 2020). However, according to seismic data, the formation time of strike-slip faults in the Tabei and Tazhong uplifts was in the late Ordovician and the strike-slip faults in the Tazhong uplift formed earlier than those in the Tabei uplift (Wu et al., 2012; Zhen et al., 2015; Han et al., 2017; Deng et al., 2018; Wu et al., 2018; Huang, 2019).

In this study, models were constructed to determine the kinematic types and analyze the plane structural framework of strike-slip deformation belts from the perspective of structural

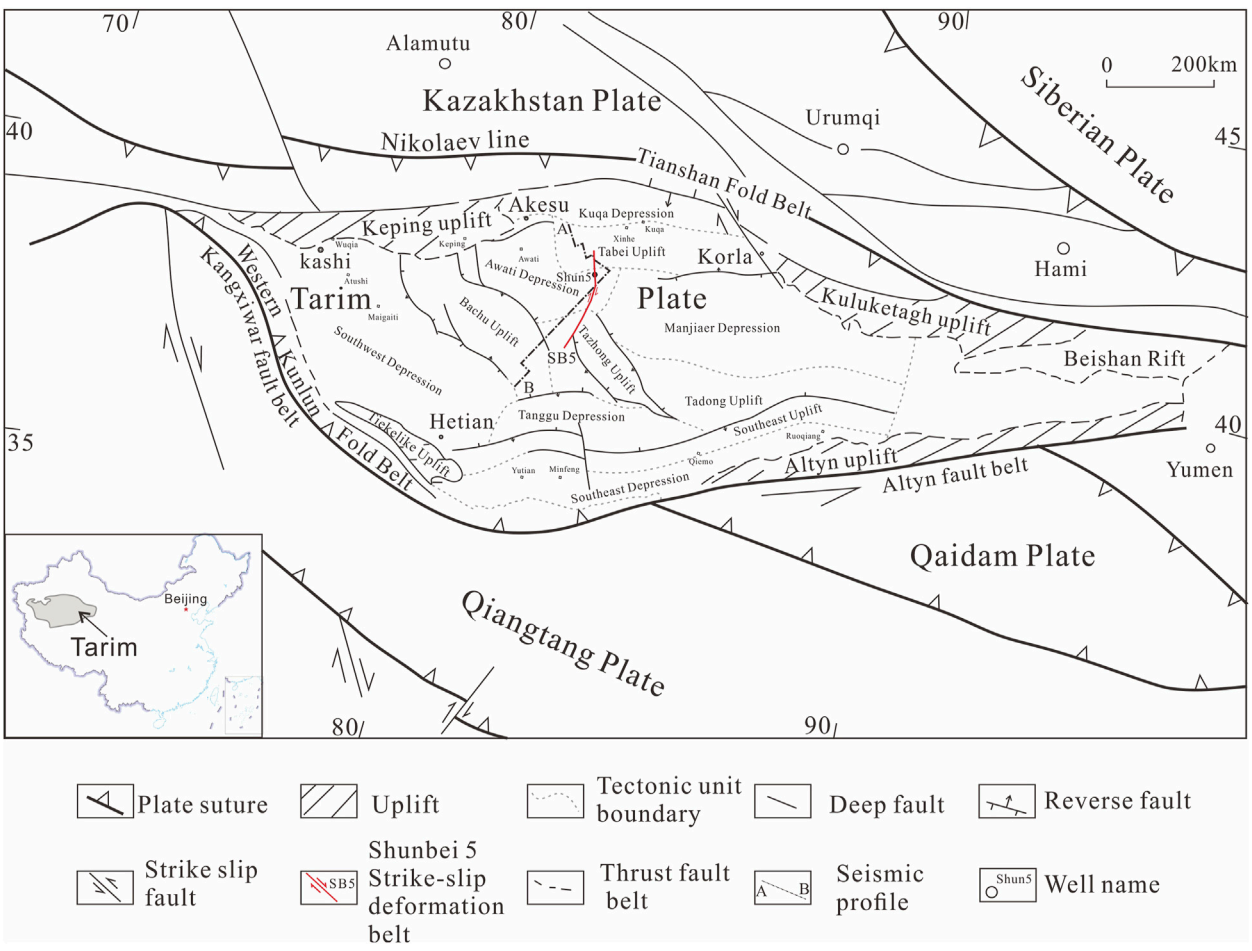

FIGURE 1 | Plate tectonics and tectonic units of the Tarim Plate (Basin).

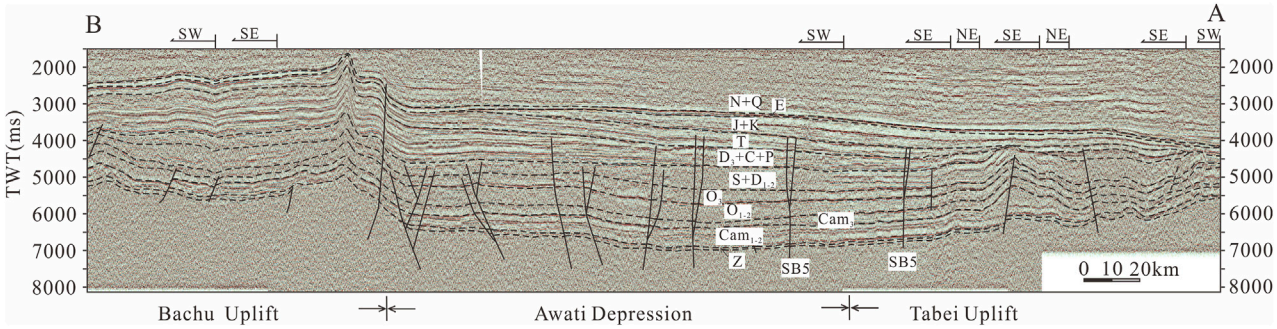

FIGURE 2 | 2D Seismic profile showing some tectonic units of the Tarim Basin. (N + Q)-Neogene and Quaternary, E-Paleogene, (J + K)-Jurassic and Cretaceous, T-Triassic, (D_3 + C + P)-Upper Devonian and Carboniferous and Permian, (S + D_{1-2})-Silurian and Lower and Upper Devonian, O_3-Upper Ordovician, O_{1-2}-Lower and Middle Ordovician, Cam_3-Upper Cambrian, Cam_{1-2}-Lower and Middle Cambrian, Z-Sinian

geology theory. Indicators for identifying the formation time of strike-slip faults in the vertical profile and plan view were initially established. Based on these models and indicators, the structural framework and formation time of SB5 were interpreted. Integrating plate tectonics, the formation mechanism of SB5 was discussed and its significance in petroleum geology was addressed. The presented formation mechanisms of the strike-slip faults can provide guidance for the exploration of the Shunbei oilfield and contribute to better understanding of global strike-slip faults.

GEOLOGICAL SETTING

The Tarim Basin is located in the Xinjiang Uygur Autonomous Region of China, with an area of 56×10^4 km^2. It is situated on the Tarim plate and is surrounded by mountains such as the Tianshan mountains to the north, Kunlun mountains to the south, and Altyn-Tagh mountains to the southeast (**Figure 1**). SB5 is located in the central Tarim Basin, across the Tazhong Uplift, Awati Depression, and Tabei Uplift (**Figure 2**).

The sedimentary cover includes Nanhua, Sinian, Paleozoic, Mesozoic, and Cenozoic sediments (**Figure 3**). The late Proterozoic Nanhua system comprises continental rift sediments; the rift occurred during the breakup of the Rodinia supercontinent (Wu L. et al., 2016; Shi et al., 2016; Ren et al., 2018; Shi et al., 2018). During the Sinian, the Tarim Basin entered a thermal depression with the deposition of cold climate marine and ice ocean carbonates, clastic rocks, and moraine and volcanic clastic rocks (Deng et al., 2019).

During the Cambrian, the south and north margins were passive margins, and the inner basin was a successive basin with marine carbonates, mudstone, gypsum salt rocks, and siliceous mudstone. The marine carbonate sedimentation continued to the end of the Middle Ordovician when the first episode of the Caledonian movement occurred (Han et al., 2021). During the Upper Ordovician, marine clastic sediments with thick mudstone were deposited, developing suitable cap rocks (Lu et al., 2015). During the Silurian, marine clastic sediments were deposited. The late Caledonian movement at the end of the late Ordovician and the early Hercynian movement caused regional unconformity between the Silurian and Upper Devonian (**Figure 3**).

From the late Devonian to the Triassic, the tectonic regime of the Tarim Basin changed into margin subduction and collision with interactive marine and terrestrial deposits. The Upper Devonian and Carboniferous strata comprise marine clastic rocks. The Permian and Triassic strata comprise terrestrial clastic rocks and volcanic rocks (**Figure 3**). The Middle Hercynian movement occurred at the end of the Carboniferous, the late Hercynian movement at the end of the Permian, and the Indochina movement at the end of the Triassic.

From the Jurassic to the Oligocene, the Tarim Basin experienced inner plate tectonics after collision, with the deposition of terrestrial clastic rocks and gypsum salt rocks (**Figure 3**). The middle Yanshanian movement occurred at the end of the Jurassic, the late Yanshanian movement at the end of the Cretaceous, and the early Himalayan movement at the end of the Paleogene.

In the Neogene, the Tarim basin was a reactive foreland basin, with the deposition of terrestrial clastic rocks and gypsum salt rocks.

The Tarim Basin is rich in oil and gas resources, with estimated oil reserves of 59.94×10^8 t (Zhou et al., 2005), ordinary gas reserves of 117398.96×10^8 m^3, and non-ordinary gas reserves of 3×10^{12} m^3 (Zhou et al., 2005; Huang, 2019). Through extensive exploration works covering more than 30 years, the source rocks, structural styles, trap types, and reservoir model have been well established in three hydrocarbon-bearing systems, the Kuqa depression, platform basin area, and the southwest depression (Du et al., 2019).

DATA AND METHODOLOGY

The Shunbei-5 strike-slip deformation belt and its related structures were determined based on 2D and 3D seismic data provided by Sinopec between 2009 and 2016 (**Figure 2**). The geochronologic calibration of the seismic reflectors was performed by the Institute of Exploration and Development and Northwest Petroleum Bureau, Sinopec. The seismic data were interpreted in OpenWorks (Halliburton Landmark). Seismic coherence slices were used to

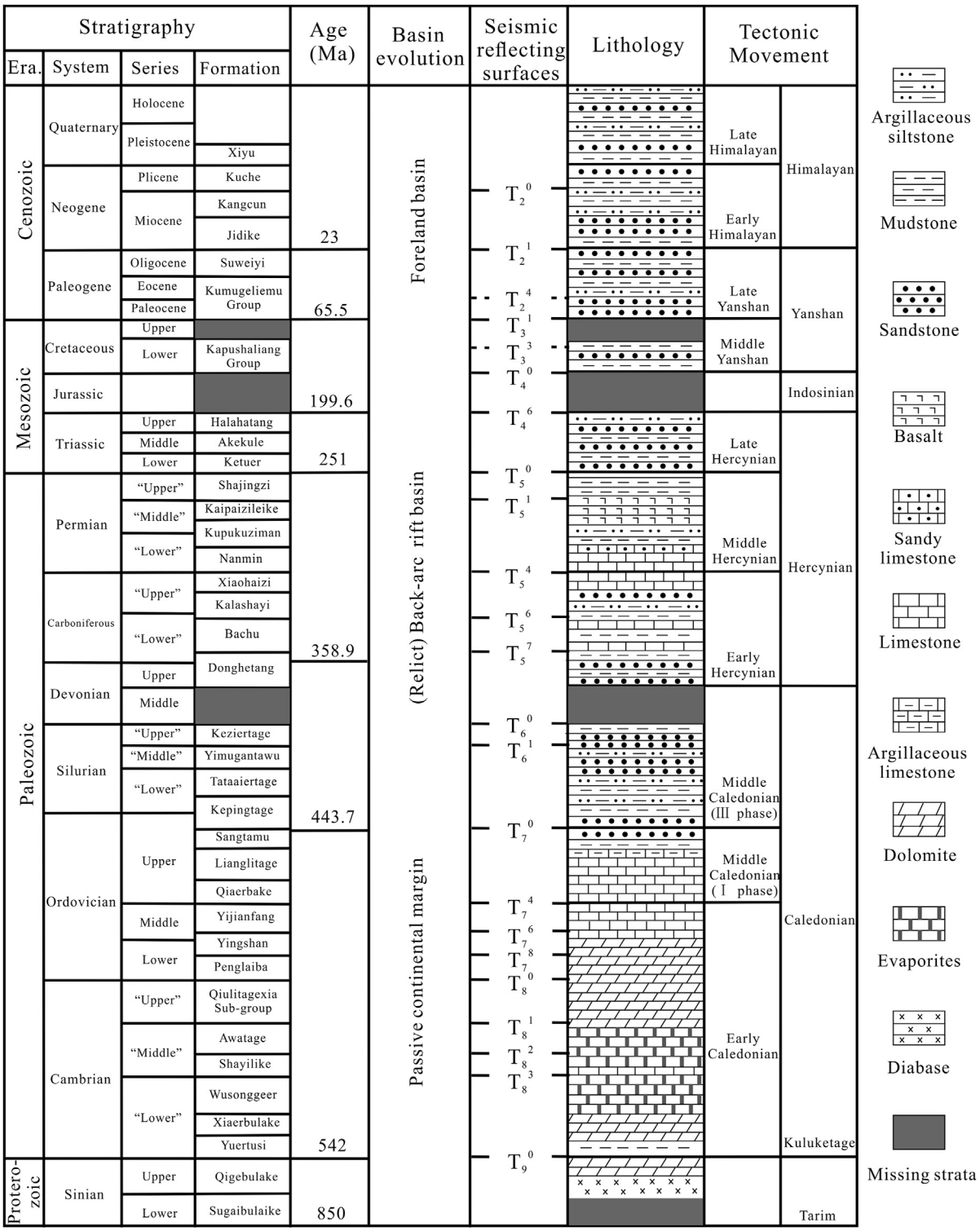

FIGURE 3 | Generalized stratigraphy of the Shunbei 5 strike-slip deformation belt in Tarim Basin (Modified after Lu et al., 2015; Deng et al., 2019; Han et al., 2021).

identify the individual fault segments (Bahorich and Farmer, 1995). The coherence slices of surface T_7^0 (stratigraphic boundary between the Kepingtage and Sangtamu Formations) and T_7^4 (stratigraphic boundary between the Upper Ordovician and Middle Ordovician) were used to analyze the structural characteristics of faults and fault combinations.

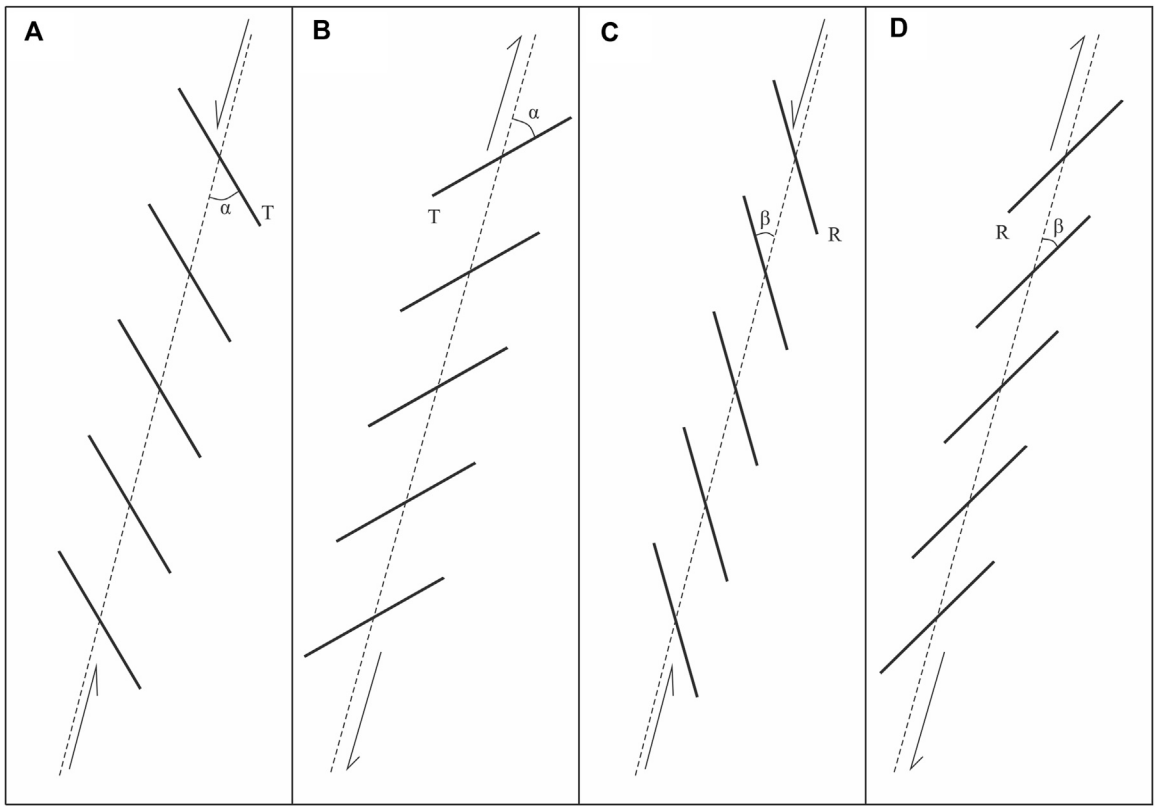

FIGURE 4 | Wrench directions and fault arraying types. **(A)** Right-stepping tensional faults indicating a sinistral strike-slip fault system, **(B)** Left-stepping tensional faults indicating a dextral strike-slip fault, **(C)** Right-stepping R-shear faults indicating a sinistral strike-slip fault system, **(D)** Left-stepping R-shear faults indicating a dextral strike-slip fault system. α is the angle between the direction of principal displacement zone and the T fracture, and β is the angle between the direction of principal displacement zone and R-shears.

A strike-slip deformation belt has various types of structures (Allen and Allen, 2013). Here, a composite strike-slip deformation belt is defined as a large-scale strike-slip deformation belt with multiphase activities, various mechanics, and directional structures both superposing in vertical sections and arraying in maps. Based on physical modeling of a wrench zone, en echelon tensional fractures (T-fracture) and shear fractures were identified (Riedel, 1929). Synthetic shears (R-shears) and antithetic shears (R'-shears) were defined as Riedel shears (Skempton, 1966; Hills, 2012). Other secondary structures in a wrench zone include P-shears, Y-shears, and convergent structures such as folds and reverse faults (Harding, 1974; Schreurs, 1994; Xu et al., 2017; Chen, 2020b; Chen, 2020a). Applying these methods and theories, the formation time and formation mechanism of SB5 were determined.

STRUCTURAL FRAME WORK OF THE SHUNBEI 5 STRIKE-SLIP DEFORMATION BELT

The Shunbei 5 strike-slip formation belt (SB5) is located in the central part of the Tarim basin (**Figure 1**). In this study, emphasis was placed on the central part of SB5.

Usually, the wrench direction of a subsurface strike-slip deformation belt is determined by the arraying styles of faults (**Figure 4**; Ghosh and Chattopadhyay, 2008). Both right-stepping tensional faults and right-stepping R-shear faults indicate a sinistral strike-slip fault (**Figures 4A,C**). Both left-stepping tensional faults and left-stepping R-shear faults indicate a dextral strike-slip fault (**Figures 4B,D**). Regarding SB5, in the T_7^0 reflector, the faults array in a right-stepping en echelon belt (**Figures 5A**,**B**, **6A**,**B**. The echelon angles of the faults generally range from 14° to 35°, with some at 44° ± 5° (**Figures 6A,B**). Along the vertical profiles, the faults appear to be normal faults (T-fracture) (**Figure 7**, **Figure 8**). Considering **Figures 4B,D**, these faults were deduced to be R-shears, and they indicate a dextral transtensional strike-slip fault. In the T_7^4 reflector, the faults array in complex patterns (**Figures 5C,D**, **6C,D**). The echelon angles of the faults generally range from 16° to 32° (counterclockwise), and from 9° to 12° (clockwise), with some at 43° (**Figures 6C,D**), corresponding to R-shears, P-shears, and several spreading branches of R-shears, respectively (**Figures 4B**, **5**). Nevertheless, these faults present the characteristics of dextral strike-slip faults on the coherence slices of surface T_7^4, accompanied by alternating transtensional and compression zones.

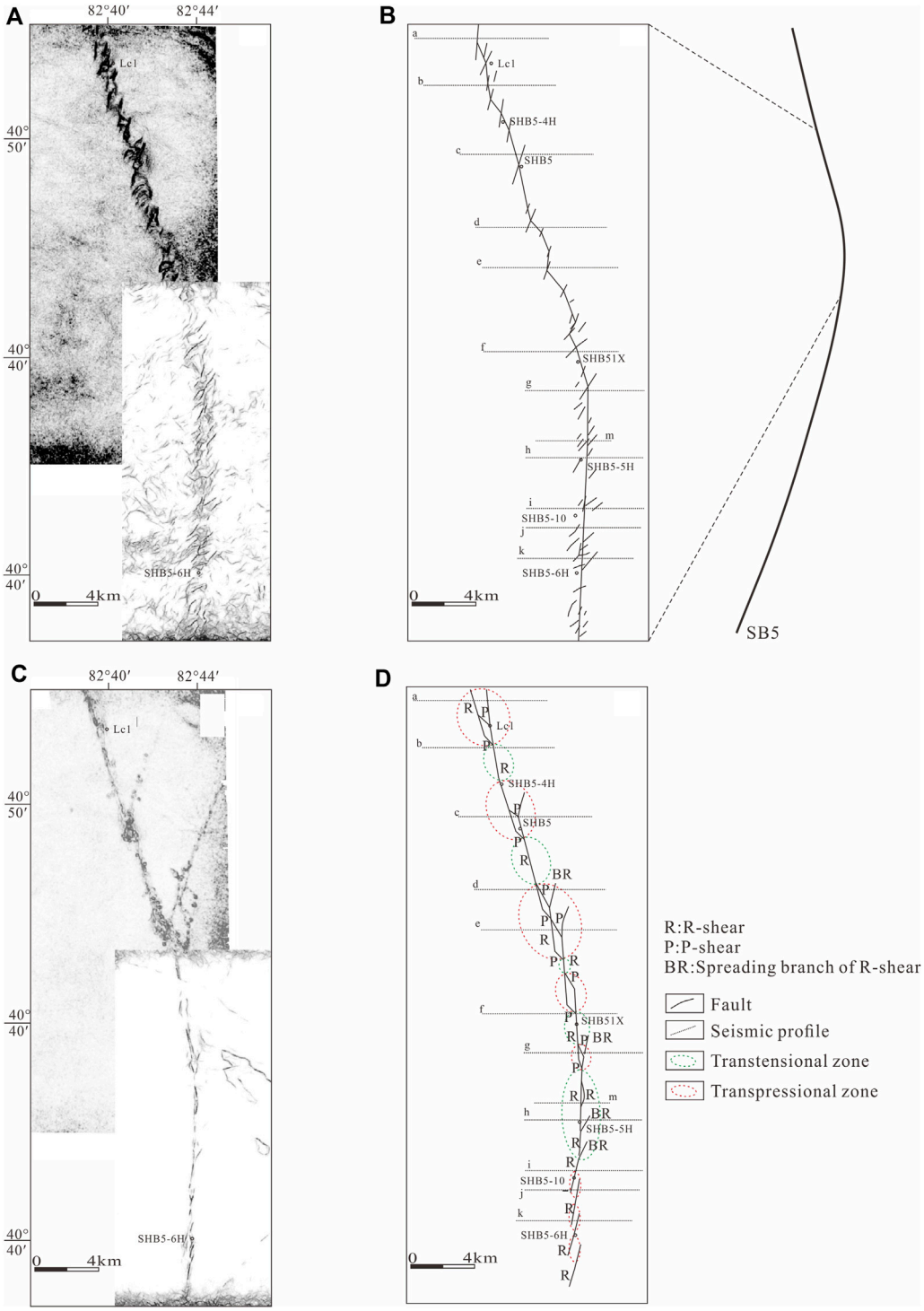

FIGURE 5 | 3D coherence slice of the Shunbei 5 strike-slip deformation belt (SB5). **(A)** T_7^0 reflector indicating the bottom of the Silurian, **(B)** Fault interpretation of a, **(C)** T_7^4 reflector indicating the bottom of the Upper Ordovician, **(D)** Fault interpretation of c.

Although strike-slip deformation belts are complex, those with a small slip distance would have a simple structure. In general, the fault mechanics of strike-slip deformation belts are determined by the mechanical properties of the rocks (Chen, 2020b). These faults can form various structural assemblages along the horizontal plane. **Figure 9** shows a dextral simple shear with a small slip distance as an example. Both physical modeling and numerical simulations such as PFC calculation indicate that

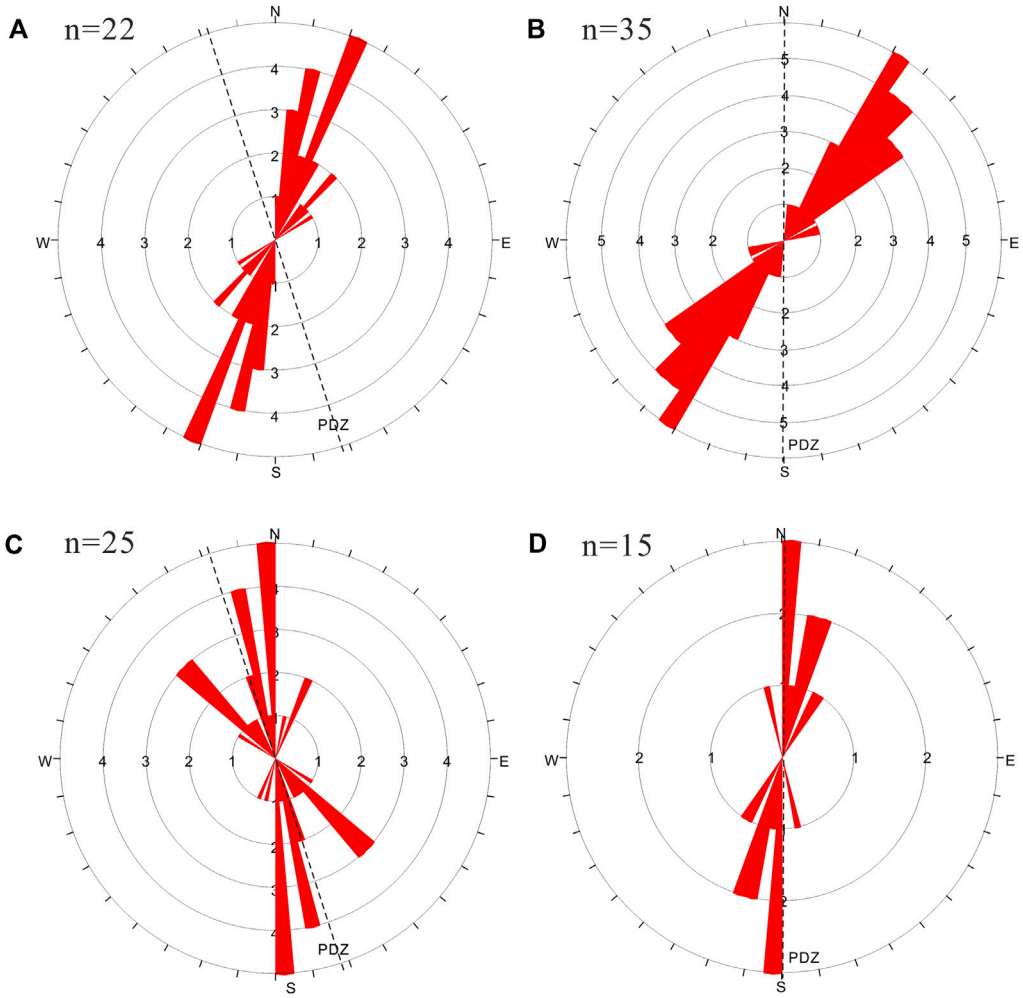

FIGURE 6 | Strike-weighted rose diagrams for each fault set in the bottom of the Silurian (T_7^0) and the bottom of the Upper Ordovician (T_7^4). **(A)** The north segment of SB5 in T_7^0; **(B)** The south segment of SB5 in T_7^0; **(C)** The north segment of SB5 in T_7^4; **(D)** The south segment of SB5 in T_7^4. PDZ = principal displacement zone. The boundary between the northern and southern segments of SB5 is the turning pint of SB5 in **Figure 5B**.

R-shears commonly occur earlier, followed by P-shears and Y-shears (Cho et al., 2008). Y-shears occur parallel to the main displacement zone, such as P1 and P11 in **Figure 9**. P-shears occur in the oversteps of R-shears, being the boundaries of convergent bends such as P3. Central parts of R-shears appear to be transtensional, such as P2. Direct slip will occur at the transitional zone between R-shears and P-shears, such as P7. In SB5, transpressional structures formed at the oversteps (**Figure 5D**). Transpressional structures are characterized by reverse faults or folds in seismic profiles, as shown in **Figures 7A,C,E,G,I–K**. Transtensional structures formed in the central part of the R-shears (**Figure 6**). Transtensional structures are characterized by normal faults or grabens in seismic profiles, as shown in **Figures 7B,F,H**. Parallel normal faults were observed in the T74 reflector along an R-shear (**Figures 6D**, **9**). The fault arraying patterns were identical to those shown in **Figure 4**. A total of eight transpressional zones and five transtensional zones were identified in SB5, alternating with each other.

TIME AND MECHANISM OF THE SHUNBEI 5 STRIKE-SLIP DEFORMATION BELT

Due to the differences in the thicknesses and mechanical properties of rocks, various structural assemblages may superpose on vertical sections to form composite superposition relationships. Consequently, the formation time of wrench formation becomes difficult to determine. Although structural assemblages on vertical sections are very complex, the wrench time can be determined from the strata cut by the strike-slip faults. As strata mechanics and rock thicknesses vary, the same tectonic movement may lead to different structural styles in various strata. In other words, various strata may exhibit different structures along the vertical profile. As shown in **Figure 10A**, these structures have clear boundaries between them, but these were correspond to the same formation time. A1 is a superposition of a compressive structure (e.g., a fold) overlain by extensive structures (e.g., normal faults), A2 a

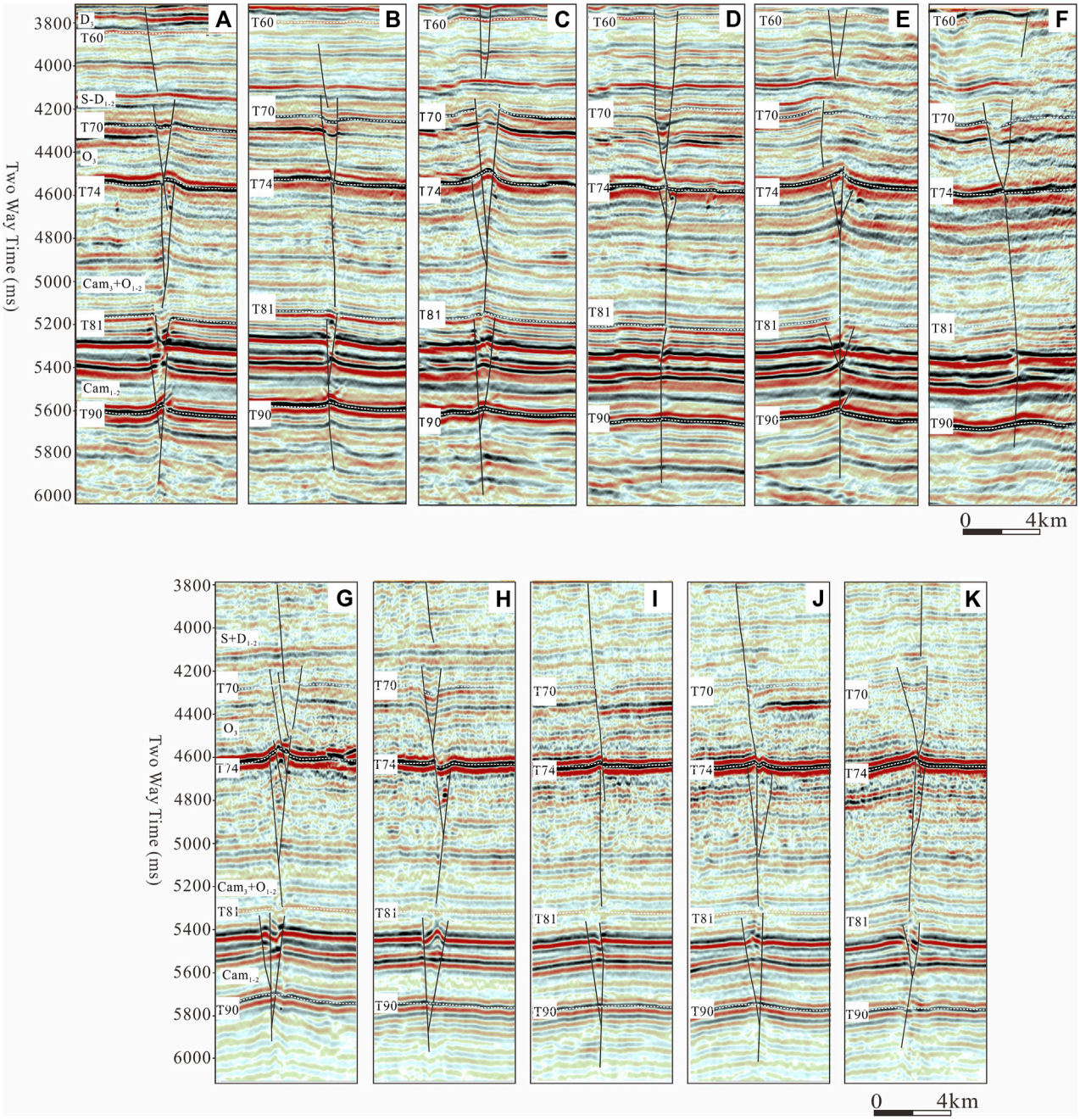

FIGURE 7 | 3D seismic profiles of the Shunbei 5 strike-slip deformation belt (SB5) (see **Figure 6** for locations).

superposition of normal faults overlain by a compressive fold, A3 a superposition of normal faults overlain by other normal faults, and A4 a superposition of a compressive fold overlain by other compressive fold and reverse faults. If various structures with different mechanical properties occur in a layer boundary, they correspond to two tectonic movements (**Figure 10B**). B1 is a superposition of first reverse faults interspersed by secondary normal faults, B2 a superposition of first normal faults interspersed by secondary reverse faults, B3 a superposition of first normal faults interspersed by other secondary normal faults, and B4 a superposition of first reverse faults interspersed by other secondary reverse faults.

The formation time should be determined based on the strata cut by wrench related faults, unconformities, and arraying patterns of the wrench related structures. In **Figures 7**, **8**, each profile exhibits different structural styles from deep to shallow areas. Through the superposition of structures from the T_9^0 and T_7^4 reflectors, the following patterns could be identified: transpressional–transtensional–transpressional

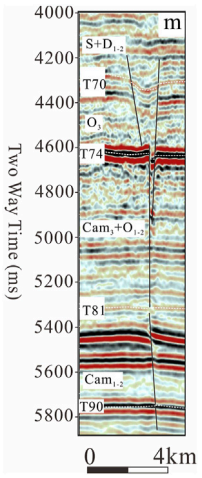

FIGURE 8 | 3D seismic profile of a transtensional part of an R-shear (see **Figure 6** for location).

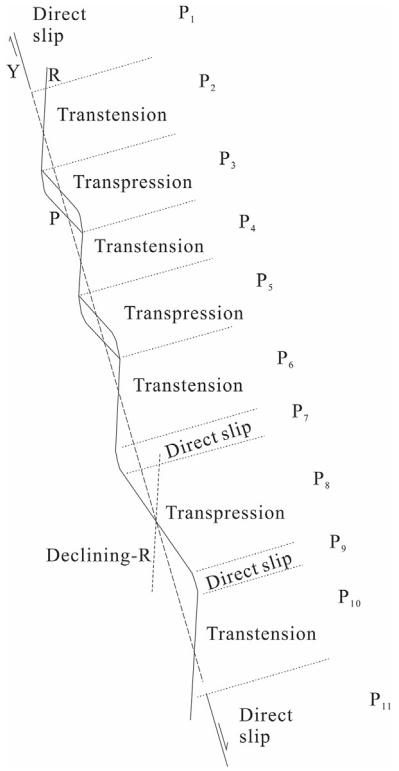

FIGURE 9 | Structures in a dextral strike-slip fault deformation belt with one-time activity and a small strike-slip distance.

(**Figure 7A**), transpressional–transtensional (**Figure 7B**), transpressional–transpressional (**Figure 7C**), transtensional–transtensional (**Figure 7D**), transpressional–transtensional–transpressional (**Figure 7E**), transtensional (Figure 7F), transtensional–transpressional (**Figure 7G**), transpressional–transtensional (**Figure 7H**), transtensional–transpressional (Figure 7I), transpressional–transpressional (**Figure 7J**), and transtensional–transpressional (**Figure 7K**). Regarding **Figure 8**, the superposition reveals a transtensional shear. These structures were delimited by layer beddings, and referring to **Figure 10A**, they were deduced to be formed at the end of the Middle Ordovician. This time is identical to the age of the first periodic calcite vein in fractures (Wu et al., 2020; Wang et al., 2021). Except for the transpressional structures in **Figures 7C,E**, the structures in the T_7^0 reflector were mostly transtensional zones, appearing as en echelon patterns on the plan view (**Figure 5B**) and normal faults in vertical profiles (**Figures 7**, **8**). The normal faults cut into the T_7^4 reflector, and referring to **Figure 10B**, their formation time was found to be different, which is the end of the Ordovician. This time is identical with the age of another penetrative calcite vein in fractures (Yang et al., 2020). As mentioned above, SB5 underwent several times of activities after the two times of activities (**Figures 2**, **7**, **8**).

The formation of the SB5 strike-slip fault is related to plate tectonics around the Tarim Plate (basin). The activity at the end of the Middle Ordovician was caused by the near N-S compression, which is related to the closing of the Proto-Tethys Ocean (Wu et al., 2020), during which the SB5 strike-slip fault was a simple shear belt. The activity at the end of the late Ordovician is related to the southward subduction of the Northern Kunlun Ocean, the northwestward subduction of the Altyn Ocean and the southward subduction of the Northeast Tianshan-Junggar Ocean (Wu G. H. et al., 2016; Wu et al., 2020), during which the SB5 strike-slip fault was a transtensional zone. From the Silurian to Middle Devonian, the east Kunlun-Qaidam Plate and middle Kunlun terrain attached to the Tarim Plate, causing the closing of the Altyn Ocean and the Northern Kunlun Ocean, respectively. At the end of the Permian, the north Tianshan-Junggar Ocean and the south Tianshan Ocean closed, making the Tarim Plate become a part of the Eurasian Plate. At the same time, the southern part of the Tarim Plate changed from a passive margin into an active margin with volcanic arcs. Collisions occurred between the Tianshuihai terrain and the Tarim Plate, and between the Qiangtang terrain and the Eurasian Plate in the early Triassic and at the end of the Triassic, respectively (Hendrix et al., 1992; Graham et al., 1993; Pan et al., 1997). In the Jurassic, the Tethys Ocean Plate was subducted beneath the Qiangtang Plate. With the Lasa collision (140–125 Ma), the Lasa Plate attached to the Qiangtang Plate. In the late Cretaceous, the Kexisitan Plate collided the Lasa Plate at the southwest part (Hendrix et al., 1992; Graham et al., 1993), causing local erosion. The Himalayan collision occurred in the middle-late Cenozoic (45 Ma), attaching the Indian Plate to the Eurasian plate and closing the Tethys Ocean. This collision caused an extensive N-S compression.

CONTROL OF THE SHUNBEI 5 STRIKE-SLIP DEFORMATION BELT ON THE FORMATION OF THE OIL RESERVOIR

The SB5 reservoir is a typical reservoir with a total oil production of 2.86×10^4 t (**Figure 11**).

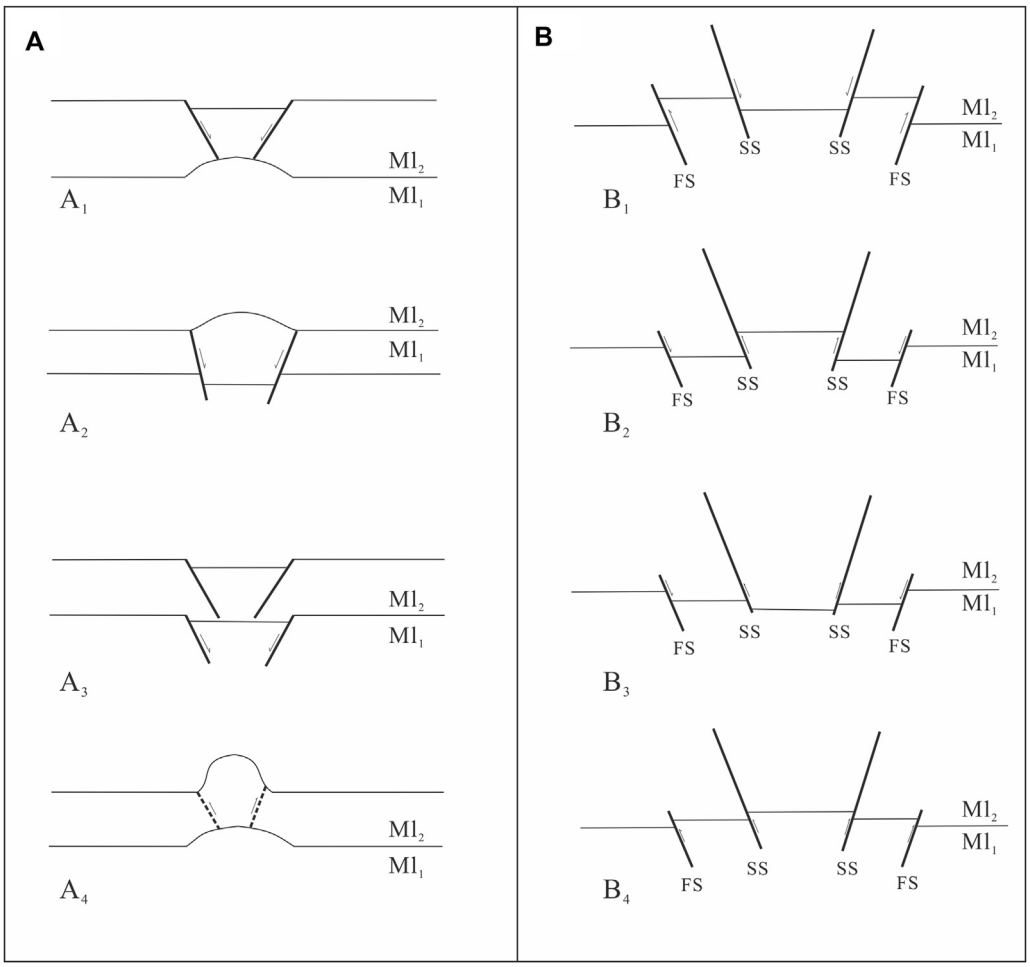

FIGURE 10 | Possible vertical superposition of wrench related structures in various strata. **(A)** Structures formed in one movement, **(B)** Structures formed in two movements; Ml_1-Mechanical layer 1, Ml_2-Mechanical layer 2, FS-First time structure, SS-Second time structure

Although there are four sets of source rocks in the Tarim basin, source analysis proved that the oil and gas in the Shunbei oilfield are contained in the source rock at the bottom of the Cambrian strata (Song et al., 2016; Gao et al., 2018; Ma et al., 2018; Gu et al., 2020; Chen et al., 2021). Analyses of the physical and geochemical properties and fluid inclusions in rocks indicate that the time of the first hydrocarbon charging in the Shunbei oilfield was in the late Silurian, following which several charging events might have occurred (Wang et al., 2019; Cao et al., 2020; Wang et al., 2020). The time of the first hydrocarbon charging agrees with the hydrocarbon expulsion peak in the Tarim Basin (Wang et al., 2020).

The reservoir lies in the Middle Ordovician stratum overlain by Upper Ordovician marl and mudstone, which serve as the cap rocks (**Figure 11**). The source rock is the base of the Lower Cambrian. The Middle Cambrian includes gypsum and salt rock formations, which are suitable cap rocks (Chen et al., 2021). SB5 played an important role both in the hydrocarbon migration from the Cambrian source rock to the reservoir and in the formation of the Ordovician reservoirs. Firstly, a strike-slip fault can cut deep to connect deep source rocks with shallow reservoirs. Normal faults and thrust faults may cut along a detachment, similar to salt layers, but they cannot penetrate deep source rocks. A typical strike-slip fault alternates between transtensional and transpressional areas; the former provide suitable migration paths and the latter form suitable traps. Transtensional areas have been found to offer higher oil output per unit pressure drop than transpressional areas (Liu, 2020). Secondly, wrenching improves the porosity and permeability of rocks. In the Shunbei oilfield, the accumulation spaces are fractures and caves; the former is related to the wrenching and the latter is related to carbonate rock corrosion along the strike-slip faults (Jiao, 2018; Qi, 2019; Lv et al., 2021).

CONCLUSION

The Shunbei 5 strike-slip deformation belt (SB5) of the Shunbei area of the central Tarim Basin is an important intracratonic strike-slip fault system with high potential for

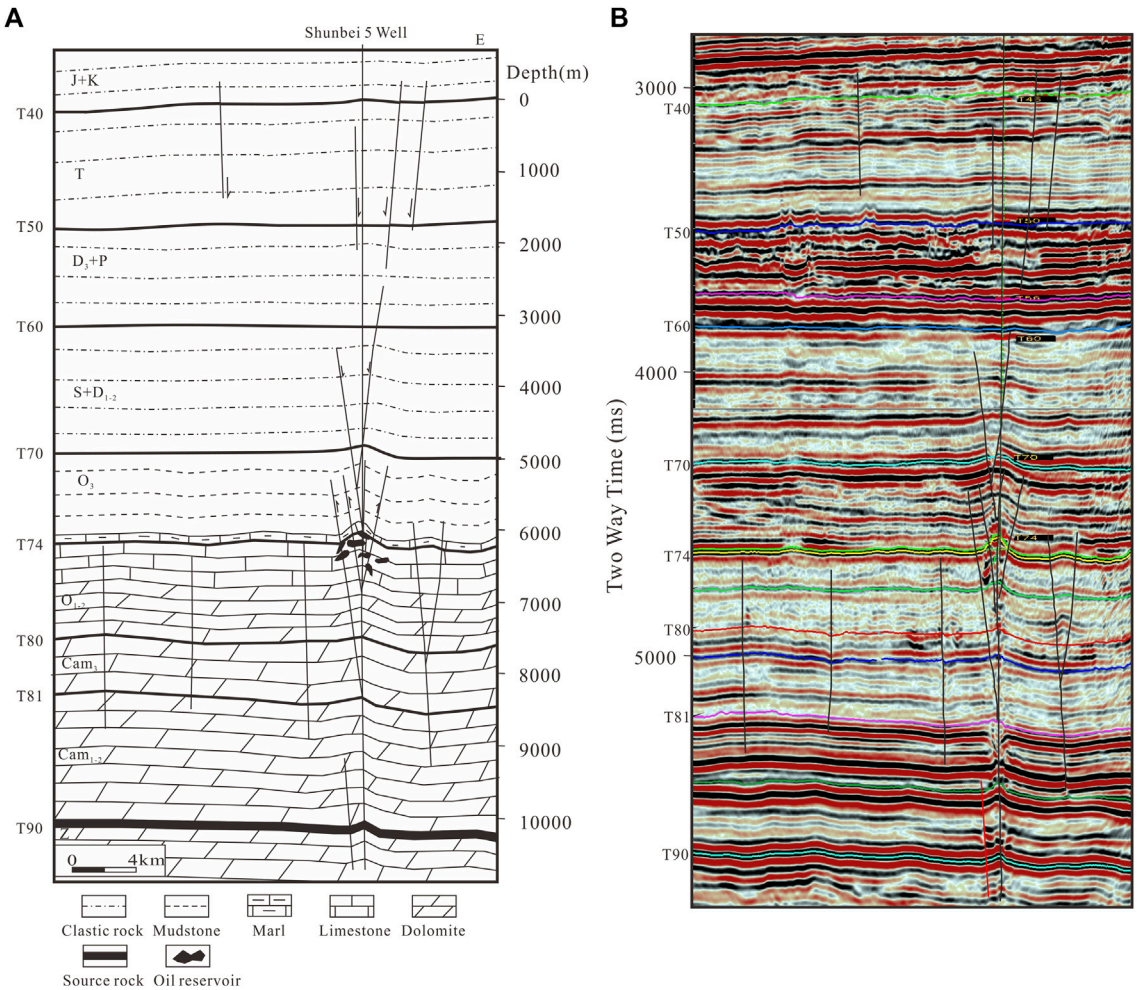

FIGURE 11 | Reservoir modeling **(A)** and vertical profile **(B)** of the Shunbei 5 reservoir.

oil and gas exploration. Based on detailed structure characterization and geometric analysis, the tectonic architecture and structural evolution of SB5 were determined and proposed, respectively. Moreover, the control of the strike-slip deformation belt on the formation of oil and gas reservoirs is discussed. The main findings can be summarized as follows:

1) The Shunbei 5 strike-slip deformation belt (SB5) was formed at the end of the Middle Ordovician with the closing of the proto-Tethys Ocean, during which it was a dextral parallel strike-slip fault belt comprising R-shears and P-shears. In the plan view, transpressional and transtensional structures are alternately arranged. Along the vertical profile, the lithological strata exhibit different structural styles, attributable to the varying mechanisms.

   At the end of the late Ordovician, SB5 was affected by the southward subduction of the Northern Kunlun Ocean, the northwestward subduction of the Altyn Ocean, and the southward subduction of the Northeast Tianshan-Junggar Ocean, during which it was a transtensional dextral strike-slip fault belt. The structures were left-stepping R-shears with transextension in the progressive deformation.

2) SB5 cut through the Middle Cambrian gypsum salt layer to connect the Lower Cambrian source rock with the Ordovician reservoirs, leading to the formation of the oil and gas reservoirs of the Shunbei oilfield.
3) A simple shear strike-slip deformation belt with a small displacement may consist mainly of R-shears. The oversteps may include transpressional structures with P-shears. Outside the oversteps, the main structures may be transtensional. Moreover, the transition of the R-shears and P-shears may exhibit a parallel pattern. Even with one tectonic movement, various rocks may exhibit various structures with different mechanical properties according to differences in their mechanical properties. This finding may facilitate a deeper

understanding of other strike-slip deformation belts around the world.

DATA AVAILABILITY STATEMENT

The original contributions presented in the study are included in the article/Supplementary Material, further inquiries can be directed to the corresponding authors.

AUTHOR CONTRIBUTIONS

HY and SC presented the idea and design of the research. HY and SC wrote the article and led the data analysis and interpreted the results with YN, HZ, SX, XW and GF. All authors contributed to the original article revision and approved it for publication.

FUNDING

This study was jointly funded by the "National Key Research and Development Plan-ultra-deep Layer, Mesoproterozoic and Neoproterozoic Cap Sealing Property and Oil-gas Preservation Mechanism" (no.2017YFC0603105), the "Mechanism of Deep Hydrocarbon Migration and Enrichment in Key Areas of Sichuan Basin" (no.XDA14010306), and the "Development in Large-scale Oil-gas Field and Coalbed Methane Project"-"Reservoir Formation Conditions and Controlling Factors in Deep-ultra-deep Cambrian in Tarim Basin" (no. 2017ZX05005-002-005).

REFERENCES

Allen, P. A., and Allen, J. R. (2013). *Basin Analysis: Principles and Application to Petroleum Play Assessment*. New Jersey: John Wiley & Sons.

Bahorich, M., and Farmer, S. (1995). 3-D Seismic Discontinuity for Faults and Stratigraphic Features: The Coherence Cube. *Leading edge* 14 (10), 1053–1058. doi:10.1190/1.1437077

Cao, Z., Lu, Q., Gu, Y., Wu, X., You, D., and Zhu, X. (2020). Characteristics of Ordovician Reservoirs in Shunbei 1 and 5 Fault Zones, Tarim Basin. *Oil Gas Geol.* 41 (5), 975–984. doi:10.11743/ogg20200508

Chen, S., Xu, S., Cai, Y., and Ma, X. (2018). Wrench Related Faults and Their Control on the Tectonics and Eocene Sedimentation in the L13-L15 Sub-sag Area, Pearl River Mouth basin, China. *Mar. Geophys. Res.* 39 (3), 363–381. doi:10.1007/s11001-017-9328-1

Chen, S., Wang, Z., Yang, W., Wang, Y., and Yuan, H. (2021). Geological Background of Early Cambrian in Tarim Basin and its Control on the Development of Source Rocks. *Sci. Technol. Eng.* 21 (1), 124–129.

Chen, S. (2020a). On the Occurrences of Fractures in Wrench Zones. *Wjm* 10 (03), 27–38. doi:10.4236/wjm.2020.103003

Chen, S. (2020b). On the Orientation of Fractures with Transpressional and Transtensional Wrenches in Pre-existing Faults. *Wjm* 10 (11), 199–209. doi:10.4236/wjm.2020.1011014

Chinnery, M. A. (1963). The Stress Changes that Accompany Strike-Slip Faulting. *Bull. Seismol. Soc. Am.* 53 (5), 921–932. doi:10.1785/bssa0530050921

Cho, N., Martin, C. D., and Sego, D. C. (2008). Development of a Shear Zone in Brittle Rock Subjected to Direct Shear. *Int. J. Rock Mech. Min. Sci.* 45 (8), 1335–1346. doi:10.1016/j.ijrmms.2008.01.019

Deng, S., Li, H., Zhang, Z., Wu, X., and Zhang, J. (2018). Characteristics of Differential Activities in Major Strike-Slip Fault Zones and Their Control on Hydrocarbon Enrichment in Shunbei Area and its Surroundings, Tarim Basin. *Oil Gas Geol.* 39 (5), 878–888. doi:10.11743/ogg20180503

Deng, S., Li, H., Zhang, Z., Zhang, J., and Yang, X. (2019). Structural Characterization of Intracratonic Strike-Slip Faults in the central Tarim Basin. *Bulletin* 103 (1), 109–137. doi:10.1306/06071817354

Du, J., Tian, J., Guoxin, L., Haijun, Y., Yijie, Z., Yong, L., et al. (2019). Strategic Breakthrough and prospect of Qiulitag Structural belt in Kuqa Depression. *China Pet. Explor.* 24 (1), 16. doi:10.3969/j.issn.1672-7703.2019.01.003

El Ghamry, M. N., El Amawy, M., and Hagag, W. (2020). The Role of Late Cretaceous Wrench Tectonics in Hydrocarbon Endowment in El-Gindi Basin, Northern Western Desert, Egypt. *Mar. Pet. Geol.* 112, 104093. doi:10.1016/j.marpetgeo.2019.104093

Gao, X., Wu, X., Hong, C., and Wen, S. (2018). Geochemical Characteristics of Ordovician Crude Oil in the No. 1 Fault Zone of Shunbei Oilfield. *Pet. Geol. Eng.* 36, 37–40.

Ghosh, N., and Chattopadhyay, A. (2008). The Initiation and Linkage of Surface Fractures above a Buried Strike-Slip Fault: An Experimental Approach. *J. Earth Syst. Sci.* 117 (1), 23–32. doi:10.1007/s12040-008-0009-y

Graham, S. A., Hendrix, M. S., Wang, L. B., and Carroll, A. R. (1993). Collisional Successor Basins of Western China: Impact of Tectonic Inheritance on Sand Composition. *Geol. Soc. Am. Bull.* 105 (3), 323–344. doi:10.1130/0016-7606(1993)105<0323:csbowc>2.3.co;2

Gu, R., Yun, L., Zhu, X., and Zhu, M. (2020). Oil and Gas Sources in Shunbei Oilfield, Tarim Basin. *Pet. Geol. Exp.* 42 (2), 248–262. doi:10.11781/ssydz202002248

Han, X., Deng, S., Tang, L., and Cao, Z. (2017). Geometry, Kinematics and Displacement Characteristics of Strike-Slip Faults in the Northern Slope of Tazhong Uplift in Tarim Basin: A Study Based on 3D Seismic Data. *Mar. Pet. Geol.* 88, 410–427. doi:10.1016/j.marpetgeo.2017.08.033

Han, J., Kang, A., Neng, Y., Huang, C., Li, Q., Chen, P., et al. (2021). Vertical Layered Structure of Shunbei No. 5 Strike-Slip Fault Zone and its Significance on Hydrocarbon Accumulation. *Xinjiang Pet. Geol.* 42 (2), 152. doi:10.7657/XJPG20210204

Harding, T. (1974). Petroleum Traps Associated with Wrench Faults. *AAPG Bull.* 58 (7), 1290–1304. doi:10.1306/83d91669-16c7-11d7-8645000102c1865d

Hendrix, M. S., Graham, S. A., Carroll, A. R., Sobel, E. R., McKNIGHT, C. L., Schulein, B. J., et al. (1992). Sedimentary Record and Climatic Implications of Recurrent Deformation in the Tian Shan: Evidence from Mesozoic Strata of the north Tarim, South Junggar, and Turpan Basins, Northwest China. *Geol. Soc. Am. Bull.* 104 (1), 53–79. doi:10.1130/0016-7606(1992)104<0053:sracio>2.3.co;2

Hills, E. S. (2012). *Elements of Structural Geology*. Wilmersdorf: Springer Science & Business Media.

Huang, C. (2019). Multi-stage Activity Characteristics of Small-Scale Strike-Slip Faults in Superimposed basin and its Identification Method: a Case Study of Shunbei Area. *Pet. Geol. Exp.* 41 (3), 379–389. doi:10.11781/sysydz201903379

Jiao, F. (2018). Significance and prospect of Ultra-deep Carbonate Fault-Karst Reservoirs in Shunbei Area, Tarim Basin. *Oil Gas Geol.* 39 (2), 207–216. doi:10.11743/ogg20180201

Li, Y., Qi, L., Zhang, S., Yun, L., Cao, Z., Han, J., et al. (2019). Characteristics and Development Mode of the Middle and Lower Ordovician Fault-Karst Reservoir in Shunbei Area, Tarim basin. *Acta Petrolei Sin.* 40, 1470–1484. doi:10.7623/syxb201912006

Liu, B. (2020). Analysis of the Main Controlling Factors of Oil and Gas Differential Accumulation in the Shunbei Area, Tarim Basin-taking Shunbei No. 1 and No. 5 Strike-Slip Fault Zones as Examples. *China Pet. Explor.* 25 (3), 83. doi:10.3969/j.issn.1672-7703.2020.03.008

Lowell, J. (1985). *Structural Styles in Petroleum Geology*, United States: OGC publications.

Lu, X., Hu, W., Wang, Y., Li, X., Li, T., Lyu, Y., et al. (2015). Characteristics and Development Practice of Fault-Karst Carbonate Reservoirs in Tahe Area, Tarim Basin. *Oil Gas Geology.* 36 (3), 347–355. doi:10.11743/ogg20150301

Lv, H., Han, J., Zhang, J., Liu, Y., and Li, Y. (2021). Development Characteristics and Formation Mechanism of Ultra-deep Carbonate Fault-Dissolution Body in Shunbei Area, Tarim Basin. *Pet. Geol. Exp.* 43 (1), 14–22. doi:10.l781/sysydz202101014

Ma, A., Zhu, C., Gu, Y., and Li, H. (2018). Concentrations Analysis of Lower Thiadiamondoids of Cambrian Oil from Well Zhongshen 1C of Tazhong Uplift, Tarim Basin, NW China. *Nat. Gas Geosci.* 29 (7), 1009–1019. doi:10.11764/j.issn.1672-1926.2018.06.007

Pan, G., Zl, C., and Xz, L. (1997). *Geological–Tectonic Evolution in the Eastern Tethys*. Beijing: Geological Publishing House, 218. (in Chinese with English abstract).

Qi, L. (2019). Characteristics and Inspiration of Ultra-deep Fault-Karst Reservoir in the Shunbei Area of the Tarim Basin. *China Pet. Exploration* 25 (1), 102–111.

Ren, R., Guan, S., Wu, L., and Zhu, G. (2018). Evolution of the Neoproterozoic Rift Basins and its Implication for Oil and Gas Exploration in the Tarim Basin. *Pet. Res.* 3 (1), 66–76. doi:10.1016/j.ptlrs.2018.03.003

Riedel, W. (1929). Zur Mechanik geologischer Brucherscheinungen ein Beitrag zum Problem der Fiederspatten. *Zentbl. Miner. Geol. Palaont. Abt.*, 354–368.

Schreurs, G. (1994). Experiments on Strike-Slip Faulting and Block Rotation. *Geol* 22 (6), 567–570. doi:10.1130/0091-7613(1994)022<0567:eossfa>2.3.co;2

Shi, K. B., Liu, B., Tian, J. C., and Pan, W. Q. (2016). Sedimentarycharac teristicsandlithofaciespaleogeographyofSinianinTarimBasin. *Acta Petrolei Sin.* 37 (11), 1343–1360. doi:10.7623/syxb201611003

Shi, K., Liu, B., Jiang, W., Luo, Q., and Gao, X. (2018). Nanhua-Sinian Tectono-Sedimentary Framework of Tarim Basin, NW China. *Oil Gas Geology.* 39 (5), 862–877. doi:10.11743/ogg20180502

Skempton, A. (1966). ""Some Observations on Tectonic Shear Zones," in *1st ISRM Congress: International Society for Rock Mechanics and Rock Engineering*. New Jersey: Springer International Publishing.

Song, D., Wang, T., and Li, M. (2016). Geochemistry and Possible Origin of the Hydrocarbons from Wells Zhongshen1 and Zhongshen1C, Tazhong Uplift. *Sci. China Earth Sci.* 59 (4), 840–850. doi:10.1007/s11430-015-5226-z

Sylvester, A. G. (1988). Strike-slip Faults. *Geol. Soc. Am. Bull.* 100 (11), 1666–1703. doi:10.1130/0016-7606(1988)100<1666:ssf>2.3.co;2

Wang, Y., Chen, H., Guo, H., Zhu, Z., Wang, Q., Yu, P., et al. (2019). Hydrocarbon Charging History of the Ultra-deep Reservoir in Shun 1 Strike-Slip Fault Zone, Tarim Basin. *Oil Gas Geol.* 40 (5), 972–989.

Wang, B., Zhao, Y., He, S., Guo, X., Cao, Z., Deng, S., et al. (2020). Hydrocarbon Accumulation Stages and Their Controlling Factors in the Northern Ordovician Shunbei 5 Fault Zone, Tarim Basin. *Oil Gas Geol.* 41 (5), 965–974. doi:10.11743/ogg20200507

Wang, B., Yang, Y., Cao, Z., He, S., Zhao, Y., Guo, X., et al. (2021). U-pb Dating of Calcite Veins Developed in the Middle-Lower Ordovician Reservoirs in Tahe Oilfield and its Petroleum Geologic Significance in Tahe Oilfield. *Earth Sci.* doi:10.3799/dakx.2020.352

Wilcox, R. E., Harding, T. T., and Seely, D. R. (1973). Basic Wrench Tectonics. *AAPG Bull.* 57 (1), 74–96. doi:10.1306/819a424a-16c5-11d7-8645000102c1865d

Wu, G., Yang, H., Qu, T., Li, H., Luo, C., and Li, B. (2012). The Fault System Characteristics and its Controlling Roles on marine Carbonate Hydrocarbon in the Central Uplift, Tarim basin. *acta Petrol. Sin.* 28 (3), 793–805.

Wu, G. H., Pang, X. Q., and Li, Q. M. (2016a). *The Structural Characteristics of Carbonate Recks and Their Effects on Hydrocarbon Exploration in Craton Basin: A Case Study of the Tarim Basin*. Beijing: Science Press.

Wu, L., Guan, S., Ren, R., Wang, X., Yang, H., Jin, J., et al. (2016b). The Characteristics of Precambrian Sedimentary basin and the Distribution of Deep Source Rock: A Case Study of Tarim Basin in Neoproterozoic and Source Rocks in Early Cambrian, Western China. *Pet. Exploration Dev.* 43 (6), 988–999. doi:10.1016/s1876-3804(16)30116-1

Wu, G., Yuan, Y., Huang, S., Vandyk, T. M., Xiao, Y., Cai, Q., et al. (2018). The Dihedral Angle and Intersection Processes of a Conjugate Strike-Slip Fault System in the Tarim Basin, NW China. *Acta Geol. Sin. - English Ed.* 92 (1), 74–88. doi:10.1111/1755-6724.13495

Wu, G., Ma, B., Han, J., Guan, B., Chen, X., Yang, P., et al. (2020). *Origin and Growth Mechanisms of Strike-Slip Faults in the central Tarim Cratonic basin, NW China*. Petroleum Exploration & Development 48 (3), 595–607. doi:10.1016/S1876-3804(21)60048-4

Xu, S., Peng, H., Angel, F., Nieto-Samaniego, C., SPand Wu, X. (2017). The Similarity between Riedel Shear Patterns and Strike-Slip Basin Patterns. *Geol. Rev.* 63, 287–300.

Yang, Y., Wang, B., Cao, Z., Huang, C., Zhao, Y., Guo, X., et al. (2020). Genesis and Formation Time of Calcite Veins of the Middle-Lower Ordovician Reservoirs in the Northern Shuntuoguole Low-Uplift, Tarim Basin. *Earth Sci.* 46 (6), 2246–2257. doi:10.3799/dqkx.2020.200

Zhen, S., Tang, L., Li, Z., Li, M., Cao, Z., and Yang, S. (2015). The Characteristics, Formation and Petroleum Geology Significance of the Strike-Slip Fault System in Shunnan Area, Northern Slope of Tazhong Uplift. *Nat. Gas Geosci.* 26 (12), 2315–2324. doi:10.11764/j.issn.1672-1926.2015.12.2315

Zhou, X., Wang, Q., Yang, W., and Xiao, Z. (2005). The Resource and Exploration of Natural Gas in Tarim Basin. *Nat. Gas Geosci.* 16 (1), 7–11.

Conflict of Interest: The authors declare that the research was conducted in the absence of any commercial or financial relationships that could be construed as a potential conflict of interest.

frontiers in Earth Science

BRIEF RESEARCH REPORT
published: 07 October 2021
doi: 10.3389/feart.2021.749181

Description of Fracture Network of Hydraulic Fracturing Vertical Wells in Unconventional Reservoirs

Jinghua Liu[1], *Mingjing Lu*[2,3] *and Guanglong Sheng*[1]*

[1]School of Petroleum Engineering, Yangtze University, Wuhan, China, [2]Petroleum Engineering Technology Research Institute of Shengli Oilfield, Dongying, China, [3]Postdoctoral Scientific Research Working Station of Shengli Oilfield, Dongying, China

Based on the distribution of complex fractures after volume fracturing in unconventional reservoirs, the fractal theory is used to describe the distribution of volume fracture network in unconventional reservoirs. The method for calculating the fractal parameters of the fracture network is given. The box dimension method is used to analyze a fracturing core, and the fractal dimension is calculated. The fractal index of fracture network in fracturing vertical wells are also firstly calculated by introducing an analysis method. On this basis, the conventional dual-media model and the fractal dual-media model are compared, and the distribution of reservoir permeability and porosity are analyzed. The results show that the fractal porosity/permeability can be used to describe the reservoir physical properties more accurately. At the same time, the flow rate calculating by conventional dual-media model and the fractal dual-media model were calculated and compared. The comparative analysis found that the flow rate calculated by the conventional dual-media model was relatively high in the early stage, but the flow rate was not much different in the later stage. The research results provide certain guiding significance for the description of fracture network of volume fracturing vertical well in unconventional reservoirs.

Keywords: unconventional reservoirs, hydraulic fracturing, fracture network, fractal dimension, fractal index

OPEN ACCESS

Edited by:
Wenhui Song,
China University of Petroleum (Huadong), China

Reviewed by:
Meng Li,
China University of Petroleum (Huadong), China
Tao Zhang,
Southwest Petroleum University, China

***Correspondence:**
Guanglong Sheng
shenggl2019@yangtzeu.edu.cn

Specialty section:
This article was submitted to Economic Geology, a section of the journal Frontiers in Earth Science

Received: *29 July 2021*
Accepted: *13 August 2021*
Published: *07 October 2021*

Citation:
Liu J, Lu M and Sheng G (2021) Description of Fracture Network of Hydraulic Fracturing Vertical Wells in Unconventional Reservoirs. Front. Earth Sci. 9:749181. doi: 10.3389/feart.2021.749181

INTRODUCTION

Unconventional reservoirs in the world are rich in resources, and have poorly reservoir porosity/permeability (Song et al., 2018; Wang et al., 2019; Chen et al., 2020). It is necessary to adopt stimulation enhancement measures to improve the physical properties in order to achieve economic development (Li et al., 2015). Considering the distribution of natural fractures in unconventional reservoirs, through technologies such as optimized displacement and low liquid viscosity, the net pressure in the fracture during volume fracturing is achieved, and the fracture opening conditions are achieved (Zhang et al., 2021). So as to extend along the wall of the main fracture and communicate with multi-scale secondary fractures, then the complex fracture network is finally formed in the formation (Manchanda et al., 2020; Qi et al., 2020; Sheng et al., 2020).

Scholars have studied the distribution of fracture network of volume fracturing from many aspects. Cheng et al. used the discrete fracture network model and line network model to characterize the complex fracture network of volume fracturing in shale reservoirs, and obtained the fracture network geometry parameter (Cheng et al., 2013). Wang et al. used numerical simulation to study the factors affecting the productivity of volume fracturing vertical wells, and the results showed that the complex fracture network formed after volume fracturing in tight reservoirs can greatly increase the productivity (Wang et al., 2013). Li et al. used dual-media

numerical simulation to simulate the fracture network from volume fracturing and optimize the parameters of fracture network (Li, 2020). They believed that the dual-media simulation method can accurately describe the complex fracture network composed of native natural fractures and artificial hydraulic fractures. The dual-media simulation method can also reflect the flow characteristics within fracture network and matrix after volume fracturing. Based on the characteristics of complex fracture network and flow mechanism of volume fracturing in tight reservoirs, Su et al. proposed a coupled dual-media composite flow model considering the limited stimulated reservoir volume, and optimized the parameters of fracture network (Su et al., 2014).

The previous research fully demonstrated the influence of the fracture network on reservoir flow and made a preliminary description of fracture network (Li, 2020). However, the distribution of fracture network cannot describe by a simple approach, such as analytical equations (Meng et al., 2020). The complex fracture network was formed based on communicating and extending natural fractures (Li et al., 2020), so the fracture network structure is consistent with the distribution of natural fractures in the reservoir. Pfeiferper and Avnir (1983), Katz and Thompson (1985), Krohn (1988) used adsorption method, electron microscope observation and mercury intrusion method to study the microscopic pore and natural fracture structure of unconventional reservoirs. A large number of research results show that the microstructure of unconventional reservoirs has fractal characteristics (Song et al., 2019), which can be studied by fractal theory. Yortsos et al. used the fractal reservoirs for the first time to describe natural fractured reservoirs (Chang and Yortsos, 1990). Aprilian et al. (1993) and Acuna et al. (1995) respectively used fractal reservoir-based well testing analysis methods to explain the well test results of complex reservoirs that were difficult to explain by conventional methods, and obtained results consistent with the actual data. Wang et al. introduced the fractal theory into trilinear flow model, and proposed a mathematical model considering complex fractures and fractal flow for pressure transient analysis of fractured horizontal wells in unconventional reservoirs. In the work, the fractal dimension and fractal index were used directly to describe the fractal fracture network (Wang et al., 2015). To tell the truth, the calculation of fractal dimension and fractal index is more important for fracture network description. The fractal dimension is usually calculated by box counting method, which is based on the specific fracture geometry. Combined with the inversion method of fracture network, the fractal dimension can be easier calculated. However, the fractal index is hardly to obtain. The fractal index is usually obtained by random walker method (O Shaughnessy and Procaccia, 1985), which is not easier in the calculation of fractal index of fracture network. Sheng et al. further gave the calculation method of the heterogeneity fractal index based on the fractal dimension, and obtained the fracture porosity and permeability distribution with the fractal fracture morphology (Sheng et al., 2019). This work presents an effective method to determine the fractal index, and make the fractal theory more reasonable to apply to the description of fracture network. However, there is no work combine the fractal index calculation method with flow simulation.

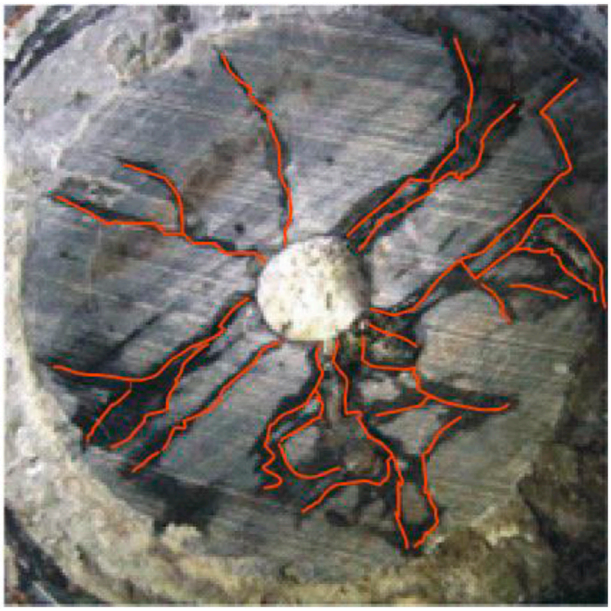

FIGURE 1 | Fracture network morphology in unconventional reservoirs (Guo et al., 2015).

Therefore, considering the fracture network morphology in unconventional reservoirs, this paper uses fractal theory to describe the distribution of induced fracture network in unconventional reservoirs. The calculation method of fractal parameters is given, and the distribution of physical properties and the production rate from conventional dual-media flow model and the fractal dual-media flow model are compared and analyzed.

DESCRIPTION OF FRACTURE NETWORK IN UNCONVENTIONAL RESERVOIRS

Researches show that the microstructure of natural fractures in unconventional reservoirs has fractal characteristics. Based on the characteristics of natural fractures in unconventional reservoirs, Hydraulic fracturing communicate with multiple induced fractures and micro-fractures, and finally generates a complex fracture network in the reservoir. Therefore, the resulting fracture network presents a multi-scale distribution and shows a certain degree of self-similarity in a statistical sense (**Figure 1**). In the conventional model, the fracture density is used to characterize the number of induced fractures, but the fracture density cannot accurately describe the tortuosity and self-similarity of the fracture network. Fractal geometry breaks through the traditional integer dimension thinking and has superiority in describing extremely complex geometric forms. When using fractal theory to characterize the structural characteristics of the fracture network, two parameters, fractal dimension and fractal index, are generally used.

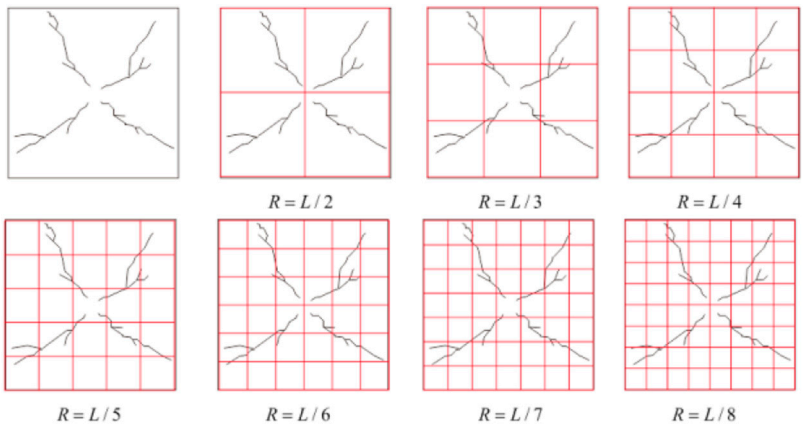

FIGURE 2 | Fracture distribution in different squares.

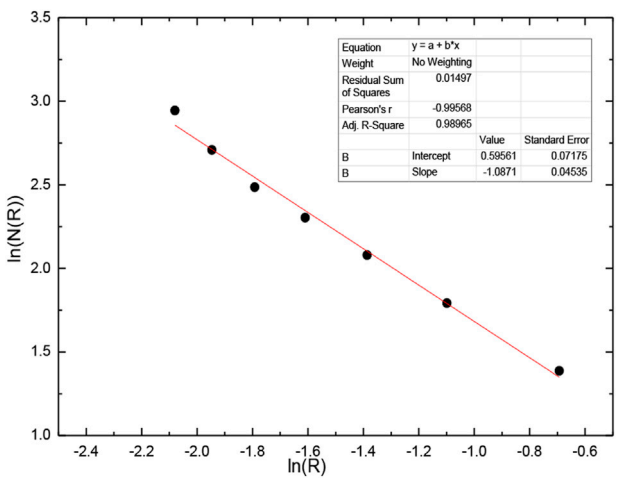

FIGURE 3 | The fractal dimension from box dimension method.

Fractal Dimension

The fractal dimension is often used in fractal geometry to reflect the density and complexity of fracture network. The experimental method to calculate the fractal dimension have the disadvantages of cumbersome operation when determining the fracture network parameters. The box dimension method based on the microseismic data is used to obtain the fractal dimension of the fracture network, which has a good effect. The specific process is: 1) divide the geometry into a grid with a square of length R, 2) count the number of grids with fractures in the grid $N(R)$, 3) repeat the above process continuously by changing the size of R, and 4) the fractal dimension can be obtained by drawing the curve of ln (R) and ln ($N(R)$)

$$d = -\frac{d(\ln(N(R)))}{d(\ln(R))} \tag{1}$$

Where R is the length of the square; $N(R)$ is the number of grids with fractures in the square of length R.

Assuming that the fractures are distributed inside a square with side length L after hydraulic fracturing (the fractal dimension has nothing to do with the value of L, this work assumes $L = 1$), as shown in **Figure 2**, the fracture distribution area is continuously divided.

Calculate the number of grids with fractures at different grid sizes (R), and draw the curve of ln(R) and ln ($N(R)$), as shown in **Figure 3**. It can be seen from the figure that the ln(R) and ln ($N(R)$) have a strong linear relationship, and the fractal dimension of the fracture network shown in **Figure 3** is 1.086.

Fractal Index

Since there are many branch and bifurcations in fractal fractures, the longer the fluid flow in the fractures, the slower the flow rate will be. This characteristic in the fractal fracture network is called fractal anomalous diffusion. The fractal index is used to characterize the fractal anomalous diffusion. The value is usually estimated by random walking method, and its absolute value is between 0 and 1. In reservoir simulation, the abnormal diffusion mainly affects the permeability.

Sheng et al. (2019) obtained the fractal index of fractal network distribution, which can be expressed as

$$\theta = \ln\left(1 + \frac{s_{fw}}{r_w}|2-d|\left(\frac{r}{r_w}\right)^{1-d}\right)\Big/\ln\left(\frac{r}{r_w}\right) \tag{2}$$

Where r_w represents a reference length, cm; r is the length from the reference point, cm; d is the fractal dimension; θ is the fractal index; s_{fw} is the fracture width at the reference point, cm.

Fractal Porosity/Permeability Equation

Based on the fractal dimension and fractal index, the fractal permeability and porosity equation of the reservoir with complex fracture network can be obtained

$$k_f(x) = k_w\left(\frac{r}{r_w}\right)^{-\frac{d(\ln(N(R)))}{d(\ln(R))}-\ln\left(1+\frac{s_{fw}}{r_w}|2-d|\left(\frac{r}{r_w}\right)^{1-d}\right)\Big/\ln\left(\frac{r}{r_w}\right)-2} \tag{3}$$

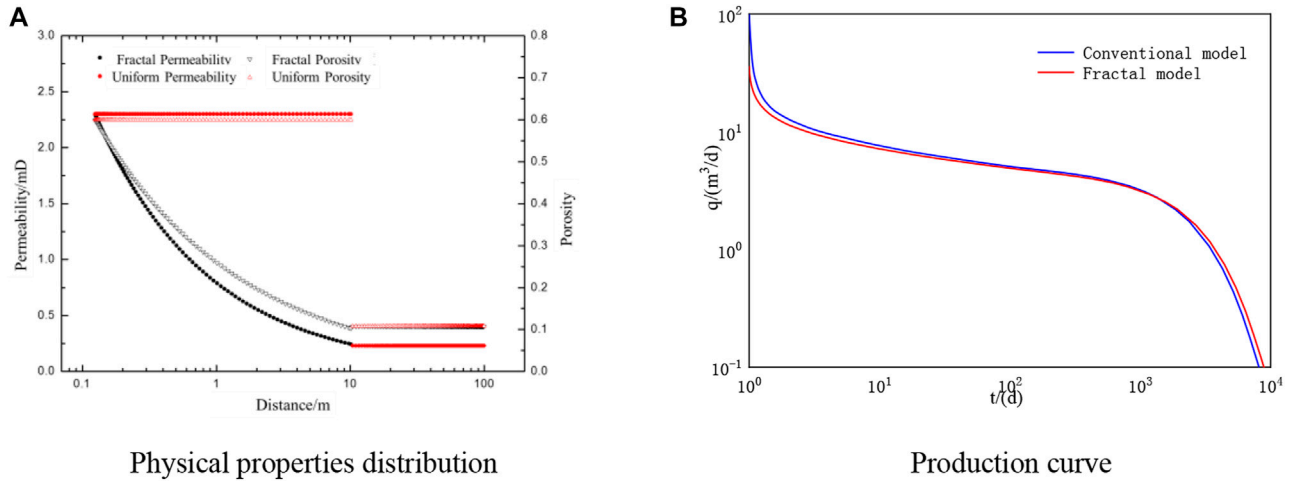

FIGURE 4 | Physical properties distribution and production in stimulated unconventional reservoirs. **(A)** is the physical properties distribution, **(B)** is the production curve.

$$\phi_f = \phi_w \left(\frac{r}{r_w}\right)^{-\frac{d(\ln(N(R)))}{d(\ln(R))}-2} \tag{4}$$

Where k_f is the equivalent permeability of fracture network in the dual media model, mD; ϕ_f is the equivalent porosity of fracture network in the dual media model.

PHYSICAL PROPERTIES AND PRODUCTION OF RESERVOIRS WITH FRACTAL FRACTURE NETWORK

Physical Properties Distribution

The fractal theory is used to accurately describe the physical parameters of fracture network in unconventional reservoirs. Assuming that a well is in the center of a circular reservoir, the wellbore radius is 12.4 cm, the permeability at the wellbore is 2.3 mD, the porosity at the wellbore is 0.6, the radius of stimulated reservoir is 10 m, the reservoir permeability is 0.23 mD, the reservoir porosity is 0.108, and the reservoir radius is 1000 m, the fractal dimension is 1.8 and fractal index is 0.1. Plotting the distribution of porosity and permeability in the reservoir is shown in **Figure 4A**. When the conventional dual-media flow model is used to describe the reservoir physical properties, the reservoir permeability and porosity will undergo abrupt changes at the boundary of the stimulated area. While when the fractal theory is adopted to describe the physical properties of the stimulated area, the permeability and porosity of the reservoir can smoothly transition between the stimulated boundary and the unstimulated boundary, which is more consistent with the actual geological characteristics. Therefore, the dual-media flow model can more accurately characterize the fluid flow in the stimulated unconventional reservoirs.

Dynamic Production of Reservoirs With Fractal Fracture Network

Assuming that there is a vertical well in the middle of a circular reservoir, producing at constant pressure. The initial reservoir pressure is 20 MPa, and the bottom hole pressure is 8 MPa. Using the above parameters and the calculated fractal dimension, daily production rate from the conventional dual-media flow model and fractal dual-media flow model are calculated, as shown in **Figure 4B**. It can be seen from the figure that the difference between the production calculated by the two models occurs in the early stage. When considering the distribution of the fractal fracture network, the early stage of production is smaller than the calculation result of the conventional dual-media flow model. However, it is close to the actual production data of the stimulated unconventional reservoirs. The results calculated by the two models are relatively similar in the middle and late stages of production.

CONCLUSION

1) Based on the complex fracture distribution of unconventional reservoirs after hydraulic fracturing, this paper uses fractal theory to describe the distribution of fracture networks, and proposes a calculation method of fractal parameters for hydraulic fracturing vertical wells in unconventional reservoirs.
2) The fractal theory are used to describe the distribution of fracture network, it can be seen from the physical property distribution that using fractal theory to describe the physical properties of stimulated area can make the reservoir permeability and porosity smoothly transition between the stimulated boundary and unstimulated boundary, which is different from the conventional methods.

3) The production changes from the conventional dual-media flow model and the fractal dual-media flow model were calculated respectively. The comparative analysis showed that the difference mainly occurred in the early stage of production, and the production considering the fractal fracture network is relatively small.

DATA AVAILABILITY STATEMENT

The original contributions presented in the study are included in the article/supplementary material, further inquiries can be directed to the corresponding author.

AUTHOR CONTRIBUTIONS

JL: Conceptualization, Methodology, Software, ML: Conceptualization, Methodology, Software, Investigation, Visualization, Project administration, Data Curation GS: Supervision, Funding acquisition.

FUNDING

This study was supported by the National Natural Science Foundation of China (52004033).

REFERENCES

Acuna, J. A., Ershaghi, I., and Yortsos, Y. C. (1995). Practical Application of Fractal Pressure Transient Analysis of Naturally Fractured Reservoirs. *Spe Formation Eval.* 10 (03), 173–179. doi:10.2118/24705-pa

Aprilian, S., Abdassah, D., and Mucharam, L. (1993). *Application of fractal reservoir model for interference test analysis in Kamojang geothermal field (Indonesia)*. Houston, TX, USA: Publ by Society of Petroleum Engineers (SPE).

Chang, J., and Yortsos, Y. C. (1990). Pressure Transient Analysis of Fractal Reservoirs[J]. *SPE Formation Eval.* 5 (1), 31–38. doi:10.2118/18170-pa

Chen, Y., Zhao, H., Zhang, Q., Zhou, Y., Wang, H., Lei, S., et al. (2020). Development and Application of a Coupling Method for Well Pattern and Production Optimization in Unconventional Reservoirs. *J. Circuit Syst. Comp.* 29 (07), 2050105. doi:10.1142/s0218126620501054

Cheng, Y., Li, Y., and Shi, X. (2013). Analysis and application of fracture network models of volume fracturing in shale gas reservoirs[J]. *Nat. Gas Industry* 33 (9), 53–59.

Guo, T., Zhang, S., Ge, H., Wang, X., Lei, X., and Xiao, B. (2015). A new method for evaluation of fracture network formation capacity of rock. *Fuel* 140, 778–787. doi:10.1016/j.fuel.2014.10.017

Katz, A. J., and Thompson, A. H. (1985). Fractal Sandstone Pores: Implications for Conductivity and Pore Formation. *Phys. Rev. Lett.* 54 (12), 1325–1328. doi:10.1103/physrevlett.54.1325

Krohn, C. E. (1988). Fractal measurements of sandstones, shales, and carbonates. *J. Geophys. Res.* 93 (B4), 3297–3305. doi:10.1029/jb093ib04p03297

Li, Q., Xing, H., Liu, J., and Liu, X. (2015). A review on hydraulic fracturing of unconventional reservoir. *Petroleum* 1 (1), 8–15. doi:10.1016/j.petlm.2015.03.008

Li, Y. (2020). Simulation of the interactions between multiple hydraulic fractures and natural fracture network based on Discrete Element Method numerical modeling. *Energy Sci Eng* 8 (8), 2922–2937. doi:10.1002/ese3.712

Li, Z., Li, X., Yu, J., and Cao, W. D. (2020). Influence of existing natural fractures and beddings on the formation of fracture network during hydraulic fracturing based on the extended finite element method[J]. *Geomechanics Geophys. Geo-Energy Geo-Resources* 6 (4), 58. doi:10.1007/s40948-020-00180-y

Manchanda, R., Shrivastava, K., and Zheng, S. (2020). *A new mechanism for the formation of hydraulic fracture swarms*. The Woodlands, TX, United states: Society of Petroleum Engineers.

Meng, M., Chen, Z., Liao, X., Wang, J., and Shi, L. (2020). A well-testing method for parameter evaluation of multiple fractured horizontal wells with non-uniform fractures in shale oil reservoirs. *Adv. Geo-energy Res.* 4 (2), 187–198. doi:10.26804/ager.2020.02.07

O Shaughnessy, B., and Procaccia, I. (1985). Diffusion on fractals[J]. *Phys. Rev. a* 32 (5), 3073.

Pfeiferper, P., and Avnir, D. (1983). Chemistry non-integral dimensions between two and Three[J][J]. *J. Chem. Phys.* 79 (7), 3369–3558. doi:10.1063/1.446210

Qi, J., Zhang, L., Zhang, K., Li, L., and Sun, J. (2020). The application of improved differential evolution algorithm in electromagnetic fracture monitoring. *Adv. Geo-energy Res.* 4 (3), 233–246. doi:10.46690/ager.2020.03.02

Sheng, G., Su, Y., and Wang, W. (2019). A new fractal approach for describing induced-fracture porosity/permeability/compressibility in stimulated unconventional reservoirs. *J. Pet. Sci. Eng.* 179, 855–866. doi:10.1016/j.petrol.2019.04.104

Sheng, G., Su, Y., Zhao, H., and Liu, J. (2020). A unified apparent porosity/permeability model of organic porous media: Coupling complex pore structure and multi-migration mechanism. *Adv. Geo-energy Res.* 4 (2), 115–125. doi:10.26804/ager.2020.02.01

Song, W., Wang, D., Yao, J., Li, Y., Sun, H., Yang, Y., et al. (2019). Multiscale image-based fractal characteristic of shale pore structure with implication to accurate prediction of gas permeability. *Fuel* 241, 522–532. doi:10.1016/j.fuel.2018.12.062

Song, W., Yao, J., Ma, J., Sun, H., Li, Y., Yang, Y., et al. (2018). Numerical Simulation of Multiphase Flow in Nanoporous Organic Matter with Application to Coal and Gas Shale Systems. *Water Resour. Res.* 54 (2), 1077–1092. doi:10.1002/2017wr021500

Su, Y., Wang, W., and Sheng, G. (2014). Compound flow model of volume fractured horizontal Well[J]. *Shiyou Xuebao/Acta Petrolei Sinica* 35 (3), 504–510.

Wang, D., Yao, J., Chen, Z., Song, W., and Sun, H. (2019). Image-based core-scale real gas apparent permeability from pore-scale experimental data in shale reservoirs. *Fuel* 254, 115596. doi:10.1016/j.fuel.2019.06.004

Wang, W., Su, Y., and Mu, L. (2013). Influencing factors of stimulated reservoir volume of vertical wells in tight oil reservoirs[J]. *Zhongguo Shiyou Daxue Xuebao (Ziran Kexue Ban)/Journal China Univ. Pet. (Edition Nat. Science)* 37 (3), 93–97.

Wang, W., Su, Y., Sheng, G., Cossio, M., and Shang, Y. (2015). A mathematical model considering complex fractures and fractal flow for pressure transient analysis of fractured horizontal wells in unconventional reservoirs. *J. Nat. Gas Sci. Eng.* 23, 139–147. doi:10.1016/j.jngse.2014.12.011

Zhang, X., He, J., Deng, H., Fu, M., Xiang, Z., Peng, X., et al. (2021). Controls of interlayers on the development and distribution of natural fractures in lacustrine shale reservoirs: A case study of the Da'anzhai member in the Fuling area in the eastern Sichuan Basin[J]. *J. Pet. Sci. Eng.*, 109224.

Conflict of Interest: Author ML is employed by SINOPEC.

The remaining authors declare that the research was conducted in the absence of any commercial or financial relationships that could be construed as a potential conflict of interest.

Publisher's Note: All claims expressed in this article are solely those of the authors and do not necessarily represent those of their affiliated organizations, or those of the publisher, the editors and the reviewers. Any product that may be evaluated in this article, or claim that may be made by its manufacturer, is not guaranteed or endorsed by the publisher.

frontiers in Earth Science

ORIGINAL RESEARCH
published: 18 October 2021
doi: 10.3389/feart.2021.748450

Quantitative Analysis of Phase Separation Using the Lattice Boltzmann Method

*Xiaoqi Li, Jichao Fang and Bingyu Ji**

Research Institute of Petroleum Exploration and Development, SINOPEC, Beijing, China

Phase separation is widely observed in multiphase systems. In this study, it has been investigated using Shan–Chen lattice Boltzmann method. The adhesion parameter in SC model leads to the desired fluid–fluid phenomenon, which was varied to specify the strength of separation between two phases to present emulsified performance in oil production. In order to describe such behaviors quantitatively, graphical distributions were described with time and were corresponded with a statistical index–Fourier structure factor that is able to predict complex phase separation behaviors, thereby providing a measurement for calculating such random distribution during the process of separation as well as evaluating heterogeneous degrees of the entire domain. The repulsive interactions are specified as low, intermediate, and high values. Phase separations with clear boundaries have been observed and each stage of separation evolvement has been discussed in this study. Magnitudes of structure factors are increased with higher degrees of fluctuations.

Keywords: phase Separation, LBM, structure factor, emulsion, oil recovery

OPEN ACCESS

Edited by:
Zheng Sun,
China University of Mining and Technology, China

Reviewed by:
Lei Wang,
Nazarbayev University, Kazakhstan
Xin LI,
Research Institute of Petroleum Exploration and Development (RIPED), China
Guodong Cui,
China University of Geosciences Wuhan, China

****Correspondence:***
Bingyu Ji
jiby.syky@sinopec.com

Specialty section:
This article was submitted to Economic Geology, a section of the journal Frontiers in Earth Science

Received: *28 July 2021*
Accepted: *30 August 2021*
Published: *18 October 2021*

Citation:
Li X, Fang J and Ji B (2021) Quantitative Analysis of Phase Separation Using the Lattice Boltzmann Method. Front. Earth Sci. 9:748450. doi: 10.3389/feart.2021.748450

INTRODUCTION

One of phase separation principles is to utilize inherent immersion in an anti-solvent way of separating, for example, emulsification (Mukherjee et al., 2019) (Fournanty et al., 2008), nuclear condensates (Zhang et al., 2019), droplet formation, and movement in microchannels. So, the underlying principle of phase separation involves utilizing the two or more fluids, such that they separate into their respective phases (Dauyeshova et al., 2018). Its fully understanding will serve as the emulsified behavior occurring in heavy oil cold production and other areas.

To understand this mechanism which can be used to manipulate the breakdown or onset of such instability, many studies have been conducted via experimental works (Peters et al., 1990) (Goldburg and Huang, 1975) (Giaconia et al., 2007). Although experiments show that critical parameters of chemical emulsifiers are associated with rheology of the oil–water interface (Moerman et al., 2018) (Wang et al., 2014) (Cui et al., 2021) (Man et al., 2018), the theoretical work for this purpose that has been developed for production scenarios remains problematic (Wu et al., 2021) (Cui et al., 2020).

However, it is impractical to obtain micro systematic and completely separate evolutions using molecular dynamics due to massive computational power, and macroscopic behaviors are not sensitive. The lattice Boltzmann method (LBM) can describe microscopic behaviors of the fluid and represent macro scale behaviors. Such a mesoscopic scheme has become a useful tool to study a variety of industrial processes including the aforementioned processes. Phase separation in lattice Boltzmann evolves from an immiscible fluid with the respective equilibrium state of each component. The Shan–Chen model proposed interaction forces acting on fluid particles, which

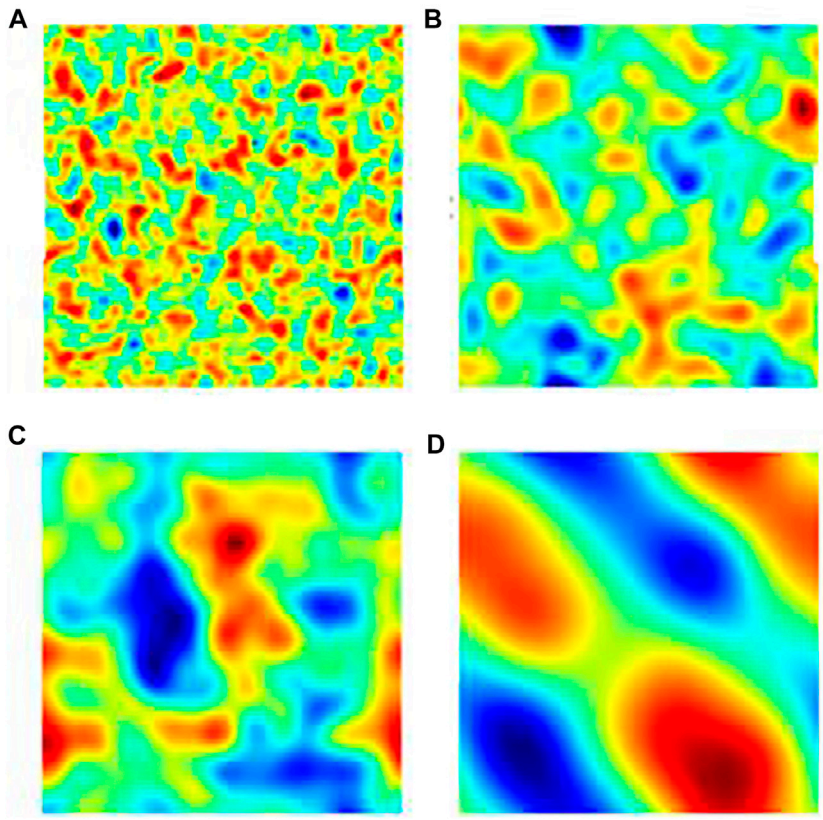

FIGURE 1 | Density fields under isothermal conditions for phase separation procedures with $\rho^* = 1.2$ and $\tau^* = 1$ using the interactive strengths with $G = -1$ at four times: **(A)** 100 ts, **(B)** 200 ts, **(C)** 300 ts, and **(D)** 1800 ts.

will be discussed later. Statistical behaviors will also be used to analyze instability due to the tangential velocity difference of the fluids, from initial random distribution to band-like structures and to the growth of droplets over the entire domain.

The structure factor of droplet evolvement via self-assembly in larger droplets is to the degree of spatial heterogeneity. In this study, it was applied to emulsification used in oil recovery engineering. Regarding the binary mixtures, we emphasize the strength of heterogeneity from emulsions inducing phase separation. If the interfacial properties and the pore size are included, we discuss how to control the spatial heterogeneity and phase separation.

METHODOLOGY

Shan–Chen Multiphase LBM

The SC LBM has been implemented in two dimensions for the multiphase system. The distribution function is introduced for fluid components. And it satisfies the following lattice Boltzmann equation:

$$f_i(\mathbf{r} + \boldsymbol{c}_i\Delta t, t + \Delta t) - f_i(\mathbf{r}, t) = -\frac{1}{\tau}\left[f_i(\mathbf{r}, t) - f_i^{eq}(\mathbf{r}, t)\right], \quad (1)$$

where $f_i(r, t)$ is the density distribution function which represents fractions of fluid molecules with a specific velocity c_i at a specific position and time t when time and space are discretized by Δt and Δx; τ is a relaxation time which is related to the kinematic viscosity as follows:

$$\mu = c_s^2\rho(\tau - 0.5). \quad (2)$$

The equilibrium distribution function $f_i^{eq}(\mathbf{r}, t)$ can be calculated as

$$f_i^{eq}(\mathbf{r}, t) = \omega_i\rho\left[1 + \frac{3(\boldsymbol{c}_i \cdot \boldsymbol{u}^{eq})}{c_s^2} + \frac{9(\boldsymbol{c}_i \cdot \boldsymbol{u}^{eq})^2}{2c_s^4} - \frac{3\boldsymbol{u}^{eq^2}}{2c_s^2}\right], \quad (3)$$

where c_i is the discrete velocity. For the D2Q9 model, they are given by

$$[\boldsymbol{c}_0, \boldsymbol{c}_1, \boldsymbol{c}_2, \boldsymbol{c}_3, \boldsymbol{c}_4, \boldsymbol{c}_5, \boldsymbol{c}_6, \boldsymbol{c}_7, \boldsymbol{c}_8] = c\begin{bmatrix} 0 & 1 & 0 & -1 & 0 & 1 & -1 & -1 & 1 \\ 0 & 0 & 1 & 0 & -1 & 1 & 1 & -1 & -1 \end{bmatrix}.$$

And where ω_i is the weighting factor:

$$\omega_i = \begin{cases} 1/4, & i = 0 \\ 1/18, i = 1 \sim 6 \\ 1/36, i = 7 \sim 18 \end{cases}, \quad (4)$$

where $c_s = c/\sqrt{3}, c = \Delta x/\Delta t$ is the ratio for lattice spacing Δx, and the time step is Δt. In **Eq. 2**, ρ is the density of fluid, which can be obtained from $\rho = \sum_i f_i$. Macroscopic velocity u^{eq} is given by

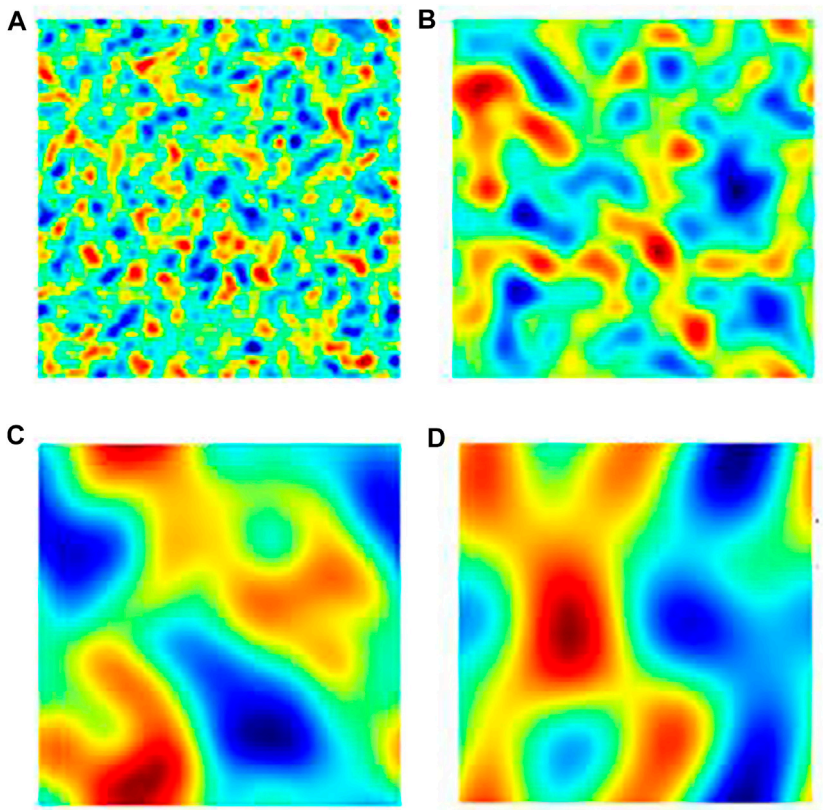

FIGURE 2 | Density fields under isothermal conditions for phase separation procedures with $\rho^* = 1.2$ and $\tau^* = 1$ using the interactive strengths with G = –30 at four times: **(A)** 100 ts, **(B)** 200 ts, **(C)** 300 ts, and **(D)** 1800 ts.

$$u_i^{eq} = u + \frac{\tau_i F_i}{\rho_i}, \tag{5}$$

where u is a velocity which is defined as

$$u = \frac{\sum_i \frac{f_i c_i}{\tau_i}}{\sum_i \frac{\rho_i}{\tau}}. \tag{6}$$

In **Eq. 5**, $F_i = F_{i,c}$ is the force acting on the fluid component, including fluid–fluid cohesion $F_{i,c}$ and excluding fluid–solid adhesion.

Fluid–Fluid Cohesion

The cohesive force acting on the fluid component is defined as

$$F_{i,c}(\mathbf{r}, t) = -G_c \rho_c(\mathbf{r}, t) \sum_i \omega_i \rho_{c'}(\mathbf{r} + \boldsymbol{c_i}\Delta t, t)\boldsymbol{c_i}, \tag{7}$$

where ρ_c and $\rho_{c'}$ denote two different fluid components, and G_c is a parameter that controls the strength of the cohesion force.

RESULTS AND DISCUSSIONS

Qualitative Analysis

In this study, the initial density is set to be 1. The periodic boundary conditions are used for all boundaries in the 301 × 301 mesh. Initially, droplets are distributed uniformly in the domain. Small droplets grow up gradually by dispersion leading to a high degree of heterogeneity because larger droplets are able to minimize surface energy. Small droplets became less by coalesce due to dispersion and local flow behaviors. In the entire domain, the interface between two phases was decomposed into several high-density zones and low-density zones. Later, phase zones can further coalesce and grow up resulting minimized total lengths of the interface under surface tension. When the computations reached to the equilibrium state, two phases will separate completely. Small structures tend to have a spherical shape with a smooth surface before evaporating by diffusion (Reis and Phillips, 2007).

Various interactive forces have effects on speeds of phase separations. The density ratio and viscosity radio between two phases are represented as ρ^* and τ^*, respectively. As expected, higher interactive strengths lead to more clear and quick separations. A two-phase system with small interaction may fail to separate. In **Figure 1**, the system with the intermediate interactive strength is able to represent similar structures like those in the system with a low interactive strength earlier. At the final stage (**Figure 1D**), phase separation was shown as top and bottom bands. Initially, intermediate and final stages of phase separations with the highest interaction show the most clear interface boundary. Initial random structures have grown up into larger band-like structures and then coalesce. Under surface

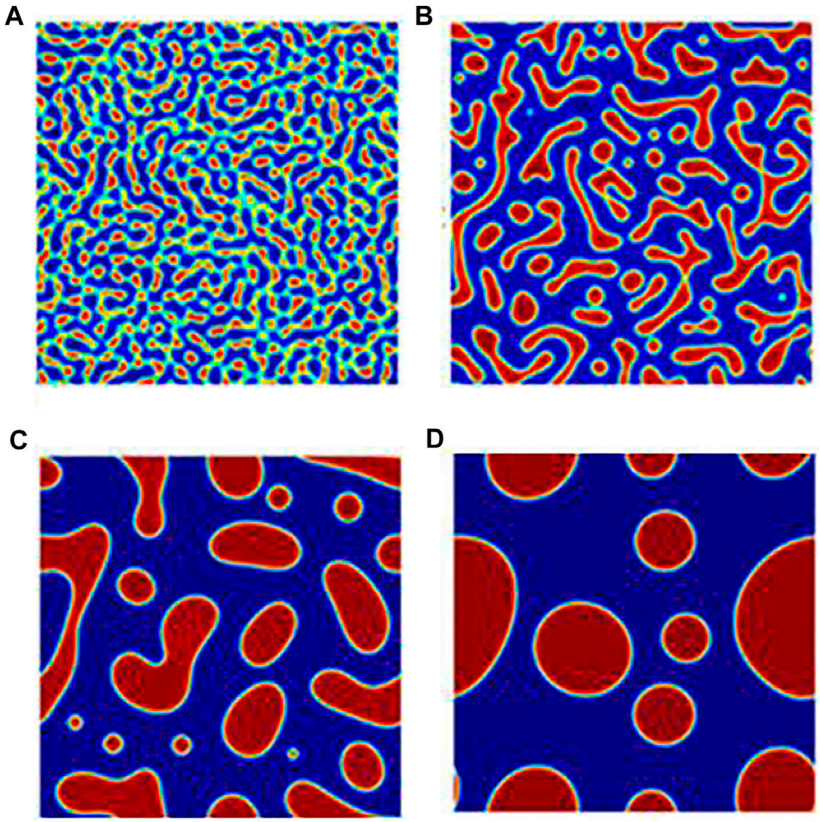

FIGURE 3 | Density fields under isothermal conditions for phase separation procedures with $\rho^* = 1.2$ and $\tau^* = 1$ using the interactive strengths with G = −100 at four times: **(A)** 100 ts, **(B)** 200 ts, **(C)** 300 ts, and **(D)** 1800 ts.

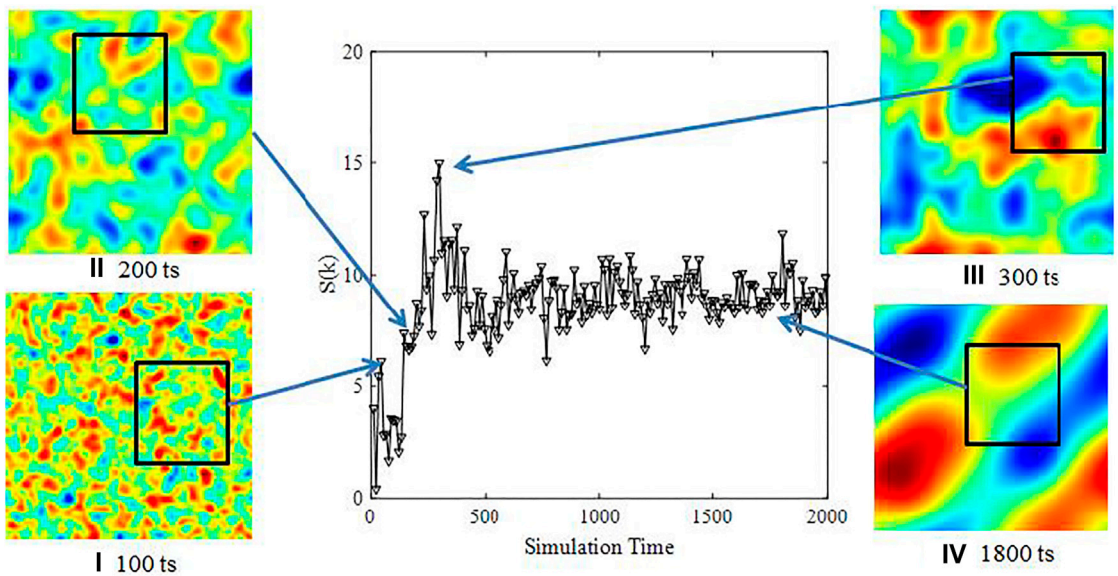

FIGURE 4 | Temporal evolution of mean structure factors over entire domain in the phase separation system with interactive strengths of $G = -1$ at four times: **(A)** 100 ts, **(B)** 200 ts, **(C)** 300 ts, and **(D)** 1800 ts.

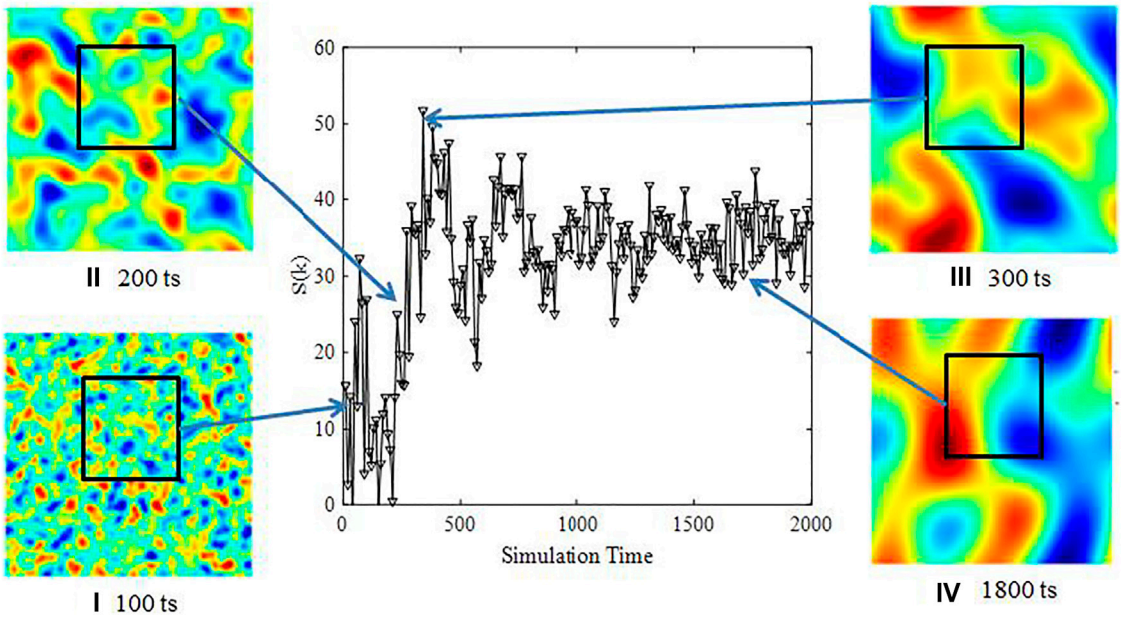

FIGURE 5 | Temporal evolution of mean structure factors over entire domain in the phase separation system with interactive strengths of $G = -30$ at four times: **(A)** 100 ts, **(B)** 200 ts, **(C)** 300 ts, and **(D)** 1800 ts.

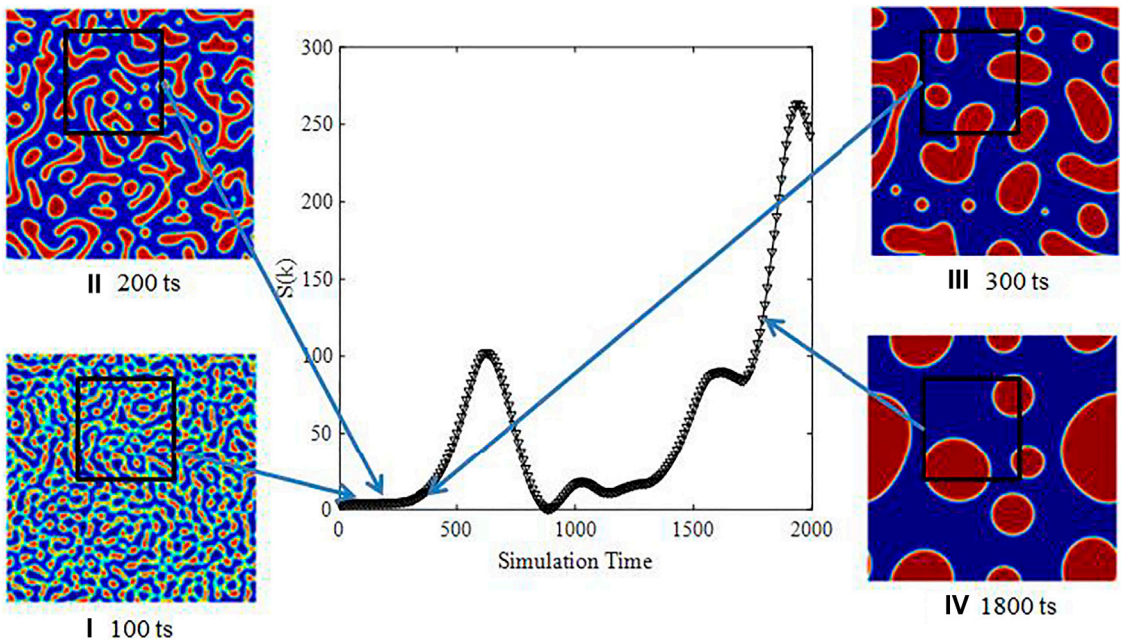

FIGURE 6 | Temporal evolution of mean structure factors over entire domain in the phase separation system with interactive strengths of $G = -30$ at four times: **(A)** 100 ts, **(B)** 200 ts, **(C)** 300 ts, and **(D)** 1800 ts.

tension, the bands reshape into small droplets or bubbles for minimizing surface energy. At last, the domain was full of stably moving big droplets. If the simulation time is long enough, all droplets will merge into one. When we observe the separation behaviors at one specific time in a row, the interaction with a small interactive strength requires more time to evolve until the separation process is complete.

Phase separation happens in a system with an intermediate specified interactive force; see **Figure 2**. A clearer structure involving separated behaviors can be seen quickly. Distinctive

band structures are formed with random swings but are hardly evolved into further structures within the simulation time.

When the interactive strength is risen to a high level with the magnitude of -100 shown in **Figure 3**, the exceptional separated structures are shown. Many smaller band structures are displayed in the earlier stage (**Figure 3B**). Subsequently, such "bands" are further combined (**Figure 3C**) and then reshaped into some round bubbles (**Figure 3D**).

Structure Factor

Structure factor is used by the Fourier transform of spatial distributions of droplets or bubbles to present instabilities observed. Here, the first structure factor evolution will be showed as the function of simulation time. The structure factor shows heterogeneity changes due to phase separation (Zou et al., 1994). The structure factor is defined based on the fluctuation–dissipation theorem within integration of the imaginary part of the density response function. For a discrete system we are studying, it is given by

$$S(k,t) = \frac{1}{N}\left|\sum\nolimits_r \left[q(\mathbf{r},t) - \overline{q(t)}\right]e^{ik\cdot r}\right|, \tag{8}$$

where N is the total number of grid points in the domain. $q(\mathbf{r},t) = n^1(\mathbf{r},t) - n^2(\mathbf{r},t)$; $k = \frac{2\pi}{L}(m\mathbf{i} + n\mathbf{j}), m.n = 1, 2, \ldots, L$, and L is the linear lattice size. $\overline{q(t)}$ is the special average of $q(\mathbf{r},t)$ at time t.

Structure factor is a quantitative measure of the structure along a prescribed direction. A value at a given wave number indicates the presence of heterogeneity in the periodic domain. Here, we present the first structure factors along the x and y directions. These structure factors are associated with heterogeneities developed to the size of the computational domain.

The onset of phase separation is defined as the time when the structure factor is above zero. In order to evaluate fluctuations from phase separation behaviors, graphic distributions are used corresponding to structure factors at selective times. Initially, random uniformed structures are specified in the domain, with a low value of structure factors; see **Figure 4A**. Then, small droplets start to merge with the neighboring ones, and therefore, relative bigger droplets or chunks were distributed with an increasing fluctuation presenting by higher structure factors, in **Figure 4B**. In **Figure 4C**, the structure factor of low interactive strengths is observed to be a peak. As separation continues, some droplets become larger than others, which results in uneven structures in the domain. These larger and more nonuniformed structures were verified by maximum of the mean structure factor value at the approximate 300th step. In **Figure 4D**, high- and low-density phases at the 1800th step were alternately distributed, and values of mean structure factors in **Figure 4** remain.

Structure factors of the system with medium interactive strengths are shown in **Figure 5**. Similarly, the initial random uniformed distribution is shown in **Figure 5A**, which corresponds to low structure factors in **Figure 5**. And such low-level fluctuations are able to stay longer until approximately 200 steps as shown in **Figure 5B** due to increasing repulsive interaction compared to the low interactive strength. When large droplets further combine with neighboring same materials, some laminated structures appeared, and mean structure factors reach a peak at the approximate 800th step (**Figure 5C**). Although similar band structures are seen as those in the system with the low interactive strength, a clearer boundary between two phases is revealed.

When the interactive strength is increased to 100, quite clear phase separation is observed as shown in **Figure 6**. Highest values of mean structure factors among three systems are shown. From the beginning, distinct boundaries enclosing large droplets or chunks were taken shape as shown in **Figures 6A and B**. But, structure factors are low because degree of heterogeneity at these stages is relatively small. At the approximate 300th step (**Figure 6C**), structure factors are gradually fortified as a variety of sizes of droplets or chunks. Additionally, structure factors in this systems exhibit a smooth profile that is different from previous two systems with curved trends. This suggests that a two-phase system with strong repulsive interaction involves continuous fluctuations rather than abrupt changes.

CONCLUSION

Phase separation is studied via the LBM-SC model and analyzed quantitatively using structure factors.

- Evolution of phase separation is observed in spatial distribution in four stages within periodic domains.
- Uniformed droplets aggregate into larger ones under interactive forces.
- The structure factors of the binary mixture develop in time that corresponds to changes of fluctuation due to phase separations.

DATA AVAILABILITY STATEMENT

The original contributions presented in the study are included in the article/Supplementary Material; further inquiries can be directed to the corresponding author.

AUTHOR CONTRIBUTIONS

XL has worked on simulation and draft development, JF has contributed to double checking data and description, and BJ has funded and guided this research work.

FUNDING

This work was sponsored by both the National Key Program and Development Program of China (No.SQ2018YFA070028) and SINOPEC Technical Project (No. P21085-18).

ACKNOWLEDGMENTS

This work was financially supported by the Chinese Research and Development of National Key Program (No.SQ2018YFA070028) and SINOPEC Technical Project (No. P21085-18).

REFERENCES

Cui, G., Pei, S., Rui, Z., Dou, B., Ning, F., and Wang, F. (2021). Whole Process Analysis of Geothermal Exploitation and Power Generation from a Depleted High-Temperature Gas Reservoir by Recycling CO2. *Energy* 217, 119340. doi:10.1016/j.energy.2020.119340

Cui, G., Ren, S., Dou, B., and Ning, F. (2020). Geothermal Energy Exploitation from Depleted High-Temperature Gas Reservoirs by Recycling CO2: The Superiority and Existing Problems. *Geosci. Front.*, 101078. in press. doi:10.1016/j.gsf.2020.08.014

Dauyeshova, B., Rojas-Solórzano, L. R., and Monaco, E. (2018). Numerical Simulation of Diffusion Process in T-Shaped Micromixer Using Shan-Chen Lattice Boltzmann Method. *Comput. Fluids* 167, 229–240. doi:10.1016/j.compfluid.2018.03.029

Fournanty, S., Guer, Y. L., Omari, K. E., and Dejean, J.-P. (2008). Laminar Flow Emulsification Process to Control the Viscosity Reduction of Heavy Crude Oils. *J. Dispersion Sci. Tech.* 29 (10), 1355–1366. doi:10.1080/01932690701782871

Giaconia, A., Caputo, G., Ceroli, A., Diamanti, M., Barbarossa, V., Tarquini, P., et al. (2007). Experimental Study of Two Phase Separation in the Bunsen Section of the Sulfur-Iodine Thermochemical Cycle. *Int. J. Hydrogen Energ.* 32 (5), 531–536. doi:10.1016/j.ijhydene.2006.08.015

Goldburg, W. I., and Huang, J. S. (1975). "Phase Separation Experiments Near the Critical Point," in *Fluctuations, Instabilities, and Phase Transitions*. Editor T. Riste (Springer US), 87–106. doi:10.1007/978-1-4615-8912-9_5

Man, J., Chien, S., Liang, S., Li, J., and Chen, H. (2018). Size-Dependent Phase Separation in Emulsion Droplets. *ChemPhysChem* 19, 1937. John Wiley & Sons. doi:10.1002/cphc.201800662

Moerman, P. G., Hohenberg, P. C., Vanden-Eijnden, E., and Brujic, J. (2018). Emulsion Patterns in the Wake of a Liquid-Liquid Phase Separation Front. *Proc. Natl. Acad. Sci. USA* 115, 3599–3604. National Academy of Sciences. doi:10.1073/pnas.1716330115

Mukherjee, S., Berghout, P., and Van den Akker, H. E. A. (2019). A Lattice Boltzmann Approach to Surfactant-Laden Emulsions. *Aiche J.* 65 (2), 811–828. doi:10.1002/aic.16451

Peters, B., Wingo, D., Bower, M., Amborski, R., Blount, L., Daniel, A., et al. (1990). *Fluid Phase Separation (FPS) Experiment for Flight on a Space Shuttle Get Away Special (GAS) Canister*. Available at: https://ntrs.nasa.gov/api/citations/19900016845/downloads/19900016845.pdf.

Reis, T., and Phillips, T. N. (2007). Lattice Boltzmann Model for Simulating Immiscible Two-phase Flows. *J. Phys. A: Math. Theor.* 40 (14), 4033–4053. doi:10.1088/1751-8113/40/14/018

Wang, W.-c., Pan, Y.-x., Shi, K., Peng, C., and Ji, X.-l. (2014). Hierarchical Porous Polymer Beads Prepared by Polymerization-Induced Phase Separation and Emulsion-Template in a Microfluidic Device. *Chin. J. Polym. Sci.* 32 (12), 1646–1654. doi:10.1007/s10118-014-1547-1

Wu, Y., Cheng, L., Huang, S., Fang, S., Killough, J., Jia, P., et al. (2021). A Transient Two-phase Flow Model for Production Prediction of Tight Gas Wells with Fracturing Fluid-Induced Formation Damage. *J. Pet. Sci. Eng.* 199, 108351. doi:10.1016/j.petrol.2021.108351

Zhang, Y., Bertulat, B., Tencer, A. H., Ren, X., Wright, G. M., Black, J., et al. (2019). MORC3 Forms Nuclear Condensates through Phase Separation. *IScience* 17, 182–189. Elsevier. doi:10.1016/j.isci.2019.06.030

Zou, B., Li, H., Xia, Y., and Ma, X. (1994). Cluster Structure in a Circulating Fluidized Bed. *Powder Tech.* 78 (2), 173–178. doi:10.1016/0032-5910(93)02786-a

Conflicts of Interest: Authors XL, JF, and BJ were employed by SINOPEC

frontiers in Earth Science

ORIGINAL RESEARCH
published: 19 October 2021
doi: 10.3389/feart.2021.753529

Interface Properties in Binary Fluid Using Lattice Boltzmann Method

*Xiaoqi Li, Jichao Fang and Bingyu Ji**

Petroleum Exploration and Production Institute, SINOPEC, Beijing, China

Emulsified behaviors are of importance for chemical flooding. Properties of emulsifiers relate droplets coalescence and transport. Since experiments do not provide access to observables of interest. Numerical simulations with mesoscale scheme pose attractive method to gain insight into emulsifying stability, which is defined as a period of oil droplets movements at fixed ranges. A phase field based lattice Boltzmann model is used which simulate interface behavior. Various parameters including emulsified droplet size, interface thickness, viscosity ratio and density ratio have been discussed. The aim of this study is to provide a critical suggestion that predictive emulsifying behaviors of small oil droplets immersed in water environment.

OPEN ACCESS

Edited by:
Wenhui Song,
China University of Petroleum (Huadong), China

Reviewed by:
Guodong Cui,
China University of Geosciences Wuhan, China
Qing You,
China University of Geosciences, China

***Correspondence:**
Bingyu Ji
jiby.syky@sinopec.com

Specialty section:
This article was submitted to Economic Geology, a section of the journal Frontiers in Earth Science

Received: *05 August 2021*
Accepted: *21 September 2021*
Published: *19 October 2021*

Citation:
Li X, Fang J and Ji B (2021) Interface Properties in Binary Fluid Using Lattice Boltzmann Method. Front. Earth Sci. 9:753529. doi: 10.3389/feart.2021.753529

Keywords: emulsion, phase field model, LBM, time window, surfactant

INTRODUCTION

Chemical flooding is an effective technique that plays an important role in oil production at the middle and late stages, in which basic theory is to improve mobility of the hydrocarbon by altering the interfacial conditions. Interfacial tension between oil and water can be realized by adding surfactant. Generally, some additives including high-viscosity polymer are injected with water to improve oil displacement efficiency, and therefore, oil recovery is enhanced. We found that the interfacial phenomenon produced by an emulsifier greatly impacts its emulsifying performance (Sun, Z., et al.). However, the knowledge of the interfacial properties is still lacking (Mohammed and Babadagli) (Sun, Z., et al.) (Cui, Ren, et al.) (Dicharry et al.) (Moran et al.) (Wang et al.) (Temple-Heald et al.) (Cui, Pei, et al.).

Many surfactant studies in oil production have been focused on designs of molecular structures and corresponding evaluations (Dong et al.) (Zhang and Feng) (Ding et al.) (Zhang et al.). In fact, the response time provided by an emulsifier in a target environment is directly and firstly related to its emulsifying performance. However, there are few studies regarding emulsion response time to investigate interfacial behavior. The interfacial interaction can be treated as the attractive/repulsive forces, or as both representing emulsion in numerical models (H.Nour et al.).

Unfortunately, capturing interfacial properties accurately is a challenge, numerically. The interface in numerical treatment has different strategies due to the steep gradients of properties in the normal direction. Here, the lattice Boltzmann equation (LBE) is proposed to study interfacial behavior, which should integrate both microscopic models for the interface and meso-scopic kinetic equations (Lamura et al.) (Song et al.). In the present study, the LBE with interface capturing is used to solve the velocity field, and the basic idea is developed by (Zheng et al.). Instead of recovering the fluid momentum macrodynamic equation (Swift et al.), it has better performance by recovering the fluid velocity based one (Zheng et al.).

GOVERNING EQUATIONS OF MOTION FLUIDS

Phase Field Theory

A brief outline of this method will be in this section and for more detailed discussion refer to Jacqmin (1999). An order parameter ϕ is used to define two fluids in this diffuse interface method, and a Landau free energy function is defined as

$$\psi = \int_V dV\left[\psi(\phi) + \frac{k}{2}\left|\nabla\phi^2\right|\right] \tag{1}$$

V is the control volume, k is the coefficient of surface tension, $\psi(\phi)$ is the bulk free energy density (Tóth and Kvamme), which is related to physical intermolecular interactions in gas or fluids. The free energy density in an isothermal system can be used:

$$\psi(\phi) = \beta(\phi - \phi_w)^2(\phi - \phi_o)^2 \tag{2}$$

Where β is the constant dependence on the interfacial properties including thickness and surface tension. ϕ_w and ϕ_o are the constants based on the equilibrium state corresponding marked bulk fluids A and B, respectively (Van Der Sman and Meinders). Generally, $\phi_o = -\phi_w$. The free energy ψ yields the chemical potential

$$\mu_\phi = \frac{\partial\psi}{\partial\phi} - k\nabla^2\phi \tag{3}$$

$$= 4\beta(\phi - \phi_w)(\phi - \phi_o)(\phi - \overline{\phi}) - k\nabla^2\phi \tag{4}$$

Where $\overline{\phi} = (\phi_o + \phi_w)/2$. The interface plane profile can be obtained by solving $\mu_\phi = 0$, then the interface is

$$\phi(\xi) = \frac{(\phi_w + \phi_o)}{2} - \frac{(\phi_w - \phi_o)}{2}\tanh\left(\frac{2\xi}{d}\right) \tag{5}$$

Where ξ is the coordinate normal to the interface and d is the interfacial thickness that is given by

$$d = \frac{4}{\left|\phi_w - \phi_o\right|}\sqrt{\frac{k}{2\beta}} \tag{6}$$

The surface tension between fluid and fluid is represented as

$$\sigma_{wo} = \frac{\left|\phi_w - \phi_o\right|^3}{6}\sqrt{2k\beta} \tag{7}$$

Cahn and Hillard approximated interfacial diffusion fluxes which is proportional to chemical potential gradients (Zu and He). The interface profile can be described with respect to ϕ:

$$\frac{\partial\phi}{\partial t} + \nabla\cdot(\phi\mathbf{u}) = \mathbf{M}\nabla^2\mu_\phi \tag{8}$$

Where $\boldsymbol{u}$ and t are the velocity and time, and $\mathbf{M}$ is a mobility coefficient.

Hydrodynamic equations in the phase-field model for incompressible multiphase flows are given by

$$\nabla\cdot\mathbf{u} = 0 \tag{9}$$

$$\rho\frac{\partial\mathbf{u}}{\partial t} + \rho\nabla\cdot(\mathbf{uu}) = -\nabla\cdot p + \nabla\cdot\Pi + \boldsymbol{F_s} \tag{10}$$

ρ is the density of fluid; p is the hydrodynamic pressure which emphasizes incompressibility; $\Pi = \mu(\nabla\mathbf{u} + \mathbf{u}\nabla)$ is the viscous stress tensor, and μ is the dynamic viscosity; $F_s = -\phi\nabla\mu_\phi$ is the force associated with surface tension.

LBE for a Velocity Based Method

A standard LBE form for hydrodynamic properties is represented as

$$f_i(\mathbf{r} + \mathbf{c_i}\Delta t,\ t + \Delta t) - f_i(\mathbf{r}, t) = -\frac{f_i(\mathbf{r}, t) - f_i^{eq}(\mathbf{r}, t)}{\tau_f} + \frac{2\tau_f - 1}{2\tau_f}F_i\Delta t \tag{11}$$

For particle distribution function in the phase space, it has the microscopic velocity $\boldsymbol{c_i}$ and an external body force may be added F_i at the r space coordinate and time t; $f_i^{eq}(\mathbf{r}, t)$ is the its corresponding equilibrium state; τ_f is dimensionless relaxation time for velocity field; Δt is a time step.

In the present study, a 2-dimensional 9-velocity (D2Q9) LBM structure is used to solve the field in 2D.

The particle velocity in the D2Q9 structure can be given using Gauss-Hermite quadrature in

$$[e_\alpha] = \begin{cases} (0,0) & \alpha = 0 \\ c\left(\left[\frac{\cos[\alpha-1)\pi}{2}\right], \sin\left[\frac{(\alpha-1)\pi}{2}\right]\right) & \alpha = 1,2,3,4 \\ \sqrt{2}c\left(\cos\left[\frac{(2\alpha-1)\pi}{4}\right], \sin\left[\frac{(2\alpha-1)\pi}{4}\right]\right) & \alpha = 5,6,7,8 \end{cases} \tag{12}$$

Where $c = \Delta x/\Delta t$ and Δx is the streaming length. In performing LBM in recovering the incompressible flow condition, we introduced a set of relations to be compiled by the zeroth, first and second moments of the equilibrium distribution function $f_i^{eq}(\mathbf{r}, t)$:

$$\sum_i f_i^{eq} = 0 \tag{13}$$

$$\sum_i \mathbf{c_i} f_i^{eq} = 0 \tag{14}$$

To satisfy the function above, the following equilibrium distribution function is.

Introduced as:

$$f_i^{eq} = \omega_i\rho\left[1 + \frac{3(\mathbf{c_i}\cdot\mathbf{u})}{c_s^2} + \frac{9(\mathbf{c_i}\cdot\mathbf{u})^2}{2c_s^4} - \frac{3\mathbf{u}^2}{2c_s^2}\right], i \neq 0 \tag{15}$$

For D2Q9 model, weighting factor ω_i is given by

$$\omega_i = \begin{cases} 1/4, & i = 0 \\ 1/18, & i = 1 \sim 6 \\ 1/36, & i = 7 \sim 18 \end{cases} \tag{16}$$

The reference speed of sound $c_s = \frac{1}{\sqrt{3}}$.

Interface Capturing

Interface capturing is proposed to be given as:

$$g_i(\mathbf{r} + \boldsymbol{c_i}\Delta t,\ t + \Delta t) = -\frac{g_i(\mathbf{r}, t) - g_i^{eq}(\mathbf{r}, t)}{\tau_g} + \eta\left[g_i^{eq}(\mathbf{r} + \mathbf{c_i}\Delta t,\ t) - g_i^{eq}(\mathbf{r}, t)\right] \tag{17}$$

Where $g_i(\mathbf{r}, t)$ is the distribution for the order parameter; $g_i^{eq}(\mathbf{r}, t)$ is its corresponding equilibrium state; τ_g is a relaxation time for the order parameter; and η is a constant as $\eta = 2\tau_g - 1$.

The moments of the equilibrium distribution satisfy

$$\sum_i g_i^{eq} = \phi \tag{18}$$

$$\sum_i \boldsymbol{c_i} g_i^{eq} = \frac{\phi u}{1 - \eta} \tag{19}$$

Then, density can be calculated according to mass conservation as in Owengrub and Truskinovsky (1998)

$$\rho = \frac{\phi - \phi_B}{\phi_A - \phi_B}(\rho_A - \rho_B) + \rho_B \tag{20}$$

The viscosity distribution within interface in the LB is given by

$$\mu = \frac{\phi - \phi_B}{\phi_A - \phi_B}(\mu_A - \mu_B) + \mu_B \tag{21}$$

Discretization

The Laplacian of the force terms can be discretized and interfacial force is adopted

$$\nabla\varphi = \frac{\sum_{i\neq 0}\omega_i \mathbf{c_i}(\mathbf{c_i} \cdot \nabla\varphi)}{c_s^2} \tag{21}$$

$$\nabla^2\varphi = \frac{\sum_{i\neq 0}\omega_i (\boldsymbol{c_i} \cdot \nabla)^2\varphi}{c_s^2} \tag{22}$$

Where φ is any macroscopic quantity. We use second-order central difference to the directional derivatives in $\boldsymbol{c_i}$ direction as

$$\boldsymbol{c_i} \cdot \nabla\varphi\big|_r = \frac{\varphi(\mathbf{r} + \mathrm{c_i}\Delta t) - \varphi(\mathbf{r} - \mathrm{c_i}\Delta t)}{2\Delta t} \tag{23}$$

$$(\boldsymbol{c_i} \cdot \nabla)^2\varphi\big|_r = \frac{\varphi(\mathbf{r} + \mathrm{c_i}\Delta t) - 2\varphi(\mathbf{r}) + \varphi(\mathbf{r} - \mathbf{c_i}\Delta t)}{\Delta t^2} \tag{24}$$

VALIDATION

A test with one static droplet is to verify the phase field multiphase lattice Boltzmann model. Initially, a static water droplet is placed in the middle region of a computational domain. Periodic boundary conditions are applied to all boundaries. Physical properties of two phases are given by $\rho_w = \rho_o = 1000\,\mathrm{kg/m^3}$, $\mu_w = 0.125\mu_o = 0.001\mathrm{Pa}\cdot\mathrm{s}$, and surface tension is 0.0005 N/m the lattice spacing Δx is 1 μm in physical units. $\xi = 1.5\Delta x$. Order parameter relaxation time τ_g is $1/(3 - \sqrt{3})$. At last, the bubble reaches the equilibrium. The pressure difference $\Delta p = p_{in} - p_{out}$ across a static bubble is related to the surface tension σ according to Laplace's law:

$$\Delta p = \frac{\sigma}{R} \tag{25}$$

The radius of the droplet R occupies several lattice units, which are surrounded by a quiescent phase. The boundaries of the computational domain are set to be periodic.

There is a good agreement between simulation results and the theoretical predictions, see **Figure 1**. The maximum error is less than 2.5%. This indicates that the surface tension simulations in the LB multiphase model have great accuracy.

RESULTS AND DISCUSSIONS

The parameters in the model are specified as dimensionless ratios between oil and water including viscosity and density ratios that represent external conditions. Interface thickness reflects the chemical properties of various surfactants. Radius depicts the size of the potential emulsified droplet.

Simulations of the binary droplet collision were carried out. Slip and no penetration boundary conditions are imposed at all boundaries of the computational domain. Two droplets are initially located at a far-center distance of $4R$, and are moved towards each other by an attractive force until contact.

Head-On Collisions and Pre-coalescence of Binary Droplets

In order to evaluate the effects of various dominant parameters on emulsifier performance, a measurement is proposed. Two moving oil droplets immersed in water (light fluid) have interfacial behavior with the following procedures, see **Figure 2**. Initially, two bodies move from far afield. When the two reach the region where the distance between the two body centers is smaller than $2R$, the first time is reckoned in as t_1. The two droplets continue to move until they make contact; the second time point is then recorded at the contact, t_2. Later, they start to merge into one, since the interface with double thickness would become small, if enough time would be given.

To quantify the balance between surface tension and interactive strength numerically, the selection of time window is defined as effective moving time. Here, effective moving time starts from the distance between droplets smaller than two radiuses to the nearest boundary distance equal to twice interface thickness, $t_2 - t_1$. This time window represents degree of emulsified stability, i.e. the larger the time window is offered by specified emulsion, the better performance is showed, and vice versa.

Quantitative Measurements of Time Windows

To advise engineers to select one surfactant with good expectation, the effects of various parameters on the time window have been studied quantitatively.

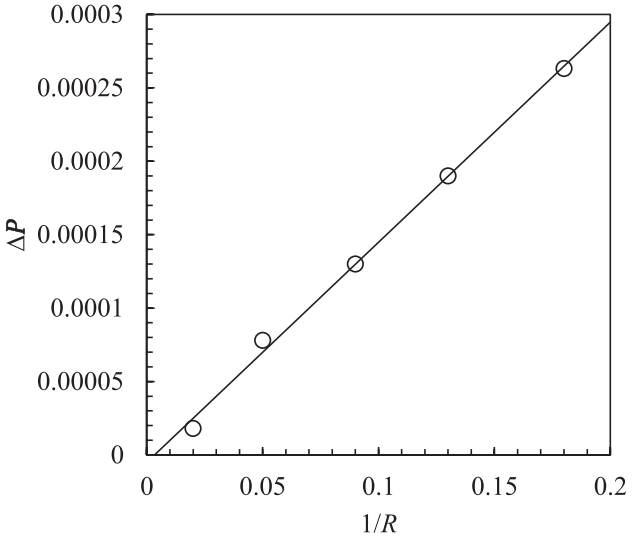

FIGURE 1 | Theoretical prediction (solid line) and numerical measurements of Laplace law (circles).

Sizes of Existing Droplets, *R* and Interface Thickness *d*

Surface tension is used to reflect the interactive strength of the two emulsified droplets and has significant effect on two phase interfacial behavior, and thereby the time window within effective contact distance between two droplets is measured as defined in *Head on Collisions and Pre Coalescence of Binary Droplets*. In order to keep surface tension acting on two phase systems at a reasonable level, various parameters are evaluated. In **Figures 3**, **4**, effective time windows are decreased with the increase of magnitudes of surface tensions in systems with different radiuses and surface thicknesses. Weak interfacial strengths from two phases induce large time windows in which emulsifiers perform small surface tensions that are convenient for managing and controlling the cost of emulsifying stability.

Figures 3, **4** both show the same trends on sizes of dispersed phases in terms of the effective time window. Smaller droplets have a wider time window due to increased total surface energy. Therefore, smaller ones are able to perform better stability and improve flow capability. On the other hand, larger droplets remain with a short duration that is used to govern contact behavior.

Shells of oil droplets and dimensions of emulsified droplets relate to emulsifying performance from chemical components of a specified emulsifier. To assess the effects of surface thicknesses and droplet radius on the time window, two thicknesses were specified on droplets surfaces as 5 and 10 lattice units and three droplets R = 15, 25 and 35 lattice unit (lu) are simulated, respectively. As the interface thickness is increased (empty symbols), the overlapped symbols indicate that sizes of internal phases have little effect on effective contact time. Meanwhile, if the thin shells with small surface thicknesses are attached onto oil droplets, the impact of the existing droplet dimension becomes significant, especially when surface tension is small. This means that the emulsifier with a capability of forming small oil droplets and a thick interface would be recommended. Furthermore, slopes of systems with thicker interfaces in both figures point out that it is sensitive to interface thickness as it changes faster at relatively high surface tension coefficients from 2.0×10^{-4} to 2.5×10^{-4} mu/ts^2. Surface energy of the dispersed phase under high surface tensions is declined, so droplets carrying thicker interfaces are easier to shrink. Therefore, time windows are decreased dramatically.

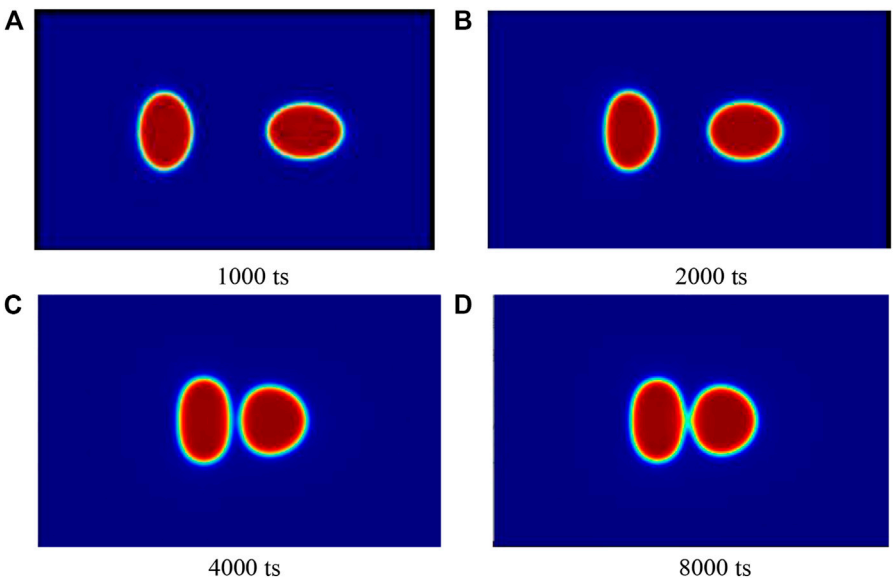

FIGURE 2 | Temporal snapshots of two moving droplets within the time window from start time point to contact time point: $\sigma = 1.0 \times 10^{-4}$, surface thickness $d = 25$ lattice units, viscosity ratio, and density ratio are set to be 10.

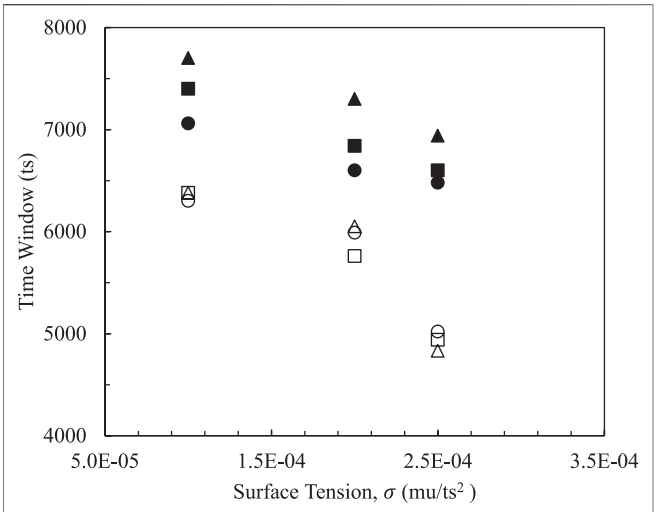

FIGURE 3 | Effects of droplets sizes on time windows: circles (R = 35 lu), squares (R = 25 lu) and triangles (R = 15 lu) represent three specified droplet sizes, respectively; empty symbols stand for thick surfaces (d = 10 lu) and solid symbols mean thin surfaces (d = 5 lu), respectively.

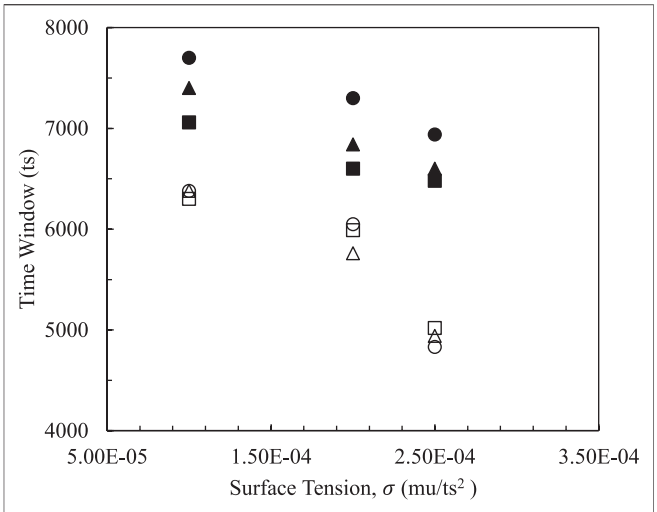

FIGURE 4 | Effects of surface thicknesses on time windows with ρ^* = 10 and μ^* = 10: empty symbols stand for thicker surfaces (d = 10 lu) and solid symbols mean thin surfaces (d = 5 lu), respectively; squares (R = 35 lu), triangles (R = 25 lu), and circles (R = 15 lu) represent three specified droplet sizes, respectively.

Effect of Density Ratio, μ^*

In **Figure 5**, differences in viscosities between oil and water are dimensionlized as $\mu^* = \mu_o/\mu_w$. Simulation results imply that emulsified heavy oil droplets have less time than emulsified lighter oil droplets due to narrow time windows in high viscosity ratio systems, while this does not mean, conflictingly, that heavy oil is easier to emulsify. Once the oil phase has been emulsified, such a dispersed state would have stayed longer in the water phase. Decreased viscosity differences between oil and water can increase the retention time of the dispersed phase, so some emulsifiers like polymer with high viscosities have been widely applied to enhanced oil recovery. The emulsifiers with different properties are represented by three different surface tensions, but the same interfacial thickness is kept. It suggests that to decreased surface tension is still an efficient way to manage emulsifying behavior easily. Besides, decreasing the dimension of droplets can enhance the impact on time windows shown from more dispersed symbols (empty). It is thereby confirmed that some emulsifiers can make small droplets stay dispersed longer when the viscosity of the external phase is high, and it does agree with our common sense.

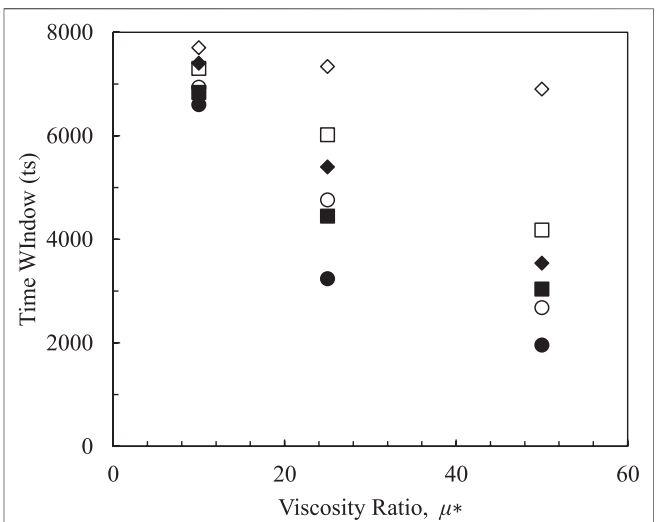

FIGURE5 | Effects of viscosity ratio μ^* on time windows: solid symbols represent large droplets (R = 25 lu) and empty symbols stand for small droplets (R = 15 lu), respectively; diamond ($\sigma = 1\times10^{-4}$ mu/ts^2), squares ($\sigma = 2\times10^{-4}$ mu/ts^2) and circles (σ = 2.5e-4 mu/ts2) represent three specified surface tensions, respectively.

Effect of Density Ratio ρ^*

Density is one of the most remarkable parameters in oil production. Density ratios in our LB simulations are varied from 0.8 to 1.4 recovering ranges of light to heavy oil extraction in reality. Simulation results from **Figure 6** demonstrate that emulsifiers having increasing probability of emulsifying smaller droplets are recommended which not only show good emulsifying performance, but also are beneficial to manage the emulsifying process due to the large time windows left for engineers. Generally, physical properties of oil and water are fixed, small slopes (empty symbols) of systems with small droplets impact on time windows denote that increased density ratios between oil and water that can ensure relatively long durations of being dispersed. Therefore, the emulsifier carried by water should be designed to increase the density of the external phase comparing the density of the internal phase. This is to say that the less difference in density between the internal and external phases, the better emulsifying performance should be expected.

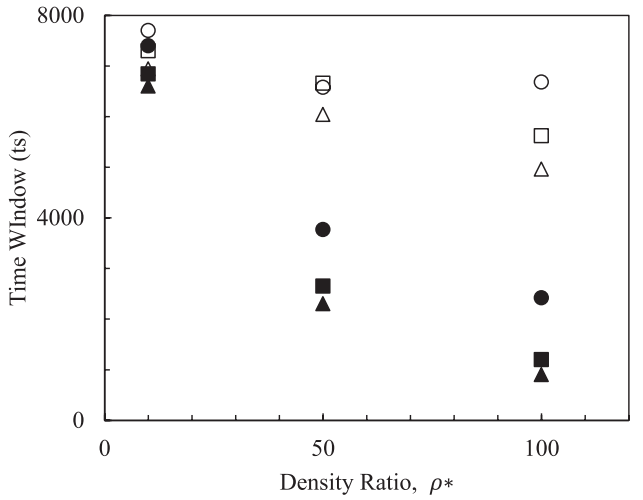

FIGURE 6 | Effects of density ratio ρ^* on time windows: solid symbols represent large droplets (R = 25 lu) and empty symbols stand for small droplets (R = 15 lu), respectively; circles ($\sigma = 1\times10^{-4}$ mu/ts^2), squares ($\sigma = 2\times10^{-4}$ mu/ts^2) and triangles ($\sigma = 2.5\times10^{-4}$ mu/ts^2) represent three specified surface tensions coefficients, respectively.

REMARK CONCLUSIONS

In this study, an effective time window is defined to measure emulsifying properties via staying times of dispersed phases. Interfacial tension, interfacial thickness, and differences of density and viscosity between dispersed and continuous phases have been simulated for the management and design of the emulsifiers.

1)Emulsifiers with a capability of forming small droplets and a thin interface outside are suggested, since small time windows indicate the good emulsifying performance can keep the droplets dispersed longer.
2)Small interfacial tensions provided by emulsifiers are still desired.
3)Decreasing differences of viscosities and densities between oil and water are also advised to design a binary emulsifying system.
4)A suitable emulsifier is not controlled by only one parameter. The difficulty in designing better performing emulsifiers relies on balancing these various parameters.

DATA AVAILABILITY STATEMENT

The original contributions presented in the study are included in the article/Supplementary Material, further inquiries can be directed to the corresponding author.

AUTHOR CONTRIBUTIONS

XL has contributed to simulation and datat analysis, JF has worked on double check manuscript, and BJ has worked for supervisor.

FUNDING

This work is financially supported by Chinese National Key Research and Development Program (No.SQ2018YFA070028) and SINOPEC Technical Project (No. P21085-18).

REFERENCES

Cui, Guodong., Pei, Shufeng., Rui, Zhenhua., Dou, Bin., Ning, Fulong., and Wang, Jiaqiang. (2020). Whole Process Analysis of Geothermal Exploitation and Power Generation from a Depleted High-Temperature Gas Reservoir by Recycling CO2. *Energy* 217, 119340 doi:10.1016/j.energy.2020.119340

Cui, Guodong., Ren, Shaoran., Bin, Dou., and Fulong, Ning. (2020). Geothermal Energy Exploitation from Depleted High-Temperature Gas Reservoirs by Recycling CO2: The Superiority and Existing Problems. *Geosci. Front.* in press, doi:10.1016/j.gsf.2020.08.014

Dicharry, C., Arla, D., Sinquin, A., Graciaa, A., and Bouriat, P. (2006). Stability of Water/Crude Oil Emulsions Based on Interfacial Dilatational Rheology. *J. Colloid Interf. Sci.* 297 (2), 785–791. doi:10.1016/j.jcis.2005.10.069

Ding, D., Sun, Z., and Xu, M. (1998). Properties of Surface Film of Oil Components. *J. Univ. Petroleum* 22 (3), 82–83

Dong, Z., Lin, M., Wang, H., and Li, M. (2010). Influence of Surfactants Used in Surfactant-Polymer Flooding on the Stability of Gudong Crude Oil Emulsion. *Pet. Sci.* 7 (2), 263–267. doi:10.1007/s12182-010-0031-y

Jacqmin, D. (1999). Calculation of Two-phase Navier-Stokes Flows Using Phase-Field Modeling. *J. Comput. Phys.* 155 (1), 96–127. doi:10.1006/jcph.1999.6332

Lamura, A., Gonnella, G., and Yeomans, J. M. (1999). A Lattice Boltzmann Model of Ternary Fluid Mixtures. *Europhys. Lett.* 45 (3), 314–320. doi:10.1209/epl/i1999-00165-4

Mohammed, M., and Babadagli, T. (2021). New Insights into the Interfacial Phenomena Occurring between Hydrocarbon Solvent and Heavy Oil. *J. Pet. Sci. Eng.* 196, 108022. doi:10.1016/j.petrol.2020.108022

Moran, K., Yeung, A., and Masliyah, J. (2006). The Viscoplastic Properties of Crude Oil-Water Interfaces. *Chem. Eng. Sci.* 61 (18), 6016–6028. doi:10.1016/j.ces.2006.05.026

Nour, H. A., Yunus, R. M., and Anwaruddin, H. (2007). Water-in-Crude Oil Emulsions: Its Stabilitzation and Demulsification. *J. Appl. Sci.* 15, 12–130

Owengrub, J., and Truskinovsky, L. (1998). Quasi-Incompressible Cahn-Hilliard Fluids and Topological Transitions. *Proc. R. Soc. A: Math. Phys. Eng. Sci.* 454, 2617–2654. doi:10.1098/rspa.1998.0273

Song, W., Yin, Y., Landry, C. J., Prodanovic, M., Qu, Z., and Yao, J. (2021). A Local-Effective-Viscosity Multirelaxation-Time Lattice Boltzmann Pore-Network Coupling Model for Gas Transport in Complex Nanoporous Media. *SPE J.* 26 (01), 461–481. doi:10.2118/203841-pa

Sun, Z., Li, X., Liu, W., Zhang, T., He, M., and Nasrabadi, H. (2020). Molecular Dynamics of Methane Flow Behavior through Realistic Organic Nanopores under Geologic Shale Condition: Pore Size and Kerogen Types. *Chem. Eng. J.* 398 (124341), 1–10. doi:10.1016/j.cej.2020.124341

Sun, Z., Shi, J., Wu, K., Zhang, T., Feng, D., and Li, X. (2019). Effect of Pressure-Propagation Behavior on Production Performance: Implication for Advancing Low-Permeability Coalbed-Methane Recovery. *SPE J.* 24 (02), 681–697. doi:10.2118/194021-pa

Swift, M. R., Orlandini, E., Osborn, W. R., and Yeomans, J. M. (1996). Lattice Boltzmann Simulations of Liquid-Gas and Binary Fluid Systems, *Phys. Rev. E*, 54, 5, 5041–5052. doi:10.1103/physreve.54.5041

Temple-Heald, C., Davies, C., Wilson, N., and Readman, N. (2014). Developing New Surfactant Chemistry for Breaking Emulsions in Heavy Oil. *J. Pet. Technology* 66 (01), 30, doi:10.2118/0114-0030-jpt

Tóth, G. I., and Kvamme., B. (2015). Phase Field Modelling of Spinodal Decomposition in the Oil/Water/Asphaltene System, *Phys. Chem. Chem. Phys.* 17. (31), 20259–20273. doi:10.1039/c5cp02357b

Van Der Sman, R. G. M., and Meinders, M. B. J. (2016). Analysis of Improved Lattice Boltzmann Phase Field Method for Soluble Surfactants, *Computer Phys. Commun.* 199, 12–21. doi:10.1016/j.cpc.2015.10.002

Wang, H. Y., Liu, Ai-qin., and Wen, Xin-min. (2008). *Factors Influencing Interfacial Electric Properties of Produced Water from Oilfield* Jining: Journal of the University of Petroleum, 143–146+151

Zhang, Bingzhu., and Feng, Shubo. (2010). Advances in the Modelling and Simulation of Emulsion Polymerisation. *Int. J. Model.* 11 (Nov), 262–273. doi:10.1504/ijmic.2010.037038

Zhang, J. Y., Wang, X. P., Liu, H. Y., Tang, J. A., and Jiang, L. (1998). Interfacial Rheology Investigation of Polyacrylamide-Surfactant Interactions. *Colloids Surf. A: Physicochemical Eng. Aspects* 132 (1), 9–16. doi:10.1016/s0927-7757(97)00151-9

Zheng, H. W., Shu, C., Chew, Y. T., and Sun, J. H. (2008). Three-dimensional Lattice Boltzmann Interface Capturing Method for Incompressible Flows. *Int. J. Numer. Meth. Fluids* 56, 1653–1671. doi:10.1002/fld.1563

Zu, Y. Q., and He, S. (2013). Phase-Field-Based Lattice Boltzmann Model for Incompressible Binary Fluid Systems with Density and Viscosity Contrasts. *Phys. Rev. E - Stat. Nonlinear, Soft Matter Phys.* 87 (4), 1–23. doi:10.1103/physreve.87.043301

Conflicts of Interest: Authors XL, JF, BJ are employed by SINOPEC.

frontiers in Earth Science

ORIGINAL RESEARCH
published: 17 November 2021
doi: 10.3389/feart.2021.765139

Numerical Study of Reactive Flow in Fractured Carbonate Rock

Xu Zhou[1,2], *Qingfu Zhang*[3], *Hongchuan Xing*[1], *Jianrong Lv*[2], *Haibin Su*[2] *and Zhaoqin Huang*[1]*

[1]School of Petroleum Engineering, China University of Petroleum (East China), Qingdao, China, [2]Research Institute and Exploration and Development, XinJiang Oilfield Company, PetroChina, Karamay, Xinjiang, China, [3]Exploration and Development Research Institute, Shengli Oilfield Company, SINOPEC, Dongyig, China

Acidizing technology is an effective reformation method of oil and gas reservoirs. It can also remove the reservoir pollution near wellbore zones and enhance the fluid transmissibility. The optimal injection rate of acid is one of the key factors to reduce cost and improve the effect of acidizing. Therefore, the key issue is to find the optimal injection rate during acid corrosion in fractured carbonate rock. In this work, a novel reactive flow mathematical model based on two-scale model and discrete fracture model is established for fractured carbonate reservoirs. The matrix and fracture are described by a two-scale model and a discrete fracture model, respectively. Firstly, the two-scale model for matrix is combined with the discrete fracture model. Then, an efficient numerical scheme based on the finite element method is implemented to solve the corresponding dimensionless equations. Finally, several important aspects, such as the influence of the injection rate of acid on the dissolution patterns, the influence of fracture aperture and fracture orientations on the dissolution structure, the breakthrough volume of injected acid, and the dynamic change of fracture aperture during acidizing, are analyzed. The numerical simulation results show that there is an optimal injection rate in fractured carbonate rock. However, the fractures do not have an impact on the optimal acid injection rate, they only have an impact on the dissolution structure.

Keywords: fractured carbonate rock, two-scale model, the discrete fracture model, reactive flow, numerical simulation

OPEN ACCESS

Edited by:
Jianlin Zhao,
ETH Zürich, Switzerland

Reviewed by:
Na Zhang,
Chengdu University of Technology, China
Jingfa Li,
King Abdullah University of Science and Technology, Saudi Arabia

***Correspondence:**
Zhaoqin Huang
huangzhqin@upc.edu.cn

Specialty section:
This article was submitted to Economic Geology, a section of the journal Frontiers in Earth Science

Received: *26 August 2021*
Accepted: *08 October 2021*
Published: *17 November 2021*

Citation:
Zhou X, Zhang Q, Xing H, Lv J, Su H and Huang Z (2021) Numerical Study of Reactive Flow in Fractured Carbonate Rock. Front. Earth Sci. 9:765139. doi: 10.3389/feart.2021.765139

INTRODUCTION

Since the 1980s, many scholars have conducted systematic research on matrix acidizing. Hoefner (Hoefner and Fogler, 1989; Fredd et al., 1997) and (Fredd et al., 1997) first undertook studies on the dissolution patterns of porous media. They injected the inorganic acid into limestone, then, injected the low melting point alloy into limestone after acid etching. They studied the dissolution structure of porous media by observing the shape of the alloy. (Hoefner and Fogler, 1988) used the network model to study the wormhole propagation and formation in the porous media and performed a series of experiments to analyze the mechanism of wormhole formation and many numerical simulations to study the characteristics of the mass-transfer limited regime and reaction-limited regime. These results suggested that the branch length of the main channel will never exceed the distance between the branch and the main channel. Next, based on this mathematical model, (Budek and Szymczak, 2012) improved the extended pore network model to qualitatively characterize the dissolution patterns at different Damköhler numbers and analyze optimal injection velocity. (Kim and Santamarina, 2015) explored how CO_2 dissolves into water and flows into the reservoir with a 2-D pore network model. (Wang et al., 1993) adopted the core displacement method to study the

influence of temperature, acid concentration, and the velocity of the injected acid on the wormhole. Finally, (Frick et al., 1994) also found the optimal injection rate at different acid concentrations and temperatures in the radial core. These analysis result consistent with their mathematical model, which can predict the wormhole diameter and the permeability influences the breakthrough time in the cross-section of the core.

(Bazin et al., 1995) proposed a pressure drop function based on morphology after acidizing. (Daccord et al., 1989) used water flowing on gypsum to simulate wormhole formation, three dissolution patterns were obtained: compaction, wormhole, and uniform. (Bazin, 2001) studied the optimal injection rate of injected acid using CT scanning technology and (Ziauddin and Bize, 2007) discusses the influence of the heterogeneity of porous media on the dissolution patterns based on CT scanning technology, NMR, and SEM technologies. (Zhang et al., 2017) studied the dissolution structure of acid-etched core by CT scanning technology, undertaking (He, 2009) an acid erosion experiment on carbonate rocks with undeveloped fractures, but the permeability is so low that the injected acid struggles to form a wormhole and break through the core end. (Yang and Pan, 2000) studied the influence of the injection rate and type of acid on dolomite based on the mechanism of acid filtration. (Daccord et al., 1989) described the dissolution structure based on fractal theory. (Golfier et al., 2001) studied the reactive flow combined with Brinkman. They found that the optimal condition was related to the acid concentration and the length of the core. This was the first confirmation that the acid capacity number affects the breakthrough time of injected acid.

A.D.Hill (Hill et al., 2009) built a model of wormhole formation considering acid filtration theory. (Liu et al., 1997) developed a simulator to describe the dissolution patterns. (Chen and Ying, 2006) deduced the equations of acid diffusion and acid surface reaction rate of reactive flow. (Catherine, 2004) injected the CO2-enriched water into the limestone to study the relationship between porosity and permeability, which are distinct at different dissolution stages in the core. (Andersen and Evje, 2016) considered flow through a fracture coupled with diffusion to the surrounding matrix, where the reaction occurring presented a reactive flow model in the fractured medium. (Nierode and Williams, 1971) established description equation for reactive flow based on the reaction kinetics, indicating that the mass transfer coefficient of solute in acid affects the result of acidizing treatment, and the effect of matrix acidizing was related to the injection rate of acid in the ground.

The above physical experiments and numerical simulation experiments did not consider the influence of natural complex fractures on the dissolution patterns and the dynamic change of fracture aperture during acid-rock reaction time. In response, this paper established a novel mathematical model of reactive flow in a fractured medium based on the two-scale model and the discrete fracture model. The numerical simulation of reactive flow in the fractured medium was realized.

In ***The Mathematical Model for Matrix*** of this paper, the two-scale mathematical model in matrix is presented. ***The Mathematical Model for Fracture*** outlines the mathematical model of reactive flow in a fractured medium based on the discrete fracture model. Then, in ***Dimensionless*** the governing equations and boundary conditions are written in a dimensionless formula. ***Validation of the Model verifies*** the theoretical model by examining the conclusions of previous studies. In ***Numerical Results and Discussion***, the numerical simulation of reactive flow is studied in different conditions. Finally, the paper is summarized by conclusions in ***Conclusion***.

THE MATHEMATICAL MODEL FOR MATRIX

Darcy Scale Model

The flow equation of injected acid in a porous medium is described by Darcy's law, the formula is written as:

$$\boldsymbol{v} = -\frac{\boldsymbol{K}}{\mu}\nabla P \tag{1.1}$$

Where, $\boldsymbol{v}$ is the vector of Darcy's velocity, m/s; $\boldsymbol{K}$ is the tensor of permeability in study region, m^2; μ is fluid viscosity, mPa·s; P is fluid pressure, Pa. The continuity equation is derived from the law of mass conservation, the formula is as follows:

$$\frac{\partial \phi}{\partial t} + \nabla \cdot \boldsymbol{v} + Q_{\mathrm{mf}} = 0 \tag{1.2}$$

Where, ϕ is the porosity of carbonate rock; t is reaction time, s. Q_{mf} is the normal flow rate through the interface between the matrix system and the fracture system.

Generally, when the acid is injected into the carbonate rock, the equation of acid transport in the rock is described by the following mass balance equation.

$$\frac{\partial (\phi C_{\mathrm{f}})}{\partial t} + \nabla \cdot (\boldsymbol{v} C_{\mathrm{f}}) = \nabla \cdot (\phi \boldsymbol{D}_{\mathrm{e}} \cdot \nabla C_{\mathrm{f}}) + R + \Phi_{\mathrm{mf}} \tag{1.3}$$

Where, C_{f} is acid concentration in a liquid phase, mol/m^3; $\boldsymbol{D}_{\mathrm{e}}$ is the tensor of the diffusion coefficient, m/s^2; Φ_{mf} is solute mass transmitted into the matrix system through the interface between matrix medium and fracture medium. R is reaction term, its physical significance is that the amount of acid transferred to the liquid-solid surface is equal to the consumption of surface reaction, the formula of reaction term is expressed as:

$$R = -a_{\mathrm{v}} \cdot k_{\mathrm{c}} (C_{\mathrm{f}} - C_{\mathrm{s}}) \tag{1.4}$$

Where, a_{v} is specific surface area, m^{-1}; k_{c} is local transport coefficient of acid, m/s; C_{s} is the acid concentration of liquid-solid surface in core pore, mol/m^3, it is calculated by:

$$C_s = \frac{C_{\mathrm{f}}}{\left(1 + k_{\mathrm{s}}/k_{\mathrm{c}}\right)} \tag{1.5}$$

The porosity will change as acid corrodes carbonate rock. The calculation formula of dynamic change of porosity is as follows:

$$\frac{\partial \phi}{\partial t} = \frac{a_{\mathrm{v}} \cdot \alpha \cdot k_{\mathrm{c}} (C_{\mathrm{f}} - C_{\mathrm{s}})}{\rho_s} \tag{1.6}$$

Where, α is the dissolving power of acid, kg/mol; ρ_{s} is the density of carbonate rock, kg/m^3.

Pore Scale Model

The porosity, radius of the pore, and specific surface area of rock are decided by pore structure. It is a dynamic process and the injected acid changes the pore structure of rock when it continuously erodes porous media. This means that the different kinds of physical parameters of carbonate rock will change dynamically. There are two methods to compute the physical parameters of carbonate rock in reactive flow (Panga et al., 2005; Kalia and Balakotaiah, 2009; Maheshwari et al., 2013; Ghommem et al., 2015; Liu et al., 2020). In the first method, these various physical parameters are computed based on the dynamic change of pore structure obtained through the laboratory. Another method is to calculate the various physical parameters of rock according to empirical or semi-empirical formulas. This paper adopts the modified Carman Kozeny equation to describe the dynamic change of porosity and permeability, the formulas are as follows:

$$\begin{cases} \dfrac{k}{k_0} = \dfrac{\phi}{\phi_0}\left(\dfrac{\phi(1-\phi_0)}{\phi_0(1-\phi)}\right)^{2\beta} \\ \dfrac{r_\mathrm{p}}{\overline{r}_0} = \sqrt{\dfrac{k\phi_0}{k_0\phi}} \\ \dfrac{a_\mathrm{v}}{\overline{a}_0} = \dfrac{\phi\overline{r}_0}{\phi_0 r_\mathrm{p}} \end{cases} \tag{1.7}$$

Where, r_p is pore radius, m; $\overline{a}_0$ is initial specific surface area, m-1; k_0 is initial permeability, m^2; ϕ_0 is initial porosity; β is a constant that depends on the structure of the medium.

When solute of liquid phase flows in the pores, the velocity of solute in the acid through the pore flows from liquid phase to pore surface and contact with the pore surface is expressed by the rate of the mass transfer. It can be seen from **Eq. 1.5** that the effect of the rate of mass transfer on reactive flow cannot be ignored when the acid system is certain, because its magnitude makes a difference to the chemical reaction. (Panga et al., 2010) defined a dimensionless number to the analysis of the associated factors, it is referred to the Sherwood number and represents the dimensionless mass transfer coefficient, it is given by:

$$Sh = \frac{2k_\mathrm{c}\overline{r}_\mathrm{p}}{D_\mathrm{m}} = Sh_\infty + b\mathrm{Re}_\mathrm{p}^{\frac{1}{2}}Sc^{\frac{1}{3}} \tag{1.8}$$

Where, r_p is the average pore radius of porous media, m; D_m is the molecular diffusion coefficient, m/s^2; Sh_∞ is asymptotic Sherwood number of the pore, b is a constant number related to the structure of porous media, $b = 0.7/m^{1/2}$, where, the m is the ratio of pore length to pore radius, Re_p is pore Reynolds number, $Re_\mathrm{p} = 2ur_\mathrm{p}/\nu$, where, ν is hydrodynamic viscosity; Sc is Schmidt number, $\mathrm{Sc} = \nu_\mathrm{k}/D_\mathrm{m}$, ν_k is hydrodynamic viscosity.

Diffusion Coefficient

When the acid is transported in the homogeneous and anisotropic matrix, in 2D, the diffusion tensor is characterized by axial diffusion coefficient D_eX and transverse diffusion coefficient D_eT. There is only solute molecular diffusion in the liquid phase and the transverse diffusion coefficient equals the axial diffusion coefficient when the fluid does not flow, the formula is as follows:

$$D_\mathrm{eX} = D_\mathrm{eT} = \alpha_\mathrm{os}D_\mathrm{m} \tag{1.9}$$

Where, D_m is the molecular diffusion coefficient, m/s^2; α_os is a constant related to the structure of porous media (such as tortuosity or connectivity between pores). The two-dimensional diffusion coefficient of acid relates to the geometry of porous media, the flow pattern of pore scale, and the properties of acid. Researchers usually define a dimensionless Peclet number to describe the contrast between convection and diffusion. The expression formula of the Peclet number is found to be

$$Pe_\mathrm{p} = \frac{|\boldsymbol{v}|d_\mathrm{h}}{\phi D_\mathrm{m}} \tag{1.10}$$

Where, $|\boldsymbol{v}|$ describes the magnitude of Darcy's velocity, m/s; d_h is pore diameter of porous media, m.

The formula of diffusion coefficient derived by Panga (Panga et al., 2010) is used to describe the diffusion of acid in porous media in this paper. the diffusion coefficient can be computed as:

$$D_\mathrm{eX} = \alpha_\mathrm{os}D_\mathrm{m} + \lambda_\mathrm{X}D_\mathrm{m}Pe_\mathrm{p} \tag{1.11}$$

$$D_\mathrm{eT} = \alpha_\mathrm{os}D_\mathrm{m} + \lambda_\mathrm{T}D_\mathrm{m}Pe_\mathrm{p} \tag{1.12}$$

Where, the subscript of X and T denotes the injection direction and vertical transverse direction of acid injection; α_os, $\lambda_\mathrm{T,}$ and λ_x are constants that have typical values of 0.5, 0.5,0.1 for a packed-bed of spheres (Kalia, 2008; Kalia and Balakotaiah, 2009; Liu et al., 2017), respectively.

Initial Conditions and Boundary Conditions

The pressure at the outlet is constant and the outlet boundary is a constant pressure boundary. The upper and down boundaries are closed boundaries. The specific expression of boundary conditions is given by:

$$P = 0, C_\mathrm{f} = 0, \; at\, t = 0 \tag{1.13}$$

$$u_0 = -\frac{k_x}{\nu}\frac{\partial P}{\partial x}, \frac{\partial P}{\partial y} = 0, C_\mathrm{f} = C_0, \; at\, x = 0 \tag{1.14}$$

$$u_0 = -\frac{k_x}{\nu}\frac{\partial P}{\partial x}, \frac{\partial P}{\partial y} = 0, C_\mathrm{f} = C_0, \; at\, x = 0 \tag{1.15}$$

$$\frac{\partial C_\mathrm{f}}{\partial x} = 0, P = P_e, \; at\, x = L \tag{1.16}$$

$$\frac{\partial P}{\partial y} = 0, \frac{\partial C_\mathrm{f}}{\partial y} = 0, \; at\, y = 0 \; and \; y = L \tag{1.17}$$

Where, u_0 is initial injection velocity, m/s; C_0 is a concentration of injected acid at the inlet, mol/m^3; P_e is a constant, it is boundary pressure at the outlet, Pa.

A random function $\widehat{f}$ is defined to simulate the heterogeneity of rock. Its value varies from $-\Delta\phi_0$ to $+\Delta\phi_0$ and satisfies the random function of uniform distribution, the generated initial porosity field is shown in **Figure 1**. The heterogeneity of fracture aperture is defined in this way.

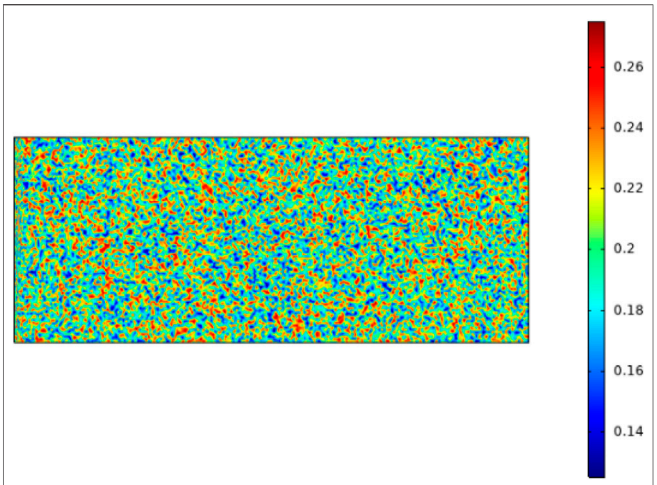

FIGURE 1 | Initial porosity field.

THE MATHEMATICAL MODEL FOR FRACTURE

The governing equation of the fracture system is written as:

$$d\frac{\partial(\rho\phi_{\mathrm{f}})}{\partial t}+\nabla\cdot\left(d\rho\boldsymbol{v}_{\mathrm{f}}\right)+Q_{\mathrm{fm}}=0 \tag{1.18}$$

Where, $\boldsymbol{v}_{\mathrm{f}}$ is the velocity vector of injected acid in the fracture system, the subscript f denotes fracture, d is fracture aperture, ϕ_{f} is fracture porosity; Q_{mf} is the flow exchange between the matrix system and fracture system. According to the cubic law, the flow velocity of injected acid in fracture system is expressed by the Poiseuille equation, the expression equation of flow velocity is given as:

$$\boldsymbol{v}_{\mathrm{f}}=-\frac{d^2}{12\mu}\nabla P \tag{1.19}$$

The expression equation of permeability in fracture system is derived as:

$$K_{\mathrm{f}}=\frac{d^2}{12} \tag{1.20}$$

Similarly, the convection-diffusion equation in fracture system is obtained as:

$$d\left(\frac{\partial(\phi_{\mathrm{f}}C_{\mathrm{f}})}{\partial t}+\nabla\cdot\left(\boldsymbol{v}_{\mathrm{f}}C_{\mathrm{f}}\right)-\nabla\cdot\left(\phi_{\mathrm{f}}D_{\mathrm{e,f}}\cdot\nabla C_{\mathrm{f}}\right)\right)+\Phi_{\mathrm{fm}}=0 \tag{1.21}$$

Where, C_{f} is the concentration of injected acid in the fracture system, $D_{\mathrm{e,f}}$ is the effective diffusion coefficient of solute in acid in the fracture system. Φ_{mf} is solute mass transmitted into the fracture system through the interface between matrix medium and fracture medium. Fracture aperture changes when the acid flow in the fracture system alters. The dynamic change process of fracture aperture can be obtained as:

$$\frac{\partial d}{\partial t}=\frac{2R_{\mathrm{c,f}}\left(C_{\mathrm{f}}-C_{\mathrm{s}}\right)\alpha}{\rho_{\mathrm{s}}} \tag{1.22}$$

The effective diffusion coefficient (Steefel and Lichtner, 1998) of solute in acid in fracture system is as follows:

$$D_{\mathrm{e,f}}=\alpha_{\mathrm{f}}\cdot|\boldsymbol{v}_{\mathrm{f}}|+D_{\mathrm{m}} \tag{1.23}$$

Where α_{f} is constant, which is equal to 0.5 in this paper.

DIMENSIONLESS

Many factors affect the process of reactive flow. The above governing equations and boundary conditions are written in a dimensionless formula to make the numerical solution of reactive flow easier and numerical simulation results more clear. The expression equations are defined:

$$x^*=\frac{x}{L},\ y^*=\frac{y}{L},\ \boldsymbol{U}^*=\frac{\boldsymbol{v}}{u_0},t^*=\frac{t}{(L/u_0)},\ r_{\mathrm{p}}^*=\frac{r_{\mathrm{p}}}{\overline{r}_0},\ a_{\mathrm{v}}^*=\frac{a_{\mathrm{v}}}{\overline{a}_0},$$
$$\boldsymbol{K}^*=\frac{\boldsymbol{K}}{k_0},\ \boldsymbol{D}^*=\frac{\boldsymbol{D}_{\mathrm{e}}}{D_{\mathrm{m}}},\ C_{\mathrm{f}}^*=\frac{C_{\mathrm{f}}}{C_0},\ P^*=\frac{P-P_{\mathrm{e}}}{(\mu u_0L)/K_0},\ h_{\mathrm{T}}^2=\frac{2k_{\mathrm{s}}\overline{r}_0}{D_{\mathrm{m}}},$$
$$Da=\frac{k_{\mathrm{s}}\overline{a}_0L}{u_0},\ Pe_{\mathrm{L}}=\frac{u_0L}{D_{\mathrm{m}}},\ N_{\mathrm{ac}}=\frac{\alpha C_0}{\rho_{\mathrm{s}}},\ \Phi^2=\frac{k_{\mathrm{s}}\overline{a}_0L^2}{D_{\mathrm{m}}},\ \eta=\frac{2r_0}{L},$$
$$\boldsymbol{U}_{\mathrm{f}}^*=\frac{\boldsymbol{v}_{\mathrm{f}}}{u_0},\ B=\frac{d}{L},\ K_{\mathrm{f}}^*=\frac{K_{\mathrm{f}}}{k_0},\ D_{\mathrm{f}}^*=\frac{D_{\mathrm{e,f}}}{D_{\mathrm{m}}}$$

Where the superscript $*$ denotes dimensionless; L is a characteristic length of the research area of the mathematical model; x,y are parameters of the coordinate system; U^* indicates that velocity vector is dimensionless; $\boldsymbol{K}^*$ indicates that the permeability vector is dimensionless; k_0 is initial permeability of porous media; $\overline{r}_0$ is average pore radius of porous media; $\overline{a}_0$ is initial specific surface area, B indicates that fracture aperture is dimensionless; the subscript f denotes fracture; D_{f}^* indicates diffusion coefficient is dimensionless; $\boldsymbol{K}^*$ indicates that permeability vector of fracture is dimensionless. Da represents the rate of reaction velocity to convection velocity at the core scale.

Based on the expression of the above-mentioned variables, dimensionless variables are substituted into governing equation. The dimensionless equations are obtained:

$$\boldsymbol{U}^*=-\boldsymbol{K}^*\cdot\nabla P_D \tag{1.24}$$

$$\frac{\partial\phi}{\partial t^*}+\nabla\cdot\boldsymbol{U}^*+Q_{\mathrm{mf}}^*=0 \tag{1.25}$$

$$\frac{\partial(\phi C_{\mathrm{f}}^*)}{\partial t^*}+\nabla\cdot\left(\boldsymbol{U}^*C_{\mathrm{f}}^*\right)=\nabla\cdot\left(\boldsymbol{D}^*\cdot\nabla C_{\mathrm{f}}^*\right)-\frac{Da\cdot a_{\mathrm{v}}^*\cdot C_{\mathrm{f}}^*}{\left(1+\frac{h_T^2\cdot r_{\mathrm{p}}^*}{Sh}\right)}+\Phi_{\mathrm{mf}}^* \tag{1.26}$$

The dimensionless equation of porosity changing is

$$\frac{\partial\phi}{\partial t^*}=\frac{Da\cdot N_{ac}\cdot a_{\mathrm{v}}^*\cdot C_{\mathrm{f}}^*}{\left(1+\frac{h_T^2\cdot r_p^*}{Sh}\right)} \tag{1.27}$$

The dimensionless equation of diffusion coefficient is rewritten as:

$$\boldsymbol{D}^* = \left(D_x, D_y\right) = \begin{pmatrix} \dfrac{\alpha_{os}\phi Da}{\Phi^2} + \lambda_X |U| r_p^* \eta \\ \dfrac{\alpha_{os}\phi Da}{\Phi^2} + \lambda_T |U| r_p^* \eta \end{pmatrix}^T \tag{1.28}$$

The above equations are mathematical models of matrix systems for reactive flow. The dimensionless mathematical equations in the fracture system for reactive flow are

$$\boldsymbol{U}_f^* = -K_f^* \cdot \nabla P^* \tag{1.29}$$

$$\nabla \cdot \left(B\boldsymbol{U}_f^*\right) + Q_{fm}^* = 0 \tag{1.30}$$

$$B\left(\frac{\partial\left(\phi C_f^*\right)}{\partial t^*} + \nabla \cdot \left(\boldsymbol{U}_f^* C_f^*\right) - \nabla \cdot \left(D_f^* \cdot \nabla C_f^*\right)\right) + \Phi_{fm}^* = 0 \tag{1.31}$$

Where, the expression equation of diffusion coefficient D_f^* is

$$D_f^* = \frac{\alpha_{os}}{L}\left|\boldsymbol{U}_f^*\right| + \frac{1}{Pe_L} \tag{1.32}$$

The dimensionless boundary conditions and initial conditions are arranged as:

$$\begin{cases} U^*|_{injection\ boundary} = 1 \\ P^*|_{outer\ boundary} = 0 \\ \left.\dfrac{\partial P^*}{\partial \vec{n}}\right|_{outer\ boundary} = 0 \\ C_f^*|_{injection\ boundary} = 1 \\ \left.\dfrac{\partial C_f^*}{\partial \vec{n}}\right|_{outer\ boundary} = 0 \\ \left.\dfrac{\partial P^*}{\partial \vec{n}}\right|_{horizontal\ boundary} = 0 \end{cases} \tag{1.33}$$

$$\begin{cases} C^*|_{t^*=0} = 0 \\ U^*|_{t^*=0} = 0 \end{cases} \tag{1.34}$$

VALIDATION OF THE MODEL

In this section, the correctness of the mathematical model of the matrix is verified. The numerical simulation results are compared with (Fredd and Fogler, 1999) physical experiment results. In the physical experiment, the diameter of the core is 3.8 cm and the length of the core is 10.2 cm. The comparison results of numerical simulation and physical experiment are shown in **Figure 2**.

Through the comparison results, there are five different dissolution patterns. The results of numerical simulation in this paper are consistent with physical experiment in Fredd's paper. A numerical example is used to test the accuracy of the mathematical model in Panga's paper (Panga et al., 2010). The length and width of the model are 5 and 2 cm, separately. The initial porosity is 0.2, the fluctuation range is 0.05, $\Phi^2 = 10^5$, $N_{ac} =$ 0.1, $h_T^2 = 0.07$. The comparison cures are shown in **Figure 3**. It shows that the two cures are not coincident. The reasons are the difference between accurate value and solving algorithm.

NUMERICAL RESULTS AND DISCUSSION

In this section, the numerical simulation of reactive flow in the fractured medium is implemented based on the above dimensionless mathematical model. The parameters and values in the numerical simulation are shown in **Table 1**. Unless otherwise specified, all parameters remain unchanged. The corresponding dissolution patterns in complex fractured media are studied, then, the effect of fracture aperture and the fracture orientation on dissolution structure and breakthrough volume of injected acid are studied in a single fracture system. The effect of heterogeneity of initial fracture aperture and dynamic variation of fracture aperture with dissolution on dissolution patterns, dissolution structure, and breakthrough volume of injected acid are studied. In this case, $Da = 250$.

The definition equation of the breakthrough volume of injected acid is as follows:

$$PV_{BT} = \frac{V_{acid}}{V_{ip}} = \frac{Q_{acid} T_{bt}}{V_{ip}} \tag{1.35}$$

Where, V_{acid} is the consumption volume of injected acid; V_{ip} is the initial pore volume of the core; Q_{acid} is the flow rate of injected acid, T_{bt} is waste time that injected acid breaks through core when the pressure rate of inlet end to outlet end is 0.01 at each time point.

Dissolution Patterns at Different Damköhler Number

The results of the numerical simulation are shown in **Figure 4**. There are five different dissolution patterns with Damköhler number changing. They are face dissolution, conical dissolution, wormhole, branch dissolution, and uniform dissolution. **Figure 4A** is the concentration field, **Figure 4B** is the porosity field. Column (A) is the concentration field and porosity field in the initial phase. (B) is the concentration field and porosity field when injected acid breaks through the core. It can be seen that there is a big difference among dissolution patterns. The reason is that the dissolution patterns are determined by the combined effect of convection velocity and reaction velocity of the solute in acid. When the convection velocity is smaller than the diffusion velocity and reaction velocity, the reaction between acid and rock is mainly controlled by the diffusion and reaction velocity of solute in acid. Therefore, the hydrogen ions transferred from the center of the pore to the surface of the pore will be completely consumed by the chemical reaction, and the rate of injected acid cannot promote the injected acid to penetrate the core deeper. In this case, the dissolution of acid in the core is named surface dissolution. As the rate of injected acid gets higher, so does the convection velocity of solute in acid, and the convection velocity is dominant for diffusion velocity and reaction velocity.

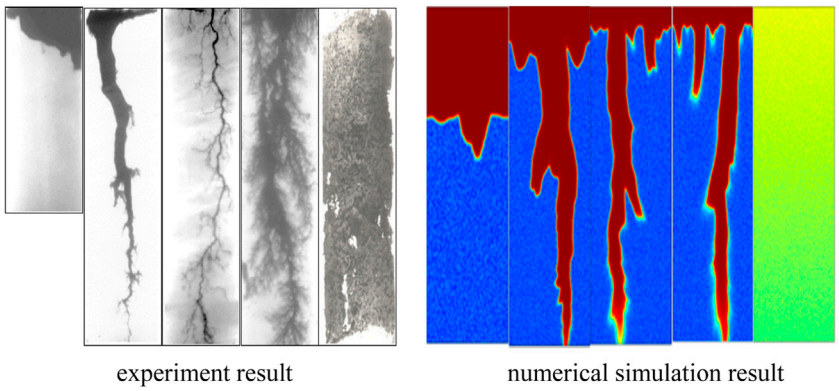

FIGURE 2 | Comparison of physical experiment and numerical simulation.

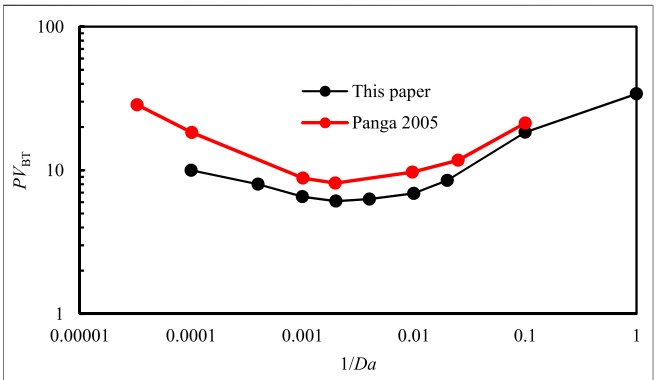

FIGURE 3 | Comparsion chart of fitting cure.

TABLE 1 | The parameters and values in numerical simulation.

Parameters	Value
ρ_L	1.1 g/ cm^3
C_0	20%
μ	1m Pa•s
D_m	3.6 e-6 cm^2/ s
k_s	0.001 cm/ s
k_0	1×10^{-3} μm^2
ϕ_0	0.2
b	1 e-3 cm
$\Delta\phi_0$	0.1
a_0	50 cm^2/cm^3
r_0	0.0001 cm
ρ_s	2.7 g/ cm^3
L	5 cm
W	2 cm
λ_T	0.1
λ_X	0.5
α_{os}	0.5
Sh_∞	3
h_T^2	0.005
Sc	252.53
N_{ac}	0.1
Φ^2	34722
η	4 e-5

The solute in the acid flows away before it reacts on the pore surface of carbonate rock. This results in the core pores being filled with acid and leads to a uniform variation in pore porosity. There is no dominant channel in the core like wormhole, and the dissolution pattern is called uniform dissolution.

As can be seen from **Eq. 1.4**, the reaction rate is determined by the properties of acid and rock, and have nothing to do with the existence of fractures in the matrix. In this case, we can draw an important conclusion: in the case of the same acid-rock reaction system, whether there are fractures in the matrix has no effect on the dissolution patterns of the fractured medium.

In addition, the comparison results of numerical simulation show that the fracture is equivalent to the main advantage channel in the matrix. An injection rate that is too high or too low will not substantially change the dissolution patterns. This is because the injected acid has already reacted with the rock completely when the acid is injected into the core at a low injection rate and there is no excess acid to flow into the fracture. In the case of high injection velocity, the dominant role of fracture in the flow is negligible and may even play a negative role. In the above situations, the existence of fractures does not affect the dissolution patterns, however, the dissolution structure will change when the injection rate of acid is between the two. This is because the flow of injected acid is controlled by fracture conductivity, and the ultimate dissolution pattern is closely related to the distribution of fracture in the fractured medium.

The Effect of Fracture Orientations

In this section, the effect of fracture orientations on the wormhole structure is studied when Damkohler number is 250. Firstly, a fracture is located in the matrix and then the dissolution structure is obtained by numerical simulation. The results of numerical simulation are compared with the results obtained in a matrix

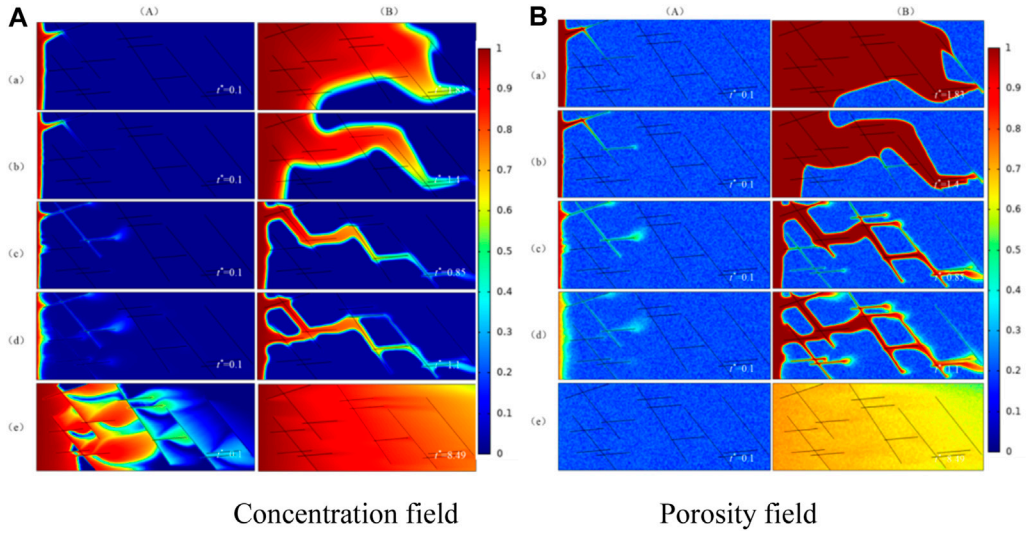

FIGURE 4 | Dissolution patterns of different Damkohler numbers. (a) Face dissolution, *Da* = 2,000; (b) Concial dissolution, *Da* = 1,000; (c) Wormhole, *Da* = 250; (d) Branching dissolution, *Da* = 100; (e) Uniform dissolution, *Da* = 1. **(A)** The initial phase; **(B)** The dissolution structure when injected acid breaks through the core.

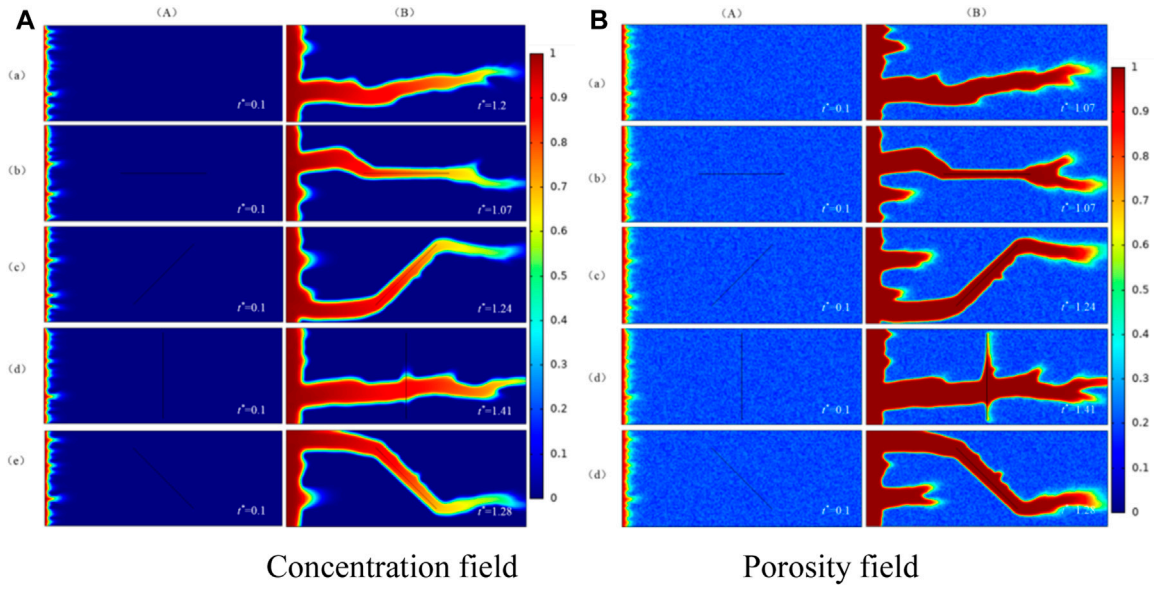

FIGURE 5 | Wormhole structure in the presence of different fracture orientations. (a) No fracture; (b) Fracture orientation is 0°; (c) Fracture orientation is 45°; (d) Fracture orientation is 90°; (e) Fracture orientation is 135°; **(A)** The initial phase; **(B)** The dissolution structure when injected acid breaks through core.

without fracture. The numerical simulation results of a porosity field and concentration field are shown in **Figure 5**.

(A) is concentration field and porosity field of numerical simulation in the initial phase and (B) is the concentration field and porosity field of numerical simulation when injected acid breaks through the core. In **Figure 5**, it can be obtained from column (A), the existence and orientations of fracture in the matrix do not affect the formation of the initial wormhole, but the direction of wormhole formation is consistent with the injected port of fractures. (B) shows that the fracture orientations influence the orientation of the wormhole and the fracture gradually becomes the part of the wormhole. The generation trend of the wormhole is random and branching in the matrix without fracture. When the orientation of fracture and injection direction of acid is at an angle of 90°, as shown in row (d) of **Figure 5**, the formation direction of the wormhole is not controlled by the orientation of the fracture. Instead, it is consistent with the direction of injected acid. Different from

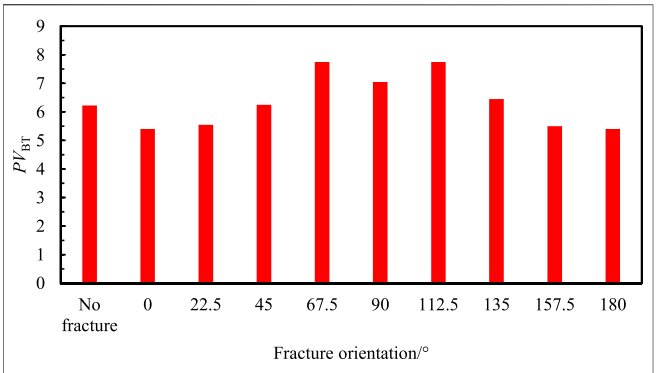

FIGURE 6 | The breakthrough volume of injected acid at different fracture orientations.

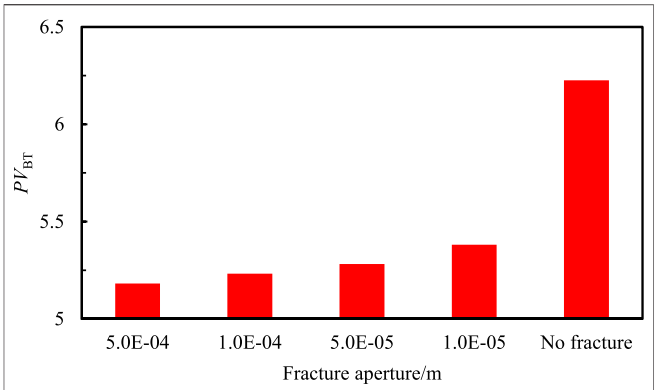

FIGURE 8 | Effect of the fracture aperture on the breakthrough volume of injected acid.

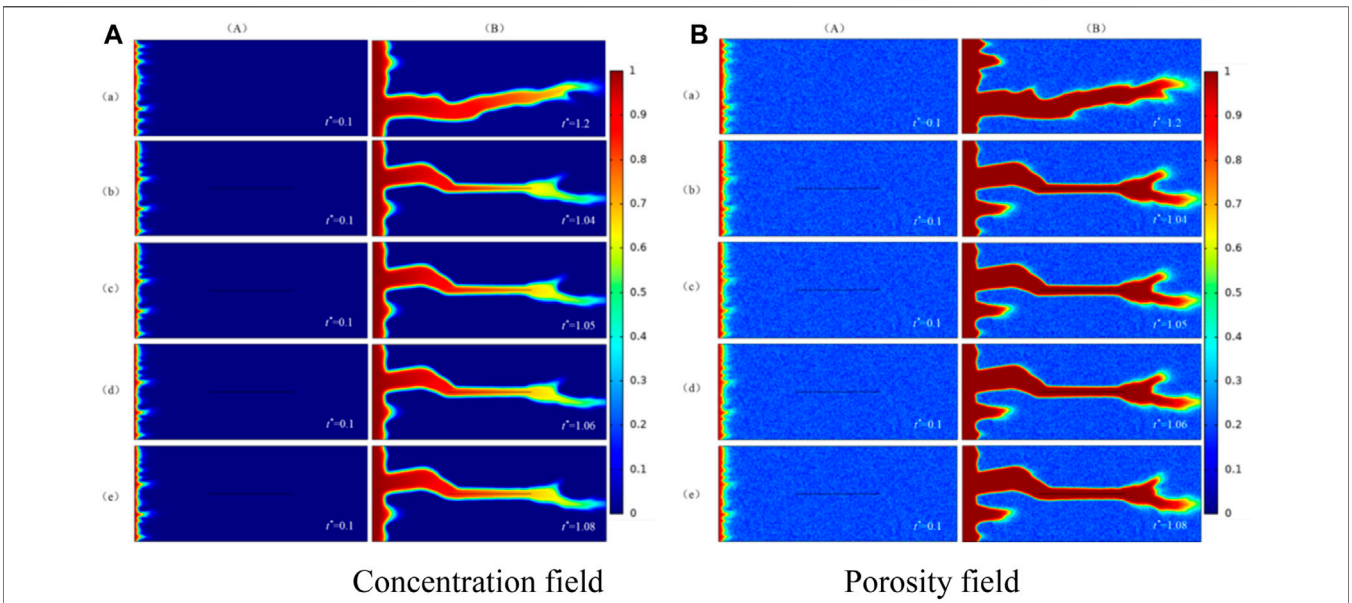

FIGURE 7 | Wormhole structure in the presence of different fracture aperture. (a) No fracture; (b) *b* = 5e-4 m; (c) *b* = 1e-4 m; (d) *b* = 5e-5 m; (e) *b* = 1e-5 m; **(A)** The initial phase; **(B)** The dissolution structure when injected acid breaks through core.

the wormhole in the matrix without fractures, the wormhole radius has increased and the direction of the wormhole has also changed in the fractured medium. This shows that the influence mechanism of fracture orientation on the formation direction of the wormhole is like to a high permeability zone.

The breakthrough volume of injected acid in a matrix with different fracture orientations is drawn in **Figure 6**. It shows that when the orientation of fracture is consistent with the injection direction of acid or the orientation of fracture is similar with horizontal direction, the breakthrough volume of injected acid is smaller than the breakthrough volume in the matrix without fracture, the branching randomness of the wormhole is also getting weaker. When the direction of fracture is bigger than a certain angle, the breakthrough volume of injected acid becomes larger, and so does the consumption of acid. At this time, the effect of fracture inhibits the flow of acid in the fractured medium. The waiting time in the fractured medium becomes larger and then consumes more acid. When the direction of fracture is between 67.5° and 112.5°, the breakthrough volume of injected acid increases first and then decreases. It is because the conductivity of fracture has a smaller impact on the development and formation of the wormhole. When the direction of fracture is bigger than 90°, the breakthrough volume of acid is similar to volume when the angle is less than 90°, the slight difference is due to the heterogeneity of the core.

In this example, the breakthrough volume of injected acid is largest in the core with a single fracture and the orientation of fracture is 67.5. The consumption of injected acid is even larger than the matrix without fracture.

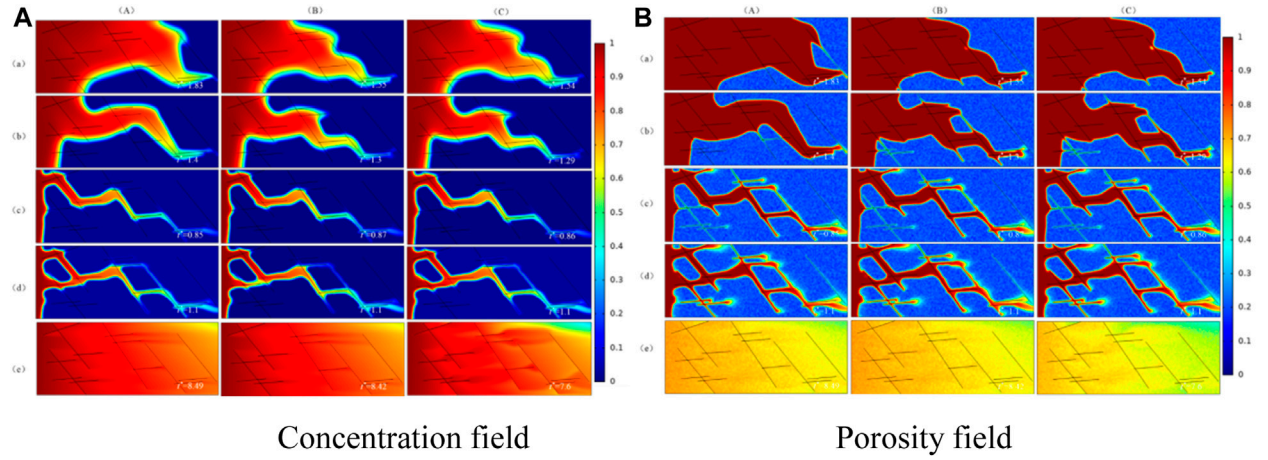

FIGURE 9 | Dissolution patterns of homogeneity of initial fracture aperture, heterogeneity of initial fracture aperture, and dynamic change of fracture aperture in fractured medium. (a) Face dissolution, *Da* = 2000; (b) Concial dissolution, *Da* = 1,000; (c) Wormhole, *Da* = 250; (d) Branch dissolution, *Da* = 100; (e) Uniform dissolution, *Da* = 1. **(A)** The initial phase; **(B)** The dissolution structure when injected acid breaks through core.

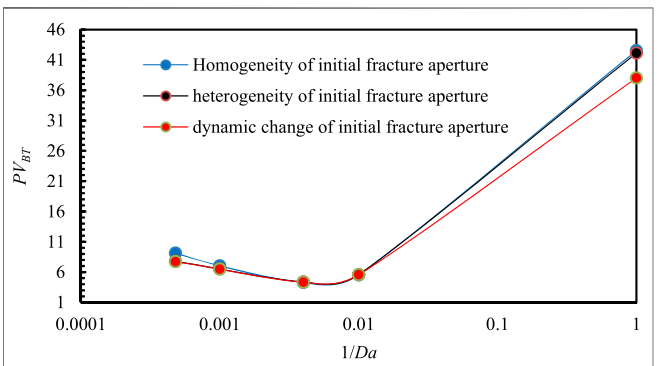

FIGURE 10 | Influence of homogeneity of initial fracture aperture, of the heterogeneity of initial fracture aperture, and the changing of fracture aperture on the breakthrough volume of injected acid.

The Effect of Fracture Aperture

In this section, the effect of fracture aperture on wormhole structure is studied when Damkohler number is 250. This model contains a fracture. The numerical simulation results are compared with the matrix without fracture, and the result of the numerical simulation is shown in **Figure 7**.

(A) is concentration field and porosity field of numerical simulation in the initial phase and (B) is the concentration field and porosity field of numerical simulation when injected acid breaks through the core in **Figure 7**. In column (A) of the concentration field and porosity field in **Figure 7**, whether the fracture exists or not and no matter how the fracture aperture changes, it does not affect the initial wormhole structure.

From column (B), it can be concluded that fracture aperture don't affect the formation trend of the wormhole and the fracture gradually becomes a part of the wormhole. The fracture aperture has no significant effect on the dissolution structure. The relationship between the breakthrough volume of injected acid and the fracture aperture is plotted as a columnar graph shown in **Figure 8**.

Figure 8 shows that the breakthrough volume of injected acid is the smallest when the fracture aperture is largest. In the mathematical model of this paper, the calculation equation of permeability is obtained by the cubic law: the larger the fracture aperture and the higher the fracture permeability, the conductivity of fracture will become stronger. This means that the fracture has a stronger impact on the formation of the wormhole. As a result, the breakthrough volume of injected acid will become smaller and the consumption of acid will become less. In the same way, the smaller the fracture aperture, the lower the fracture permeability. The efforts of fracture on the formation of the wormhole are weaker and the breakthrough volume and consumption of injected acid are less than before. When the fracture aperture equals 5e-5m, the breakthrough volume of injected acid is the smallest in the study.

The Effect of Heterogeneity of Initial Fracture Aperture and Dynamic Variation of Fracture Aperture

The numerical simulation results are shown in **Figure 9**. With the increase of injected acid and the Damköhler number, there are five different dissolution patterns in fractured medium: face dissolution, conical dissolution, wormhole, branch dissolution, uniform dissolution.

The breakthrough volume curve of injected acid is plotted in **Figure 10**. It depicts the effect of homogeneity of the initial fracture aperture, the heterogeneity of initial fracture aperture, and the dynamic change of fracture aperture to the breakthrough volume of injected acid.

As shown in **Figure 10**, The dissolution patterns are unchangeable regardless of whether the initial fracture aperture is homogeneous, heterogeneous or fracture aperture is dynamic change with the acid etching fracture wall, the optimal injection rate of acid solution will not change when *Da* = 250.

CONCLUSION

A mathematical model of reactive flow in a fractured medium based on the two-scale model and discrete fracture model is built in this paper. This paper uses studies by predecessors, including physical experiments and numerical simulation experiments, to verify the correctness of the theoretical model of reactive flow in a matrix.

The discrete fracture model is solved numerically under the condition of two-dimensional linear flow. There are five different kinds of dissolution patterns according to the velocity of injected acid: face dissolution, conical dissolution, wormhole, branch dissolution, and uniform dissolution.

In the fractured medium, the existence of fracture does not affect the dissolution patterns of the matrix. The homogeneity and heterogeneity of fracture aperture and dynamic change of fracture aperture do not affect the optimal injection rate of injected acid.

DATA AVAILABILITY STATEMENT

The original contributions presented in the study are included in the article/**Supplementary Material**, further inquiries can be directed to the corresponding authors.

AUTHOR CONTRIBUTIONS

ZX: Conceptuation, Methodology, Software,Writing-Draft preparation ZF:Data curation, Validation, Writing-Reviewing and Editing HQ:Investigation, software. LR:Funding acquisition. SB:supervision. XC:Investigation.

FUNDING

This study received funding from the National Nature Science Foundation of China (52074336) and the Major Science and Technology Projects of China National Petroleum Corporation (ZD2019-183-008).

SUPPLEMENTARY MATERIAL

The Supplementary Material for this article can be found online at: https://www.frontiersin.org/articles/10.3389/feart.2021.765139/full#supplementary-material

REFERENCES

Andersen, P. Ø., and Evje, S. (2016). A Model for Reactive Flow in Fractured Porous media. *Chem. Eng. Sci.* 145, 196–213. doi:10.1016/j.ces.2016.02.008

Bazin, B. (2001). From Matrix Acidizing to Acid Fracturing: A Laboratory Evaluation of Acid/Rock Interactions. *SPE Prod. Facil.* 16 (01), 22–29. doi:10.2118/66566-pa

Bazin, B., Roque, C., and Bouteca, M. (1995). "A Laboratory Evaluation of Acid Propagation in Relation to Acid Fracturing: Results and Interpretation[A]," in Proceedings of the SPE European Formation Damage Conference[C], Hague, Netherlands, May 15–16, 1995 (Society of Petroleum Engineers).

Budek, A., and Szymczak, P. (2012). Network Models of Dissolution of Porous Media. *Phys. Rev. E Stat. Nonlin Soft Matter Phys.* 86 (5), 056318. doi:10.1103/PhysRevE.86.056318

Catherine, N. (2004). Investigation of Porosity and Permeability Effects from Microstructure Changes during limestone Dissolution[J]. *Geophys. Res. Lett.* 31 (24). doi:10.1029/2004GL021572

Chen, G., and Ying, H. (2006). An Analysis of Acidizing Reaction Mechanism of Carbonates[J]. *Nat. Gas Industry* 26 (1), 104–108.

Daccord, G., Touboul, E., and Lenormand, R. (1989). Carbonate Acidizing: Toward a Quantitative Model of the Wormholing Phenomenon. *Spe Prod. Eng.* 4 (01), 63–68. doi:10.2118/16887-pa

Fredd, C. N., and Fogler, H. S. (1999). Optimum Conditions for Wormhole Formation in Carbonate Porous Media: Influence of Transport and Reaction. *SPE J.* 4 (03), 196–205. doi:10.2118/56995-pa

Fredd, C., Tjia, R., and Fogler, H. (1997). "The Existence of an Optimum Damkohler Number for Matrix Stimulation of Carbonate Formations[A]," in Proceedings of the SPE European Formation Damage Conference[C], Hague, Netherlands, June 2–3, 1997 (OnePetro).

Frick, T., Mostofizadeh, B., and Economides, M. (1994). "Analysis of Radial Core Experiments for Hydrochloric Acid Interaction with Limestones[A]," in Proceedings of the SPE Formation Damage Control Symposium[C] Lafayette, Louisiana, February 7–10, 1994 (Society of Petroleum Engineers).

Ghommem, M., Zhao, W., Dyer, S., Qiu, X., and Brady, D. (2015). Carbonate Acidizing: Modeling, Analysis, and Characterization of Wormhole Formation and Propagation. *J. Pet. Sci. Eng.* 131, 18–33. doi:10.1016/j.petrol.2015.04.021

Golfier, F., Bazin, B., and Zarcone, C. (2001). Acidizing Carbonate Reservoirs: Numerical Modelling of Wormhole Propagation and Comparison to Experiments[C]. SPE European Formation Damage Conference, Hague, May 21–22, 2001. doi:10.2118/68922-MS

He, C. (2009). Study on Acidizing Wormhole of Tight Carbonate Reservoir[J]. *Fault-Block Oil & Gas Field*.

Hill, A. D., Zhu, D., and Wang, Y. (2009). The Effect of Wormholing on the Fluid Loss Coefficient in Acid Fracturing. *SPE Prod. Facil.* 10 (04), 257–264. doi:10.2118/27403-pa

Hoefner, M. L., and Fogler, H. S. (1989). Fluid-Velocity and Reaction-Rate Effects During Carbonate Acidizing: Application of Network Model. *Spe Prod. Eng.* 4 (01), 56–62. doi:10.2118/15573-pa

Hoefner, M. L., and Fogler, H. S. (1988). Pore Evolution and Channel Formation during Flow and Reaction in Porous media. *Aiche J.* 34 (1), 45–54. doi:10.1002/aic.690340107

Kalia, N. (2008). Modeling and Analysis of Reactive Dissolution of Carbonate Rocks[J]. *Dissertations & Theses - Gradworks* 8 (2), 67–151.

Kalia, N., and Balakotaiah, V. (2009). Effect of Medium Heterogeneities on Reactive Dissolution of Carbonates. *Chem. Eng. Sci.* 64 (2), 376–390. doi:10.1016/j.ces.2008.10.026

Kim, S., and Santamarina, J. C. (2015). Reactive Fluid Flow in CO 2 Storage Reservoirs: A 2-D Pore Network Model Study. *Greenhouse Gas Sci. Technol.* 5 (4), 462–473. doi:10.1002/ghg.1487

Liu, P., Li, J., and Sun, S. (2020). Numerical Investigation of Carbonate Acidizing with Gelled Acid Using a Coupled Thermal-Hydrologic-Chemical Model[J]. *Int. J. Therm. Sci.* 160 (106700), 23955–26900. doi:10.1016/j.ijthermalsci.2020.106700

Liu, P., Yao, J., Couples, G. D., Huang, Z., Sun, H., and Ma, J. (2017). Numerical Modelling and Analysis of Reactive Flow and Wormhole Formation in Fractured Carbonate Rocks. *Chem. Eng. Sci.* 172, 143–157. doi:10.1016/j.ces.2017.06.027

Liu, X., Ormond, A., and Bartko, K. (1997). A Geochemical Reaction-Transport Simulator for Matrix Acidizing Analysis and Design[J]. *J. Pet. Sci. Eng.* 17 (1-2), 181–196. doi:10.1016/s0920-4105(96)00064-2

Maheshwari, P., Ratnakar, R. R., Kalia, N., and Balakotaiah, V. (2013). 3-D Simulation and Analysis of Reactive Dissolution and Wormhole Formation in Carbonate Rocks. *Chem. Eng. Sci.* 90, 258–274. doi:10.1016/j.ces.2012.12.032

Nierode, D. E., and Williams, B. B. (1971). Characteristics of Acid Reaction in Limestone Formations. *Soc. Pet. Eng. J.* 11 (04), 406–418. doi:10.2118/3101-pa

Panga, M. K. R., Ziauddin, M., and Balakotaiah, V. (2005). Two-Scale Continuum Model for Simulation of Wormholes in Carbonate Acidization. *Aiche J.* 51 (12), 3231–3248. doi:10.1002/aic.10574

Panga, M., Ziauddin, M., and Ba Lakotaiah, V. (2010). Two-Scale Continuum Model for Simulation of Wormholes in Carbonate Acidization[J]. *AIChE J.* 51 (12), 3231–3248. doi:10.1002/aic.10574

Steefel, C. I., and Lichtner, P. C. (1998). Multicomponent Reactive Transport in Discrete Fractures: I. Controls on Reaction Front Geometry[J]. *J. Hydrol.* 209 (1-4), 186–199. doi:10.1016/s0022-1694(98)00146-2

Wang, Y., Hill, A., and Schechter, R. (1993). "The Optimum Injection Rate for Matrix Acidizing of Carbonate Formations[A]," in Proceedings of the SPE Annual Technical Conference and Exhibition[C], Houston, Texas, October 3–6, 1993 (Society of Petroleum Engineers).

Yang, X., and Pan, Q. (2000). Acidizing Fluid Leakoff Mechanism Studying on Dolomite Reservoir[J]. *Drilling Prod. Technol.*

Zhang, H., Zou, H., and Liu, S. (2017). Dual Fractal Model of Carbonate Acidizing Wormholes[J]. *Nat. Gas Geosci.* 28 (3), 466–472. doi:10.11764/j.issn.1672-1926.2017.01.010

Ziauddin, M. E., and Bize, E. (2007). "The Effect of Pore Scale Heterogeneities on Carbonate Stimulation Treatments[A]," in Proceedings of the SPE Middle East Oil and Gas Show and Conference[C], Kingdom of Bahrain, March 11–14, 2007 (Society of Petroleum Engineers).

Conflict of Interest: Authors ZX, LR, and SB were employed by the company Xinjiang Oilfield Company, PetroChina. Author ZF was employed by the company Shengli Oilfield Company, SINOPEC.

The remaining authors declare that the research was conducted in the absence of any commercial or financial relationships that could be construed as a potential conflict of interest.

frontiers in Earth Science

BRIEF RESEARCH REPORT
published: 29 November 2021
doi: 10.3389/feart.2021.767738

Study on Production Optimization Method of Fractured Reservoir Based on Connectivity Model

Dajian Li[1†], Zhenfeng Zhao[1], Bai Wang[1], Haitao Yang[1], Wenhao Cui[1], Jiayu Ruan[2†], Yuxin Zhang[2] and Fan Wang[2]*

[1]Oil and Gas Technology Research Institute, PetroChina Changqing Oilfield Company, Xi'an, China, [2]School of Petroleum Engineering, Yangtze University, Wuhan, China

Due to the extensive development of fractures and serious heterogeneity in fractured reservoirs, it is difficult for the traditional numerical simulation method to invert its geology, which greatly limits the efficiency and accuracy of simulation and cannot realize the real-time optimization of production scheme. The connectivity model can only consider the two characteristic parameters of conductivity and connectivity volume, which does not involve complex and rigorous geological modeling. It can quickly and accurately reflect the state of the real reservoir, greatly reducing the simulation time, and is suitable for real-time production performance prediction of the reservoir. Due to the large difference in conductivity of fractured reservoirs, the difficulty of fitting increases. In this paper, the connectivity model is first applied to fractured reservoirs to realize the production dynamic simulation of fractured reservoirs. The optimization principle is used to optimize the injection-production scheme with the economic net present value as the objective function. In order to verify the method, the connectivity model is applied to Mu 30 of Changqing Oilfield in this paper. The results show that this method can effectively reflect the real production situation of the oilfield and the connectivity of the reservoir, and the simulation time is relatively fast. After optimization, the cumulative oil production of the reservoir increases by 8.1%, the cumulative water injection decreases by 2.3%, and the rising rate of water cut decreases by 58.8%, indicating that the connectivity model can realize the real-time production optimization of the reservoir.

Keywords: fractured reservoir, connectivity model, optimization, horizontal well, gradient-free algorithm

OPEN ACCESS

Edited by:
Wenhui Song,
China University of Petroleum (Huadong), China

Reviewed by:
Shiyuan Zhan,
Chengdu University of Technology, China
Qi Zhang,
China University of Geosciences Wuhan, China

****Correspondence:***
Jiayu Ruan
spritelemontea@163.com

[†]These authors contributed to the work equally and should be regarded as co-first authors

Specialty section:
This article was submitted to Economic Geology, a section of the journal Frontiers in Earth Science

Received: *31 August 2021*
Accepted: *06 October 2021*
Published: *29 November 2021*

Citation:
Li D, Zhao Z, Wang B, Yang H, Cui W, Ruan J, Zhang Y and Wang F (2021) Study on Production Optimization Method of Fractured Reservoir Based on Connectivity Model. Front. Earth Sci. 9:767738. doi: 10.3389/feart.2021.767738

INTRODUCTION

With the progress of global, low permeability reservoir exploration and fracturing technology, the development of fractured reservoirs has become more and more common. The BP2030 World Energy Outlook report shows the world's tight oil reservoir development prospects. The tight oil resources in North America are about 100×10^8 t, and those in Asia-Pacific region are about 90×10^8 t. Almost half of the current increase in global oil production is expected to come from tight oil reservoirs by 2030, which will meet 5–9% of global demand (Li, 2013). Most of the exploitation of tight oil needs fracturing, so it can be said that fractured reservoirs are the main theme of future reservoir exploitation.

A fractured reservoir is a reservoir where fractures have an important impact on fluid flow or effective permeability of porous media (Xu, 2017). It is a manifestation of reservoir permeability and

porosity heterogeneity. Fractured reservoirs are more complex than ordinary sandstone reservoirs due to the extensive development of fractures and serious heterogeneity. Since the large-scale development of fractured reservoirs in 1970s, the development of most fractured reservoirs has been unsatisfactory. Even if fractured reservoirs are successfully economically exploited, the recovery factor is generally only 13–15%, which remains to be improved. One of the reasons for this situation is the lack of understanding of fracture identification, distribution law and fluid flow dynamics in fractures (Xu et al., 2021).

Fracture is the main channel of oil and gas seepage in fractured reservoirs, and its location distribution and characteristics are crucial to the productivity of oil and gas reservoirs (Sheng et al., 2019). Therefore, it is of great significance to accurately simulate the fracture seepage characteristics of oil and gas reservoirs. Interwell connectivity research is an important tool for reservoir description and dynamic analysis (Liu et al., 2003; Yang, 2004; Tang et al., 2008). Common connectivity methods, such as tracer, well test, and interwell micro seismic, are complex in implementation, long in interpretation cycle, and affect normal production. Therefore, the application range is limited, and it is difficult to meet the needs of rapid understanding of reservoirs (Liao et al., 2002; Yang et al., 2002; Du and Yang, 2007). The reservoir is a dynamic system. The fluctuation of liquid production caused by the change of injection volume is the characteristic reflection of the connection between oil and water wells, and the fluctuation range of liquid production is also related to the degree of connection (Zhao et al., 2010). Therefore, using injection-production data to study interwell connectivity becomes a very important method.

On the connectivity between wells, scholars have done much research, Yousef et al. (2006) based on the principle of hydropower similarity and material balance equation, introduced capacitance and reactance two parameters, established a data-driven model based on injection well production data--capacitance resistance model (CRM), using fitting and inversion algorithm, inversion of well connectivity. Subsequently, in order to consider the effects of well logging, shut-in, capillary force and other functions, and accelerate the calculation speed of the model, many scholars have improved the CRM (Kaviani et al., 2008; Sayarpour, 2008; Sayarpour et al., 2010; Nguyen et al., 2011; Salazar-Bustamante et al., 2012). Because CRM is difficult to consider the physical properties of reservoir and fluid in the process of seepage, the long-term prediction effect is poor. Therefore, Gherebati et al. (2016) simplified the reservoir into a series of connected networks of injection and production wells by using well location information and production data of injection and production wells. According to the principle of seepage mechanics and material balance equation, the connectivity conductivity between wells was calculated by inversion of production data of injection and production, and then a data-driven reservoir connected network model was formed. All kinds of data-driven models proposed by the above scholars have basically realized the prediction of production performance and the evaluation of interwell connectivity, but there are some shortcomings, such as the model is too ideal, the consideration factors are less, the inversion parameters are lack of clear geological significance, the oil-water two-phase data cannot be predicted and fitted, the water content cannot be predicted, and the volume of dominant channels cannot be obtained. In view of the shortcomings of the above methods, Hui et al. (2015) first created a Physics-Based Data-Driven Model with clear physical meaning, which was named INSIM (Interwell Numerical Simulation Model). The data-driven model uses parameters such as interwell conductivity and connected volume to reflect the entire reservoir. The reservoir is simplified into a series of connected units. Taking the connected unit as the object, the material balance equation can be established and the pressure can be calculated. At the same time, the shock wave theory is introduced to track the saturation front, so as to obtain the dynamic data such as injection-production well pressure and production, and realize the rapid simulation and prediction of oil and water wells. This method is the first to achieve the goal of production prediction and optimization decision of water flooding reservoir using actual production data. The method uses historical fitting and optimization algorithm to solve the model, inverses the conductivity and connectivity volume between wells, and identifies connectivity. It quantitatively reveals the dominant connectivity direction, water injection splitting effect, water intrusion, etc. The interwell connectivity method only considers two characteristic parameters of conductivity and connectivity volume, which does not involve complex and rigorous geological modeling. It can quickly and accurately reflect the state of the real reservoir, greatly shortening the simulation time, and is suitable for real-time production performance prediction of the reservoir.

At present, the INSIM model has been widely used in reservoirs such as single medium, and it has not been applied to fractured reservoirs. In this paper, the INSIM model is first applied to fractured reservoirs to realize the production dynamic simulation of fractured reservoirs, and the injection-production scheme is optimized by using the optimization principle with the economic net present value as the objective function. In order to show that the method is suitable for fractured reservoirs, the method is applied to Mu 30 of Changqing Oilfield with prominent fracture development. The results show that the method can effectively reflect the real production and connectivity of the reservoir, and the simulation time is relatively rapid.

RESERVOIR CONDITION

The development layer of Mu 30 is Chang 8. The geology of Chang 8 is dominated by sandy debris flow deposits, followed by semi-deep lake and deep lake mud microfacies. The sand body connectivity is good, and the sand body is plane distribution. The natural fractures in the reservior are prominent, mostly in the northeast-southwest direction. Sand body thickness is 13.4 m, average porosity is 10.10%, average permeability is 0.79×10^{-3} μm^2, average surface crude oil viscosity is 5.59 mPa s, average reservoir thickness is 10.9 m, original formation

pressure is 19.89 Mpa, formation pressure maintains 79.4%. Mu 30 has been put into production since January 2010. As of March 2021, the reservoir has been put into production for 4,108 days. At present, there are 143 wells (81 horizontal wells and 62 vertical wells) and 106 injection wells in Mu 30. The daily liquid production level of the reservoir is 537 t (440 t for horizontal wells), the daily oil production level is 263 t (217 t for horizontal wells), the comprehensive water cut is 51.0% (50.6% for horizontal wells), the recovery degree is 2.41%, the oil-bearing area is 74 km^2, the geological reserves are 2,965 × 10^4 t, the recoverable reserves are 542.19 × 10^4 t, and the calibration recovery rate is 18.3%. The development of five-spot well pattern and seven-spot well pattern is given priority. The well spacing is 600 × 150 m. There are 30 five-spot well pattern, 755 m horizontal section, 23 seven-spot well pattern, 850 m horizontal section, 16 seven-spot to five-spot, 802 m horizontal section, 12 irregular well pattern and 1166 m horizontal section. Fractures in Mu30 are prominent. At present, there is no scientific injection-production scheme to guide mining, resulting in a rapid increase in water content and low recovery in this reservoir. Although the traditional numerical simulation can carry out geological inversion and simulation, and then get a more suitable injection and production scheme, the production cycle of Mu 30 is too long, the traditional numerical simulation fitting is difficult, the efficiency is too low, and it cannot be quickly and accurately optimized in real time.

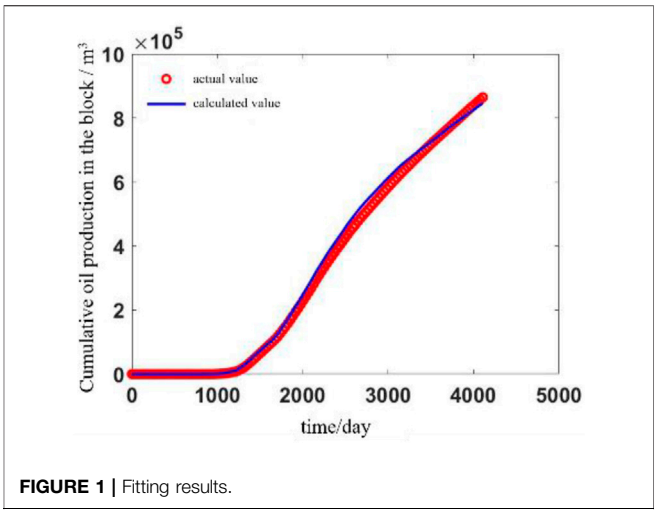

FIGURE 1 | Fitting results.

NUMERICAL SIMULATION

Overview of INSIM Method

The interwell connectivity model takes well points as the basic unit, and simplifies the complex geological description between well points into two important characteristic parameters: the interwell conductivity T_{ij} and the connected volume V_{pi}, The interwell connectivity model takes well points as the basic unit, and simplifies the complex geological description between well points into two important characteristic parameters: the interwell conductivity T_{ij} and the connected volume V_{pi}. The former represents the seepage velocity under unit pressure difference, which can better reflect the average seepage capacity and dominant conduction direction between wells. The latter represents the material basis of the connected unit, which can reflect the control range and volume of water flooding between wells.

Setting i well as production well and j well as injection well, taking injection-production unit composed of i well and j well as reference, considering only oil-water two-phase flow and ignoring the influence of temperature, regardless of gravity and viscosity, the material balance equation is established as follows (Zhao et al., 2016):

$$\sum_{j=1}^{N_w} T_{ij}\left(p_j^n - p_i^n\right) + q_i^n = C_t V_{pi} \frac{p_i^n - p_i^{n-1}}{\Delta t} \tag{1}$$

Where i, j represents well number; N_w is the total number of wells; T_{ij} represents the average conductivity of wells i and j, m^3/(d·MPa); n is time step; p_i^n and p_j^n represent the average reservoir pressure at time n in well i and well j, respectively, MPa; q_i^n is the flow rate of the well i at the time n, water injection is positive, oil production is negative, m^3/d; C_t is the reservoir comprehensive compression coefficient, MPa^{-1}; Δt is time interval, d; V_{pi} is the connected volume of the drainage area of the well i, m^3.

The pressure of the above equation is solved to obtain the bottom hole flow pressure of each node. On this basis, the saturation is tracked, and the saturation equation is obtained as follows:

$$\frac{df_{w,j,i}^n}{dS_{w,j,i}^n} = \min\left\{\frac{df_{w,j}^p}{dS_{w,j}^p}\frac{Q_{pv,i,j}^p}{Q_{pv,i,j}^n}, \frac{df_{w,i}^n}{dS_{w,i}^n} + \frac{1}{Q_{pv,j,i}^n}\right\} \tag{2}$$

For multiple perforation points of the horizontal well, the pressure loss in the horizontal section is ignored in flow simulation, and the horizontal well is represent as multiple connected virtual well points. Taking into the original material balance equation can be solved to obtain oil production rate, water content and other related production index function.

Connectivity Model of Mu 30

When establishing the model, the initial value of conductivity and connectivity volume is assigned based on the physical properties of each well point in the reservoir, so that the initial connectivity model is consistent with the reservoir. Since there are too many perforation points in horizontal wells in the reservoir, in order to facilitate the analysis and judgment of the established connectivity model, the perforation points of each horizontal well are simplified into four. After simplification, the number of summary points in the reservoir is 492. In order to accurately reflect the actual situation of the reservoir, it is necessary to conduct historical fitting. The oil production of a single well and reservoir is used as the fitting index, and the conductivity and connected volume of the connectivity model are automatically, historically fitted. The reservoir fitting results are shown in

FIGURE 2 | Inversion of connected parameter.

Figure 1, and the inversion results of characteristic parameters are shown in **Figure 2**.

The fitting results show that the overall fitting rate reaches more than 80%, and the oil-water dynamic fitting results of the reservoir and single well are relatively accurate, which can better reflect the real geological conditions of the reservoir. It is worth noting that the automatic historical fitting stage of the model takes about 48 hours, which is greatly shortened compared with the traditional numerical simulation software ECLIPSE fitting 7–14 days. It can be seen that the model has good application effect for actual reservoirs and can provide help for real-time production optimization strategy formulation.

RESEARCH ON PRODUCTION OPTIMIZATION OF MU 30

Automatic Optimization Method

Based on the fitted reservoir model, the production optimization control model is established considering various constraints, so as to realize the dynamic optimization of injection-production measures. The production optimization of reservoirs usually uses the economic net present value NPV as the optimization objective function to establish a mathematical model. The three-dimensional three-phase reservoir simulator is used to describe the reservoir development and production system, and the economic net present value (NPV) during the production period is used as the performance index function to evaluate the economic benefits. The expression is:

$$J(u) = \sum_{n=1}^{L}\left[\sum_{j=1}^{N_P}\left(r_o q_{o,j}^n - r_w q_{w,j}^n\right) - \sum_{i=1}^{N_I} r_{wi} q_{wi,i}^n\right]\frac{\Delta t^n}{(1+b)^{t^n}} \quad (3)$$

Where J is the performance index function to be optimized; L is control steps; N_P is the total number of production wells; N_I is the total number of water injection wells; r_o is crude oil price, \$/STB; r_w is cost price for water production, \$/STB; r_{wi} is the water injection price, \$/STB; $q_{o,j}^n$ is the average oil production rate at time n of the production well j, STB/d; $q_{w,j}^n$ is the average water production rate at time n of the production well j, STB/d; $q_{wi,i}^n$ is the average water injection rate at time n of the injection well i, STB/d; b is the average annual interest rate, %; Δt^n is the time step of the simulation calculation at time n, d; t^n is the cumulative calculation time at time n, year; u is theN_u-dimensional control variable vector.

In actual production, it is necessary to implement certain restrictions on the operation of wells, that is, the control variables need to meet certain constraints. The constraint conditions are mainly linear or nonlinear, including equality, inequality and boundary constraints. Equation constraints such as reservoir overall liquid production or injection volume is a certain value. Inequality constraints usually require liquid production and injection volume of the reservoir to be limited by the working capacity of oilfield equipment.

The constraint conditions can be expressed as follows:

$$e_i(u, y, m) = 0, \quad i = 1, 2, \cdots, n_e \quad (4\text{-}1)$$

$$c_j(u, y, m) \le 0, \quad j = 1, 2, \cdots, n_c \quad (4\text{-}2)$$

$$u_l^{low} \le u_l \le u_l^{up}, \quad l = 1, 2, \cdots, N_u \quad (4\text{-}3)$$

Where u_l^{low} and u_l^{up} represent the upper and lower boundaries of the l control variable u_l; $e_i(u, y, m) = 0$ and $c_j(u, y, m) < 0$ are equality constraint conditions and inequality constraint conditions, respectively. It can be seen that for the reservoir production optimization problem, it is to obtain the maximum value of the objective function J and the corresponding optimal control variable u^* under the condition that the control variables meet various constraints.

After the optimization model is established, it is necessary to solve the model. Since the model has many dimensions and

TABLE 1 | Optimizing production measures.

	MP91 (m^3)	M110-1 (m^3)	M110-2 (m^3)	M108-2 (m^3)	M108-1 (m^3)
2021/5/1	7.77	5.00	11.00	6.00	12.00
2021/5/31	7.34	9.00	16.00	7.00	14.00
2021/6/30	7.29	9.00	14.00	6.00	19.00
2021/7/30	7.16	12.00	14.00	6.00	21.00
2021/8/29	7.55	11.00	13.00	7.00	17.00
2021/9/28	7.45	8.00	9.00	6.00	14.00
2021/10/28	7.85	7.00	8.00	7.00	15.00
2021/11/27	8.19	6.00	6.00	9.00	11.00
2021/12/27	7.48	6.00	6.00	9.00	16.00
2022/1/26	7.65	6.00	7.00	8.00	17.00
2022/2/25	7.53	10.00	10.00	8.00	10.00
2022/3/27	6.69	9.00	10.00	7.00	7.00

constraints, and the optimization gradient is difficult to calculate, the gradient-free random disturbance algorithm is selected for solving.

The gradient-free stochastic perturbation algorithm, also known as SPSA (Simultaneous Perturbation Stochastic Approximation), is a perturbation method similar to the finite difference method, which was first proposed by Spall et al., in 1992. The characteristic of SPSA algorithm is that random variables are used to disturb all control variables at the same time in an iterative step, so that the computational cost of gradient solution is greatly reduced. The SPSA algorithm can quickly find the local optimal solution of the complex model, which is suitable for solving the problems that the model has, its many dimensions, many constraints and the when the optimization gradient is difficult to calculate.

Optimization Results of Mu 30

As can be seen from the formula **(3)**, if $r_o = 1$, $r_w = 0$, $b = 0$, $r_{wi} = 0$, the objective function is changed from economic net present value to cumulative oil production. In this way, we can take the improvement of cumulative oil production as the optimization objective and the single well water injection rate as the optimization object. The final water injection and liquid production simulation for 1 year are used as the original scheme, and the automatic algorithm is used to optimize the scheme with 30 days as the time step. Finally, the production optimization scheme obtained. **Table 1** shows the injection-production optimization scheme of MP 91 well group in Mu 30. In order to ensure the feasibility of field implementation, the optimization constraint conditions limit the upper and lower boundaries of oil well liquid production and water injection, so that the liquid production and water injection fluctuate by 20% in the current system. However, the current liquid production of the oil well is very small, so the liquid production of the oil well does not change much.

The cumulative oil production in the following year increased by 8.5% from 59,800 to 64,900 m^3. The cumulative water injection decreased by 3.3% from 4.181 to 4.043 million m^3. It can be seen from **Figure 3** that the water content in the historical stage of the reservoir has been

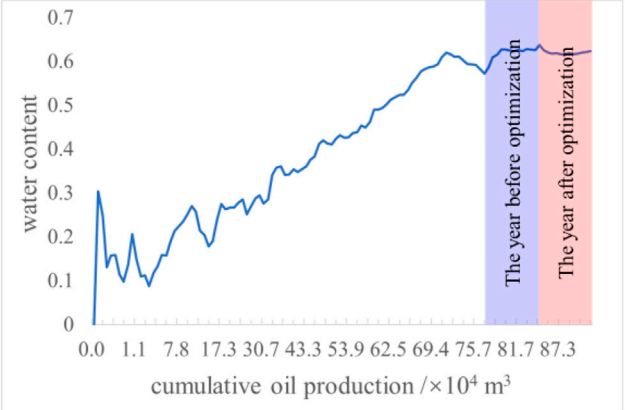

FIGURE 3 | Optimization results.

increasing. The water content in the last year has increased by 0.46%. After 1 year of optimization, the water content began to decline, and the water content decreased by 0.13%. Compared with the previous year of optimization, the water content increased by 58.8%.

CONCLUSION

1) The INSIM model is used to simulate and match the history of fractured reservoirs. The simulation results show that the model can effectively reflect the real production and connectivity of fractured reservoirs, and the simulation time is relatively fast, which can lay the foundation for real-time production optimization of reservoirs.
2) According to the optimization principle, the economic net present value NPV is used as the optimization objective function, and the upper and lower limits of single well production or water injection are used as the constraint conditions to establish the optimization mathematical model. The model is solved by the gradient-free stochastic disturbance automatic optimization algorithm. The results show that the cumulative oil production of the optimized reservoir increases by 8.1%, the cumulative

water injection decreases by 2.3%, and the water cut increase rate decreases by 58.8%. The gradient-free intelligent optimization method based on interwell connectivity used in this paper can realize the real-time production optimization of fractured reservoirs.

DATA AVAILABILITY STATEMENT

The original contributions presented in the study are included in the article/Supplementary Material, further inquiries can be directed to the corresponding author.

AUTHOR CONTRIBUTIONS

DL: Conceptualization, Methodology, Data analysis, Project administration, ZZ: Conceptualization, Investigation, Visualization BW: Supervision, Data processing HY: Supervision, Investigation WC: Supervision, Investigation JR: Conceptualization, Methodology, Project implementation.

REFERENCES

Du, Juan., and Yang, S. M. (2007). Analysis to the Field Application Effect of Inner Well Micro Seismic Monitoring Technique [J]. *petroleum geology. oilfield development daqing* (04), 120–122. doi:10.3969/j.issn.1000-3754.2007.04.030

Gherabati, S. A., Hughes, R. G., Zhang, H., and White, C. D., (2016). A Large Scale Network Model to Obtain Interwell Formation Characteristics. Paper presented at the SPE Western Regional Meeting, Bakersfield, CA, March 2012. doi:10.2118/153386-MS

Hui, Z., Kang, Z., and Zhang, X. (2015). *INSIM: A Data-Driven Model for History Matching and Prediction for Waterflooding Monitoring and Management with a Field Application: Spe Reservoir Simulation Symposium*. Houston, TX. https://doi.org/SPE-173213-MS

Kaviani, D., Jensen, J. L., and Lake, L. W. (2008). Estimation of Interwell Connectivity in the Case of Fluctuating Bottomhole Pressures: Abu Dhabi International Petroleum Exhibition and Conference. Paper presented at the Abu Dhabi International Petroleum Exhibition and Conference, Abu Dhabi, United Arab Emirates, November, 2008. doi:10.2118/117856-MS

Li, X. Y. (2013). Unconventional Resources Will Affect Global Energy Pattern - - Interpretation of BP2030 World Energy Outlook [J]. *Int. Petreleum Econ.* 21 (04), 17–24. doi:10.3969/j.issn.1004-7298.2013.04.003

Liao, H., Wang, C., and Zuo, D. (2002). Applying Transient Testing to the Judgment of Inter-well Connectivity [J]. *Pet. Exploration Dev.* 29 (4), 87–89. doi:10.3321/j.issn:1000-0747.2002.04.027

Liu, Z., and Zeng, Z. (2003). Study on Connectivity of Low-Permeability Reservoirs with Pulse-Testing Method [J]. *Acta Petrolei Sinica* 24 (01), 73–77. doi:10.3321/j.issn:0253-2697.2003.01.014

Nguyen, A. P., Kim, J. S., and Lake, L. W. (2011). *Integrated Capacitance Resistive Model for Reservoir Characterization in Primary and Secondary Recovery[J]*. Denver, CO: Society of Petroleum Engineers.

Salazar-Bustamante, M., Gonzalez-Gomez, H., and Matringe, S. F. (2012). Combining Decline-Curve Analysis and Capacitance/Resistance Models to Understand and Predict the Behavior of a Mature Naturally Fractured Carbonate Reservoir under Gas Injection[J]. Paper presented at the SPE Latin America and Caribbean Petroleum Engineering Conference, Mexico, April, 2012. doi:10.2118/153252-MS

Sayarpour, M. (2008). *Development and Application of Capacitance-Resistive Models to Water/carbon Dioxide floods[M]*. Austin, TX: The University of Texas at Austin. http://hdl.handle.net/2152/15357

Sayarpour, M., Kabir, S., and Sepehrnoori, K. (2010). Probabilistic History Matching with the Capacitance-Resistance Model in Waterfloods: A Precursor to Numerical Modeling. Paper presented at the SPE Improved Oil Recovery Symposium, Tulsa, OK, April, 2010. doi:10.1016/j.petrol.2011.05.005

Sheng, G., Su, Y., and Wang, W. (2019). A New Fractal Approach for Describing Induced-Fracture Porosity/permeability/Compressibility in Stimulated Unconventional Reservoirs. *J. Pet. Sci. Eng.* 179, 855–866. doi:10.1016/j.petrol.2019.04.104

Tang, L. (2008). Study on Connectivity of Injection - Production System [J]. *J. Oil Gas Techn. (J.JPI)* 30 (04), 134–136. doi:10.3969/j.issn.1000-9752.2008.04.030

Xu, C. (2017). *Discrete Fracture Modeling of Fractured Reservoirs [D]*. Wuhan, China: University of Science and Technology of China.

Xu, Y., Sheng, G., Zhao, H., Hui, Y., Zhou, Y., Ma, J. et al. (2021). A New Approach for Gas-Water Flow Simulation in Multi-Fractured Horizontal wells of Shale Gas Reservoirs. *J. Pet. Sci. Eng.* 199, 108292. doi:10.1016/j.petrol.2020.108292

Yang, H., Wang, D., Huang, M., Jie, L. M., Zhuang, W. G., and Li, L. (2002). A Case of Using Water Soluble Tracer to Investigate Inter-well Connectivity at Fault Block Y8 [J]. *Oilfield Chem.* 19 (4), 343–345. doi:10.3969/j.issn.1000-4092.2002.04.016

Yang, M. (2004). Interwell Connectivity of Karst Fractured-Vuggy Carbonate Reservoirs in Block 4 of Tahe Oilfield [J]. *Xinjiang Geology.* 22 (02), 196–199. doi:10.3969/j.issn.1000-8845.2004.02.015

Yousef, A. A., Gentil, P. H., Jensen, J. L., and Lake, L. W. (2006). A Capacitance Model to Infer Interwell Connectivity from Production and Injection Rate Fluctuations. *SPE Reservoir Eval. Eng.* 9 (06), 630–646. doi:10.2118/95322-pa

Zhao, H., and Kang, Z. (2016). An Interwell Connectivity Inversion Model for Waterflooded Multilayer Reservoirs [J]. *Petroleum Exploration Development* 43 (01), 99–106. doi:10.1016/s1876-3804(16)30012-x

Zhao, H., Li, Y., Gao, D., and Cao, L. (2010). Research on Reservoir Interwell Dynamic Connectivity Using Systematic Analysis Method [J]. *Acta Petrolei Sinica* 31 (04), 633–636.

Conflict of Interest: Authors DL, ZZ, BW, HY, and WC are employed by the company PetroChina.

The remaining authors declare that the research was conducted in the absence of any commercial or financial relationships that could be construed as a potential conflict of interest.

Publisher's Note: All claims expressed in this article are solely those of the authors and do not necessarily represent those of their affiliated organizations, or those of the publisher, the editors and the reviewers. Any product that may be evaluated in this article, or claim that may be made by its manufacturer, is not guaranteed or endorsed by the publisher.

frontiers in Earth Science

ORIGINAL RESEARCH
published: 20 December 2021
doi: 10.3389/feart.2021.797617

Research on Boundary Layer Effect in Fractured Reservoirs Based on Pore-Scale Models

Deqiang Wang[1,2]*, *Xiansong Zhang*[1,2] *and Jian Zhang*[1,2]

[1]State Key Laboratory of Offshore Oil Efficient Development, Beijing, China, [2]CNOOC Research Institute Co. Ltd, Beijing, China

It is of great significance to study the seepage characteristics of heavy oil reservoirs, which are conducive to the efficient development of resources. Boundary layer effect (BLE) exists in the pore-scale flow process of macromolecular fluid media, which is different from the flow law of conventional fluid in the pore, yet the influence of BLE is ignored in the previous pore-scale simulation. Conventional porous media simulations have difficulty analyzing the mass transfer law of small-scale models under the influence of microfractures. Based on the CT scanning data and thin section data of the real core in the target area, the rock skeleton and flow space were extracted according to the maximum ball algorithm, and the pore network model representing the complex structure was constructed. The microscale effect of macromolecules in the flow process in the pores was characterized by modifying the effective flow. The effects of the BLE on the effective connectivity, displacement process, and oil distribution law were analyzed. The seepage characteristics of different wettability conditions and different water cut stages were compared. The results show that BLE reduces the effective flow space and leads to deviations in the relative permeability curve and capillary curve. For fractured porous media, the irregular shape of porous media was characterized by the morphological method, and the mass transfer process was analyzed by the equivalent flux method. The influence of the porous media shape on the macromass transfer process was compared. This study provides a solution to the problem of BLE in pore-scale simulation.

Keywords: numerical simulation, pore network model, porous media, microscale seepage, fluid–solid interaction

OPEN ACCESS

Edited by:
Yanyong Wang,
Chengdu University of Technology, China

Reviewed by:
Jiazheng Qin,
Southwest Petroleum University, China
Lijun Liu,
Chengdu University of Technology, China

***Correspondence:**
Deqiang Wang
2017312038@student.cup.edu.cn

Specialty section:
This article was submitted to Economic Geology, a section of the journal Frontiers in Earth Science

Received: *19 October 2021*
Accepted: *16 November 2021*
Published: *20 December 2021*

Citation:
Wang D, Zhang X and Zhang J (2021) Research on Boundary Layer Effect in Fractured Reservoirs Based on Pore-Scale Models. Front. Earth Sci. 9:797617. doi: 10.3389/feart.2021.797617

INTRODUCTION

Heavy oil has great development potential, and the analysis of its seepage characteristics is of great significance to enhance oil recovery. In the study of pore-scale BLE, macromolecular fluid media is different from the regular fluid flow in pores. It is necessary to analyze the flow characteristics of macromolecular fluid media under the influence of pore-scale BLE. Along with the promotion of reservoir fracturing, fractured reservoirs have become the focus of research, yet conventional porous media simulations have difficulty analyzing the mass transfer law of microscale models under the influence of microfractures.

In an experimental simulation, Secchi (Secchi et al., 2016) confirmed the existence of microscale effect in the microscale flow process in a study published in Nature. The study observed the movement of particles by sending particles into the tracer, and the trajectory of particle movement indicated that the flow process on a small scale was affected by fluid–solid

interaction. Wu et al. (2017a) analyzed the influence of wettability at the microscale and summarized microscale molecular simulations, physical simulations, and other relevant experiments. The existence of slippage distance was confirmed in the microscale fluid flow process, which reduces the effective flow space of the fluid. Wu et al. (2017b) analyzed the existence of a nonflow boundary in the flow process at the pore scale based on a physical simulation experiment of a microcircular tube and characterized the fluid–solid interaction through a large number of physical simulation experiments. The results show that the microscale fluid–solid interaction was primarily affected by viscosity, pore radius, and pressure gradient. For fractured media, Cheng et al. (2020) conducted water-flooding experiments with fractured cores and analyzed the influence of fracture length on water flooding. J.-T. (Cheng et al., 2004) analyzed the single-phase flow in a rock fracture by micromodels fabricated using projection photolithography to produce voids with known geometry. Tang et al. (2007) used a 2D micromodel of carbonate fracture media to verify a complex-segmenting correlation between the fluid pressure and volume of flow and a simple positive correlation was not adopted. Su et al. (2020) revealed the importance of microfractures in oil primary migration by interdisciplinary and several experimental methods. Many micro mechanisms can be explored by physical simulation, but the cost of research is much higher than numerical simulation.

In the numerical simulation, He et al. (2021) analyzed the influence of thin water film in the pore boundary on a two-phase relative permeability curve by a pore network model. Circular, triangular, and rectangular pores have nonflow films on the boundary, which affect the two-phase permeability curve. For fractured media, Wang and Sheng (2019) analyzed the impact of BLE on macroscale flow characteristics and evaluated the impact of large-scale fractures on productivity but ignored the seepage law of porous media containing microscale fractures. Sun et al. (2019) studied the influence of microfractures on the flow based on pore network models. However, the macromass transfer with microfractures was not analyzed. Wu et al. (2021) used dissipative particle dynamics to analyze the influence of the fluid–solid interaction force on microflow in shale slits, but this method required a large amount of calculations. Chen et al. (2018) used a pore network to simulate fluid–solid interaction, but the research was only applicable to tight reservoirs and lacked macrosimulation analysis.

The aforementioned researchers primarily focus on the study of single-pipe microscale and macroscale reservoirs, which lacked the study of pore scale. The pore network model can simulate the small-scale flow process without fracture, and the amount of calculation is greatly reduced because the pores and throats are simplified into spherical geometry space and rod geometry space. Fluid–solid interaction exists in the pore-scale flow process of macroscopic fluid media, such as heavy oil (Yin and Liu, 2015; Bazazi et al., 2019; Ke et al., 2020). Hydraulic fractured or naturally fractured heavy oil reservoirs lead to the formation including fractures and heavy oil (Babadagli, 2003; Rahnema et al., 2008; Souraki et al., 2011). However, the influence of microscale BLE was not considered in the previous pore-scale simulation. However, the mass transfer process, including microfractures, still needs to be effectively characterized. In this study, the pore network was extracted based on CT data to simulate the flow process for porous media without fractures. The microscale effect of macromolecules was characterized by modifying the seepage model of macromolecular fluid media in the pores to analyze the influence of BLE on the seepage characteristics. For fractured porous media, the irregular shape of porous media was characterized by a morphological method, and the mass transfer process was analyzed by the equivalent flux method. The effects of fractured porous media on the macromass transfer process were compared.

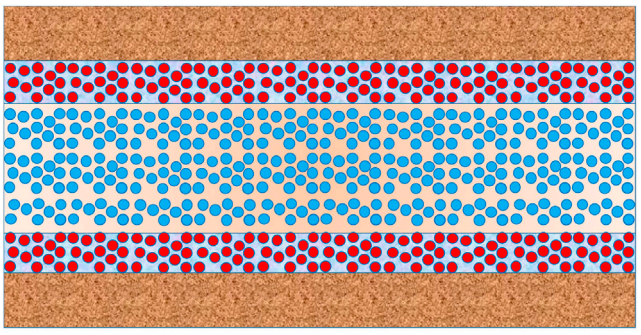

FIGURE 1 | Schematic diagram of the presence of BLE at the boundary.

METHODS

Effect of BLE

He and Wu (Wu et al., 2017a; He et al., 2021) proved that van der Waals forces between the solid wall and the fluid lead to the fluid medium near the edge of the pipe wall adsorbing on the wall to form a nonflow film for microscale flow, which was called BLE (Wang and Sheng, 2019). The flow process is shown in **Figure 1**. The brown area represents the solid phase, and the yellow area represents the flowable area. The blue area near the wall represents the nonflowable liquid phase area. The fluid adheres to the wall due to the BLE as shown by the red dot. There are only blue dots that can flow freely away from the wall in the flowable space. Therefore, there is a nonflow film at the pore boundary, resulting in the reduction of effective flow space in the pores.

Pore network simulation has been widely used in reservoir simulation because of its high-calculation efficiency (Blunt, 2001; Dong and Blunt, 2009; Gostick et al., 2016). In the conventional pore network simulation, it is assumed that the micropore throat flow conforms to Hagen–Poiseuille's law, but many researchers have confirmed that Hagen–Poiseuille's law is not applied to the pore-scale flow characteristics under the influence of BLE

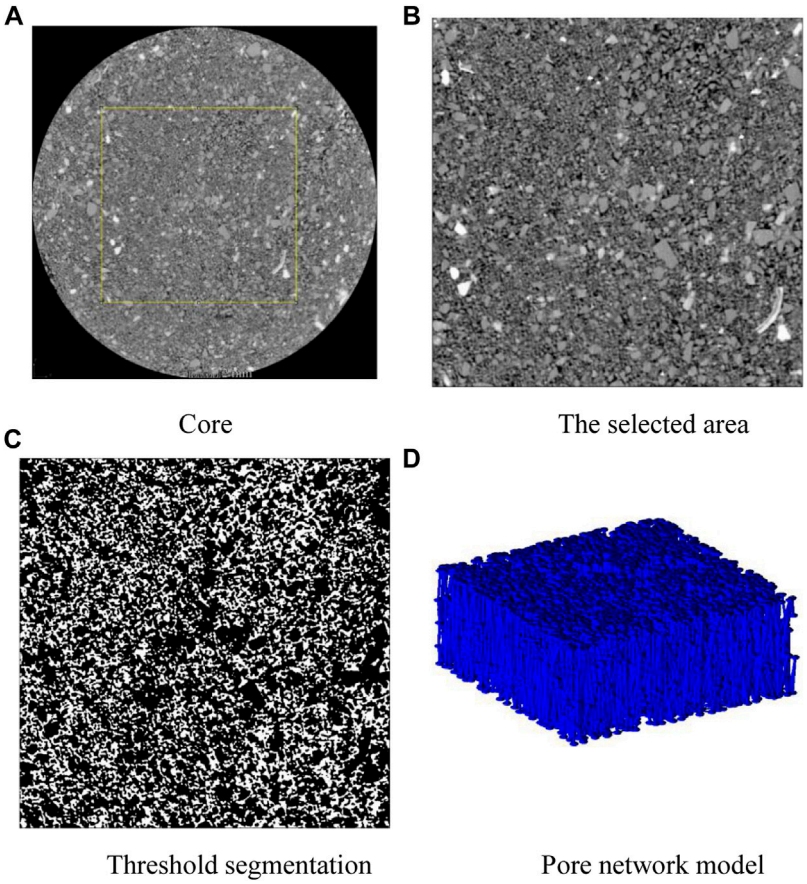

FIGURE 2 | Formation process of the pore network model. **(A)** Core, **(B)** selected area, **(C)** threshold segmentation, and **(D)** pore network model.

through micro-round pipe physical simulation experiments and molecular simulation. Therefore, the flow characterization formula of the pore network model needs to be modified.

Wu et al. proposed the microscale effect, in which there was no flow area at the boundary due to fluid–solid interactions at the pore scale and proposed the expression equation of the modified flow rate for the microscale effect, as shown in **Eq. 1**. In this study, the improved effective flow velocity is shown in **Eq. 2**.

Aiming at the BLE at the boundary, Wu et al. (Wu et al., 2017b) proposed the expression equation of modified flow based on a large number of micro-tube experiments, as shown in **Eq. 1**. The improved effective flow velocity was corrected in **Eq. 2**.

$$h = are^{br}(\nabla P)^{c} \cdot \mu, \tag{1}$$

where a, b, and c are parameters related to BLE, r is pore radius, ∇P is pressure gradient, μ is the viscosity of fluid, and h is the thickness of the nonflow interface.

$$v_{eff} = \frac{Q}{A_{eff}} = \frac{(r-h)^4}{8\mu r^2}\nabla P, \tag{2}$$

where v_{eff} is the effective flow velocity and A_{eff} is the effective flow space.

Construction and Analysis of the Unfractured Model

For porous media without fractures, a pore network model was used to describe the process of seepage in the matrix, and the fluid flow in the flowable area follows NS equation. To establish a network model representing the real pore structure of the matrix, the 600 × 600 × 3-pixel central area was selected in **Figure 2A** and **Figure 2B**. Threshold segmentation was conducted to divide the rock skeleton and flow area in **Figure 2C**. In addition, its voxel size was 15 μm. The maximum sphere algorithm was used to extract the network model, and the reconstruction result is shown in **Figure 2D**.

To analyze the pore structure characteristics of the target area, the shape factors in pores and throats were counted in **Figure 3** and **Figure 4**. The shape factor can characterize the irregularity of the cross section. The shape factor of the triangular space changed in the range of 0–0.048, and the shape factor increases gradually when the pore space was close to circular. Eighty percent of the shape factor of the extracted throat space cross section was less than 0.04 in **Figure 3A**. The results showed that most of the cross-sectional shapes were close to triangles, and the proportion of circular pores was lower. The shape factor of the extracted pore space cross section basically conformed to the normal

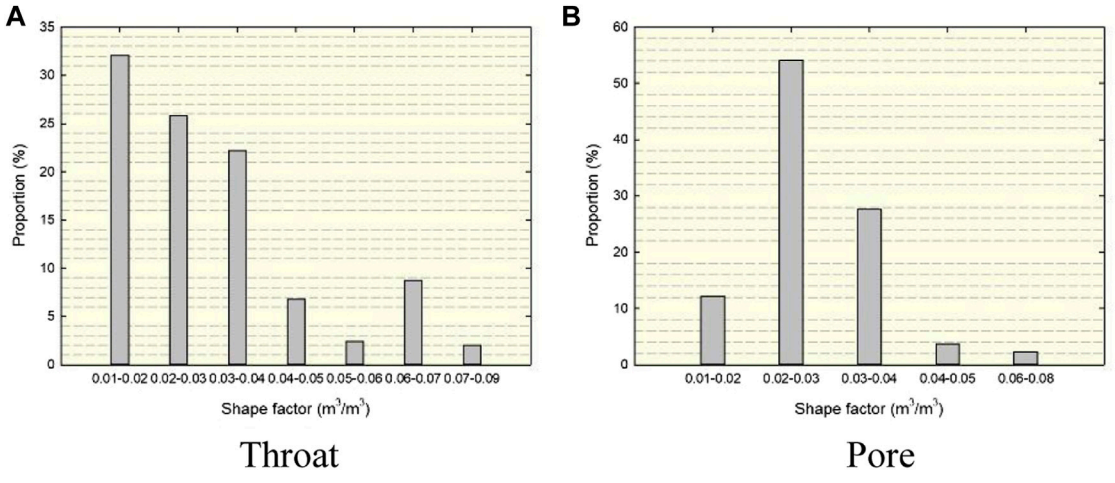

FIGURE 3 | Statistical graph of real core shape factors. **(A)** Throat **(B)** and pore.

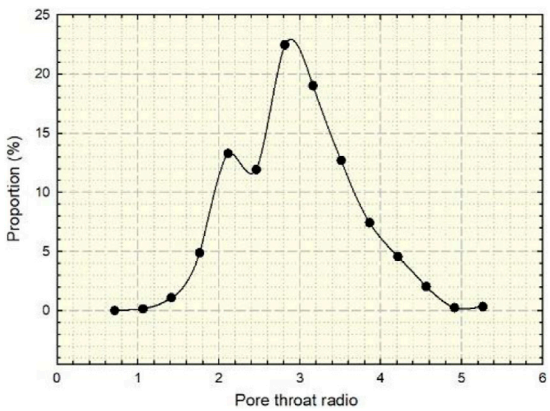

FIGURE 4 | Statistical graph of the real core pore–throat ratio.

distribution, and 94% of the shape factor of the pore space cross section was in the range of 0.01–0.04 in **Figure 3B**, indicating that the shape of most pore space cross sections was close to triangle. The low shape factor led to an increase in the water saturation in the pore throat and a decrease in the residual oil saturation when a snap-off event occurs. The larger proportion of triangular pores means that the proportion of angular water increased. These two factors led to an increase in water phase permeability in irregular pores (He et al., 2021). The statistical results of the real core pore–throat ratio are shown in **Figure 4**, which basically conformed to a normal distribution, and the pore–throat ratio was concentrated at approximately 3. However, the distribution curve had a bimodal shape due to the heterogeneity of connectivity.

Construction and Analysis of the Fractured Model

For fractured porous media with irregular shapes, morphological operation was applied to describe the shape of the connection between porous media and fracture. The equivalent flux method was used to describe the mass transfer process in irregular porous media.

Morphological operations can perform a series of operations including shape simplification and enhancement of the image based on set theory (Wang et al., 1995). Morphological operation was used to describe the structural characteristics of pores and throats, which can preserve the details of porous media and reduce the amount of calculation. The obtained injected thin section was divided into dyeing areas in **Figure 5A**(FISHMEMORY, 2016). The colored grid represents the flowable areas, and the colorless area represents the nonflowable area. First, the open operation was conducted. The original configuration in **Figure 5** was corroded leaving the green grid in **Figure 5B**. Then, the expansion operation was conducted to form the grid area composed of green and yellow as shown in **Figure 5C**. The purpose of the opening operation was to eliminate small particles, separate small throats, and smooth the boundary of the matrix.

The close operation was applied after the open operation in **Figure 6**. First, the original configuration in **Figure 6A** was expanded to obtain the red and green regions in **Figure 6B**. Then, the corrosion operation was conducted to obtain the yellow grid area in **Figure 6C**. The close operation can fill the small cavities in the matrix, connect the adjacent areas, and smooth the boundary.

The dark area in the cast sheet is the flowable area, and the light-colored area is the nonflowable area in **Figure 7A**. The dye enters the fracture for the thin slice with fracture. The dyeing range can be described by morphological operation to extract the fracture morphology. The fracture is assumed as the blue line in **Figure 7B**. The wall of the fracture was set to the flux boundary for characterization because the injected medium quickly entered the fracture and continued to propagate. Therefore, the red area in **Figure 7C** represents the fracture. The fracture can be characterized in the matrix. This method was suitable for the fracture of any shape.

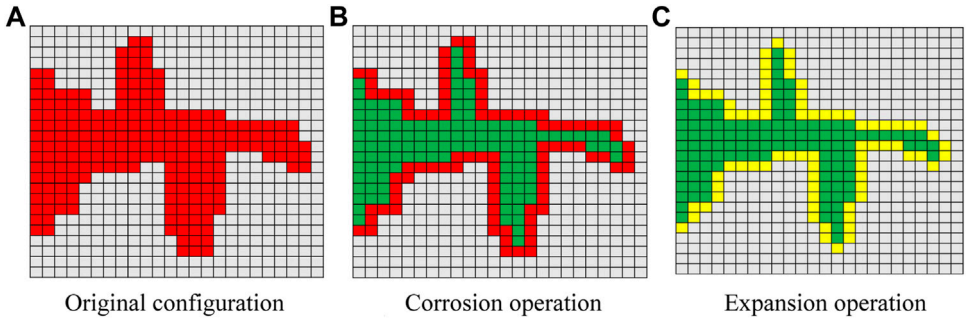

FIGURE 5 | Schematic diagram of open operation (FISHMEMORY, 2016). **(A)** Original configuration, **(B)** corrosion operation, and **(C)** expansion operation.

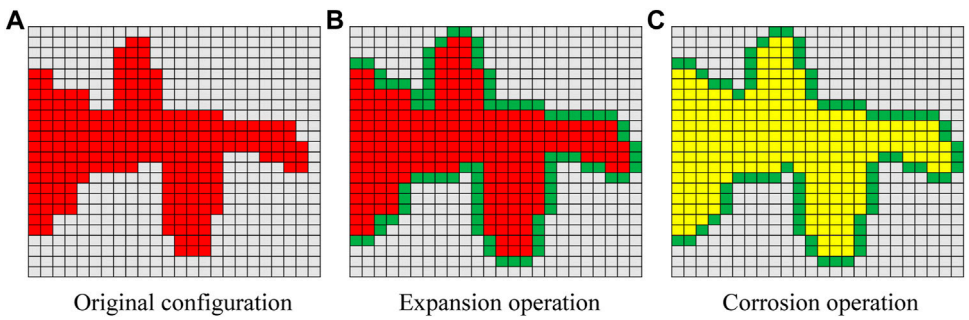

FIGURE 6 | Schematic diagram of closed operation (FISHMEMORY, 2016). **(A)** Original configuration, **(B)** expansion operation, and **(C)** corrosion operation.

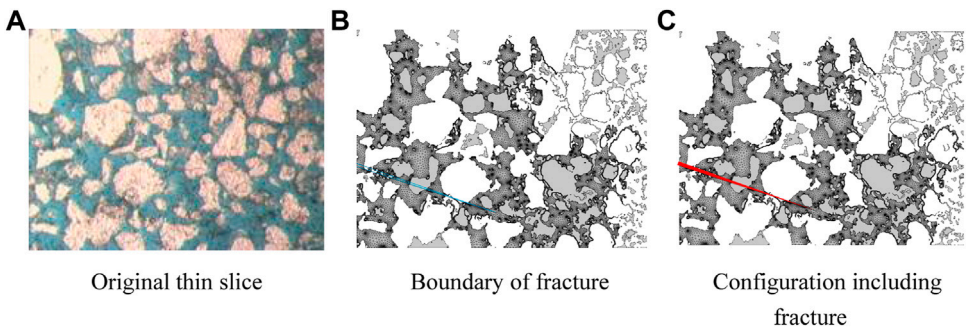

FIGURE 7 | Schematic diagram of the construction process. **(A)** Original thin slice, **(B)** boundary of fracture, and **(C)** configuration including.

The injected medium entered the microfractures due to the much higher conductivity than that of the matrix at 0.01 ms in **Figure 8A**. The injected medium filled the microfractures under a pressure difference at 0.1 ms, as shown in **Figure 8B**. Under a concentration difference and pressure difference of 1 ms, the fluid in the fracture continuously transfers into the matrix, as shown in **Figure 8C**.

Verification of the Mass Transfer Model in Porous Media

To quantitatively characterize the mass transfer of concentration diffusion, it was necessary to calculate the effective concentration diffusion coefficient of the characterization unit. The diffusion coefficient of the equivalent homogenous model was calculated by the effective diffusion coefficient of boundary concentration flux of the micromodel (Zimmerman, 2006; Ershadi and Allahverdizade, 2019). The average flux in the red dotted box was calculated by averaging the mass transfer integral at the boundary in **Eq. 3**.

$$\frac{1}{L}\int_0^L k_m (c - c_0) dL = \Phi, \tag{3}$$

where Φ is the flux at the boundary, molm^2/s; k_m is the mass transfer coefficient, m/s; L is the length of the real model, m; c is

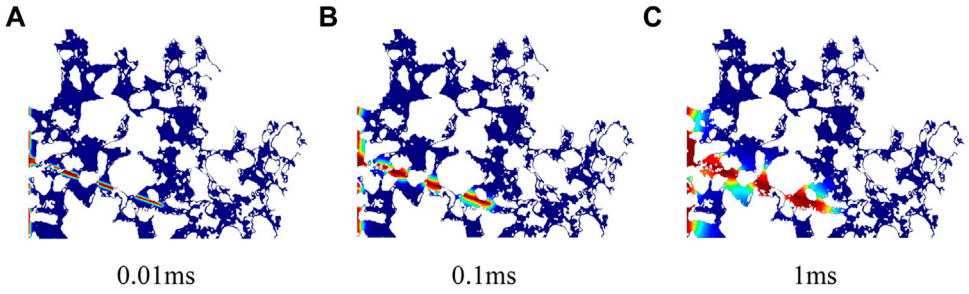

FIGURE 8 | Mass transfer for fractured porous media at different time. **(A)** 0.01ms, **(B)** 0.1ms, and **(C)** 1ms.

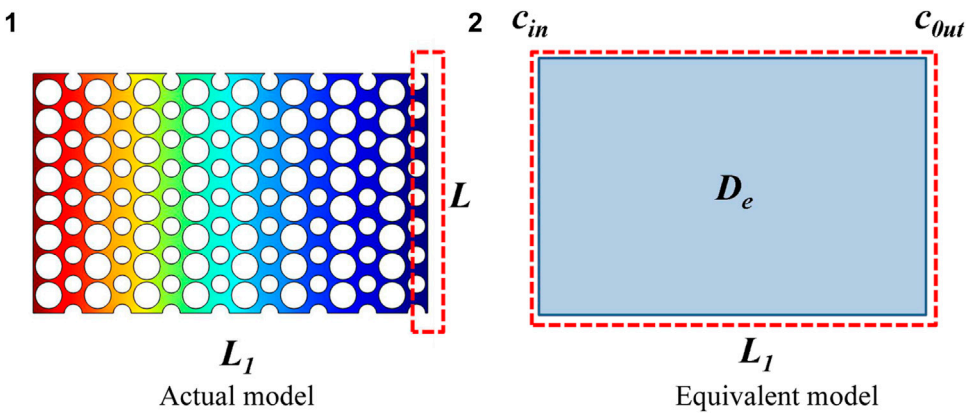

FIGURE 9 | Schematic diagram of the concentration flux calculation. **(A)** Actual model and **(B)** equivalent model.

TABLE 1 | Basic parameters of the porous model.

Parameter	Value	Parameter	Value
Mass transfer coefficient, m/s	5	Outlet concentration, mol/m^3	0
Effective diffusion coefficient, m^2/s	3×10^{-7}	Inlet concentration, mol/m^3	3
Temperature, K	293.15	Equivalent model length, μm	1900
Width of the actual model, μm	1610	Actual model length, μm	1900

the concentration at the boundary, mol/m^3; and c_0 is the concentration of the outlet, mol/m^3.

The macroscopic micro real model can be regarded as a homogenous model, and the microscopic concentration diffusion model was equivalent to the representative elementary volume in **Figure 9**. The equivalent flux between the equivalent model and the real model means that the equivalent model can calculate the effective concentration diffusion coefficient D_e in **Eq. 4**:

$$\frac{D_e}{L_1}(c_{in} - c_{out}) = \Phi_1, \tag{4}$$

where Φ_1 is the equivalent flux at the boundary, molm^2/s; D_e is the calculated effective concentration diffusion coefficient, m^2/s; L_1 is the length of the equivalent model, m; c_{in} is the concentration at the inlet, mol/m^3; and c_{out} is the concentration at the outlet, mol/m^3.

The microconcentration diffusion model was established by the aforementioned method, and the parameters are shown in **Table 1**. The mass transfer process in the real pore and throat is shown in **Figure 10**. According to **Eq. 4**, the diffusion coefficient of the equivalent model can be calculated to be 4.6×10^{-8} m^2/ s.

The porous media model was divided into two parts, including unfractured model, which was suitable for the matrix without fractures, and fractured model, which was suitable for the matrix with fractures.

For the unfractured model, the simulated data were basically consistent with the experimental relative permeability in **Figure 11A** for the matrix without fractures, which showed that the pore network model is accurate.

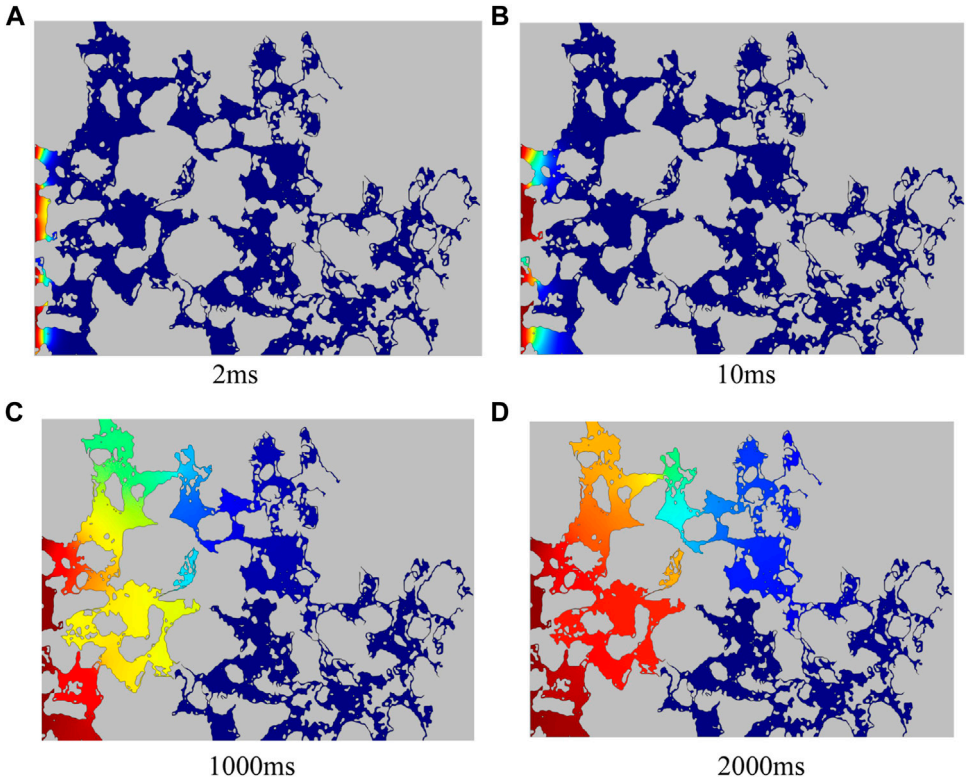

FIGURE 10 | Mass transfer process in porous media at different times. **(A)** 2ms, **(B)** 10ms, **(C)** 1000ms, and **(D)** 2000ms.

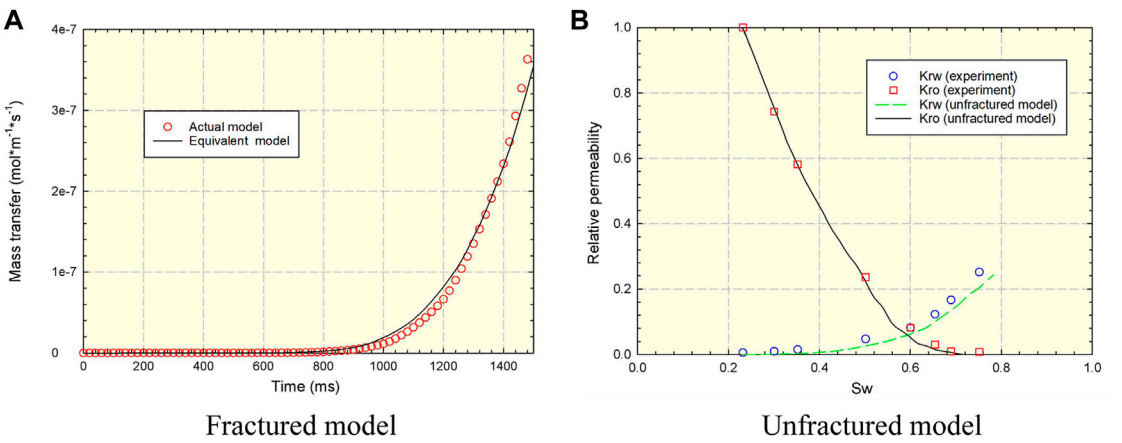

FIGURE 11 | Verification of the mass transfer model in porous media. **(A)** Fractured model and **(B)** unfractured model.

For the fractured model, the actual model and the equivalent model with the modified effective diffusion coefficient were compared. The boundary flux of the two models is basically the same in **Figure 11B**. The modified diffusion coefficient obtained by the equivalent flux method can be used to describe the mass transfer process of injected media in porous media.

RESULTS AND DISCUSSION

The unfractured model is built for the unfractured matrix with pore network model in **Appendix**, and the fractured model is built for the fractured core with the discretized mesh. The influence of effective connectivity and wettability, the characteristics of two-phase flow and water cut stage, and distribution of fluids are discussed based on

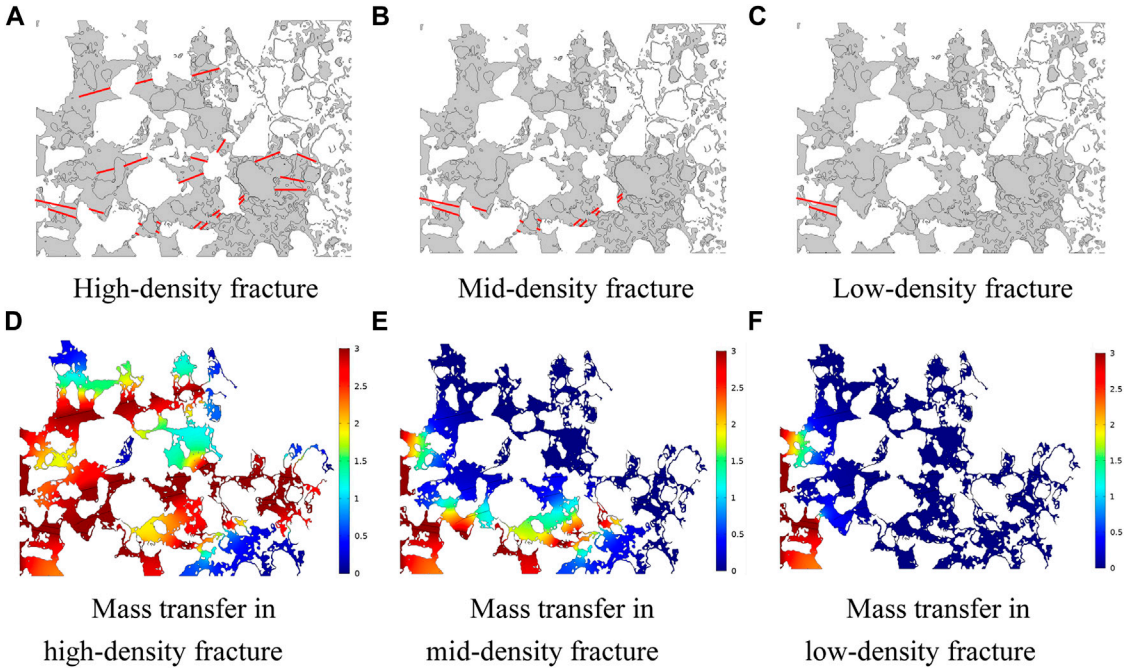

FIGURE 12 | Comparison of mass transfer at 1ms with different fracture density. **(A)** High-density fracture, **(B)** mid-density fracture, **(C)** low-density fracture, **(D)** mass transfer in the high-density fracture, **(E)** mass transfer in the mid-density fracture, and **(F)** mass transfer in the low-density fracture.

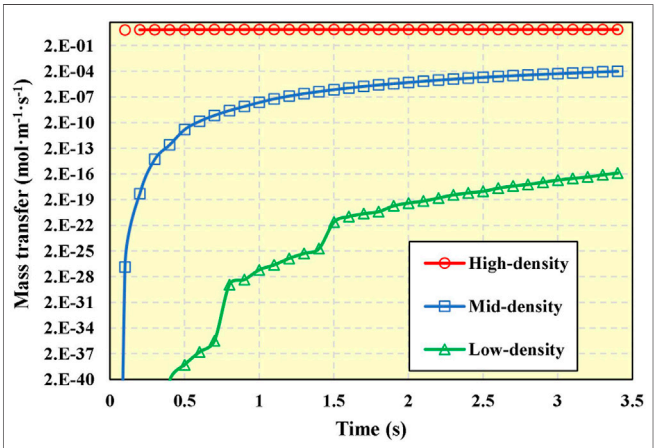

FIGURE 13 | Comparison of mass transfer with different fracture density.

the unfractured model for the matrix without fracture. The effect of irregular porous media and density of fractures is discussed based on the fractured model.

Effect of the Fracture Density

Hydraulic-fractured or naturally fractured reservoirs lead to different fracture densities in the reservoir. The influence of different fracture density on the mass transfer process is analyzed based on the fractured model. **Figure 12** shows the mass transfer state of the representative elementary volume with different fracture densities at 1 ms, which includes high-density, mid-density, and low-density. The comparison of mass transfer effects under different densities is shown in **Figure 13**. There is no effective flow channel in porous media with the low-density fracture. The mass transfer of the boundary increases with time but always remains at a low level. For reservoirs with mid-density fractures, the existence of fractures expands the range of mass transfer and greatly improves the mass transfer of the boundary. For reservoirs with high-density fractures, fractures form effective flow channels. Injection fluid enters the fracture quickly, which leads to high mass transfer efficiency in the media porous with the high-density fracture. The effect of microfracture on mass transfer cannot be ignored.

Impact on Effective Connectivity

BLE reduces the effective connection space resulting in a difference in seepage characteristics. This section analyzes the difference in effective flow space under BLE. **Figure 14A** shows the effective connection between the pore and throat without considering the BLE, and **Figure 14B** shows the connection considering the BLE. The small throat was blocked due to the BLE, and the number of effectively connected throats was reduced, shown as the area within the blue circle. The microscale BLE was greatly affected by the flow radius, so the microscale effect mainly exists on the flow process in small throats, and the effect on large pores can be almost ignored.

To quantitatively analyze the effective connectivity, the influence of BLE on the effective coordination number is compared in **Figure 15**. The average effective coordination number decreased from 6.49 to 6.46 due to the BLE. Specifically, the average effective coordination number was slightly reduced due to BLE, where the effective coordination

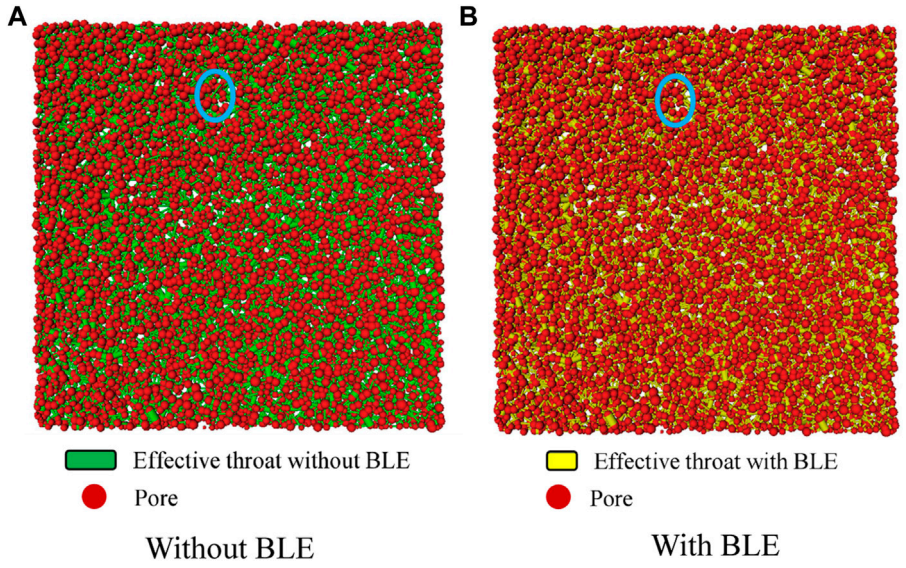

FIGURE 14 | Comparison of effective connections between pores and throats. **(A)** Without BLE and **(B)** with BLE.

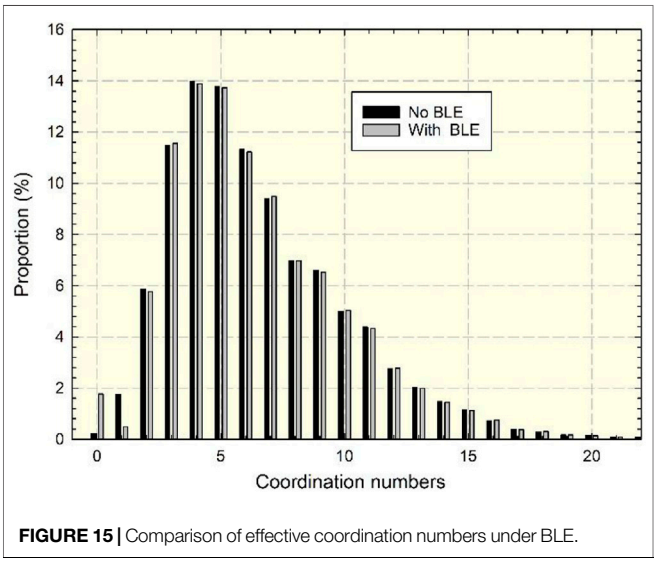

FIGURE 15 | Comparison of effective coordination numbers under BLE.

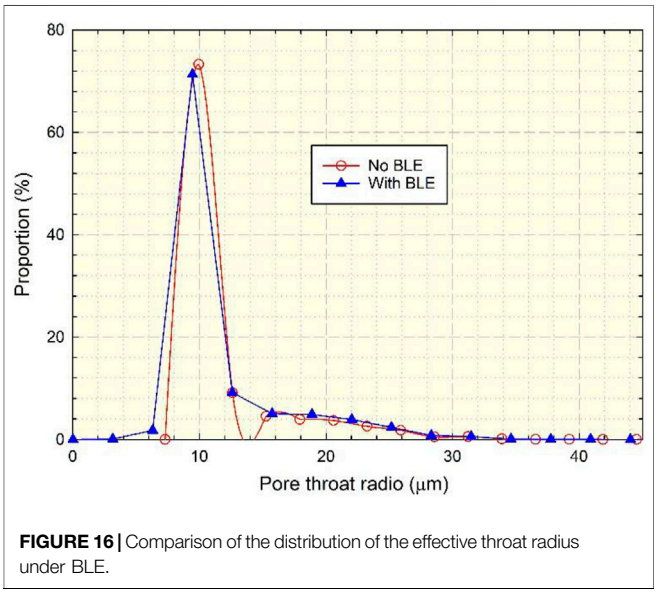

FIGURE 16 | Comparison of the distribution of the effective throat radius under BLE.

number was greater than 2. It has the greatest impact on the low-coordination number pores. The attached fluid blocks the small throat, and some pores become isolated pores.

The distribution of the effective throat is shown in **Figure 16**. BLE reduces the flow space of the effective throat, the number of effective throats decreases, and the distribution curve shifts to the left. Therefore, the influence of BLE on flow characteristics in small pores and throats should be considered.

Impact on Characteristics of Two-Phase Flow

The two-phase permeability curve is an important parameter of macronumerical simulation (Gao and Hu, 2016). The conventional simulation ignored the influence of BLE on microscale two-phase flow (Hughes and Blunt, 2000). When the water saturation was less than 0.3, the capillary force increases, and the water phase permeability increases. The effective throat space was compressed due to BLE in **Figure 17** and **Figure 18**. In the initial stage, a large capillary force was required for displacement. With the process of water flooding, the water film in the pores increased, resulting in the sticking of crude oil in the pores. Therefore, when the water saturation was greater than 0.3, the capillary force decreases. The water film and the water phase permeability increase, and the oil phase permeability decreases. The two-phase seepage area

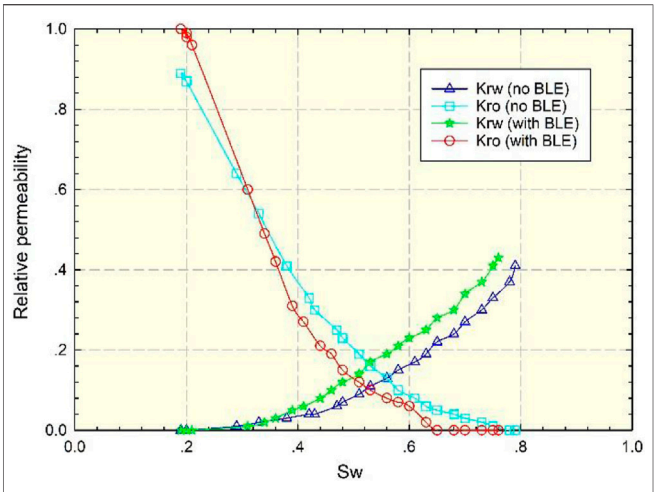

FIGURE 17 | Comparison of relative permeability with BLE.

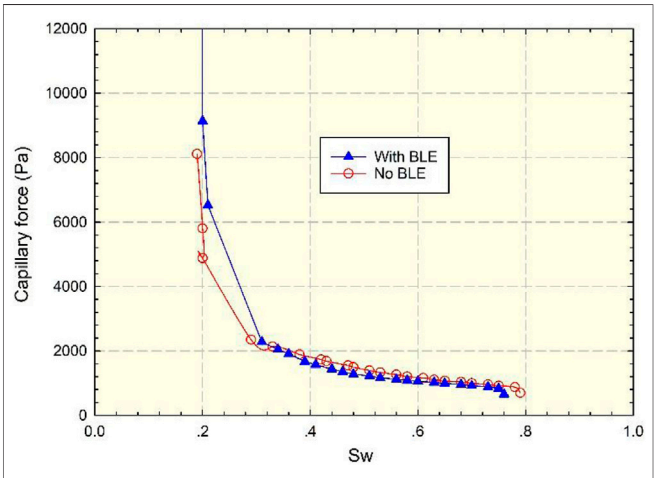

FIGURE 18 | Comparison of capillary forces with BLE.

decreased, leading to more residual oil and a worse effect on displacement.

Impact on Oil and Water Distribution

Heavy oil has issues of difficult production and a low-recovery degree, which is different from conventional crude oil (Thomas, 2008; Wassmuth et al., 2009). This section focuses on the analysis of residual oil with BLE. The distribution of oil–water after displacement is compared in **Figure 19**, and the oil–water distribution is counted to quantitatively compare the displacement effect. The number of pores with only bulk water decreased from 1,082 to 1,052 with BLE, and the number of pores containing bulk oil and water film increased from 4,762 to 4,819, which indicated that fluid more easily adhered to the wall and that the displacement efficiency was reduced with BLE. The pore number of only bulk oil remained at 6, indicating that the BLE has little effect on the residual displacement difficulty.

Influence of Wettability

Wettability had an important impact on EOR (Leach et al., 1962; Morrow, 1990). Many researchers propose injecting chemicals to transform oil wet reservoirs into water wet reservoirs to improve oil recovery (Ali et al., 2020; Nazarahari et al., 2021; Wang et al., 2021). The oil displacement effect under different wettability conditions is compared in this section (contact angle includes 30°, 60°, 120°, and 150°), and the impact on wettability on the relative permeability curve and capillary force curve is analyzed in **Supplementary Figure S1** and **Supplementary Figure S2**. After the reservoir wettability was enhanced, the higher water phase permeability led to a better oil displacement effect. Under the same saturation condition, the capillary force in the wet water reservoir was the driving force, and the capillary force in the wet oil reservoir was the resistance, as shown in **Supplementary Figure S2**. Therefore, the utilization degree of small pores and throats is improved after wetting reversal by the injection of chemicals.

Influence of the Water Cut Stage

It is of great significance to take different injection measures in different water cut stages (Rez-Morejó et al., 2019; Zhu et al., 2020). Many researchers proposed early polymer injection (Shi et al., 2020), where polymer is injected in the low water-cut to improve the recovery of heavy oil. This section focuses on the comparison of displacement effects in different water cut stages (20, 40, and 60%). In the displacement of the low water-cut stage, the oil phase permeability increased, and the flow capacity became stronger, as shown in **Supplementary Figure S3**. However, the two-phase area was wider, and the production range was wider. Therefore, from the perspective of two-phase flow capacity, it was better to inject fluid and implement adjustment measures in the low

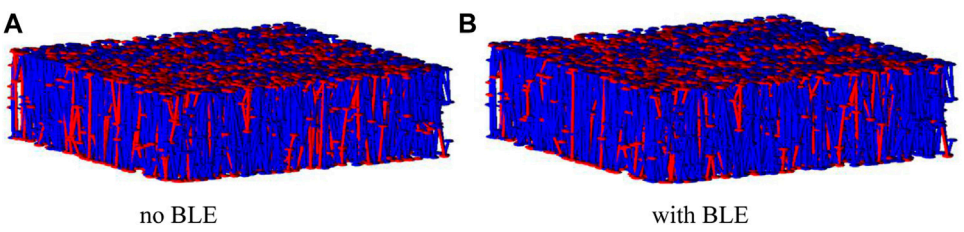

FIGURE 19 | Comparison of oil–water distribution under BLE. **(A)** Without BLE and **(B)** with BLE.

TABLE 2 | Basic parameters of the target block.

Parameter	Value	Parameter	Value
Initial water saturation	0.4	Water compressibility, MPa^{-1}	0.00000303
Initial formation pressure, MPa	12.8	X*Y*Z, m	1100*200*2
Porosity, %	25	Comprehensive compressibility coefficient, MPa^{-1}	0.00004
Permeability, mD	37	Reservoir depth, m	1,350
Reservoir temperature, °C	85	Crude oil volume factor, m^3/m^3	1.036

water-cut stage. The blue curve was much higher than the red curve in **Supplementary Figure S4**, which means that the injected fluid needs to overcome more capillary resistance in the high water-cut stage. Therefore, it was beneficial to implement various adjustment measures in the low water-cut stage, which had a better displacement effect and lower injection difficulty.

Effect of Irregular Porous Media

Porous media have irregular shapes, especially fractured porous media. The representative elementary volume has used a homogenous medium in conventional simulation and ignores the influence of the porous media shape. The irregular shape influences the mass transfer process, which is compared in this section. The effective diffusion coefficient decreases from 3×10^{-7} m^2/s to $4.6 \times 10^{-8} m^2/s$ considering the shape of porous media in **Section 2**, and the effect on macromass transfer was analyzed based on the modified effective diffusion coefficient. The production well in the target block, where the five-spot pattern was used for gas injection, was selected to compare the effect of irregular porous media. The oil production is shown in **Supplementary Figure S5**, and the basic physical property parameters of the block are shown in **Table. 2**. At the initial stage of production, the crude oil near the well was mainly produced by horizontal wells, so the production was essentially the same. At this time, the production was mainly affected by gas displacement, and the diffusion has little impact. In the later stage of development, the diffusion effect was gradually reflected. A part of the injected gas spread to nearby areas, which reduced the displacement effect. The diffusion effect was weakened considering the irregular shape of porous media, so the production was higher than the unmodified production. The irregular shape of porous media should be considered in the macrosimulation process.

CONCLUSION

In this study, a three-dimensional pore network model was extracted from the CT scanning data and thin-section data of a real core, and the seepage model was modified to analyze the influence of the BLE on seepage characteristics.

1. Morphological operation can extract the real shape of a porous media model based on cast sheets, which can preserve the characteristics of pores and reduce the number of simulation calculations. The fractured model can be used to quantitatively describe the mass transfer, and the effect of microfracture on mass transfer should be considered by the comparison of different fracture densities.

2. CT scan data of the target block can be extracted according to the maximal sphere algorithm to establish a three-dimensional real pore structure, and the parameters of the pore structure can be statistically analyzed. The BLE at pore scale can be characterized in the pore network model by modifying the effective flow rate. The existence of BLE reduces the effective flow space by comparing the effective pore–throat ratio, effective coordination number, and other structural parameters. The BLE offsets the two-phase permeability curve and capillary force curve. The fluid more easily adhered to the wall, and the microscopic oil displacement efficiency was reduced.

3. By comparing the changes of two-phase seepage characteristics under different conditions, it was found that the sweep efficiency of the small pore throat was improved after wettability alteration. It is more advantageous to conduct various adjustment measures in the low water-cut stage due to the higher sweep efficiency and lower difficulty of injection.

DATA AVAILABILITY STATEMENT

The original contributions presented in the study are included in the article/**Supplementary Material**; further inquiries can be directed to the corresponding author.

AUTHOR CONTRIBUTIONS

DW, JZ, and XZ contributed to the conception and design of the study. DW organized the database. DW performed the statistical analysis. DW wrote the first draft of the manuscript. All authors contributed to manuscript revision and read and approved the submitted version

ACKNOWLEDGMENTS

We thank the support of "Chemical Flooding Technology for Offshore Oil Fields," (No. 2016ZX05025-003) a major national special project during the 13th Five-Year Plan period, and "Heavy Oil Chemical Flooding Mechanism and Simulation Technology Research" (No. 2019- YXKJ -008).

SUPPLEMENTARY MATERIAL

The Supplementary Material for this article can be found online at: https://www.frontiersin.org/articles/10.3389/feart.2021.797617/full#supplementary-material

Supplementary Figure 1 | Comparison of relative permeability under different wettability conditions.

Supplementary Figure 2 | Comparison of capillary force curves under different wettability 318 conditions.

Supplementary Figure 3 | Comparison of relative permeability in different water cut stages.

Supplementary Figure 4 | Comparison of capillary force curves at different 335 water cut stages.

Supplementary Figure 5 | Effect of irregular porous media during the macroscopic 357 mass transfer process.

REFERENCES

Ali, M., Sahito, M. F., Jha, N. K., Arain, Z.-U. -A., Memon, S., Keshavarz, A., et al. (2020). Effect of Nanofluid on CO2-wettability Reversal of sandstone Formation; Implications for CO2 Geo-Storage. *J. Colloid Interf. Sci.* 559, 304–312. doi:10.1016/j.jcis.2019.10.028

Babadagli, T. (2003). Evaluation of EOR Methods for Heavy-Oil Recovery in Naturally Fractured Reservoirs. *J. Pet. Sci. Eng.* 37 (1), 25–37. doi:10.1016/s0920-4105(02)00309-1

Bazazi, P., Sanati-Nezhad, A., and Hejazi, S. H. (2019). Role of Chemical Additives on Water-Based Heavy Oil Mobilization: A Microfluidic Approach. *Fuel* 241, 1195–1202. doi:10.1016/j.fuel.2018.12.099

Blunt, M. J. (2001). Flow in Porous media - Pore-Network Models and Multiphase Flow. *Curr. Opin. Colloid Interf. Sci.* 6 (3), 197–207. doi:10.1016/s1359-0294(01)00084-x

Chen, M., Cheng, L., Cao, R., and Lyu, C. (2018). A Study to Investigate Fluid-Solid Interaction Effects on Fluid Flow in Micro Scales. *Energies* 11 (9), 2197. doi:10.3390/en11092197

Cheng, J.-T., Morris, J. P., Tran, J., Lumsdaine, A., Giordano, N. J., Nolte, D. D., et al. (2004). Single-phase Flow in a Rock Fracture: Micro-model Experiments and Network Flow Simulation. *Int. J. rock Mech. mining Sci.* 41 (4), 687–693. doi:10.1016/j.ijrmms.2004.01.003

Cheng, L., Wang, D., Cao, R., and Xia, R. (2020). The Influence of Hydraulic Fractures on Oil Recovery by Water Flooding Processes in Tight Oil Reservoirs: an Experimental and Numerical Approach. *J. Pet. Sci. Eng.* 185, 106572. doi:10.1016/j.petrol.2019.106572

Dong, H., and Blunt, M. J. (2009). Pore-network Extraction from Micro-computerized-tomography Images. *Phys. Rev. E Stat. Nonlin Soft Matter Phys.* 80 (3), 036307. doi:10.1103/PhysRevE.80.036307

Ershadi, M. N., and Allahverdizade, M. (2019). "Introduction to COMSOL Multiphysics and Numerical Simulations (In Persian)," in *Journal of Scientific Association of Mechanical Engineering- University of Tabriz* (Tabriz: Scientific Association of Mechanical Engineering- University of Tabriz).

FISHMEMORY (2016). Morphology-corrosion, Expansion, Open Operation, Close Operation. Available at: https://blog.csdn.net/fishmemory/article/details/53113746.

Gao, Z., and Hu, Q. (2016). Initial Water Saturation and Imbibition Fluid Affect Spontaneous Imbibition into Barnett Shale Samples. *J. Nat. Gas Sci. Eng.* 34, 541–551. doi:10.1016/j.jngse.2016.07.038

Gostick, J., Aghighi, M., Hinebaugh, J., Tranter, T., Hoeh, M. A., Day, H., et al. (2016). OpenPNM: a Pore Network Modeling Package. *Comput. Sci. Eng.* 18 (4), 60–74. doi:10.1109/mcse.2016.49

He, M., Zhou, Y., Wu, K., Hu, Y., Feng, D., Zhang, T., et al. (2021). Pore Network Modeling of Thin Water Film and its Influence on Relative Permeability Curves in Tight Formations. *Fuel* 289, 119828. doi:10.1016/j.fuel.2020.119828

Hughes, R. G., and Blunt, M. J. (2000). Pore Scale Modeling of Rate Effects in Imbibition. *Transport in Porous Media* 40 (3), 295–322. doi:10.1023/a:1006629019153

Ke, H., Yuan, M., and Xia, S. (2020). A Review of Nanomaterials as Viscosity Reducer for Heavy Oil. *J. Dispersion Sci. Tech.* 3, 1–12. doi:10.1080/01932691.2020.1851246

Leach, R. O., Wagner, O. R., Wood, H. W., and Harpke, C. F. (1962). A Laboratory and Field Study of Wettability Adjustment in Water Flooding. *J. Pet. Technol.* 14 (02), 206–212. doi:10.2118/119-pa

Morrow, N. R. (1990). Wettability and its Effect on Oil Recovery. *J. Pet. Technol.* 42484 (121)–14761.

Nazarahari, M. J., Manshad, A. K., Ali, M., Ali, J. A., Shafiei, A., Sajadi, S. M., et al. (2021). Impact of a Novel Biosynthesized Nanocomposite (SiO2@Montmorilant@Xanthan) on Wettability Shift and Interfacial Tension: Applications for Enhanced Oil Recovery. *Fuel* 298, 120773. doi:10.1016/j.fuel.2021.120773

Rahnema, H., Kharrat, R., and Rostami, B. (2008). "Experimental and Numerical Study of Vapor Extraction Process (VAPEX) in Heavy Oil Fractured Reservoir," in Canadian International Petroleum Conference, Calgary, Alberta, Canada, June 17-19, 2008. doi:10.2118/2008-116

Rez-Morejó, J. J., Bertin, H., Omari, A., Hamon, G., Cottin, C., Morel, D., et al. (2019). A New Approach to Polymer Flooding: Effects of Early Polymer Injection and Wettability on Final Oil Recovery. *SPE Journal-Richardson* 24, 129–139. doi:10.2118/190817-pa

Secchi, E., Marbach, S., Niguès, A., Stein, D., Siria, A., and Bocquet, L. (2016). Massive Radius-dependent Flow Slippage in Carbon Nanotubes. *Nature* 537 (7619), 210–213. doi:10.1038/nature19315

Shi, L., Zhu, S., Guo, Z., Zhao, W., Xue, X., Wang, X., et al. (2020). Experimental Study on the Effect of Polymer Injection Timing on Oil Displacement in Porous media. *Processes* 8 (1), 93. doi:10.3390/pr8010093

Souraki, Y., Ashrafi, M., Karimaie, H., and Torsaeter, O. (2011). "Experimental Investigation and Numerical Simulation of Steam Flooding in Heavy Oil Fractured Reservoir," in SPE Western North American Region Meeting, Anchorage, Alaska, USA, May 7-11, 2011. doi:10.2118/144552-ms

Su, K., Lu, J., Zhang, H., Chen, S., Li, Y., Xiao, Z., et al. (2020). Quantitative Study on Hydrocarbon Expulsion Mechanism Based on Micro-fracture. *Geosci. Front.* 11 (6), 1901–1913. doi:10.1016/j.gsf.2020.05.013

Sun, H., Duan, L., Liu, L., Fan, W., Fan, D., Yao, J., et al. (2019). The Influence of Micro-fractures on the Flow in Tight Oil Reservoirs Based on Pore-Network Models. *Energies* 12 (21), 4104. doi:10.3390/en12214104

Tang, X., Jin, Z., Yang, M., and Ming, H. (2007). Experimental Study on Water-Oil Migration and Accumulation in a 2D Micro-model of Carbonate Fracture media. *Front. Earth Sci. China* 1 (2), 251–256. doi:10.1007/s11707-007-0031-4

Thomas, S. (2008). Enhanced Oil Recovery - an Overview. *Oil Gas Sci. Tech. - Rev. IFP* 63 (1), 9–19. doi:10.2516/ogst:2007060

Wang, D., Haese-Coat, V., and Ronsin, J. (1995). Shape Decomposition and Representation Using a Recursive Morphological Operation. *Pattern Recognition* 28 (11), 1783–1792. doi:10.1016/0031-3203(95)00036-y

Wang, X., and Sheng, J. J. (2019). Multi-scaled Pore Network Modeling of Gas-Water Flow in Shale Formations. *J. Pet. Sci. Eng.* 177, 899–908. doi:10.1016/j.petrol.2019.03.005

Wang, Y., Liang, L., Li, Y., Liu, B., and Tang, L. (2021). Preparation and Application of a Fluoropolymer Emulsion as Novel Wettability Reversal Agent. *Colloids Surf. A: Physicochemical Eng. Aspects* 612, 125985. doi:10.1016/j.colsurfa.2020.125985

Wassmuth, F. R., Green, K., Arnold, W., and Cameron, N. (2009). Polymer Flood Application to Improve Heavy Oil Recovery at East Bodo. *J. Can. Pet. Tech.* 48 (02), 55–61. doi:10.2118/09-02-55

Wu, J., Cheng, L., Li, C., Cao, R., Chen, C., Cao, M., et al. (2017). Experimental Study of Nonlinear Flow in Micropores under Low Pressure gradientTransport in Porous Media. *Transp Porous Med.* 119 (1), 247–265. doi:10.1007/s11242-017-0882-4

Wu, J., Fu, W., Yan, Q., Chen, Y., Hu, Y., Wang, Z., et al. (2021). A Dissipative Particle Dynamics Study:influence of Fluid-Solid Interaction Force on Micro-flow in Shale Slits. *Arab J. Geosci.* 14 (6), 461. doi:10.1007/s12517-021-06839-4

Wu, K., Chen, Z., Li, J., Li, X., Xu, J., and Dong, X. (2017). Wettability Effect on Nanoconfined Water Flow. *Proc. Natl. Acad. Sci. USA* 114 (13), 3358–3363. doi:10.1073/pnas.1612608114

Yin, Y., and Liu, Y. (2015). FEM Analysis of Fluid-Structure Interaction in Thermal Heavy Oil Recovery Operations. *Sustainability* 7 (4), 4035–4048. doi:10.3390/su7044035

Zhu, S., Ye, Z., Zhang, J., Xue, X., Chen, Z., and Xiang, Z. (2020). Research on Optimal Timing Range for Early Polymer Injection in sandstone Reservoir. *Energ. Rep.* 6, 3357–3364. doi:10.1016/j.egyr.2020.11.247

Zimmerman, W. B. J. (2006). *Introduction to Comsol Multiphysics. Multiphysics Modeling with Finite Element Methods*. Singapore: World Scientific Publishing Company.

Conflict of Interest: Authors DW, XZ, and JZ were employed by the company CNOOC Research Institute Co. Ltd.

Publisher's Note: All claims expressed in this article are solely those of the authors and do not necessarily represent those of their affiliated organizations, or those of the publisher, the editors, and the reviewers. Any product that may be evaluated in this article, or claim that may be made by its manufacturer, is not guaranteed or endorsed by the publisher.

APPENDIX

The method by Blunt (Blunt, 2001) can be used to calculate the two-phase permeability. The absolute permeability can be calculated according to **Eq. 5**, when there is only single-phase fluid in the pores.

$$K = \frac{Q_t \mu L}{A(P_{\text{in}} - P_{\text{out}})}. \tag{5}$$

The relative permeability can be calculated according to **Eq. 6**

$$K_{rp} = \frac{Q_p}{Q_t}, \tag{6}$$

where Q_p is the flow rate of the phase fluid when multiphase fluids flow. The flow at each point can be solved according to the mass conservation:

$$\sum_{j=1}^{N} q_{ij} = \frac{g_{ij}}{L}(P_{\text{in}} - P_{\text{out}}) = 0. \tag{7}$$

The conductivity can be calculated from **Eq. 8**

$$g_{ij} = \frac{l_{ij}}{\frac{l_i}{g_i} + \frac{l_t}{g_t} + \frac{l_j}{g_j}}. \tag{8}$$

The conductivity of single phase can be determined according to the Hagen–Poiseuille equation:

$$g_p = k\frac{A^2 G}{\mu} = \frac{1}{2}\frac{A^2 G}{\mu}. \tag{9}$$

frontiers in Earth Science

ORIGINAL RESEARCH
published: 22 December 2021
doi: 10.3389/feart.2021.795842

A Study to Investigate the Viscosity Effect on Micro-Confined Fluids Flow in Tight Formations Considering Fluid–Solid Interaction

Mingqiang Chen[1,2,3]*, *Qingping Li*[1,2], *Linsong Cheng*[3], *Xiukun Wang*[3], *Chaohui Lyu*[3] and *Qi Fan*[1,2]

[1]Research Center of China National Offshore Oil Corporation, Beijing, China, [2]State Key Laboratory of Natural Gas Hydrates, Beijing, China, [3]Department of Petroleum Engineering, China University of Petroleum (Beijing), Beijing, China

Understanding different fluids flow behavior confined in microscales has tremendous significance in the development of tight oil reservoirs. In this article, a novel semiempirical model for different confined fluid flow based on the concept of boundary layer thickness, caused by the fluid–solid interaction, is proposed. Micro-tube experiments are carried out to verify the novel model. After the validation, the viscosity effect on the flow rate and Poiseuille number considering the fluid–solid interaction is investigated. Furthermore, the novel model is incorporated into unstructured networks with anisotropy to study the viscosity effect on pore-scale flow in tight formations under the conditions of different displacement pressure gradients, different aspect ratios (ratio of the pore radius to the connecting throat radius), and different coordination numbers. Results show that the viscosity effect on the flow rate and Poiseuille number after considering the fluid–solid interaction induces a great deviation from that in conventional fluid flow. The absolute permeability is not only a parameter related to pore structures but also depends on fluid viscosity. The study provides an effective model for modeling different confined fluid flow in microscales and lays a good foundation for studying fluid flow in tight formations.

Keywords: flow rate, Poiseuille number, unstructured network, absolute permeability, aspect ratio, coordination number

OPEN ACCESS

Edited by:
Wenhui Song,
China University of Petroleum (Huadong), China

Reviewed by:
Jianlin Zhao,
ETH Zürich, Switzerland
Hao Liu,
Hohai University, China
Guodong Cui,
China University of Geosciences Wuhan, China

***Correspondence:**
Mingqiang Chen
549135449@qq.com

Specialty section:
This article was submitted to Economic Geology, a section of the journal Frontiers in Earth Science

Received: *15 October 2021*
Accepted: *10 November 2021*
Published: *22 December 2021*

Citation:
Chen M, Li Q, Cheng L, Wang X, Lyu C and Fan Q (2021) A Study to Investigate the Viscosity Effect on Micro-Confined Fluids Flow in Tight Formations Considering Fluid–Solid Interaction. Front. Earth Sci. 9:795842. doi: 10.3389/feart.2021.795842

INTRODUCTION

Tight oil reservoirs have played a dominant role in the development of the petroleum industry (Cui et al., 2020; Cui et al., 2021aCui et al., 2021b; Zhao et al., 2021). However, the flow regularity in tight formations differs a lot from that in conventional reservoirs due to large numbers of microscale or even smaller pore throats (Lyu et al., 2018a). Understanding different fluid flow behavior in microscale is of great significance for a better prediction and development of tight oil reservoirs. Recently, a practical investigation of confined fluid flow has been carried out due to the availability of new tools (Nie et al., 2004; Ren and E, 2005; Zhao and Yang, 2012; Zhao et al., 2018; Zhao et al., 2020a), and advances in micro-electromechanical systems have triggered the study of microscale fluid flow (Kumar et al., 2016; Yang et al., 2016).

Many investigations have indicated that properties of confined fluids in microscales differ dramatically from those of bulk fluids (Heuberger et al., 2001; Levinger, 2002; Scatena et al., 2001), owing to the varying structures and dynamics of confined fluids induced by the fluid–solid interaction (Wu K. et al., 2017). Some novel flow phenomena have been discovered (Fei et al., 2009;

Li, 2001; Ling et al., 2002; Xiangan et al., 2010), which are helpful for theoretical investigations of the dynamics of confined fluids (Li and He, 2005; Liu et al., 2005; Wu et al., 2017c; Xu et al., 2007; Zhi, 2003). The flow rates measured by Pfahler et al. (1990) and Qu et al. (2000) for water flow through micro-tubes were found smaller than those calculated by the classic Hagen–Poiseuille equation. In addition, the relationship of the Reynolds number vs displacement pressure gradient no longer obeys the traditionally theoretical calculation in micro-confined fluid flow (Makihara et al., 1993).

The aforementioned huge differences may rise from the significantly different strengths of the fluid–solid interaction. With the decreased flow scale, the fluid–solid interaction effect on confined fluid flow becomes more severe (Gad-El-Hak, 1999; Sandeep Arya et al., 2013; Zhang et al., 2014). The fluid in the interface region is forced to stick on the wall surface due to the strong interaction and cannot move at a certain displacement pressure gradient. Jiang et al. (2006) carried out the deionized water flow experiment in micro-tubes made of quartz at high pressure under steady flow conditions and found that the deionized water cannot flow when the radius decreases to 2.32 μm, which validated the existence of the immovable layer. Mapxacin (1987) and Huang (1998) refer to this immovable fluid layer caused by the fluid–solid interaction as the boundary layer. Unlike the concept of the conventional boundary layer theory of hydromechanics (Schlichting and Gersten, 2003), the boundary layer here further shrinks the effective flow space of confined fluids and depends on the original throat radius, displacement pressure gradient, and fluid viscosity (Liu et al., 2005; Li, 2010). The emerging novel phenomena of the boundary layer should be included in order to accurately characterize confined fluid flow in microscale. Although many empirical correlations have been developed to represent boundary layer thickness (Li and He, 2005; Xu et al., 2007; Li et al., 2011; Liu et al., 2011; Cao et al., 2016; Wu et al., 2017a), most of them just take the displacement pressure gradient and original throat radius into account, while the factor of fluid viscosity is ignored, causing extreme limitation of their application when studying different fluid flow. Since multiphase flow usually occurs in tight formations (Lyu et al., 2018a), it is of great significance to take fluid viscosity into account to develop a novel model to represent the boundary layer thickness.

In this work, we first propose a novel model to represent the boundary layer thickness, which not only takes the displacement pressure gradient and throat radius into account but also the fluid viscosity. Then micro-tube experiments are used to validate the novel model. Subsequently, the viscosity effect on confined fluid flow in microscales is discussed in detail, including the flow rate and Poiseuille number. Furthermore, the novel model representing the boundary layer thickness is incorporated into unstructured networks with anisotropy to study the viscosity effect on pore-scale flow in tight formations, respectively, under the conditions of different displacement pressure gradients, different aspect ratios, and different coordination numbers. This study provides an effective model for modeling different micro-confined fluid flow and lays a good foundation for investigating fluid flow in tight formations.

REPRESENTATION OF THE BOUNDARY LAYER THICKNESS

The confined fluids in microscales possess different structural and dynamical properties from those of bulk fluids. Fluids in the inner region are attached on the wall surface and form an immovable layer due to a strong fluid–solid interaction. Since the boundary layer shrinks the flow space, the classic Hagen–Poiseuille equation is modified as **Eq. 1** according to the physical meaning (Chen et al., 2018):

$$Q = \frac{\pi (r - h)^4}{8\mu_b} \nabla P, \tag{1}$$

where Q is the flow rate, 10^{-9} cm^3/s; r and h are, respectively, the radius of micro-tubes and boundary layer thickness, μm; μ_b is the bulk fluid viscosity, mPas; and ∇P is the displacement pressure gradient, MPa/m.

To characterize confined fluid flow in microscales, the boundary layer thickness needs to be accurately represented in advance. As summarized from previous literature on the boundary layer effect (Mazzoco and Jr, 1999; Pertsin and Grunze, 2004; Liu et al., 2005; Zhang et al., 2008; Cui et al., 2010; Zhu et al., 2013), the boundary layer thickness is affected not only by the micro-tube radius and displacement pressure gradient but also by the fluid viscosity. To obtain the relationship among them, the variable-by-variable analysis method is adopted here.

First, the relationship of the boundary layer thickness vs displacement pressure gradient needs to be obtained. It is clear that the flow rate is zero when no displacement pressure gradient is exerted on the fluid, which can be reckoned that the boundary layer thickness is equal to the original micro-tube radius (ratio of the boundary layer thickness h/r equals to 1). At the same time, the boundary layer thickness decreases with an increased displacement pressure gradient due to the novel equilibrium of shear force and the displacement pressure gradient (Wu et al., 2017b). Based on the experimental data of confined fluid flow in micro-tubes (**Figure 1**) (Li, 2010), it can be seen that ratio of the boundary layer thickness decreases exponentially with an increased displacement pressure gradient.

Therefore, the relationship between the boundary layer thickness and displacement pressure gradient can be expressed as **Eq. 2**:

$$h = re^{-b\nabla P^c}, \tag{2}$$

where b and c are related to tube radius and fluid viscosity, respectively, and their values are always positive.

Second, values of b and c at different micro-tube radii but with a fixed fluid viscosity (0.92 mPa s) are obtained based on Li's micro-tube experiments (**Figure 1A**) (Li, 2010), which are shown in **Figure 2**.

To guarantee that b and c are always positive, exponential functions are used to obtain the relationship of b and c vs micro-tube radii at a fixed fluid viscosity, as given in **Eq. 3**:

$$\begin{cases} b = me^{nr}, \\ c = ke^{-gr^p}, \end{cases} \tag{3}$$

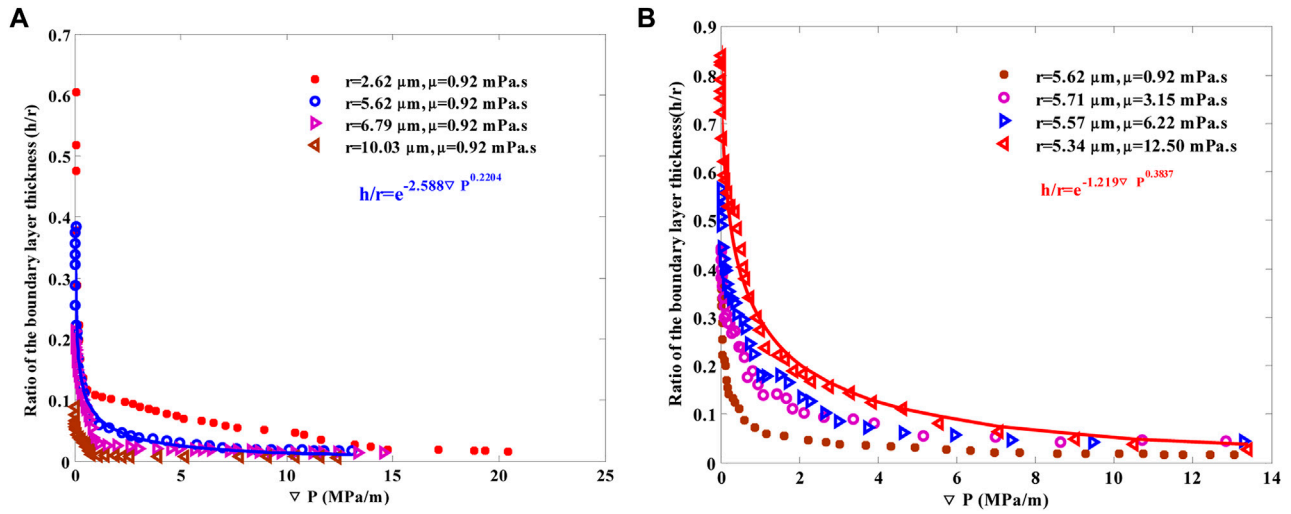

FIGURE 1 | Relationship of the ratio of boundary layer thickness at **(A)** different micro-tube radii and **(B)** fluid viscosities.

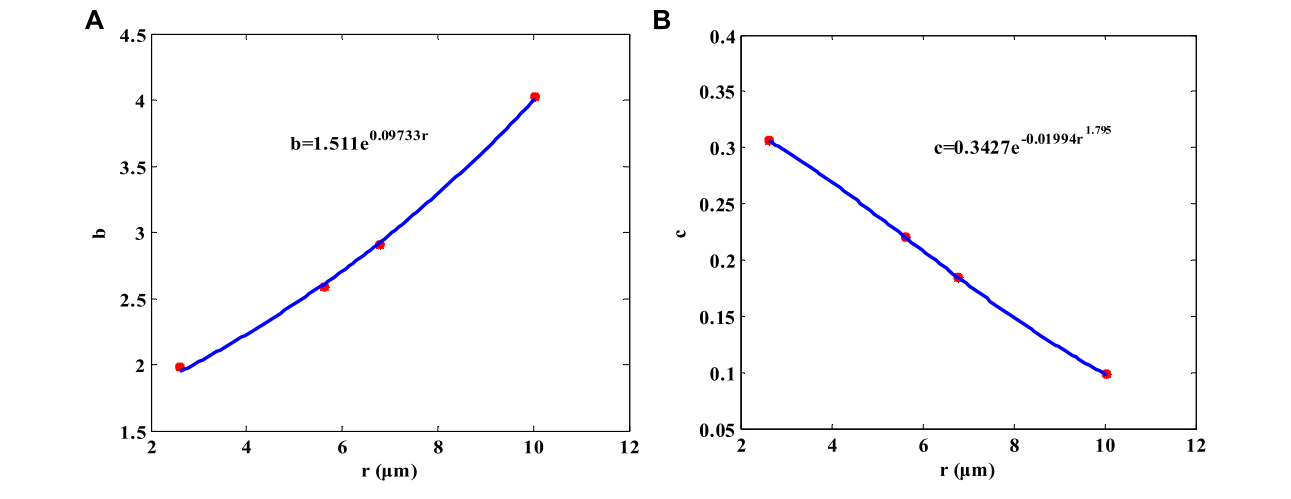

FIGURE 2 | Relationships of *b* and *c* vs micro-tube radii at a fixed fluid viscosity (0.92 mPa s).

where *m*, *n*, *k*, *g*, and *p* are related to the fluid viscosity.

Finally, relationships of parameters *m*, *n*, *k*, *g*, and *p* vs fluid viscosities are, respectively, obtained based on Li's confined fluid flow experiments in microscales with different viscosities (**Figure 1B**) (Li, 2010), using **Eq. 1**, **Eq. 2**, and **Eq. 3**. The results are relatively shown in **Figure 3**.

As can be seen from **Figure 3**, the relationships of *m*, *n*, *k*, *g*, and *p* vs fluid viscosities can be expressed as follows:

$$\begin{cases} m = 1.48\mu^{-0.1975}, \\ n = 0.03792e^{-1.127\mu} + 0.08604e^{-0.02816\mu}, \\ k = 0.3462\mu^{0.08706}, \\ g = 0.06592e^{0.02343\mu} - 0.07507e^{-0.4994\mu}, \\ p = -1.174e^{0.07147\mu} + 3.033. \end{cases} \tag{4}$$

Using the aforementioned variable-by-variable analysis method, the novel model to represent the boundary layer thickness with the consideration of displacement pressure gradient, micro-tube radius, and fluid viscosity is proposed. To validate the accuracy and reliability of the earlier novel model, Wu's (Wu et al., 2017b) experimental data of deionized water flow in different radial micro-tubes are used. Comparison results are shown in **Figure 4**. It can be seen that the calculated flow rates agree well with the experimental values, indicating the accuracy of the novel model.

Compared with other empirical correlations, the novel model not only involves more factors but also considers the variations of parameters along with the micro-tube radius and fluid viscosity. In addition, the calculated boundary layer thickness by the novel model will never exceed the original radii of micro-tubes, which

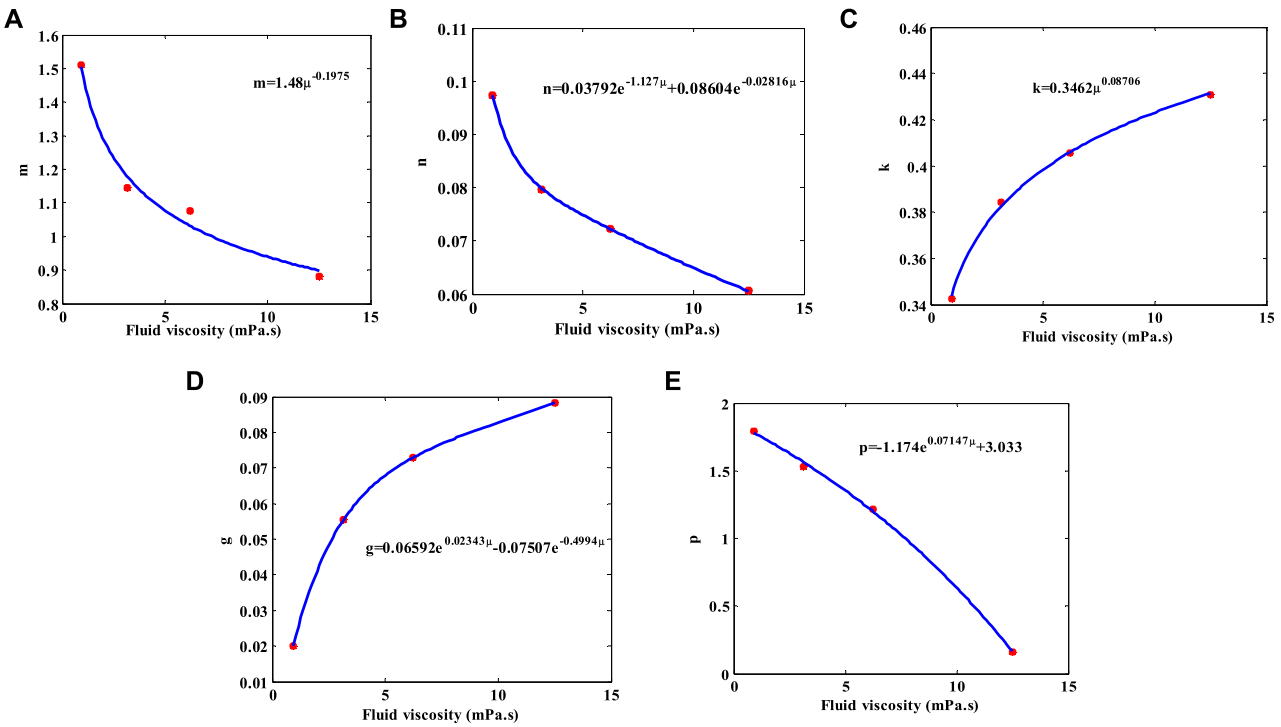

FIGURE 3 | Relationships of *m*, *n*, *k*, *g*, and *p* vs fluid viscosities.

greatly broadens its application range. Since microscale and smaller scale pore throats possess similar flow mechanisms (Striolo, 2006; Thomas and Mcgaughey, 2009), the novel model may also be valid for modeling confined fluid flow in smaller scales. Furthermore, tight formations feature abundant micro-pore throats of different sizes, and the novel model lays a good foundation for studying fluid flow in tight formations. In the following sections, the viscosity effect on confined fluid flow from the perspective of flow rate and Poiseuille number in micro-tubes will be studied at first. Then the novel model will be incorporated into unstructured networks with anisotropy to investigate the viscosity effect on pore-scale flow in tight formations.

VISCOSITY EFFECT ON CONFINED FLUID FLOW IN MICRO-TUBES AND TIGHT FORMATIONS

Viscosity Effect on Confined Fluid Flow in Micro-Tubes

Viscosity Effect on the Flow Rate

To study the effect of fluid viscosity on the flow rate due to the fluid–solid interaction, the decreasing factor, analogous to the enhancement one indicated by Mainak et al. (2005) and Holt et al. (2006), is defined as the ratio of the measured flow rate Q_{exp}–Q_n, predicted by the classic Hagen–Poiseuille equation. Since the measured flow rate can be well-predicted by our proposed novel model, it can be modeled by **Eq. 1**. Then, the decreasing factor can be expressed as follows:

$$\varepsilon = \frac{Q_{exp}}{Q_n} = \left(1 - \frac{h}{r}\right)^4 = \left(1 - e^{-b(\mu,r)\nabla P^c(\mu,r)}\right)^4. \quad (5)$$

Figure 5 shows the relationship of the decreasing factor vs the displacement pressure gradient at different radii and fluid viscosities, respectively, with and without considering the fluid–solid interaction. It is indicated that the decreasing factor keeps a constant (with its value 1) at any given displacement pressure gradient, pore throat radius, and fluid viscosity when the fluid–solid interaction is not included. However, great deviation occurs when the fluid–solid interaction is taken into consideration. The decreasing factor is no longer a constant, which gradually increases with the increased displacement pressure gradient. This phenomenon can be accounted for by the variation of the effective flow space. Due to the strong fluid–solid interaction, the fluid in the interface region is attached to the wall surface and cannot move, compressing the effective flow space, resulting in the smaller flow rate. With the increase in the displacement pressure gradient, the fluid–solid interaction gradually weakens, which enlarges the effective flow space. Therefore, the decreasing factor starts to increase and become more and more close to the one without considering the fluid–solid interaction.

In addition, the decreasing factor varies a lot at different fluid viscosities, which is quite different from its changing regularity without considering the fluid–solid interaction. The decreasing factor decreases with the increased fluid viscosity with its value being always smaller than 1. This phenomenon results from the fluid–solid interaction. With the increase in fluid viscosity, the

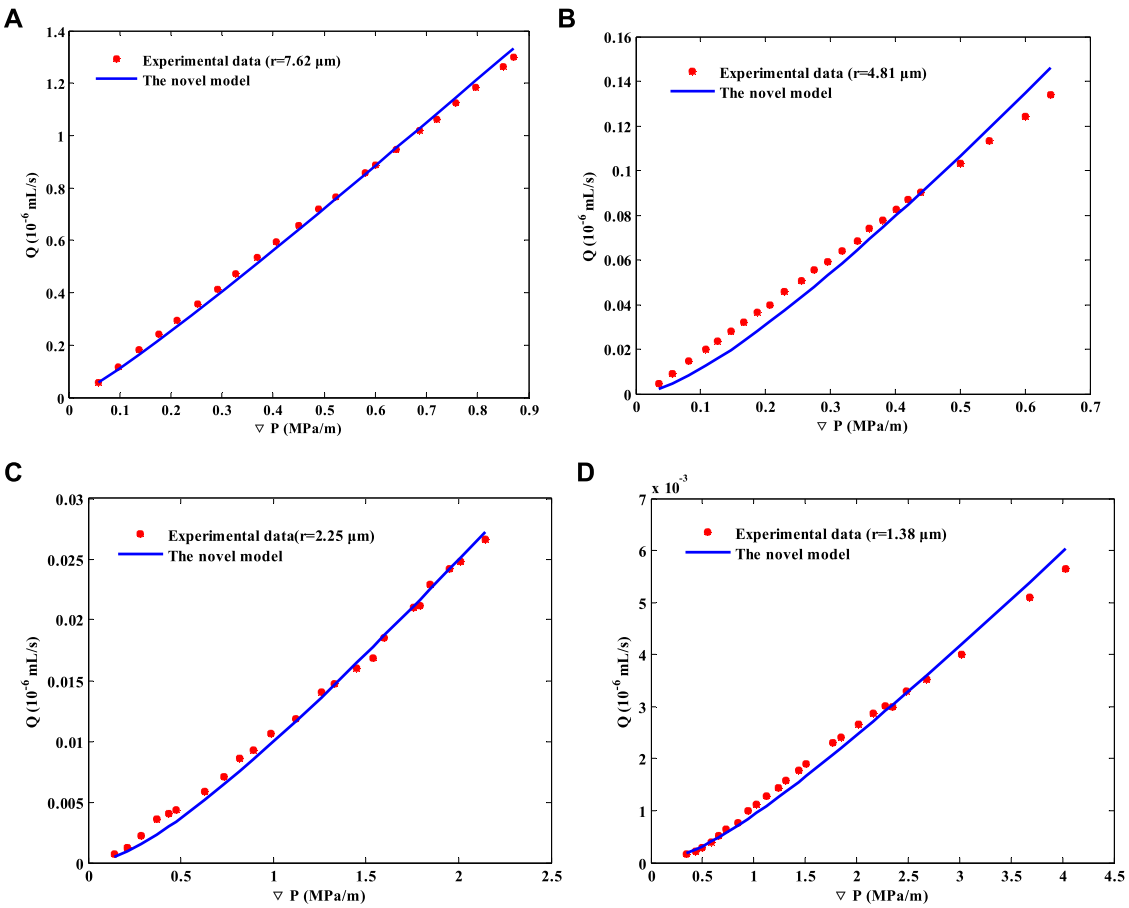

FIGURE 4 | Comparison of the flow rate calculated by the novel model and experimental data (Wu et al., 2017b).

fluid–solid interaction grows more intense, resulting in more and more fluids attached to the wall surface. Eventually, the effective flow space is further compressed as the fluid viscosity increases, resulting in the smaller flow rate and decreasing factor. Meanwhile, the smaller the original radius, the stronger will be the fluid–solid interaction. Therefore, the fluid viscosity effect on confined fluid flow will be more serious in the smaller flow space. As a result, the fluid viscosity effect is needed to be considered in tight formations, which captures large numbers of micro-/nano-pore throats.

Viscosity Effect on the Poiseuille Number

The Poiseuille number is an important parameter to characterize fluid flow, and it has been studied for many years (Damean and Regtien., 2001; Dutkowski, 2008; Hong et al., 2008; John et al., 2009; Park et al., 2002) (Krishnamoorthy and Ghajar, 2007). Churchill (Churchill, 1988) pointed out that the Reynolds number R_e is unsuitable for non-accelerating and viscous flow since density does not play a part. He suggested that the Poiseuille number P_o should be used, instead of R_e. Meanwhile, most of the initial work performed in determining P_o in microscales reported a variation from the classical theory. Several studies reported a higher value of P_o, while few reported a lower one (Krishnamoorthy and Ghajar, 2007). Even though enormous research has been performed on P_o, a complete understanding of it is still unavailable. In this part, P_o for the confined fluid flow in micro-tubes will be investigated.

Based on our proposed model, the expressions of the friction factor f and R_e in micro-tubes can be, respectively, obtained in **Eq. 6** and **Eq. 7**:

$$f = \frac{2D}{\rho v^2}\nabla P = \frac{256 r^5 \mu^2}{\rho (r-h)^8 \nabla P}. \tag{6}$$

$$R_e = \frac{\rho v D}{\mu} = \frac{\rho r (r-h)^4 \nabla P}{4(\mu r)^2}. \tag{7}$$

Since the Poiseuille number P_o is the product of the friction factor and Reynolds number $f \times R_e$ (Churchill, 1988), it can be expressed as follows:

$$P_o = f \times R_e = \frac{64 r^4}{(r-h)^4}. \tag{8}$$

Figure 6 illustrates the relationship of P_o vs displacement pressure gradient at different fluid viscosities, with and without considering the fluid–solid interaction. It is noted that P_o induces

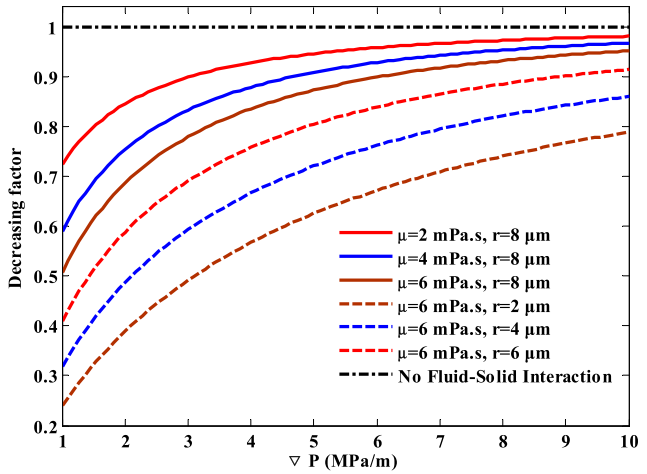

FIGURE 5 | Relationship of the decreasing factor vs displacement pressure gradient at different radii and fluid viscosities.

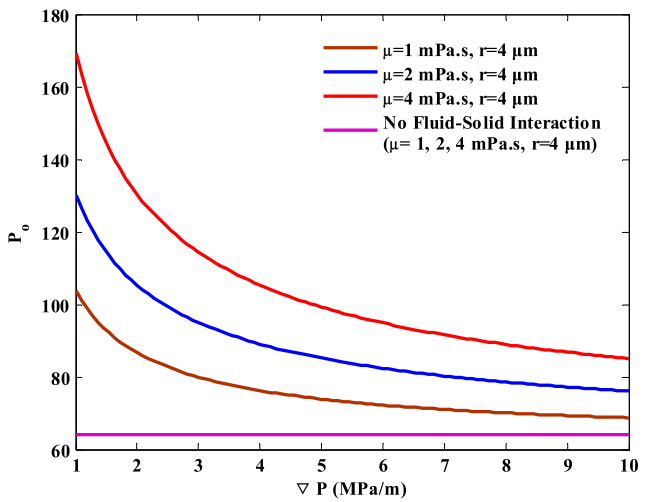

FIGURE 6 | Relationship between P_o and ∇P with and without considering the fluid–solid interaction at different fluid viscosities.

a significantly different changing rule from that in conventional fluid flow when the fluid–solid interaction is taken into consideration. P_o in consideration of the fluid–solid interaction is always larger than the one ignoring the interaction and decreases with the increased displacement pressure gradient. This deviation can be due to the variation of the effective flow space caused by the fluid–solid interaction. As a result of the strong interaction, fluid in the inner region sticks to the wall surface and cannot move at a certain displacement pressure gradient, compressing the effective flow space. However, the effective flow space enlarges gradually with the increasing displacement pressure gradient, making P_o more and more close to the value without considering the fluid–solid interaction.

At the same time, it can be seen that P_o also shows different values at different fluid viscosities. P_o stays at a constant value of 64 when no fluid–solid interaction is considered, indicating that the fluid viscosity has no effect on it. In contrast, P_o is no longer a constant after considering the fluid–solid interaction. With the increasing fluid viscosity, more and more fluid will be attached to the wall surface, reducing the effective flow space and resulting in larger flow resistance. Therefore, P_o at large fluid viscosity is always higher than that at small one when the fluid–solid interaction is involved.

Viscosity Effect on Pore-Scale Flow in Tight Formations

Construction of Pore Networks and Pore-Scale Flow Network Model

Fluid flow not only occurs in single tubes but also in tight formations with different pore throat radii and complex topologies (Lyu et al., 2019; Lyu et al., 2018c). In order to improve the recovery of tight oil reservoirs, fluid flow in tight formations should be studied correctly. In this section, the fluid viscosity effect on pore-scale flow in tight formations will be investigated.

For investigation, a platform which can represent the complex structures of tight formations is required to establish (Dong et al., 2017; Huaimin et al., 2019; Raeini et al., 2018; Wang and Sheng, 2018; Zhao et al., 2020b). Here, an unstructured stochastic network model with anisotropy is first constructed. The anisotropy here means that not all pores in the pore network possess the same coordination number. Each pore is assigned a coordination number based on the distribution of coordination numbers. Compared with other generation methods (Idowu, 2009; Raoof and Hassanizadeh, 2010), the method developed here can be applied to any coordination number distribution and is more flexible (Chalendar et al., 2018; Chen et al., 2019; Wang and Sheng, 2019). The detailed construction process is shown as follows:

1) An overall physical size of the network $L_x \times L_y \times L_z$ and resolution *Res* are given. Based on the parameters, numbers of lattices $[L_x/Res] \times [L_y/Res] \times [L_z/Res]$ are determined. Then the pore body of the network is randomly assigned on these lattices. Subsequently, the pore body radius is assigned based on the pore radius distribution. The following pore bodies are assigned on the remaining lattices, and the pore body radii are given one by one if the throat lengths between the pore body to be incorporated and incorporated pore bodies are all larger than the minimal pore radius of the pore radius distribution. The aforementioned operations are repeated until the overall porosity reaches the target (it is 0.12 in our study).
2) Coordination numbers are sampled from the probability distribution. We assume that the closer the distance of the pores, the easier they will be connected. Based on this assumption, we rank the pore bodies by their distances to the ninth most adjacent pores (since the largest coordination number in our study is 9) and assign the coordination number correspondingly.

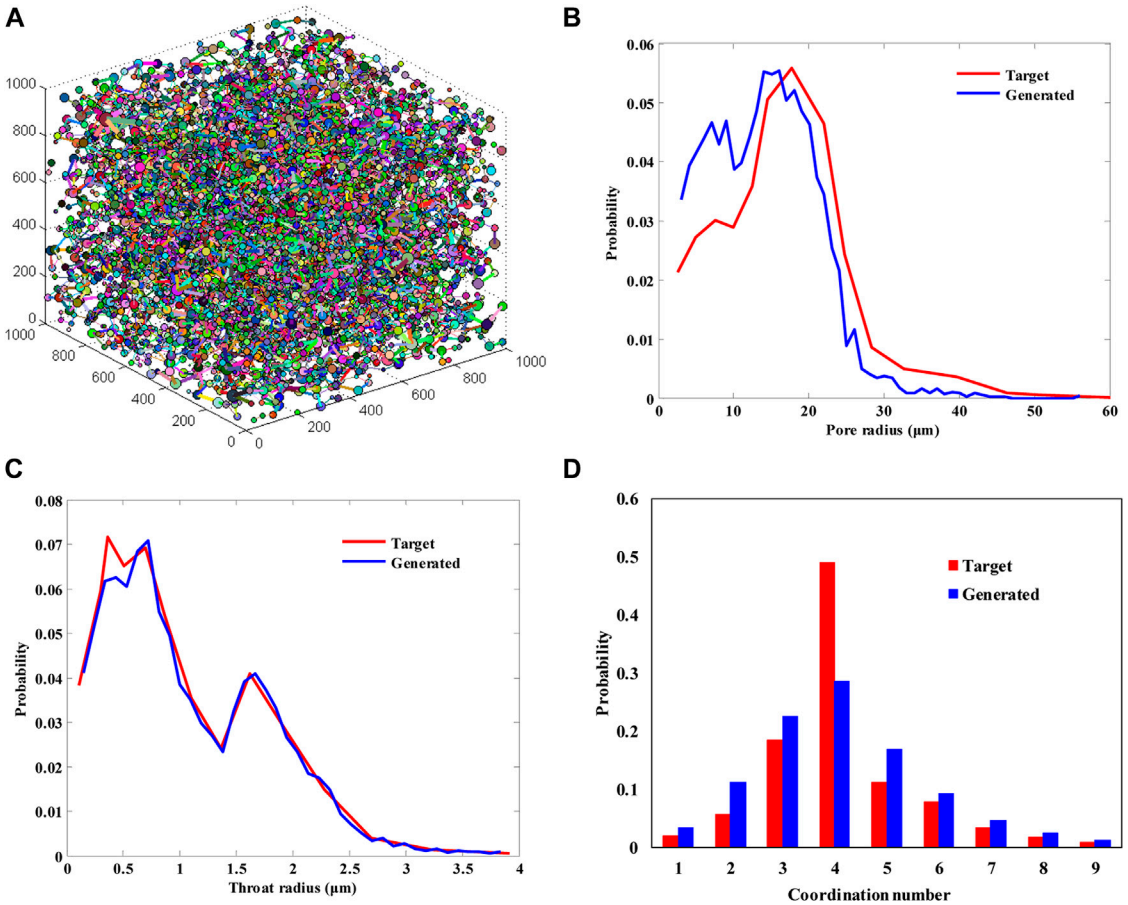

FIGURE 7 | (A) Visualization of the network (1 mm × 1 mm × 1 mm) and **(B)** distributions of pore radii, **(C)** throat radii, and **(D)** coordination number.

3) For every pore body, we connect its nearest pores one by one until the connectivity reaches the assigned coordination number in step (2).
4) We sample the throat radii from the input probability distribution and rank them in ascending order. Then we assign the ranked throat radii to the throats by ranking the mean radii of their connecting pore bodies.

The input data here are based on the extracted pore network of Berea 3D digital rock data by Dong and Blunt (Hu and Blunt, 2009). We reduce the throat radius distribution by a factor of 10 to make the pore throat radius in the range of tight formations. Visualization of the stochastic network along with its distributions of pore radii, throat radii, and coordination number is presented in **Figure 7**. It can be seen that generated distributions of the pore radii, throat radii, and coordination number agree well with the target data, illustrating the reliability of the aforementioned generation method.

When the network is fully saturated with a single-phase p, its flow rate at every pore satisfies the mass conservation as follows:

$$\sum_j q_{p,ij} = 0, \tag{9}$$

where j runs over all the throats connected to the pore i.

The flow rate between two pores i and j is given as follows:

$$q_{p,ij} = g_{p,ij} \nabla P_{p,ij}, \tag{10}$$

where $g_{p,ij}$ and$\nabla P_{P,ij}$ are, respectively, the conductance and displacement pressure gradient between the pore bodies i and j.

The conductance between two pore bodies $g_{p,ij}$ is taken to be the harmonic mean of each individual conductance as follows:

$$\frac{L_{ij}}{g_{p,ij}} = \frac{L_{p,i}}{g_{p,i}} + \frac{L_{p,t}}{g_{p,t}} + \frac{L_{p,j}}{g_{p,j}}, \tag{11}$$

where t indicates the connecting throat. The pore body lengths, L_i and L_j, are the lengths from the pore–throat interface to the pore center.

Since the aspect ratio is large in tight formations (Zhao et al., 2015), the fluid–solid interaction in the pores is much smaller compared to that in the throats. Hence, the fluid–solid interaction will only be considered in the throats. Fluid conductance g of the pore and throat in single-phase laminar flow can be expressed as follows:

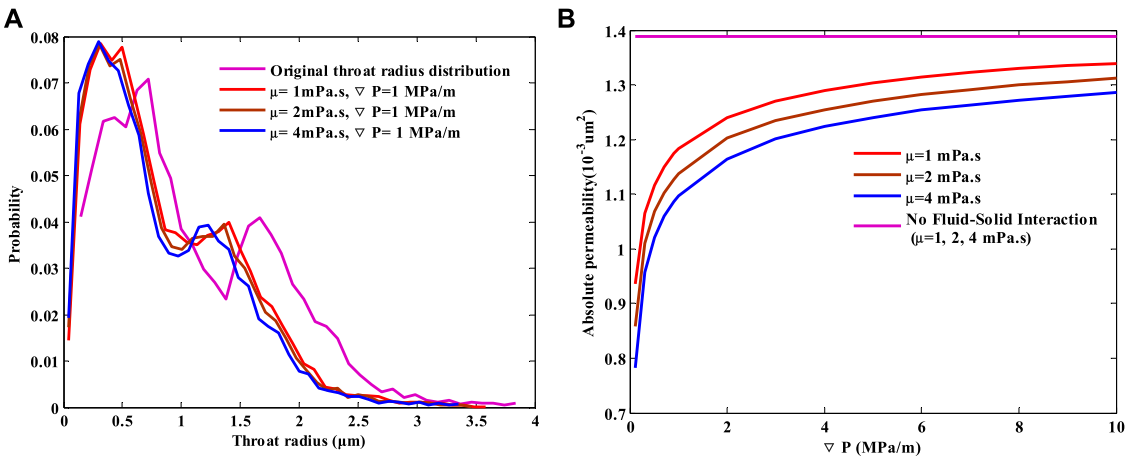

FIGURE 8 | (A) Viscosity effect on the effective throat radius and **(B)** absolute permeability at different displacement pressure gradients with and without considering the fluid–solid interaction.

$$\begin{cases} g_p = \dfrac{\pi r_p^4}{8\mu_b}, \\ g_t = \dfrac{\pi (r_t - h)^4}{8\mu_b} = \dfrac{\pi\left(r_t - r_t e^{-b(\mu,r)\nabla P^{c(\mu,r)}}\right)^4}{8\mu_b}, \end{cases} \tag{12}$$

where g_t and r_t are, respectively, the throat conductance and radius.

Then a non-linear set of equations can be formed by combining **Eq. 9** and **Eq. 10**, which has to be solved in terms of pore pressures through repeated iterations. The absolute permeability K of the network is found from Darcy's law:

$$K = \frac{\mu_b q_t L}{A(P_{in} - P_{out})}, \tag{13}$$

where K is the absolute permeability, um^2; q_t is the flow rate, cm^3/s; P_{in} and P_{out} are respectively inlet and outlet pressures, 0.1 MPa; A and L are the cross-sectional area and length of the network, cm^2 and cm.

Based on the aforementioned constructed network and fluid flow calculation process, the viscosity effect on pore-scale flow in tight formations can be realized. In the following part, the viscosity effect on pore-scale flow in tight formations will be studied under three different conditions, which are, respectively, different displacement pressure gradients, different aspect ratios, and coordination numbers.

Viscosity Effect on Pore-Scale Flow at Different Displacement Pressure Gradients

Figure 8 shows the fluid viscosity effect on the effective throat radius and absolute permeability at different displacement pressure gradients, with and without considering the fluid–solid interaction.

It can be seen that the absolute permeability keeps a constant with the same value at a series of different displacement pressure gradients and fluid viscosities when the fluid–solid interaction is ignored. This phenomenon indicates that displacement pressure gradients and fluid viscosities have nothing to do with the absolute permeability which is in agreement with our common sense. However, the effective flow structures of tight formations are influenced when the fluid–solid interaction is taken into consideration, which results in a significantly different changing rule of the absolute permeability from that in conventional fluid flow. The absolute permeability no longer keeps the same constant and changes with the variation of displacement pressure gradient and fluid viscosity. As displacement pressure gradient decreases, part of the boundary fluid that can originally participate in pore-scale flow is attached on the wall surface and cannot move, reducing the effective flow space. As a result, the absolute permeability is smaller than that ignoring the fluid–solid interaction. With the displacement pressure gradient continuing to decrease, the effective flow space grows smaller and smaller, and the deviation of the absolute permeability with and without considering the fluid–solid interaction turns larger and larger. Meanwhile, with the increase in fluid viscosity, the number of molecules in the fluid becomes large, resulting in a larger fluid–solid interaction. More and more fluid is attached on the pore wall and increases the boundary layer thickness. The effective flow space becomes smaller, which results in larger flow resistance. As a result, the absolute permeability decreases with increased fluid viscosity. The larger the fluid viscosity, the smaller will be the absolute permeability.

Viscosity Effect on Pore-Scale Flow at Different Aspect Ratios

So as to investigate the fluid viscosity effect on pore-scale flow at different aspect ratios, we scale down the original throat radius distribution (**Figure 7C**) to a series of different values from 0.6 to 1 with the interval of 0.05, five of which are shown in **Figure 9A** in particular. Meanwhile, the other parameters in the aforementioned network (**Figure 7**) such as the distributions

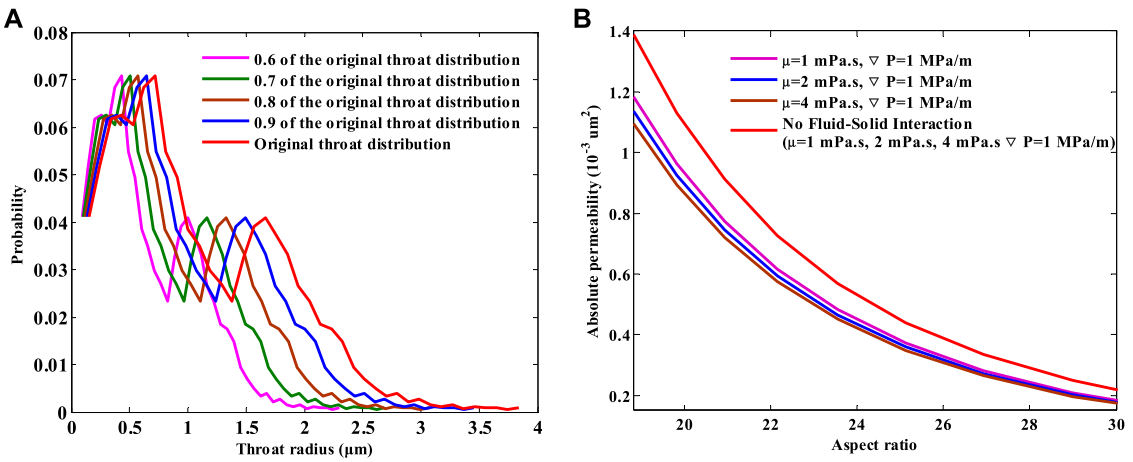

FIGURE 9 | (A) Different distributions of original throat radius and **(B)** viscosity effect on the absolute permeability with and without considering fluid–solid interaction based on these different aspect ratios.

of the pore radii and coordination number, positions of the pore bodies and the physical size stay unchanged.

Figure 9B shows the fluid viscosity effect on the absolute permeability at a series of the above different aspect ratios, with and without considering the fluid–solid interaction.

It is noted from **Figure 9B** that the effect of fluid viscosity on the absolute permeability considering the fluid–solid interaction differs significantly from that ignoring the interaction. The absolute permeability curves at different fluid viscosities overlap when the fluid–solid interaction is excluded, indicating that the fluid viscosity has no effect on the absolute permeability. This is in accordance with the common sense that the absolute permeability is only the function of pore structures, which has nothing to do with fluid properties. However, the absolute permeability curves separate with each other when the fluid–solid interaction is involved. The absolute permeability decreases with increased fluid viscosity at a certain aspect ratio. This special behavior can be accounted for from the perspective of the fluid–solid interaction. As the fluid viscosity increases, the number of molecules in the fluid increases, resulting in larger surface microscopic forces. More and more fluid which can be driven at smaller fluid viscosity are attached on the wall surface due to the strong interaction, further compressing the effective flow space and resulting in larger flow resistance. Therefore, the absolute permeability decreases with the increased fluid viscosity at a constant aspect ratio.

Viscosity Effect on Pore-Scale Flow at Different Coordination Numbers

For the sake of studying the fluid viscosity effect on pore-scale flow at different coordination numbers, the following process is developed to keep other structural parameters such as the distributions of the pore and throat radii, the positions of the pore bodies, and the physical size unchanged, except the coordination numbers.

1) We first generate the pore bodies including the radii and positions until the overall porosity reaches the target 0.12, as mentioned in the first step of constructing a stochastic network in section 3.2.
2) Based on the established pore bodies, we, respectively, set the coordination number as 4, 6, 8, and 10 and assign them to each pore correspondingly as the rule indicated in the second step in section 3.2
3) The remaining steps are the same as the ones (steps 3) and 4) of constructing the network) listed in section 3.2.

Through the aforementioned construction process, four stochastic networks with different coordination numbers but the same positions and radii distributions of pore bodies and the physical size are established. The generated distributions of throat radii with four different coordination numbers are shown in **Figure 10A**. It can be seen that the generated distributions of throat radii agree well with each other, guaranteeing the reliability of studying the viscosity effect on pore-scale flow at different coordination numbers.

Figure 10B shows the fluid viscosity effect on the absolute permeability at different coordination numbers. It is clear that the viscosity effect on the absolute permeability differs a lot with and without considering the fluid–solid interaction. The absolute permeability curves overlap at different fluid viscosities when no fluid–solid interaction is taken into account, implying that the absolute permeability is independent of the fluid viscosity. However, the absolute permeability curves separate with each other when the fluid–solid interaction is involved. The larger the fluid viscosity, the smaller is the absolute permeability. This difference can also be due to the fluid–solid interaction. At a constant coordination number, the fluid–solid interaction grows more and more intense with the increased fluid viscosity. More and more fluid is attached on the wall surface, resulting in larger flow resistance and smaller absolute permeability.

CONCLUSION

In this work, a novel model considering the fluid–solid interaction is developed to characterize the confined fluid flow

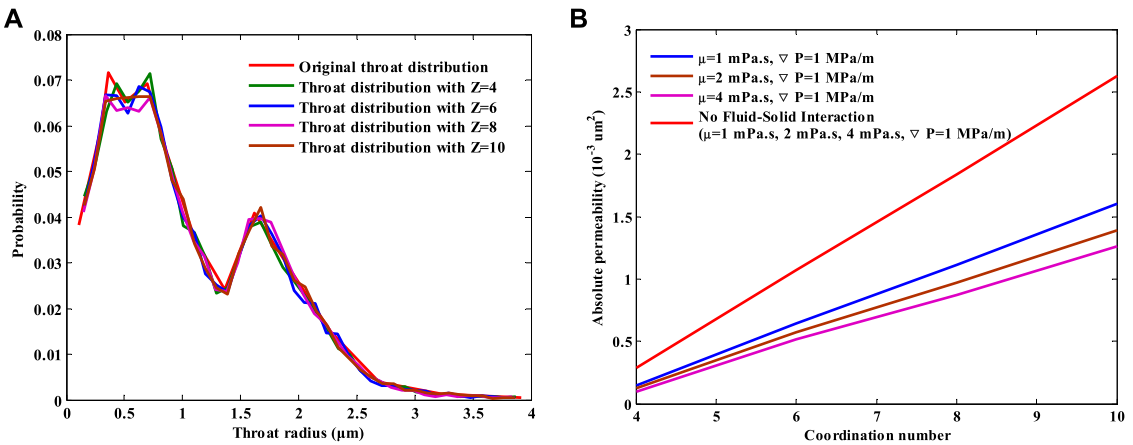

FIGURE 10 | (A) Distribution of throat radius and **(B)** viscosity effect on the absolute permeability at different coordination numbers with and without considering fluid–solid interaction.

in microscales based on the concept of boundary layer. Micro-tube experiments with different scales are used to verify the accuracy and reliability of the novel model. Subsequently, the fluid viscosity effect on confined fluid flow in micro-tubes and pore-scale flow in tight formations are, respectively, studied. The following conclusions are arrived:

1) The viscosity effect on confined fluid flow in micro-tubes induces significant differences from that in conventional flow. With the increased fluid viscosity, the molecular density of the fluid increases which greatly strengthens the fluid–solid interaction. More and more boundary fluid is attached to the wall surface and cannot be driven at a certain displacement pressure gradient. Therefore, the effective flow space is narrowed and the flow resistance is magnified, which results in the smaller decreasing factor and larger Poiseuille number.
2) The absolute permeability is no longer a constant when considering the fluid–solid interaction into pore-scale flow in tight formations. The absolute permeability is not only related to pore structures of the porous media but also affected by the fluid viscosity, which is unlike our previous common sense.
3) The fluid–solid interaction grows with the increase in fluid viscosity, which compresses the efficient flow space. As a result, the absolute permeability decreases with increased fluid viscosity, respectively, under the conditions of different displacement pressure gradient, different aspect ratios, and different coordination numbers.

DATA AVAILABILITY STATEMENT

The original contributions presented in the study are included in the article/supplementary material, and further inquiries can be directed to the corresponding author.

AUTHOR CONTRIBUTIONS

MC is responsible for the main work and writing of the manuscript; QL and LC are responsible for the guidance and modifications of the manuscript; XW provides the thoughts of constructing networks and modifications of the manuscript; and CL and QF helps to improve English grammar of the manuscript.

FUNDING

Exploration on accumulation regularity and prospecting criteria of seepage gas hydrate in Lingshui 18 sea area; Science Foundation of China University of Petroleum, Beijing (Grant No. 2462021XKBH007). Exploration on accumulation regularity and prospecting criteria of seepage gas hydrate in Lingshui 18 sea area; Science Foundation of China University of Petroleum, Beijing (Grant No. 2462021XKBH007). The National Basic Research Program of China (U19B2005), the National Science and Technology Major Project of China (No.2017ZX05069003), and the sponsorship of China Scholarship Council (2019-2020).

REFERENCES

Arya, Sandeep., Khan, Saleem., Vaid, Akhil., Kour, Harneet., and Lehana, P. (2013). Microfluidic Mechanics and Applications: a Review. *J. nano- Electron. Phys.* 5 (4), 04047–04112.

Cao, R., Wang, Y., Cheng, L., Ma, Y. Z., Tian, X., and An, N. (2016). A New Model for Determining the Effective Permeability of Tight Formation. *Transp Porous Med.* 112 (1), 21–37. doi:10.1007/s11242-016-0623-0

Chen, M., Cheng, L., Cao, R., and Lyu, C. (2018). A Study to Investigate Fluid-Solid Interaction Effects on Fluid Flow in Micro Scales. *Energies* 11 (9), 2197–2217. doi:10.3390/en11092197

Chen, M., Cheng, L., Wang, X., Lyu, C., and Cao, R. (2019). Pore Network Modelling of Fluid Flow in Tight Formations Considering Boundary Layer Effect and media Deformation. *J. Pet. Sci. Eng.* 180, 643–659. doi:10.1016/j.petrol.2019.05.072

Churchill, S. W. (1988). Viscous Flows : the Practical Use of Theory. *Harv. Educ. Rev.* 67 (1), 105–106.

Cui, D. S., Xiang, W., Cao, L. J., and Liu, Q. B. (2010). Experimental Study on Reducing Thickness of Adsorbed Water Layer for Red clay Particles Treated by Ionic Soil Stabilizer. *Chin. J. Geotechnical Eng.* 32 (6), 944–949.

Cui, G., Ning, F., Dou, B., Li, T., and Zhou, Q. (2021b). Particle Migration and Formation Damage During Geothermal Exploitation From Weakly Consolidated Sandstone Reservoirs *via* water and CO_2 Recycling. *Energy* 2022, 122507. doi:10.1016/j.energy.2021.122507

Cui, G., Ren, S., Dou, B., and Ninga, F. (2020). *Whole Process Analysis of Geothermal Exploitation and Power Generation from a Depleted High-Temperature Gas Reservoir by Recycling CO 2*.

Cui, G., Ren, S., Dou, B., and Ning, F. (2021a). Geothermal Energy Exploitation from Depleted High-Temperature Gas Reservoirs by Recycling CO2: The Superiority and Existing Problems. *Geosci. Front.* 12 (6), 101078. doi:10.1016/j.gsf.2020.08.014

Damean, N., and Regtien, P. P. L. (2001). Poiseuille Number for the Fully Developed Laminar Flow through Hexagonal Ducts Etched in (1 0 0) Silicone. *Sensors Actuators A Phys.* 90 (1), 96–101. doi:10.1016/s0924-4247(01)00457-5

de Chalendar, J. A., Garing, C., and Benson, S. M. (2018). Pore-scale Modelling of Ostwald Ripening. *J. Fluid Mech.* 835, 363–392. doi:10.1017/jfm.2017.720

Dong, H., Sun, J., Li, Y., Cui, L., Yan, W., and Zhang, J. (2017). Verification of the Carbonate Double-Porosity Conductivity Model Based on Digital Cores. *Interpretation* 5 (2), T173–T183. doi:10.1190/int-2016-0071.1

Dutkowski, K. (2008). Experimental Investigations of Poiseuille Number Laminar Flow of Water and Air in Minichannels. *Int. J. Heat Mass Transfer* 51 (25), 5983–5990. doi:10.1016/j.ijheatmasstransfer.2008.04.070

Fei, W., Xiangan, Y., Shaoliang, X., Li juan, Z., and Renbao, Z. (2009). Influence of Wettability on Flow Characteristics of Water through Microtubes and Cores. *Chin. Sci. Bull.* 54 (13), 2256–2262.

Gad-El-Hak, M. (1999). The Fluid Mechanics of Microdevices-The Freeman Scholar Lecture. *Asme J. Fluids Eng.* 121 (1), 5–33. doi:10.1115/1.2822013

Heuberger, M., Zach, M., and Spencer, N. D. (2001). Density Fluctuations under Confinement: when Is a Fluid Not a Fluid. *Science* 292 (5518), 905–908. doi:10.1126/science.1058573

Holt, J. K., Park, H. G., Wang, Y., Stadermann, M., Artyukhin, A. B., Grigoropoulos, C. P., et al. (2006). Fast Mass Transport through Sub-2-nanometer Carbon Nanotubes. *Science* 312 (5776), 1034–1037. doi:10.1126/science.1126298

Hong, C., Asako, Y., and Lee, J.-H. (2008). Poiseuille Number Correlation for High Speed Micro-flows. *J. Phys. D: Appl. Phys.* 41, 105111–105121. doi:10.1088/0022-3727/41/10/105111

Hu, D., and Blunt, M. J. (2009). Pore-network Extraction from Micro-computerized-tomography Images. *Phys. Rev. E Stat. Nonlin Soft Matter Phys.* 80 (2), 036307.

Huaimin, D., Jianmeng, S., Likai, C., Naser, G., and Weichao, Y. (2019). Characteristics of the Pore Structure of Natural Gas Hydrate Reservoir in the Qilian Mountain Permafrost, Northwest China. *J. Appl. Geophys.* 164, 153–159. doi:10.1016/j.jappgeo.2019.03.005

Huang, Y. Z. (1998). *Percolation Mechanism of Low Permeability Reservoir*. Beijing: Petroleum Industry Press.

Idowu, N. A. (2009). "Pore-Scale Modeling: Stochastic Network Generation and Modeling of Rate Effects in Waterflooding,". Doctor of Philosophy Thesis, Imperial College London, London, 156

Jiang, R. J., Song, F. Q., and Li, H. M. (2006). Flow Characteristics of Deionized Water in Microtubes. *Chin. Phys. Lett.* 23 (12), 3305–3308.

John, T. J., Mathew, B., and Hegab, H. (2009). "Experimental Analysis of Poiseuille Number in Square Microchannels," in Proceedings of the ASME 2009 International Mechanical Engineering Congress and Exposition, Lake Buena Vista, Florida, USA, November 13–19, 2009, 7. doi:10.1115/imece2009-11810

Krishnamoorthy, C., and Ghajar, A. (2007). "Single-Phase Friction Factor in Micro-tubes: A Critical Review of Measurement, Instrumentation and Data Reduction Techniques from 1991-2006," in Proceedings of ASME ICNMM2007, 5th International Conference on Nanochannels, Microchannels and Minichannels Puebla, Mexico, 13. doi:10.1115/icnmm2007-30022

Kumar, R., Islam, M., and Hasan, M. M. (2016). Recent Trends, Challenges and Scope in Single-phase Liquid Flow Heat Transfer in Microchannels-A Review. *Glob. Sci-te.* 8 (2), 113–120. doi:10.5958/2455-7110.2016.00014.8

Levinger, N. E. (2002). Water in Confinement. *Science* 298 (5599), 1722–1723. doi:10.1126/science.1079322

Li, Y., Lei, Q., Liu, X. G., and Xiao, H. M. (2011). Non-linear Seepage Flow Characteristics under Micro Scale. *Pet. Exploration Dev.* 38 (3), 336–340. doi:10.1016/s1876-3804(11)60025-6

Li, Y. (2010). "Study of Microscale Nonlinear Flow Characteristics and Flow Resistance Reducing Methods,". Doctor of Philosophy Thesis (Beijing, China: Institute of Porous Flow and Fluid Mechanics, Chinese Academy of Sciences).

Li, Z. F., and He, S. L. (2005). Influence of Boundary Layers upon Filtration Law in Low-Permeability Oil Reservoirs. *Pet. Geology. Oilfield Dev. Daqing* 24 (2), 57–59.

Li, Z. H. (2001). Characteristics of Micro Scale Flow. *J. Mech. Strength* 23 (4), 476–480.

Ling, Z. Y., Ding, J. N., Yang, J. C., Fan, Z., and Li, C. S. (2002). Research Advance in Microfluid and its Influencing Factors. *J. Jiangsu Univ. (Natural Science)* 23 (6), 1–5.

Liu, D. X., Yue, X. A., Hou, J. R., Cao, J. B., and Wang, L. M. (2005). Experimental Study of Adsorbed Water Layer on Solid Particle Surface. *Acta Mineralogica Sinica* 25 (1), 15–19.

Liu, W. D., Liu, J., Sun, L. H., and Li, Y. (2011). Influence of Fluid Boundary Layer on Fluid Flow in Low Permeability Oilfields. *Sci. Tech. Rev.* 29 (22), 42–44.

Lyu, C., Ning, Z., Chen, M., and Wang, Q. (2019). Experimental Study of Boundary Condition Effects on Spontaneous Imbibition in Tight Sandstones. *Fuel* 235, 374–383. doi:10.1016/j.fuel.2018.07.119

Lyu, C., Ning, Z., Wang, Q., and Chen, M. (2018a). Application of NMR T2 to Pore Size Distribution and Movable Fluid Distribution in Tight Sandstones. *Energy Fuels* 32 (2), 1395–1405. doi:10.1021/acs.energyfuels.7b03431

Lyu, C., Wang, Q., Ning, Z., Chen, M., Li, M., Chen, Z., et al. (2018c). Investigation on the Application of NMR to Spontaneous Imbibition Recovery of Tight Sandstones: An Experimental Study. *Energies* 11 (9), 2359–2371. doi:10.3390/en11092359

Mainak, M., Nitin, C., Rodney, A., and Hinds, B. J. (2005). Nanoscale Hydrodynamics: Enhanced Flow in Carbon Nanotubes. *Nature* 438 (7064), 44.

Makihara, M., Sasakura, K., and Nagayama, A. (1993). The Flow of Liquids in Micro-capillary Tubes. Consideration to Application of the Navier-Stokes Equations. *J. Jpn. Soc. Precision Eng.* 59 (3), 399–404. doi:10.2493/jjspe.59.399

Mapxacin (1987). *Physical and Chemical Mechanism of Reservoir*. Beijing, China: Petroleum Industry Press.

Mazzoco, R. R., and Wayner, P. C. (1999). Aqueous Wetting Films on Fused Quartz. *J. Colloid Interf. Sci.* 214 (2), 156–169. doi:10.1006/jcis.1999.6212

Nie, X. B., Chen, S. Y., and E, M. O. (2004). A Continuum and Molecular Dynamics Hybrid Method for Micro- and Nano-Fluid Flow. *J. Fluid Mech.* 500 (500), 55–64. doi:10.1017/s0022112003007225

Park, S. J., Chung, S., Bang, H- W., Chung, C., Han, D- C., and Chang, J- K. (2002). "Modeling and Designing of Microfluidic System Using Poiseuille Number," in 2nd Annual International IEEE-EMBS Special Topic Conference on Microtechnologies in Medicine and Biology, Madison, Wisconsin USA, 2-4 May 2002 (IEEE). doi:10.1109/MMB.2002.1002413

Pertsin, A., and Grunze, M. (2004). Water−Graphite Interaction and Behavior of Water Near the Graphite Surface. *J. Phys. Chem. B* 108 (4), 1357–1364. doi:10.1021/jp0356968

Pfahler, J., Harley, J., Bau, H., and Zemel, J. (1990). Liquid Transport in Micron and Submicron Channels. *Sensors & Actuators* 21 (89), 159–169. doi:10.1016/0924-4247(89)80008-1

Qu, W. L., Mala, G. M., and Li, D. Q. (2000). Pressure-driven Water Flows in Trapezoidal Silicon Microchannels. *Int. J. Heat Mass Transfer* 43 (3), 353–364. doi:10.1016/s0017-9310(00)00045-4

Raeini, A. Q., Bijeljic, B., and Blunt, M. J. (2018). Generalized Network Modeling of Capillary-Dominated Two-phase Flow. *Phys. Rev. E* 97 (2), 1–20. doi:10.1103/PhysRevE.97.023308

Raoof, A., and Hassanizadeh, S. M. (2010). A New Method for Generating Pore-Network Models of Porous Media. *Transp Porous Med.* 81 (3), 391–407. doi:10.1007/s11242-009-9412-3

Ren, W., and E, W. (2005). Heterogeneous Multiscale Method for the Modeling of Complex Fluids and Micro-fluidics. *J. Comput. Phys.* 204 (1), 1–26. doi:10.1016/j.jcp.2004.10.001

Scatena, L. F., Brown, M. G., and Richmond, G. L. (2001). Water at Hydrophobic Surfaces: Weak Hydrogen Bonding and strong Orientation Effects. *Science* 292 (5518), 908–912. doi:10.1126/science.1059514

Schlichting, H., and Gersten, K. (2003). *Boundary-Layer Theory*. New York: Springer Science & Business Media.

Striolo, A. (2006). The Mechanism of Water Diffusion in Narrow Carbon Nanotubes. *Nano Lett.* 6 (4), 633–639. doi:10.1021/nl052254u

Thomas, J. A., and Mcgaughey, A. J. H. (2009). Water Flow in Carbon Nanotubes: Transition to Subcontinuum Transport. *Phys. Rev. Lett.* 102 (18), 184502–184514. doi:10.1103/physrevlett.102.184502

Wang, X., and Sheng, J. J. (2019). Multi-scaled Pore Network Modeling of Gas-Water Flow in Shale Formations. *J. Pet. Sci. Eng.* 177, 899–908. doi:10.1016/j.petrol.2019.03.005

Wang, X., and Sheng, J. J. (2018). Pore Network Modeling of the Non-darcy Flows in Shale and Tight Formations. *J. Pet. Sci. Eng.* 163, 511–518. doi:10.1016/j.petrol.2018.01.021

Wu, J., Cheng, L., Li, C., Cao, R., Chen, C., Cao, M., et al. (2017b). Experimental Study of Nonlinear Flow in Micropores under Low Pressure Gradient. *Transp Porous Med.* 119 (1), 247–265. doi:10.1007/s11242-017-0882-4

Wu, J. Z., Cheng, L. S., Li, C. L., Cao, R. Y., Chen, C. C., Xu, Z. Y., et al. (2017a). "A Novel Characterization of Effective Permeability of Tight Reservoir - Based on the Flow Experiments in Microtubes," in 19th European Symposium on Improved Oil Recovery (Norway: Stavanger), 16. doi:10.3997/2214-4609.201700299

Wu, J. Z., Cheng, S. L., Li, C., Cao, R., Chen, C., and Xu, Z. (2017c). Flow of Newtonian Fluids with Different Polarity in Micro Scale. *Chin. Sci. Bull.* 62 (25), 2988–2996.

Wu, K., Chen, Z., Li, J., Li, X., Xu, J., and Dong, X. (2017d). Wettability Effect on Nanoconfined Water Flow. *Proc. Natl. Acad. Sci. USA* 114 (13), 3358–3363. doi:10.1073/pnas.1612608114

Xiangan, Y., Nan, W., Zhang, L. J., and Fei, W. (2010). Flow Experiments of HPAM Solution in Quartz Micro-tubes. *Mech. Eng.* 21 (3), 81–84.

Xu, S., Yue, X., and Hou, J. (2007). Experimental Investigation on Flow Characteristics of Deionized Water in Microtubes. *Chin. Sci Bull* 52 (6), 849–854. doi:10.1007/s11434-007-0118-z

Yang, R. -J., Hou, H. -H., Wang, Y. -N., and Fu, L. -M. (2016). Micro-magnetofluidics in Microfluidic Systems: A Review. *Sensors Actuators B: Chem.* 224, 1–15. doi:10.1016/j.snb.2015.10.053

Zhang, P., Zhang, L. Z., Li, W. Y., and Wang, Y. F. (2008). Experiment on the Influence of Boundary Layer on the Non-darcy Seepage Law. *J. Hebei Univ. Eng.* 25 (3), 70–72.

Zhang, X. L., Zhu, W. Y., Cai, Q., and Liu, Q. P. (2014). Analysis of Weakly Compressible Fluid Flow in Nano/micro-Size Circular Tubes Considering Solid wall Force. *Beijing Keji Daxue Xuebao/Journal Univ. Sci. Tech. Beijing* 36, 569–575.

Zhao, C., and Yang, C. (2012). Advances in Electrokinetics and Their Applications in Micro/nano Fluidics. *Microfluid Nanofluid* 13 (2), 179–203. doi:10.1007/s10404-012-0971-1

Zhao, E., Hou, J., Du, Q., Liu, Y., Ji, Y., and Bai, Y. (2021). Numerical Modeling of Gas Production from Methane Hydrate Deposits Using Low-Frequency Electrical Heating Assisted Depressurization Method. *Fuel* 290, 120075. doi:10.1016/j.fuel.2020.120075

Zhao, H., Ning, Z., Wang, Q., Zhang, R., Zhao, T., Niu, T., et al. (2015). Petrophysical Characterization of Tight Oil Reservoirs Using Pressure-Controlled Porosimetry Combined with Rate-Controlled Porosimetry. *Fuel* 154, 233–242. doi:10.1016/j.fuel.2015.03.085

Zhao, J., Kang, Q., Yao, J., Zhang, L., Li, Z., Yang, Y., et al. (2018). Lattice Boltzmann Simulation of Liquid Flow in Nanoporous media. *Int. J. Heat Mass Transfer* 125, 1131–1143. doi:10.1016/j.ijheatmasstransfer.2018.04.123

Zhao, J., Qin, F., Derome, D., and Carmeliet, J. (2020a). Simulation of Quasi-Static Drainage Displacement in Porous media on Pore-Scale: Coupling Lattice Boltzmann Method and Pore Network Model. *J. Hydrol.* 588, 125080. doi:10.1016/j.jhydrol.2020.125080

Zhao, J., Qin, F., Derome, D., Kang, Q., and Carmeliet, J. (2020b). Improved Pore Network Models to Simulate Single-phase Flow in Porous media by Coupling with Lattice Boltzmann Method. *Adv. Water Resour.* 145, 103738. doi:10.1016/j.advwatres.2020.103738

Zhi, X. L. (2003). Experimental Study on Flow Characteristics of Liquid in Circular Microtubes. *Microscale Thermophysical Eng.* 7 (3), 253–265.

Zhu, C. J., Zhang, J., and Pu, Z. (2013). Study on Influence of Boundary Layer on the Non-darcy Seepage Law. *J. Convergence Inf. Tech.* 8 (10), 960–968.

Conflict of Interest: MC, QF, and QL are employed by the China National Offshore Oil Corporation (China).

The remaining authors declare that the research was conducted in absence of any commercial or financial relationships that could be construed as a potential conflict of interest.

Publisher's Note: All claims expressed in this article are solely those of the authors and do not necessarily represent those of their affiliated organizations, or those of the publisher, the editors, and the reviewers. Any product that may be evaluated in this article, or claim that may be made by its manufacturer, is not guaranteed or endorsed by the publisher.

frontiers in Earth Science

ORIGINAL RESEARCH
published: 12 January 2022
doi: 10.3389/feart.2021.808916

Depositional Setting and Enrichment Mechanism of Organic Matter of Lower Cretaceous Shale in Ri-Qing-Wei Basin in the Central Sulu Orogenic Belt

Tengfei Zhou[1]*, *Yaoqi Zhou*[1]*, *Hanjie Zhao*[1,2], *Manjie Li*[1,3] and *Hongyu Mu*[1]

[1]School of Geosciences, China University of Petroleum, Qingdao, China, [2]Xianhe Oil Production Plant of Shengli Oilfield Company, SINOPEC, Dongying, China, [3]Shengli Oil Production Plant of Shengli Oilfield Company, SINOPEC, Dongying, China

OPEN ACCESS

Edited by:
Yanyong Wang,
Chengdu University of Technology, China

Reviewed by:
Huiwen Yue,
Helmholtz Association of German Research Centres (HZ), Germany
Guanhua Li,
University of Alberta, Canada
Liang Zhao,
Hebei GEO University, China

***Correspondence:**
Tengfei Zhou
zhoutfgeoscience@126.com
Yaoqi Zhou
zhouyq@upc.edu.cn

Specialty section:
This article was submitted to Economic Geology, a section of the journal Frontiers in Earth Science

Received: 04 November 2021
Accepted: 29 November 2021
Published: 12 January 2022

Citation:
Zhou T, Zhou Y, Zhao H, Li M and Mu H (2022) Depositional Setting and Enrichment Mechanism of Organic Matter of Lower Cretaceous Shale in Ri-Qing-Wei Basin in the Central Sulu Orogenic Belt. Front. Earth Sci. 9:808916. doi: 10.3389/feart.2021.808916

A suite of source rock consists of mudstone and shale, with great thickness and continuous deposition was found in the well LK-1 in Lingshan island in Ri-Qing-Wei basin. In order to evaluate the hydrocarbon generation prospects of these source rock and find the mechanism of organic matter enrichment, shale samples were selected from the core for TOC (total organic carbon) and element geochemistry analysis. The results show that organic matter abundance of the source rocks are generally high with average TOC content of 1.26 wt%, suggesting they are good source rocks. The geochemical features show that the sedimentary environment is mostly anoxic brackish water to salt water environment with arid to semiarid climate condition. The enrichment mechanism of organic matter varied with the evolution of the basin, which was divided into three stages according to the sedimentary characteristics. In the initial-middle period of rifting evolution (stage 1 and early stage 2), paleoproductivity is the major factor of OM-enrichment reflecting by high positive correlation between the TOC contents and paleoproductivity proxies. While with the evolution of the rift basin, redox condition and terrigenous clastic input became more and more important until they became the major factor of OM enrichment in the middle stage of rift evolution (stage 2). In the later stage of rift evolution (latest stage 2 and stage 3), besides terrigenous clastic input, the effect of paleoclimate on OM-enrichment increased gradually from a minor factor to a major factor.

Keywords: Lingshan Island, organic matter enrichment, shale, Cretaceous, depositional setting

INTRODUCTION

As the most important type of source rock, shale is widely distributed in almost every depositional setting in different tectonic settings (Verma and Armstrong-Altrin, 2013). Whatever depositional setting the shale belongs to, the Total Organic Carbon (TOC) content is the primary indicator to judge the oil and gas potential. Almost each big oil and gas field all over the world owes a suite of shale or mudstone as source rock, with huge thickness and high TOC content. Previous researches (Yan et al., 2018; Gallego-Torres et al., 2007; Mort et al., 2007) indicate that restricted basin sedimentary conditions are good for organic matter (OM) enrichment and there are two typical models for OM enrichment: the paleoproductivity model and the preservation model. The paleoproductivity model

emphasizes that large amount of OM enriched for the higher productivity in the sedimentary water. Large amount of OM consume oxygen in the water, leading to an anoxic environment which is good for preservation of OM (Sageman et al., 2003; 8; Tang et al., 2020). While the preservation model stresses the importance of the sea level fluctuation and the restricted effect of basin, proving an anoxic environment for OM accumulation (Arthur et al., 1998; Mort et al., 2007; Tang et al., 2020). In addition, the terrigenous clastic input is another important factor controlling the OM enrichment in recent study (Tang et al., 2020). Changes in sedimentary environment would affect the OM enrichment. The geochemistry of shale could reflect the sedimentary environment such as Ba, P, Cu for paleoproductivity (Paytan and Griffith, 2007; Algeo et al., 2011), Mo, U, V for redox condition and Al, Ti, Zr for terrigenous clastic input (Tribovillard et al., 2006).

There were a lot of Meso-Cenozoic basins developed in eastern China as the respond to the subduction of western Pacific plate. With the development of petroleum exploration, more and more petroliferous basins were found such as Bohai Bay basin, Songliao basin (Wang et al., 2020). However, the oil and gas potential of Jiaolai basin which is the best record with relatively complete Cretaceous strata, is not ideal. Recently, the Lingshan island scientific drilling (Well LK-1) uncovered there was a rifting basin in the central Sulu orogenic belt, beside the Jiaolai basin. Although a lot of researchers have studied Lingshan island in different aspects, the oil and gas potential is still unclear. This study focuses on the core sample of LK-1, using TOC content and element contents of shale samples to reveal the mechanism of organic matter enrichment.

GEOLOGICAL SETTING

Ri-Qing-Wei basin is located in the central Sulu orogenic belt, eastern coastal Shandong, China. It is a long and narrow late Mesozoic rift basin and is distributed along the NE-SW direction. The northwest boundary is Wulian-Qingdao faults and Jimo-Muping faults, while the southeast boundary is Qianliyan faults. Lingshan island is located in the south Ri-Qing-Wei basin (**Figure 1**). The strata in Lingshan island represents the stratigraphic sequence of Ri-Qing-Wei basin. The stratigraphic sequence is divided into two groups: 1) Laiyang group, the older one which is consisted by a series of gravity flows' deposition (Lü et al., 2011; Zhong et al., 2012; Yang and van Loon, 2016; Yang et al., 2017; Liang et al., 2018; Yang et al., 2018), mainly developed in the west island, including several outcrops (**Figure 2A**) such as Beilaishi, Qiancengya, Chuanchang, Dengta et al., and 2) Qingshan group, the younger one which is mainly dominated by volcanic deposition and a suite of terrestrial clastic deposits (Wang et al., 2015; Zhou et al., 2017; Zhou et al., 2018).

In order to uncover the main layer sequence of the Laiyang group, we set up the Lingshan Island Scientific Drill (Well LK-1). The depth of LK-1 is 1,350 m, and the total thickness of layers of shale and mudstone is about 550 m. This discovery further confirms the existence of Ri-Qing-Wei basin. In the layers of Laiyang group which are presented by the core of LK-1 (**Figure 2B**), various kinds of gravity flows and large amounts of soft sediments deformation structures are found. Also, a lot of markers representing deep-water sedimentary environment are observed, such as iron nodule, vitrain and plant debris. According to the lithology and sedimentary characteristics of LK-1, Yuan et al. (2019) show that the sedimentary strata of Laiyang group developed fan delta, subaqueousfan, turbidite fan and delta from the bottom to the top. In addition, the evolution of Ri-Qing-Wei basin could be divided into four stages (Yuan et al., 2019): initial stage of the basin rifting, the stage of basin expansion and subsidence, the stable stage of deep subsidence and the stage of basin uplift.

MATERIALS AND METHODS

Eighty-two samples of shale of LK-1 were selected to do TOC (total organic carbon) analysis. Thirty samples of the batch above and other 22 samples were selected to do major and trace element analysis.

TOC (total organic carbon) content analyses were done in Northeast Petroleum University. The TOC contents were measeured with acid-dissolution method. Diluted hydrochloric acid were used to removing the inorganic carbon compound of the samples' powder. After, samples were burned in the high temperature oxygen. Carbon content of CO_2 produced during the burning process are all from the organic carbon of samples. The contents of CO_2 were measured by thermal conductivity detector, to get the TOC contents. The detailed analytical method is described by Liu et al. (2019).

Chemical analyses were conducted in the laboratory of Eighth Institute of Geology and Mineral Exploration of Shandong Province, China. Fresh rock pieces without cracks were crushed to 200 meshes before experiment. Major oxides were analyzed by X-ray fluorescence spectrometry (XRF; equipment model is Axios) with the relative standard derivation (RSD) of major oxides less than 5%. Trace elements were analyzed by ICP-MS (equipment model is ICAP Qc), and detailed procedures for trace elements analysis are as described by Liang et al. (2000). The relative standard deviations (RSD) of trace elements are within 5%. The procedures for major and trace element analyses are described by Kimura (1998) and Liang et al. (2000), respectively.

RESULTS

The TOC, major element, trace element and rare element contents of LK-1 shales analyzed in this study are listed in the **Supplementary Table S1**.

TOC Contents

The TOC contents of collected samples of Laiyang group from LK-1 are generally high, with a mean TOC content at about 1.26 wt%. More than 70% of samples' TOC content are greater than 1 wt%. The TOC contents are different within different depth of LK-1. In the depth ranges below, TOC content of most samples are greater than 1 wt%: 145–246 m (average TOC,

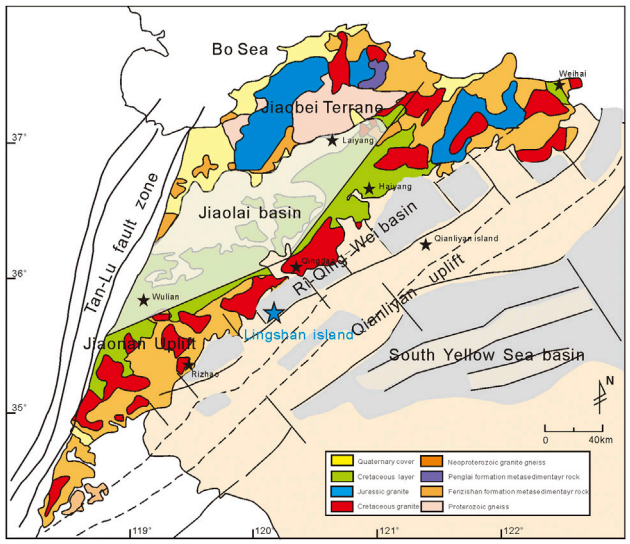

FIGURE 1 | Geological map of Ri-Qing-Wei basin and related area (modifiedfrom Zhou et al., 2015; Liu et al., 2019).

1.39 wt%), 392–453 m (1.74 wt%), 589–665 m (1.35 wt%), 696–776 m (1.46 wt%), 833–919 m (1.85 wt%), 1,031–1,136 m (1.40 wt%), 1,175–1,301 m (1.45 wt%).

Major Elements

The element composition of the shales of Laiyang group are dominated by SiO_2 (51.90–75.12 wt%, average 61.09 wt%), Al_2O_3 (8.68–18.58 wt%, average 14.86 wt%) and CaO (1.21–17.56 wt%, average 7.12 wt%). Besides, these shales also contain relative low concentrations of Fe_2O_3 (average 5.22 wt%), K_2O (average 3.59 wt%), MgO (average 3.42 wt%), Na_2O (average 3.22 wt%). Other major element contents (MnO, P_2O_5, TiO_2) are all lower than 1 wt%.

The contents of SiO_2, Al_2O_3, Fe_2O_3, K_2O and MnO of our samples are close to PAAS (Taylor and Mclennan, 1985), while the contents of CaO and P_2O_5 show much higher than the corresponding contents in PASS (**Figure 3**). The higher concentration of CaO may be related to the calcite veins which widely spread in the core. The higher content of P_2O_5 may reflect the higher paleoproductivity in the sedimentary water in Laiyang period, because P is an important nutrient element to life.

A negative correlation can be seen between SiO_2 and Al_2O_3 contents, and between Al_2O_3 and CaO contents (**Figure 4**). No obvious correlation could be observed between Al_2O_3 and P_2O_5. These indicate Si, Ca, P of samples are mainly effected by sedimentary environment, while the effect of terrigenous clastic input is relative slight. However, samples show a positive correlation between Al_2O_3 and TiO_2 contents. This indicates Ti in samples were mainly controlled by terrigenous clastic input.

Trace Elements

Different trace element owes different sensitivities to specific geological event, so sedimentary environment could be reconstructed by suitable trace elements. Selecting authigenic element composition could help reflecting the sedimentary water conditions better and also its variation during the geological period.

Element enrichment factors were used to see the enrichment or depletion of an element through comparing with selected standard value. In this study, the trace elemental compositions of the samples were compared with the composition of PAAS (Taylor and Mclennan, 1985) through Al-normalization to identify significant deviations. Element enrichment factors of X (X_{EF}) were caluculated by $X_{EF} = (X/Al)_{Sample}/(X/Al)_{PAAS}$. $X_{EF} > 1$ represents the element X was relative enriched in Sample compared to X in PAAS, while $X_{EF} < 1$ represents the situation of depletion. The X_{EF} of Co, Pb, Ba, Sr, Hf, U are obviously larger than 1 showing these trace elements are enriched in samples than PAAS. While the X_{EF} of V, Cr, Ni, Sc, Cu, Cs are much lower than 1, indicating these elements are depleted. As to the elements Li, Rb, Th, Nb and Zr, behaved similar to PAAS for their X_{EF} values are close to 1 (**Figure 3**).

Rare Earth Elements

Both sedimentary water condition and terrigenous clastic input affect the rare earth elements in shale. Because of the stability of rare earth elements after they were absorbed from the sedimentary water and preserved in sedimentary rock, they are often used to reflect the paleo-environment conditions (Sholkovitz et al., 1994; Xia et al., 2015). The∑REE of shales of Laiyang group from LK-1 range from 115.69 to 334.03 × 10^{-6}, with an average value of 225.19 × 10^{-6}, larger than ∑REE contents in UCC (148.14 × 10^{-6}) and PAAS (184.77 × 10^{-6}). The ratios of ∑LREE/∑HREE of our samples are 3.48–6.25 with a mean value of 5.10. These show shales of Laiyang group from LK-1 are enriched in LREE, relative depleted in REE.

The trends of variation of LREE and HREE contents match each other in vertical direction of well LK-1 (**Supplementary Table S1**). At the beginning, from the depth 1,312–1,032 m, the ratio of ∑LREE/∑HREE varies from 4.72 to 5.69, does not change much. The ratio show much variation (3.48–6.25) from the depth 887–412 m. From the depth of 412–24 m, the ratio does not show much fluctuation, demonstrating the similar situation as the beginning. The different variation of ∑LREE/∑HREE may be related to the terrigenous clastic input and sedimentation rate.

DISCUSSION

The calculations of proxies are represented in **Supplementary Table S1**.

Paleoproductivity Proxies

The enrichement of organic matter depends on whether there were enough organic matter sources in the geological period. The sources of organic matter mainly come from two parts: besides the partly organic matter provided by terrigenous clastic input, the biological productivity in sedimentary water is another key factor for organic matter enrichment (Authur and Sageman, 1994). The higher biological productivity in sedimentary

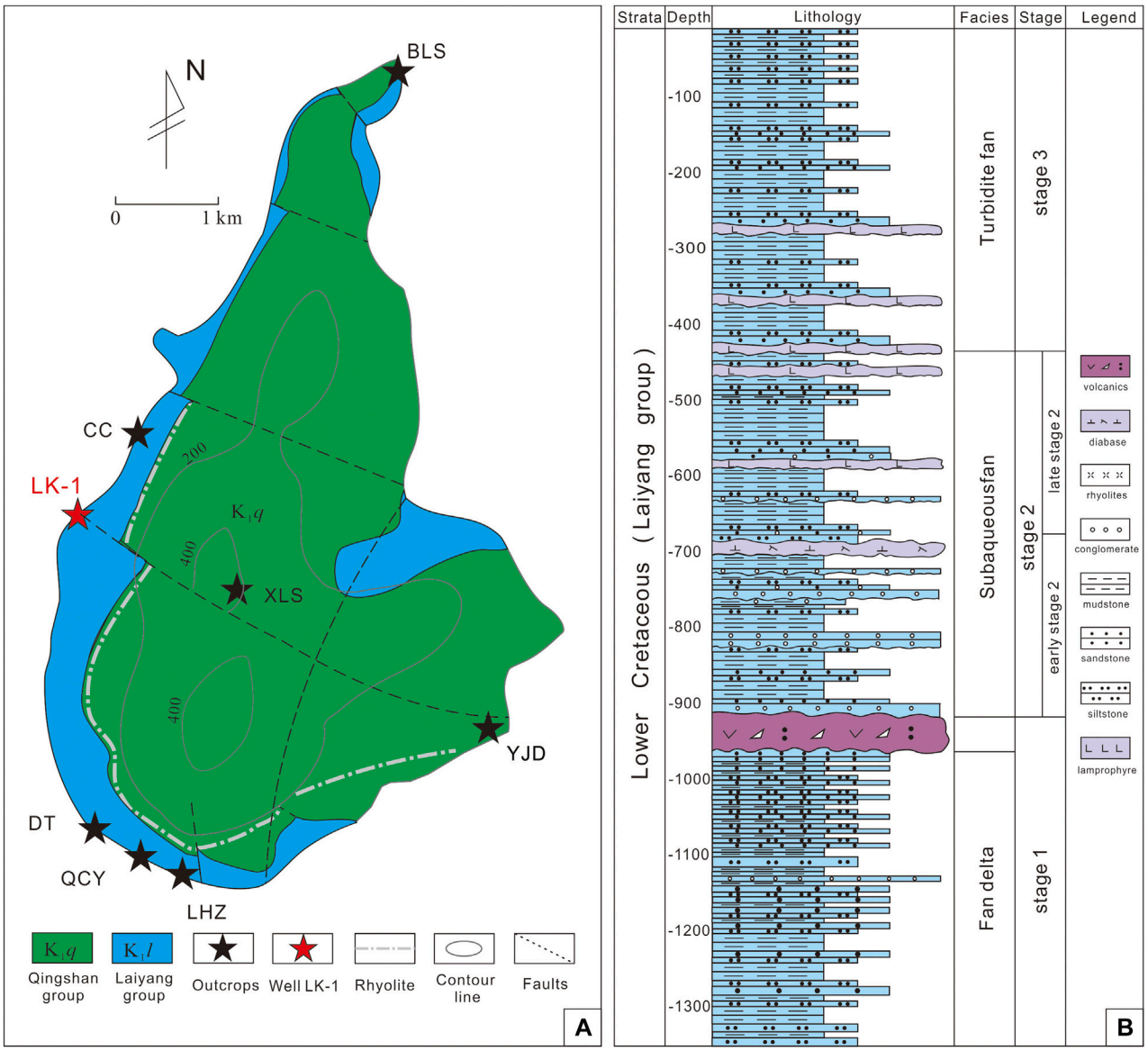

FIGURE 2 | The geological framework and lithology of the well LK-1.

water, the better sedimentary condition for organic matter enrichment. Elements such as Ba, P, Al and Ni were widely used as paleoproductivity proxies. In this study, we select P and biogenic Ba(Ba_{bio}) content to discuss the paleoproductivity of Laiyang group.

Element P is necessary for organisms to survive and reproduce in water and the content of P element could reflect the paleoproductivity. In addition, the P of organisms will transfer into sediments after their death (Shen et al., 2015). In this study, P of samples are divided by Al and Ti to avoid the effect of terrigenous clastic input, so P/Al and P/Ti could reflect the paleoproductivity more precisely. The P/Ti and P/Al of shales of Laiyang group from LK-1 vary with the depth, behaving similar trends. The ratio of P/Ti ranges from 0.14 to 0.71 with a mean value of 0.28 and the ratio of P/Al ranges from 0.007 to 0.035 with a mean value of 0.012. These two ratios are generally larger than the ones of PAAS (P/Ti = 0.12, P/Al = 0.007) according to **Figure 5**, indicating the high level of paleoproductivity in Laiyang period.

Biogenic Ba content (Ba_{bio}) has been widely used as an important paleoproductivity proxy. Also the Ba of samples were affected by terrigenous clastic as other elements, so avoiding the effects of terrigenous clastic is the first step to do. Murray and Leinen (1996) proposed the method to calculate the biogenic Ba content (Ba_{bio}): $Ba_{bio} = Ba_{Sample} - Al_{Sample} \times 0.0077$. The Ba_{bio} values of shales of Laiyang group from LK-1 range from 11.85 to 767.05 ppm with a mean value of 283.99 ppm. The trend of Ba_{bio} does not match the trends of P/Ti and P/Al perfectly

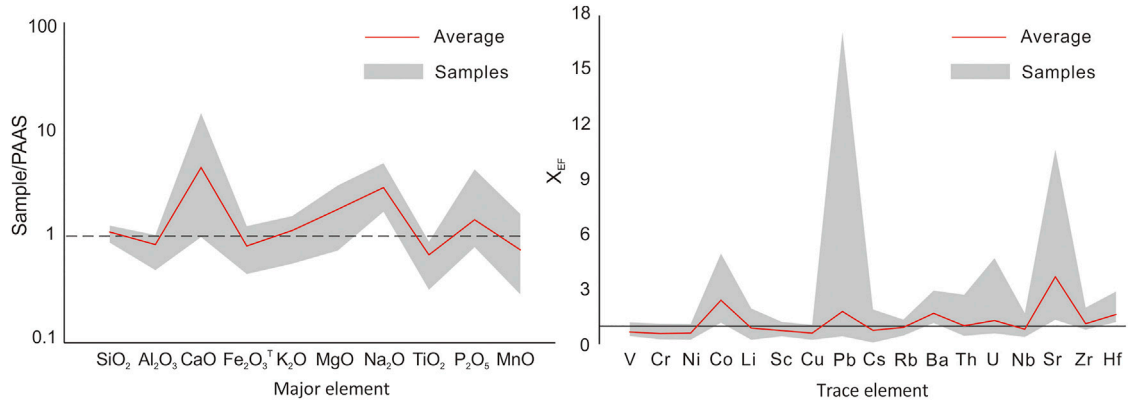

FIGURE 3 | Major elements and XEFof trace elements.

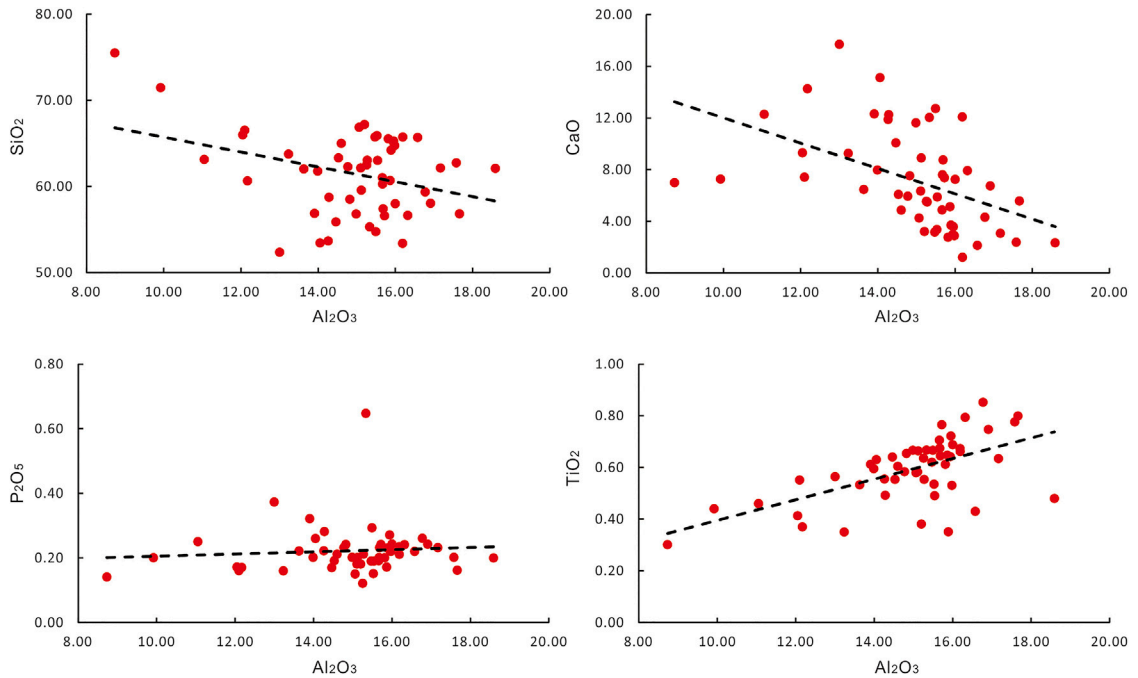

FIGURE 4 | The correlation analysis of major elements from LK-1.

because the content of Ba may be affected by the redox condition and the hydrothermal activity.

Redox Proxies

Redox condition of sedimentary water is directly related to the preservation of organic matter, so the study of redox condition is very important. V/(V + Ni) and Ce_{anom} are widely used to judge the redox condition (Abanda and Hannigan, 2006; Raiswell, 1988; Wang et al., 2014). V/(V + Ni) < 0.46 represents oxic environment, 0.46–0.57 represents semi-anoxic environment, >0.57 represents anoxic environment. Moreover, when the value of V/(V + Ni) is larger than 0.54 but less than 0.82, anoxic and a less strongly stratified water column is indicated. If the value of V/(V + Ni) is larger than 0.84, it indicates the presence of H_2S in a strongly stratified water column (Hatch and Leventhal, 1992). To avoid the potential analytical errors of single element concentration, other reliable indices such as V/Cr, Ce_{anom} and U/Th (German and Elderfield, 1990; Jones and Manning, 1994) are also used in this study. Values of V/Cr above two represent anoxic of depositional conditions, and the closer this value gets to 1, the more oxic the depositional condition it was. Ce anomaly was defined and applied by German and Elderfield (1990) as a paleoredox indicator: Ce anomaly $(Ce/Ce^*) = 3(Ce/Ce_{shale})/[(2La/La_{shale})+(Nd/Nd_{shale})]$,

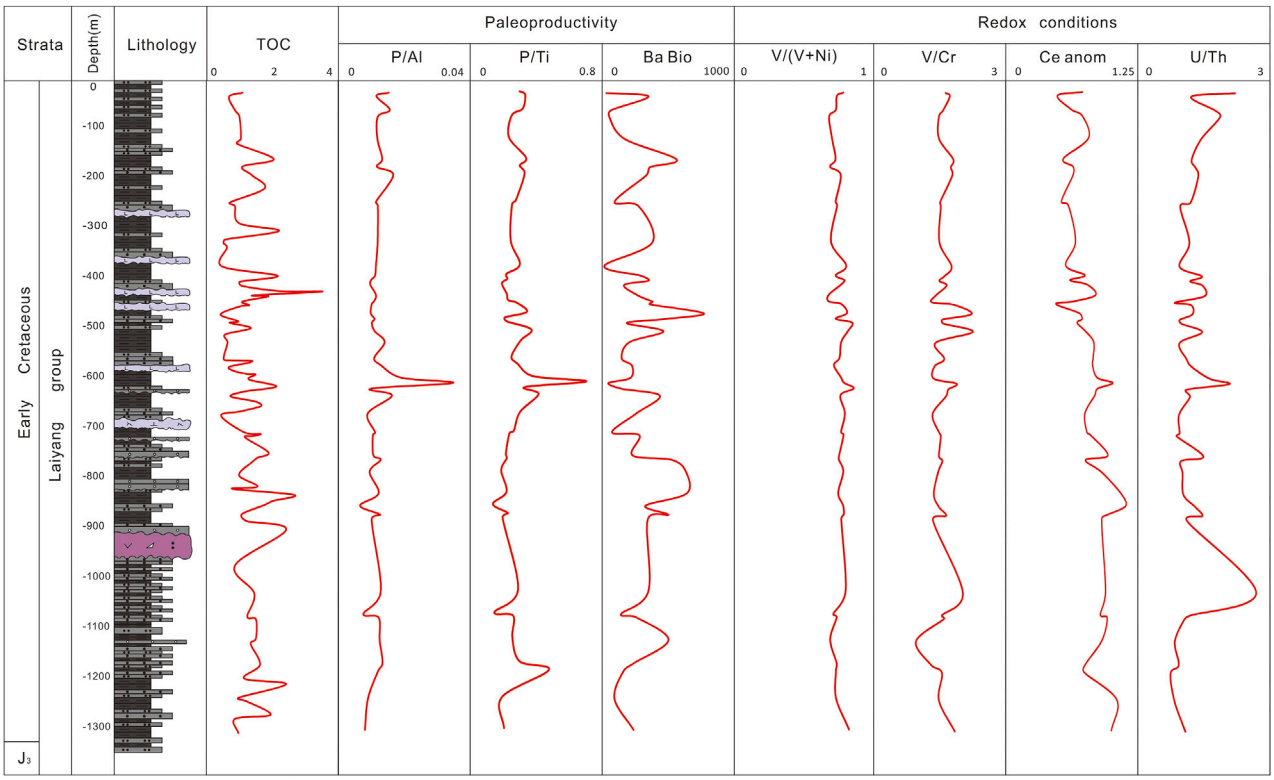

FIGURE 5 | Stratigraphic distribution of TOC, paleoproductivity proxies, redox proxies, in well LK-1.

the value of REE of the shale as normalized standard is from De Baar et al. (1985). As **Figure 5** shows, the values of V/(V + Ni) of our samples do not show obvious fluctuation with the depth, ranging from 0.68 to 0.86 with a mean value of 0.75. This indicates the depositional condition is anoxic environment with a less strongly stratified water column. The values of Ce_{anom} of our samples range from 1.09 to 1.23 with a mean value of 1.16. According to the application of Ce_{anom} from German and Elderfield (1990), the depositional conditions in Laiyang period is an anoxic environment. The values of U/Th range from 0.70 to 2.69 with a mean value of 1.26, indicating the depositional conditions varied between anoxic and dysoxic environment (Jones and Manning, 1994). The values of V/Cr of shales form LK-1 range from 0.97 to 2.26 with a mean value of 1.58. Although the ratio of V/Cr might be affected by the carbonate content (Jones and Manning, 1994), its trend with the depth shows similarity as the trend of V/(V + Ni). Combined those geochemical evidences above with widely distributed pyrite across the whole layers of Laiyang group, the redox condition of Laiyang period is mainly anoxic environment.

Paleosalinity and Paleoclimate Proxies

Paleosalinity is an important indicator to reflect the sedimentary water, and also could help to judge the marine and terrestrial environment. The ratio of Sr/Ba and the Value m (=100 × MgO/Al_2O_3) were selected as the indicators to reflect the paleosalinity. The ratio of Sr/Ba < 0.5 represents freshwater environment, 0.5 < Sr/Ba<1 represents brackish water and Sr/Ba>1 represents salt water (He et al., 2019). Zhang et al. (1988) proposed the value m (=100 × MgO/Al_2O_3) as an indicator to interpret the paleosalinity: m < 1 represents fresh water, 1 < m < 10 represents transitional environment and m > 10 represents marine environment.

The ratios of Sr/Ba of shales of Laiyang group from LK-1 (**Figure 6**) range from 0.22 to 1.89 with a mean value of 0.68 and the value m range from 10.43 to 43.57 with a mean value of 23.27. These indicate the paleosalinity condition of depositional water of Laiyang period is almost brackish water to salt water in a marine environment.

CIA (Chemical Index of Alteration), C-value and Sr/Cu were selected to interpret the paleoclimate condition of Laiyang period. Because the weathering degree of rock is different under different climate condition, the CIA were successfully applied to reflect the paleoclimate condition (McLennan, 1993): 50 to 65 (arid), 65 to 85 (semiarid to semimoist), 85 to 100 (moist). The element Sr, Cu, Mg, Ca are sensitive to the paleoclimate, so the ratios of Sr/Cu and Mg/Ca were used as indicators of paleoclimate in sedimentary period. The ratio of Sr/Cu > 10 was explained to stand for the arid and hot climate condition, while 1 < Sr/Cu < 10 indicates warm and moist climate condition. The trace elements Fe, Mn, Cr, V, Ni and Co have been proved to be relatively enriched in sediments formed under moist conditions. In contrast, the elements of Ca, Mg, K, Na, Sr and Ba exhibit higher concentrations under arid conditions because the evaporation prompts saline minerals to

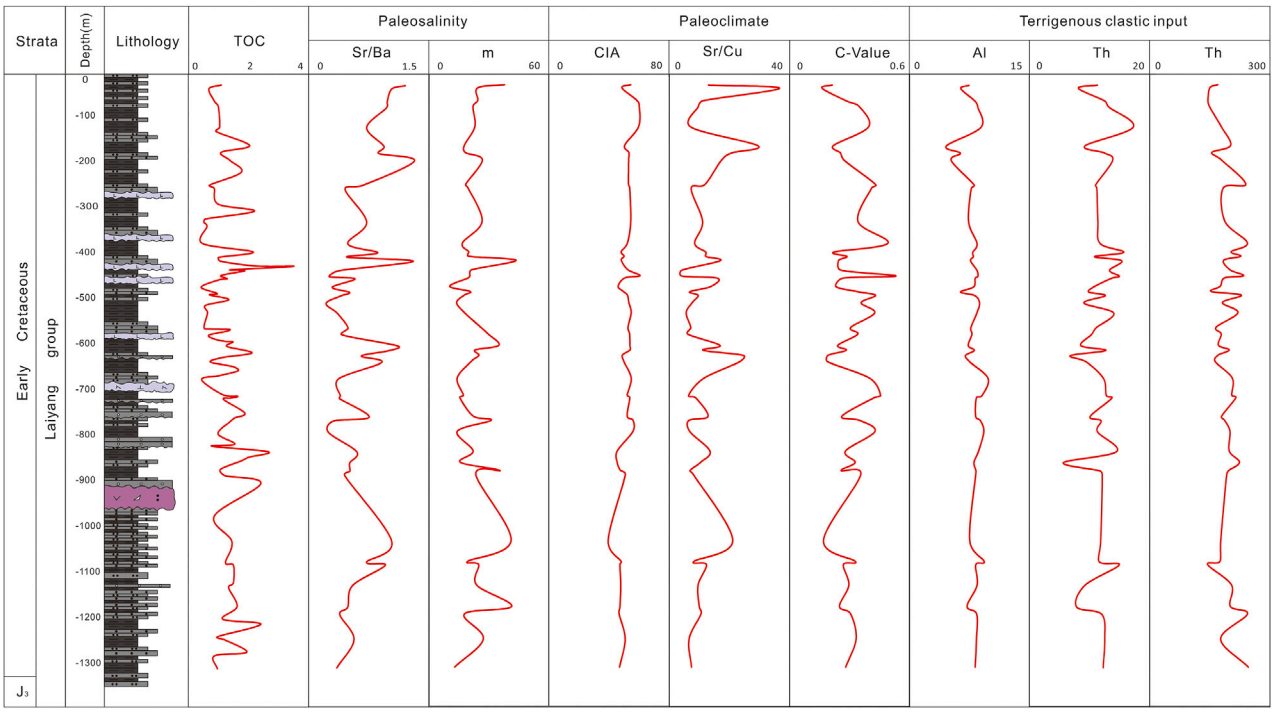

FIGURE 6 | Stratigraphic distribution of TOC, paleosalinity proxies, paleoclimate proxies, and terrigenous clastic proxies, in well LK-1.

precipitate (Cao et al., 2012). The C-value [C-value = Σ(Fe + Mn + Cr + Ni + V + Co)/Σ(Ca + Mg + Sr + Ba + K + Na)] has been applied successfully in evaluating the palaeoclimatic conditions (Cao et al., 2012; Fu et al., 2016; He et al., 2019).

In this study (**Figure 6**), the CIA of shales of Laiyang group range from 39.36 to 60.44 with an mean value 51.26, indicating an arid paleoclimate in Laiyang period. The C-values range from 0.16 to 0.53, reflecting dominant arid to semiarid climatic conditions at the time of deposition. The ratio of Sr/Cu range from 8.46 to 73.59 with a mean value of 25.12, showing an arid to semiarid paleoclimate condition.

Terrigenous Clastic Proxies

The concentration of Al, Ti, Zr, Th in sediments are mainly affected by terrigenous clastic. The latter diagenesis and weathering had little effect on their preservation. So, these elements were used to reflect the situation of terrigenous clastic input during the deposition period (Murphy et al., 2000; Tribovillard et al., 2006). In sedimentary rock, element Ti, Zr and Th are persevered in the heavy minerals such as ilmenite, zircon or in the clay minerals, while Al are mainly persevered in the clay minerals (Young and Nesbitt, 1998). The contents of Al, Ti, Th and Zr vary in a wider range among the shales of Laiyang group: Al (4.62–9.84 wt% with a mean value of 7.97 wt%), Ti (0.18–0.51 wt% with a mean value of 0.36 wt%), Zr (144.51×10^{-6} to 246.31×10^{-6} with a mean value of 191.29×10^{-6}) and Th (5.64×10^{-6} to 28.30×10^{-6} with a mean value of 12.04×10^{-6}). From the trends of variation of Al, Zr, Th, the condition of terrigenous clastic input varied during the Laiyang period. In the first sedimentary period, the change in terrigenous clastic input was quite small. The condition of terrigenous clastic input raised and then reduced for two times, showing an intermediate level. In the second sedimentary period, the change became much more fluctuant and reached the peak in the middle of this period. This may be related to the continuous input water as the rift developed. The level of terrigenous clastic input reduced at the beginning of the third sedimentary period, then raised gradually.

Controlling Factors of OM Enrichment

From the 15 different indicators above, the basic change in sedimentary condition of Laiyang period in Lingshan island could be concluded. The sedimentary environment is almost brackish water to salt water in a marine environment with redox condition of mainly anoxic. The paleoclimate condition is dominated by arid to semiarid climatic conditions. Paleoproductivity kept at a relatively high level in the whole Laiyang period, compared to PAAS. In order to find the relationship between TOC contents and those indicators of different factors and also find the key indicators in different stages, correlation analysis method were applied (**Figure 7**).

In the first stage, the index of P/Al is highly positive correlated to the TOC contents with $R^2 = 0.7655$. This suggests the paleoproductivity is the key controlling factors of OM enrichment in the initial stage. Although Ce_{anom} is slightly negative correlated with the TOC contents ($R^2 = 0.3852$), the correlation coefficients of V/(V + Ni) and V/Cr are all less than

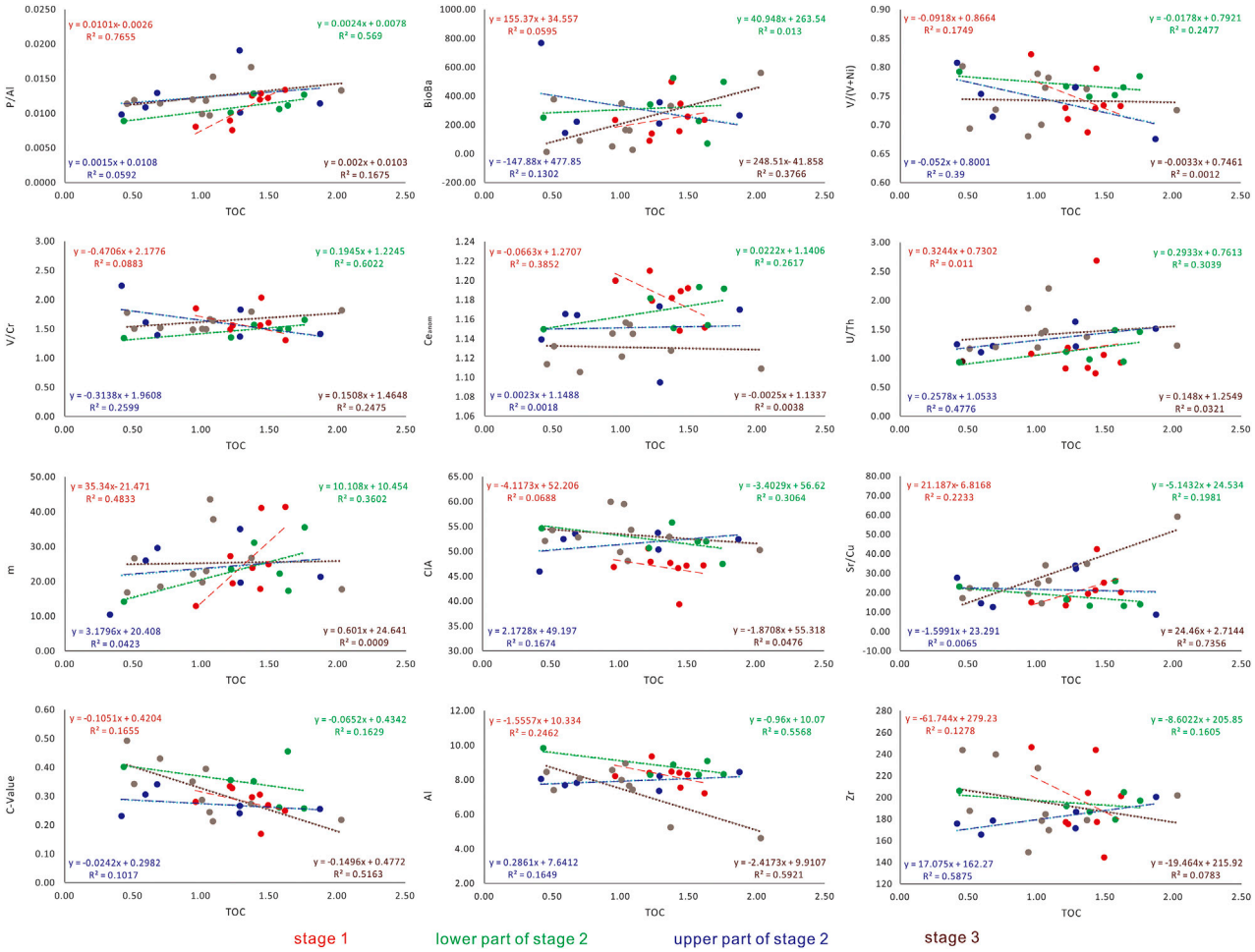

FIGURE 7 | The relationship between paleoproductivity proxies, redox proxies, paleosalinity proxies, paleoclimate proxies, terrigenous clastic proxies andTOC contents of three sedimentary stages of Laiyang group, in well LK-1.

0.2. Thus, the redox condition may be a minor factor of OM enrichment. The paleosalinity condition should be another minor factor of OM enrichment as well, reflecting by its medium positive correlation between m and TOC contents (R^2 = 0.4833). The correlation coefficients of all the other indexes versus TOC contents are less than 0.3, suggesting very little effect on OM enrichment. In the second stage, no obvious pattern were seen from the correlation analysis between the selected indexes with TOC contents if this period was regarded as a whole. This is because the variation of the factors of the upper part and the lower part of the second stage follow different trends, suggesting the controlling factors should be different between the upper and lower parts. In the lower part, the index of P/Al is medium positive correlated to the TOC contents (R^2 = 0.569), suggesting the paleoproductivity is one of the major controlling factor of OM enrichment. The indicators of redox condition show correlation with the TOC content at different level (V/Cr with R^2 = 0.6022, U/Th with R^2 = 0.3039, Ce_{anom} with R^2 = 0.2617), together suggesting the redox condition is another major controlling factor of OM enrichment in this period. The effect of terrigenous clastic in the lower part is significant, because the Al content is medium negative correlated to the TOC content (R^2 = 0.5568). The indicators of paleosalinity and paleoclimate show slightly correlated to the TOC contents (m with R^2 = 0.3602 and CIA with R^2 = 0.3064), suggesting both the paleosalinity and paleoclimate condition are minor factors of OM enrichment. While in the upper part, only the index of Zr is medium positive correlated to the TOC contents with R^2 = 0.5875. But the indexes of Al and Th are almost not correlated to the TOC contents with R^2 = 0.1649, 0.201, respectively. The indexes of redox condition show medium to slight correlation with the TOC contents: U/Th with R^2 = 0.4776, V/(V + Ni) with R^2 = 0.39 and V/Cr with R^2 = 0.2599. These together indicate the terrigenous clastic input and redox condition are the major factors of OM enrichment of the upper part of the second stage of Laiyang period. In the third stage, the indexes of Sr/Cu, C-value and Al are highly to medium correlated to the TOC contents with R^2 = 0.7356, 0.5163 and 0.5921, respectively, suggesting paleoclimate condition is the major factor and the terrigenous clastic input is the minor factor of OM enrichment.

TABLE 1 | Factor of OM-enrichment in different stages.

Peirod	Fator of OM-enrichment	Grade	Represented proxies and correlation coefficient
Stage 1	Paleoproductivity	Major	P/Al with R^2 = 0.7655, positive
	Paleosalinity	Minor	m with R^2 = 0.4833, positive
	Redox condition	Minor	Ce_{anom} with R^2 = 0.3852, negative
Lower part of Stage 2	Paleoproductivity	Major	P/Al with R^2 = 0.569, positive
	Redox condition	Major	V/Cr with R^2 = 0.6022, positive
	Terrigenous clastic input	Major	Al with R^2 = 0.5568, negative
	Paleosalinity	Minor	m with R^2 = 0.3602, positive
	Paleoclimate	Minor	CIA with R^2 = 0.3064, negative
Upper part of Stage 2	Terrigenous clastic input	Major	Zr with R^2 = 0.5875, positive
	redox condition	Major	U/Th with R^2 = 0.4776, positive
			V/(V + Ni) with R^2 = 0.39, negative; and V/Cr with R^2 = 0.2599, negative
Stage 3	Paleoclimate	Major	Sr/Cu with R^2 = 0.7356, positive
			C-value with R^2 = 0.5163, negative
	Terrigenous clastic input	Major	Al with R^2 = 0.5921, negative
	Paleoproductivity	Minor	BioBa with R^2 = 0.3766, positive

The paleoproductivity also show slightly to not positive correlated to the TOC contents, reflecting by the indexes of BioBa (R^2 = 0.3766), P/Ti (R^2 = 0.1836) and P/Al (0.1675). However, the other indicators are not obviously correlated to the TOC contents.

Above all, the controlling factors of OM enrichment varied during the three sedimentary periods (**Table 1**). This may be affected by the different sedimentary mircrofacies of the shale in different depth. Such as the geochemical features of shale from the "Te" part of turbidite may be closely related to the terrigenous clastic input, while the one from deep lake/marine should be much more affected by the paleoproductivity, redox condition and paleosalinity condition. In addition, the paleoclimate didn't change much during Laiyang period. Thus, the evolution of the rift basin which controlled the sedimentary facies should be the primitive factor controlling the OM-enrichment of shale.

CONCLUSION

The TOC contents of shale samples of Laiyang group from the well LK-1 are generally higher than 1 wt%, indicating that they are good source rocks. The factors controlling OM-enrichment varied in different sedimentary period of Laiyang period, recorded by the geochemical features of the shale samples. In the early period of rifting evolution (the stage 1 and the early stage 2), paleoproductivity is the major factor of OM-enrichment. The role of redox condition and terrigenous clastic input became more and more important. When the rift evolution entered the late period (the late stage 2 and the stage 3), terrigenous clastic input is the most important factor controlling the OM-enrichment.(Mcmanus et al., 1998)., (Raiswell et al., 1988)

DATA AVAILABILITY STATEMENT

The original contributions presented in the study are included in the article/**Supplementary Material**, further inquiries can be directed to the corresponding authors.

AUTHOR CONTRIBUTIONS

All authors listed have made a substantial, direct, and intellectual contribution to the work and approved it for publication.

FUNDING

This study was supported by the Project of Department of Science and Technology of Sinopec (No. P20028) and the Fundamental Research Funds for the Central Universities grant (No. 18CX06019A).

SUPPLEMENTARY MATERIAL

The Supplementary Material for this article can be found online at: https://www.frontiersin.org/articles/10.3389/feart.2021.808916/full#supplementary-material

REFERENCES

Abanda, P. A., and Hannigan, R. E. (2006). Effect of Diagenesis on Trace Element Partitioning in Shales. *Chem. Geology.* 230 (1-2), 42–59. doi:10.1016/j.chemgeo.2005.11.011

Algeo, T. J., Kuwahara, K., Sano, H., Bates, S., Lyons, T., Elswick, E., et al. (2011). Spatial Variation in Sediment Fluxes, Redox Conditions, and Productivity in the Permian–Triassic Panthalassic Ocean. *Palaeogeogr. Palaeoclimatol. Palaeoecol.* 308 (1-2), 65–83. doi:10.1016/j.palaeo.2010.07.007

Arthur, M. A., Dean, W. E., and Laarkamp, K. (1998). Organic Carbon Accumulation and Preservation in Surface Sediments on the Peru Margin. *Chem. Geol.* 152 (3), 273–286. doi:10.1016/s0009-2541(98)00120-x

Arthur, M. A., and Sageman, B. B. (1994). Marine Black Shales:Depositional Mechanisms and Environments of Ancient Deposits. *Rev. Earth Plan. Sci.* 22, 499–551. doi:10.1146/annurev.ea.22.050194.002435

De Baar, H. J. W., Bacon, M. P., Brewer, P. G., and Bruland, K. W. (1985). Rare Earth Elements in the Pacific and Atlantic Oceans. *Geochimica Et Cosmochimica Acta* 49 (9), 1943–1959. doi:10.1016/0016-7037(85)90089-4

Gallego-Torres, D., Martínez-Ruiz, F., Paytan, A., Jiménez-Espejo, F. J., and Ortega-Huertas, M. (2007). Pliocene-Holocene Evolution of Depositional Conditions in the Eastern Mediterranean: Role of Anoxia vs. Productivity at Time of Sapropel Deposition. *Palaeogeogr. Palaeoclimatol. Palaeoecol.* 246 (2), 424–439. doi:10.1016/j.palaeo.2006.10.008

German, C. R., and Elderfield, H. (1990). Application of the Ce Anomaly as a Paleoredox Indicator: The Ground Rules. *Paleoceanography* 5 (5), 823–833. doi:10.1029/pa005i005p00823

He, C., Ji, L., Su, A., Wu, Y., Zhang, M., Zhou, S., et al. (2019). Source-rock Evaluation and Depositional Environment of Black Shales in the Triassic Yanchang Formation, Southern Ordos Basin, north-central China. *J. Pet. Sci. Eng.* 173, 899–911. doi:10.1016/j.petrol.2018.10.089

Jones, B., and Manning, D. A. C. (1994). Comparison of Geochemical Indices Used for the Interpretation of Palaeoredox Conditions in Ancient Mudstones. *Chem. Geology.* 111, 111–129. doi:10.1016/0009-2541(94)90085-x

Kimura, T. (1998). Relationships between Inorganic Elements and Minerals in Coals from the Ashibetsu District, Ishikari Coal Field. *Jpn. Fuel Process. Technol.* 56 (1-2), 1–19. doi:10.1016/s0378-3820(97)00089-1

Leventhal, J. R., and Leventhal, J. S. (1992). Relationship between Inferred Redox Potential of the Depositional Environment and Geochemistry of the Upper Pennsylvanian (Missourian) Stark Shale Member of the Dennis Limestone, Wabaunsee County, Kansas, U.S.A. *Chem. Geology.* 99 (1-3), 65–82. doi:10.1016/0009-2541(92)90031-Y

Liang, Q., Jing, H., and Gregoire, D. C. (2000). Determination of Trace Elements in Granites by Inductively Coupled Plasma Mass Spectrometry. *Talanta* 51 (3), 507–513. doi:10.1016/s0039-9140(99)00318-5

Liang, Z., Zhou, Y., and van Loon, A. J. (2018). Soft-sediment Deformation Structures Induced by Rapid Sedimentation in Early Cretaceous Turbidites, Lingshan Island, Eastern China. *Can. J. Earth Sci.* 55 (2), 118–129. doi:10.1139/cjes-2017-0106

Liu, B., Wang, H., Fu, X., Bai, Y., Bai, L., Jia, M., et al. (2019). Lithofacies and Depositional Setting of a Highly Prospective Lacustrine Shale Oil Succession from the Upper Cretaceous Qingshankou Formation in the Gulong Sag, Northern Songliao Basin, Northeast China. *Bulletin* 103 (2), 405–432. doi:10.1306/08031817416

Lu, H. B., Wang, J., and Zhang, H. C. (2011). Discovery of the Late Mesozoic Slump Beds in Lingshan Island, Shandong, and a Pilot Research on the Regional Tectonics. *Acta Geologica Sinica* 85 (6), 938–946. (in Chinese with English abstract).

Mclennan, S. M., Hemming, S., Mcdaniel, D. K., and Hanson, G. N. (1993). "Geochemical Approaches to Sedimentation, Provenance, and Tectonics," in *Processes Controlling the Composition of Clastic Sediments* (Boulder, Colorado: Geological Society of America Special Paper), 284. doi:10.1130/spe284-p21

Mcmanus, J., Berelson, W. M., Klinkhammer, G. P., Johnson, K. S., Coale, K. H., Anderson, R. F., et al. (1998). Geochemistry of Barium in marine Sediments: Implications for its Use as a Paleoproxy. *Geochimica Et Cosmochimica Acta* 62 (21-22), 3453–3473. doi:10.1016/s0016-7037(98)00248-8

Mort, H., Jacquat, O., Adatte, T., Steinmann, P., Föllmi, K., Matera, V., et al. (2007). The Cenomanian/Turonian Anoxic Event at the Bonarelli Level in Italy and Spain: Enhanced Productivity And/or Better Preservation? *Cretaceous Res.* 28 (4), 597–612. doi:10.1016/j.cretres.2006.09.003

Murphy, J. B., Strachan, R. A., Nance, R. D., Parker, K. D., and Fowler, M. B. (2000). Proto-Avalonia: A 1.2-1.0 Ga Tectonothermal Event and Constraints for the Evolution of Rodinia. *Geology* 28 (12), 1071–1074. doi:10.1130/0091-7613(2000)028<1071:paagte>2.3.co;2

Murray, R. W., and Leinen, M. (1996). Scavenged Excess Aluminum and its Relationship to Bulk Titanium in Biogenic Sediment from the central Equatorial Pacific Ocean. *Geochimica Et Cosmochimica Acta* 60 (20), 3869–3878. doi:10.1016/0016-7037(96)00236-0

Paytan, A., and Griffith, E. M. (2007). Marine Barite: Recorder of Variations in Ocean export Productivity. *Deep Sea Res. Part. Top. Stud. Oceanogr.* 54 (5-7), 687–705. doi:10.1016/j.dsr2.2007.01.007

Raiswell, R., Buckley, F., Berner, R., and Anderson, T. (1988). Degree of Pyritization of Iron as a Paleoenvironmental Indicator of Bottom-Water Oxygenation[J]. *J. Sediment. Petrology* 58 (5), 812–819.

Raiswell, R., Buckley, F., Berner, R. A., and Anderson, T. F. (1988). Degree of Pyritization of Iron as a Paleoenvironmental Indicator of Bottom-Water Oxygenation. *J. Sediment. Petrology* 58 (5), 812–819. doi:10.1306/212f8e72-2b24-11d7-8648000102c1865d

Sageman, B. B., Murphy, A. E., Werne, J. P., Straeten, C. A. V., Hollander, D. J., and Lyons, T. W. (2003). A Tale of Shales: the Relative Roles of Production, Decomposition, and Dilution in the Accumulation of Organic-Rich Strata, Middle-Upper Devonian, Appalachian basin. *Chem. Geol.* 195 (1-4), 229–273. doi:10.1016/s0009-2541(02)00397-2

Shen, J., Schoepfer, S. D., Feng, Q., Zhou, L., Yu, J., Song, H., et al. (2015). Marine Productivity Changes during the End-Permian Crisis and Early Triassic Recovery. *Earth-Science Rev.* 149, 136–162. doi:10.1016/j.earscirev.2014.11.002

Sholkovitz, E. R., Landing, W. M., and Lewis, B. L. (1994). Ocean Particle Chemistry: The Fractionation of Rare Earth Elements between Suspended Particles and Seawater. *Geochimica Et Cosmochimica Acta* 58 (6), 1567–1579. doi:10.1016/0016-7037(94)90559-2

Tang, S. H., Xi, Z. D., Zhu, W. P., Li, Y., and Yan, X. L. (2020). Factors Controlling Organic Matter Accumulation in the Upper Ordovician Wufeng Shale from Upper Yangtze Platform. *J. China coal Soc.* 45 (1), 285–295. (in Chinese with English abstract). doi:10.1016/j.marpetgeo.2020.104597

Taylor, S. R., and Mclennan, S. M. (1985). "The Continental Crust: its Composition and Evolution," in *An Examination of the Geochemical Record Preserved in Sedimentary Rocks* (Hoboken, New Jersey, US: Blackwell Scientific Pub).

Tribovillard, N., Algeo, T. J., Lyons, T., and Riboulleau, A. (2006). Trace Metals as Paleoredox and Paleoproductivity Proxies: An Update. *Chem. Geol.* 232 (1-2), 12–32. doi:10.1016/j.chemgeo.2006.02.012

Verma, S. P., and Armstrong-Altrin, J. S. (2013). New Multi-Dimensional Diagrams for Tectonic Discrimination of Siliciclastic Sediments and Their Application to Precambrian Basins. *Chem. Geology.* 355, 117–133. doi:10.1016/j.chemgeo.2013.07.014

Wang, J., Chang, S.-C., Wang, K.-L., Lu, H.-B., and Zhang, H.-C. (2015). Geochronology and Geochemistry of Early Cretaceous Igneous Units from the central Sulu Orogenic belt: Evidence for Crustal Delamination during a Shift in the Regional Tectonic Regime. *J. Asian Earth Sci.* 112, 49–59. doi:10.1016/j.jseaes.2015.09.009

Wang, M., Chen, Y., Bain, W. M., Song, G., Liu, K., Zhou, Z., et al. 2020). Direct Evidence for Fluid Overpressure during Hydrocarbon Generation and Expulsion from Organic-Rich Shales. *Geology*, 48(4), 374–378.doi:10.1130/g46650.1

Wang, X. X., Zheng, R. C., Yan, G. Q., Wang, C. Y., and Chen, H. R. (2014). The Mudstone Sedimentary Environment and Provenance Analysis Based on the Geochemical Evidence of Rare Earth Elements: Take Chang 9 Oil-Bearing Layer in Longdong Area of Ordos Basin as an Example. *Nat. Gas Geosci.* 25 (9), 1387–1394. (in Chinese with English abstract). doi:10.11764/j.issn.1672-1926.2014.09.1387

Xia, W., Yu, B. S., and Sun, M. D. (2015). Depositional Setting and Enrichment Mechanism of Organic Matter of the Black Shales of Niutitang Formation at the Bottom of Lower Cambrian, in Well Yuke 1, Southeast Chongqing. *J. Mineral. Petrol.* 35 (2), 70–80. (in Chinese with English abstract). doi:10.19719/j.cnki.1001-6872.2015.02.009

Yan, C. N., Jin, Z. J., Zhao, J. H., Du, W., and Liu, Q. Y. (2018). *Influence of Sedimentary Environment on Organic Matter Enrichment in Shale: A Case Study of the Wufeng and Longmaxi Formations of the Sichuan Basin*. China.

Yang, R., Fan, A., Han, Z., and van Loon, A. J. T. (2017). A Marine or Continental Nature of the Deltas in the Early Cretaceous Lingshandao Formation-Evidences from Trace Elements. *Acta Geologica Sinica - English Edition* 91 (1), 367–368. doi:10.1111/1755-6724.13094

Yang, R., and van Loon, A. J. (2016). Early Cretaceous Slumps and Turbidites with peculiar Soft-Sediment Deformation Structures on Lingshan Island (Qingdao, China) Indicating a Tensional Tectonic Regime. *J. Asian Earth Sci.* 129, 206–219. doi:10.1016/j.jseaes.2016.08.014

Yang, T., Cao, Y., Friis, H., Liu, K., and Wang, Y. (2018). Origin and Evolution Processes of Hybrid Event Beds in the Lower Cretaceous of the Lingshan Island, Eastern China. *Aust. J. Earth Sci.* 65 (4), 517–534. doi:10.1080/08120099.2018.1433236

Young, G. M., and Nesbitt, H. W. (1998). Processes Controlling the Distribution of Ti and Al in Weathering Profiles, Siliciclastic Sediments and Sedimentary Rocks. *J. Sediment. Res.* 68 (3), 448–455. doi:10.2110/jsr.68.448

Zhang, S. S. (1988). Study on the Ratio of Mg and Al in Sedimentary Layer and its Application. *Bull. Mineralogy,Petrology Geochem.* 1(02), 112–113. (in Chinese with English abstract).

Zhong, J. H. (2012). Lingshan Island Mesozoic Sedimentary Rocks in Deep Water Far Source Turbidite or continental delta Deposits? A Discussion with Professor Lu Hongbo. *Geol. Rev.* 58 (6), 1180–1182. (in Chinese with English abstract). doi:10.1016/j.jop.2017.02.002

Zhou, Y.-Q., Peng, T.-M., Zhou, T.-F., Zhang, Z.-K., Tian, H., Liang, W.-D., et al. (2017). Soft-sediment Deformation Structures Related to Volcanic Earthquakes of the Lower Cretaceous Qingshan Group in Lingshan Island, Shandong Province, East China. *J. Palaeogeogr.* 6 (2), 162–181. doi:10.1016/j.jop.2017.02.002

Zhou, Y. Q., Zhou, T. F., Ma, C. Q., Zhang, Z. K., Dong, S. H., Gu, Y. J., et al. (2018). Transcrustal Magmatic System of Early Cretaceous (Qingshan Stage) in Eastern Shandong and the Basin Formation Related to "Thermal Upwelling-Detachment". *Earth Sci.* 43 (10), 3373–3390. (in Chinese with English abstract). doi:10.3799/dqkx.2018.998

Conflict of Interest: Author HZ is employed by the company Xianhe Oil Production Plant of Shengli Oilfield Company, SINOPEC; and Author ML is employed by the company Shengli Oil Production Plant of Shengli Oilfield Company, SINOPEC.

The remaining authors declare that the research was conducted in the absence of any commercial or financial relationships that could be construed as a potential conflict of interest.

Publisher's Note: All claims expressed in this article are solely those of the authors and do not necessarily represent those of their affiliated organizations, or those of the publisher, the editors and the reviewers. Any product that may be evaluated in this article, or claim that may be made by its manufacturer, is not guaranteed or endorsed by the publisher.

frontiers in Earth Science

ORIGINAL RESEARCH
published: 31 January 2022
doi: 10.3389/feart.2021.824410

Study of Water Huff-n-Puff in Low-Permeability Oil Reservoirs With Horizontal Fractures: A Case Study of Chang 6 Reservoir in Yanchang, China

Xuangang Meng[1], Song Hang[1], Heng Zhang[2], Feilong Gao[2], Yong Gao[2] and Xiangfang Li[1]*

[1]MOE Key Laboratory of Petroleum Engineering, China University of Petroleum, Beijing, China, [2]Qilicun Oil Production Plant, Yanchang Oilfield, Yan'an, China

Water huff-n-puff is an effective technology to enhance oil recovery (EOR) of low-permeability reservoirs, which are usually developed with hydraulic fracturing. Fluid exchange between fractures and the matrix is the main EOR mechanism. However, the presented water huff-n-puff simulations usually assume vertical fracture morphology, while the horizontal fractures formed in shallow reservoirs are rarely reported. In this study, we first introduced the water huff-n-puff process in a low-permeability oil reservoir with horizontal fractures and described the multiphase flow characteristics during the huff, soak, and puff stages. Then combined with a series of experiments, a comprehensive method is used to determine the key flow parameters, that is, capillary pressure and relative permeability. Finally, using the Chang 6 reservoir as an example, a series of numerical simulations were conducted to demonstrate the effect of water huff-n-puff on the well performance in this field. The simulation results showed that oil production is mainly affected by the injection volume and injection rate, while water production mainly depends on the well shut-in time. For a typical well in this field, the optimal injection volume, injection rate, and well shut-in time are 300 m^3, 10 m^3/d, and 30 days, respectively. In addition, our results showed that increasing the number of cycles not only benefits fluid exchange but also enhances the formation pressure. Both of them can accelerate the development of low-permeability oil reservoirs.

Keywords: water huff-n-puff, low-permeability reservoirs, horizontal fracture, Chang 6 reservoir, imbibition

OPEN ACCESS

Edited by:
Yu Pang,
University of Calgary, Canada

Reviewed by:
Yanwei Wang,
Jilin University, China
Liang Huang,
Chengdu University of Technology, China
Lei Li,
China University of Petroleum (Huadong), China

****Correspondence:***
Xuangang Meng
mxuangang@163.com

Specialty section:
This article was submitted to Economic Geology, a section of the journal Frontiers in Earth Science

Received: *29 November 2021*
Accepted: *29 December 2021*
Published: *31 January 2022*

Citation:
Meng X, Hang S, Zhang H, Gao F, Gao Y and Li X (2022) Study of Water Huff-n-Puff in Low-Permeability Oil Reservoirs With Horizontal Fractures: A Case Study of Chang 6 Reservoir in Yanchang, China. Front. Earth Sci. 9:824410. doi: 10.3389/feart.2021.824410

1 INTRODUCTION

With the depletion of conventional resources and the increase in energy demand, low-permeability oil reservoirs play an important role in the world energy map (Wang et al., 2018; Rao et al., 2020; Feng et al., 2021). Due to the poor physical properties of the reservoir, that is, small pore size, low porosity, and low permeability, hydraulic fracturing becomes the necessary technology to develop these types of reservoirs in a commercial and effective way (Takahashi and Kovscek, 2010; Ren et al., 2016; Huang et al., 2021a; Huang et al., 2021b). However, the fields usually show a rapid decline in the production rate and formation pressure, which corresponds to low recovery that depends only on elastic energy (Han et al., 2021). Therefore, how to improve oil recovery after depletion production has become an urgent target for researchers and engineers. Due to its wide distribution in nature, water is considered the most appropriate medium to supplement formation energy. Moreover, in

order to extract more oil from low-permeability reservoirs, water huff-n-puff is the preferred technology because injected water in the fractures and crude oil in the matrix can exchange with each other under the drive of capillary force (Wang et al., 2018). Moreover, this technology has been already put into practice in some areas, such as the Changqing oil field and the Yanchang oil field in China. Therefore, research studies on the dynamic process and influencing factors of water huff-n-puff are important to improve the well performance of reservoirs with low permeability.

During the water huff-n-puff process, the well is shut down for a period of time after the injection of water. Under the drive of capillary pressure, injected water is imbibed into the matrix and displaces the oil into the fracture or into the area near the wellbore. Subsequently, the well is reopened, and the oil in the fractures or the near-wellbore area can be produced easily (Wang et al., 2021a; Wang et al., 2021b). Therefore, imbibition under the drive of capillary pressure is considered to be the main mechanism of water huff-n-puff to improve the recovery of low-permeability reservoirs. According to this mechanism, researchers have conducted numerous laboratory experiments and numerical simulations (Wilsey and Bearden, 1954; Graham and Richardson, 1959; Tavassoli et al., 2005; Sun et al., 2022). Rangel-German and Kovscek (2004) used a microscopic visualization model to observe the fluid exchange between fractures and the sandstone matrix, and the results showed that the fluid exchange is affected by the injection rate and the relative permeability of the media. Wang et al. (2018) conducted a series of imbibition experiments and found that there is an optimum permeability for spontaneous imbibition. This is because the variation of permeability has contradictory effects on spontaneous imbibition, that is, the decrease in capillary pressure and the increase of water flow space. Rao et al. (2020) investigated the mechanisms of water puff-n-huff in low-permeability reservoirs with complex fracture networks, and the results showed that the surface area of fractures determines the imbibition efficiency. His results suggest that increasing the complexity of fractures can promote fluid exchange between the fractures and the matrix. In addition, formation energy supplementation and unstable displacement are also considered to contribute to EOR. Wang et al. (2019) conducted a simulation to evaluate the effect of multiple cycles on well production in a tight oil block. The results showed that increasing the number of cycles can increase the injection pressure and decrease the capillary pressure, leading to a decrease in development effects.

Although researchers have conducted many experiments and simulations to investigate the effects of water huff-n-puff on well performance in low-permeability reservoirs, most of the work focuses on reservoirs with vertical fractures. In fact, the morphology of hydraulic fractures strongly depends on the relative magnitude of stress in the vertical and horizontal directions. For example, in a deposit with deep burial depth, the hydraulic fractures usually expand in the vertical direction because the stress in this direction is much greater than that in the horizontal direction. However, for a reservoir with shallow burial depth, the stress in the horizontal direction is in the advantage position, leading to the formation of horizontal fractures (Hartsock and Warren, 1961). Fisher and Warpinski (2012) made a statistical analysis of ten thousand of hydraulic fractures in North America and found that the morphology of hydraulic fractures is horizontal when the depth of the reservoirs is less than 2000 ft; at a depth greater than 4000 ft, mainly vertical fractures are found. At the Yanchang oil field in China, the burial depth of the reservoirs is in the range of 500–700 m. Thus, the morphology of fractures in this area usually extends in the horizontal direction. However, the huff-n-puff process of water and its effects on the well performance in these reservoirs have not been well studied.

In this article, we first presented the process of water huff-n-puff in a low-permeability oil reservoir with horizontal fractures, accompanied by the multiphase flow characteristics during huff, soak, and puff stages. Then in combination with the imbibition experiments, a comprehensive method is used to determine the key flow parameters, that is, capillary pressure and relative permeability. Finally, using the Chang 6 reservoir as an example, the impact of the water huff-n-puff method on the well performance of low-permeability oil reservoirs with horizontal fractures is evaluated with a series of numerical simulations.

2.MECHANISM ANALYSIS OF WATER HUFF-N-PUFF

Water huff-n-puff could enhance oil recovery because of the supplement of formation energy and the exchange between crude oil in the matrix and injected water in the fractures. Based on the migration of fluids, water huff-n-puff can be divided into huff, soak, and puff stages (Wang et al., 2018; Gao et al., 2022).

As illustrated in **Figure 1A**, in the huff stage, water is injected into the reservoirs with high pressure to create the fracture networks. For a reservoir with low permeability and shallow depth, the horizontal morphology with an elliptical shape is the most common. In this stage, the injected water fills the fractures and then flows into the matrix in the vertical direction and the radial direction. Overall, the injected water increases the pressure of the formation and lowers the oil saturation near the wellbore. After the water injection, the well is shut down for a period of time, which can be referred to the soak stage. As illustrated in **Figure 1B**, capillary pressure plays the main role in this stage and determines the redistribution of fluids, that is, oil and water. Under the drive of capillary pressure, the convective motion of oil and injected water is achieved by spontaneous imbibition. Overall, the main objective of well shut-in is to exchange the crude oil at depth to the fracture or near-wellbore zone. After a certain period of shut-in, the well is reopened and the oil starts to be produced. As illustrated in **Figure 1C**, under the drive of drawdown pressure, the oil in the fractures flows rapidly to the bottom hole, resulting in higher production that lasts only for a short time. With the continuous production, both of the fluids in the radial and vertical directions would flow into the fractures. After a period of production, the oil in the fractures

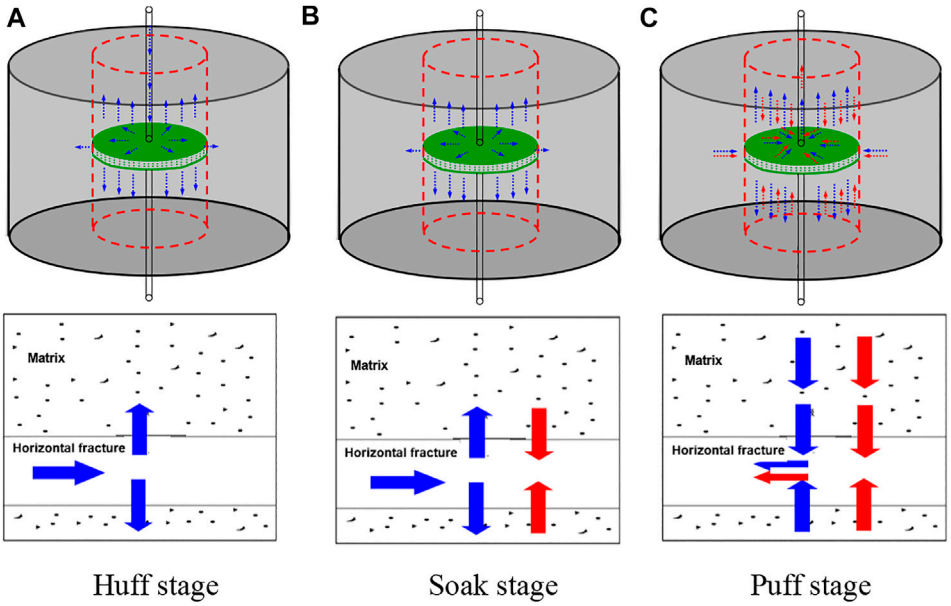

FIGURE 1 | Schematic diagram for the water huff-n-puff in low-permeability reservoirs with a horizontal fracture. **(A)** Huff stage, **(B)** soak stage, **(C)** puff stage.

TABLE 1 | Sample properties in the Chang 6 reservoir.

Parameter	Length (cm)	Radius (cm)	Porosity (%)	Permeability (mD)	$r_{ave}(\mu m)$
Sample 1	5.02	2.50	10.2	0.34	0.48
Sample 2	5.02	2.51	11.4	0.48	0.47

and near-wellbore zone is essentially removed, and the well shows the characteristics of depletion development again.

3 ESTIMATION OF CAPILLARY PRESSURE AND RELATIVE PERMEABILITY

Based on the analysis of the mechanism of water huff-n-puff, the imbibition effect is the key factor for the migration and redistribution of fluids. Therefore, in this part, two cores from the Chang 6 reservoir are selected to conduct the imbibition experiments. Meanwhile, some related experiments, such as, wettability measurement, mercury injection test, and interfacial tension (IFT) measurement, are also conducted. Based on the experimental results, we used a comprehensive method to determine the capillary pressure and relative permeability, which are the fundamental parameters for numerical simulations.

Capillary Pressure

Two sandstones with low permeability from the Chang 6 reservoir were used for the experiments. The information of porosity and permeability is given in **Table 1**. Mercury injection and pore size distribution (PSD) curves were measured using an AutoPore IV mercury-injection analyzer with the highest pressure of 204 MPa and the pore size ranging from 0.006–360 μm, as shown in **Figure 2**.

It should be noted that the capillary pressure curves of the oil–water system can be estimated based on the mercury injection curves by correcting the difference between the oil–water system and the Hg–air system. Before the correction, the wettability of the rock and the IFT of the oil–water system should be determined. In this study, the sessile drop method was used to measure the contact angle, and the results for our samples are 16.6° and 8.2°, respectively (**Figure 3**). Therefore, it is assumed that the Chang 6 reservoir is water-wet. Meanwhile, the interfacial tension (IFT) of the crude oil is measured by a spinning drop tensiometer at room temperature of 20°C and reservoir temperature of 35°C, and the results are shown in **Figure 4**. At room temperature, the IFT is 35 mN/m, while at reservoir temperature, the IFT decreases to 22 mN/m.

Based on the measured contact angle and IFT, the capillary pressure of the oil–water system at room temperature (20°C) and reservoir temperature (35°C) is shown in **Figure 5**. In this study, the capillary pressure at reservoir temperature is considered as the representative one in the reservoir. it should be noted that this replacement is based on the following assumptions: 1) the effect of pressure on IFT is ignored because IFT results from the density

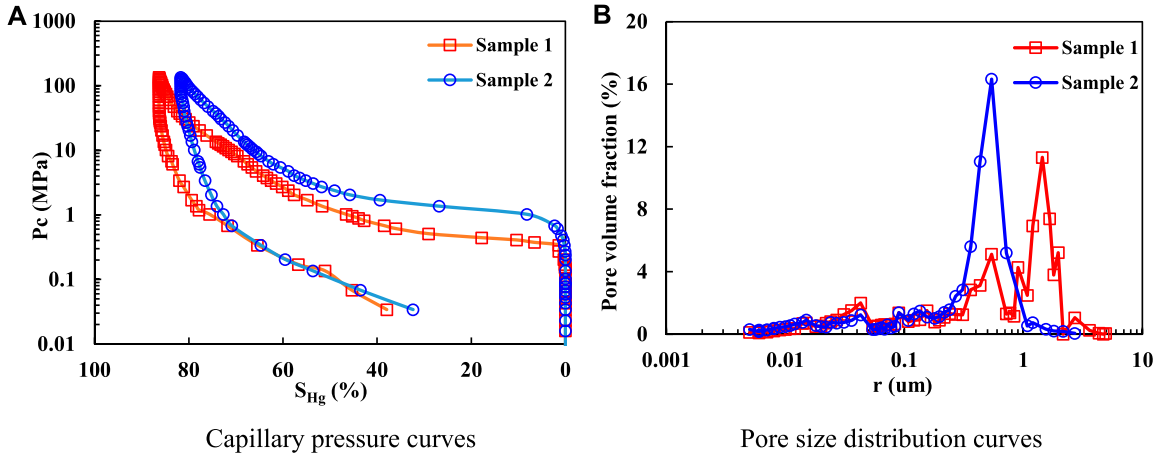

FIGURE 2 | Results of mercury injection test of our samples. **(A)** Capillary pressure curves. **(B)** Pore size distribution curves

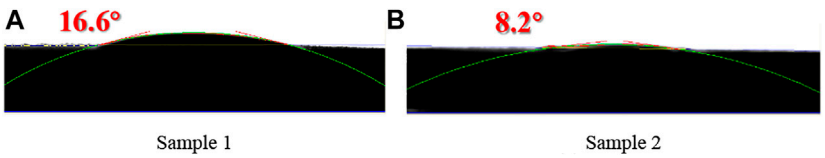

FIGURE 3 | Contact angle of two samples. **(A)** Sample 1. **(B)** Sample 2

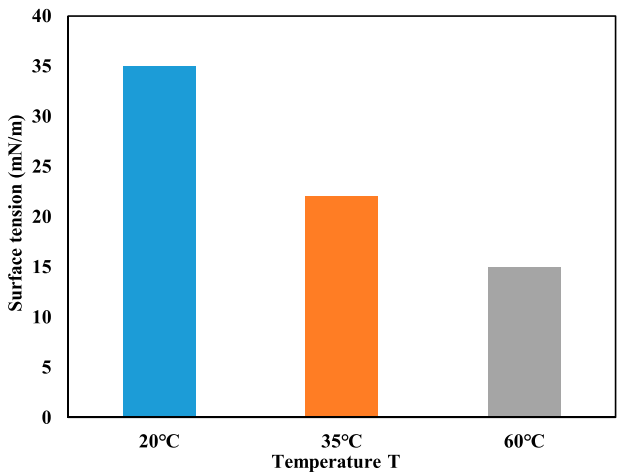

FIGURE 4 | IFT of crude oil–water system with different temperature.

difference of two immiscible fluids, and pressure has no significant effect on water density and oil density. 2) The effect of temperature on wettability is ignored. At room temperature, our samples have already shown strong hydrophilicity. In general, when the surface is hydrophilic, increasing the temperature can enhance the affinity to water molecules. Thus, the influence of temperature is insignificant.

Spontaneous Imbibition Experiments

As illustrated in **Figure 6**, the experiment of spontaneous imbibition is performed with an automatic metering system, which is assembled by an electronic balance and a computer. In this experiment, the samples are held under a rigid metal frame with a non-elastic and impermeable string, and their mass can be measured by the electronic balance (JJ632BC), whose accuracy is 0.0001 g and measuring range is 620 g. Meanwhile, the change of mass is transmitted to the computer in real time. The experiments were conducted in a constant temperature chamber (T = 20°C) to mitigate the effects of temperature variation in the environment. The procedure of experiments is as follows: 1) the geometrical parameters of the samples, that is, length and radius, are measured. 2) The samples are cleaned and the impurities in the core, that is, crude oil and bitumen, are removed. 3) The samples are dried at a temperature of 105°C for 8 h. The mass of the dry samples is determined if the mass difference between the two successive measurements is less than 0.01 g. 4) The clean samples are immersed in crude oil for 48 h to ensure that the pores are filled with crude oil. Then the samples are suspended by an impermeable string and immersed into the water. 5) The mass of imbibed water is recorded automatically until the mass remains constant within 1 hour.

As illustrated in **Figure 7A**, our results indicate that the imbibition curves of the two samples are very close because their physical properties are very similar. From **Figure 7A**, it can be seen that the imbibition rate gradually decreases and finally approaches equilibrium. The reason is that the imbibition

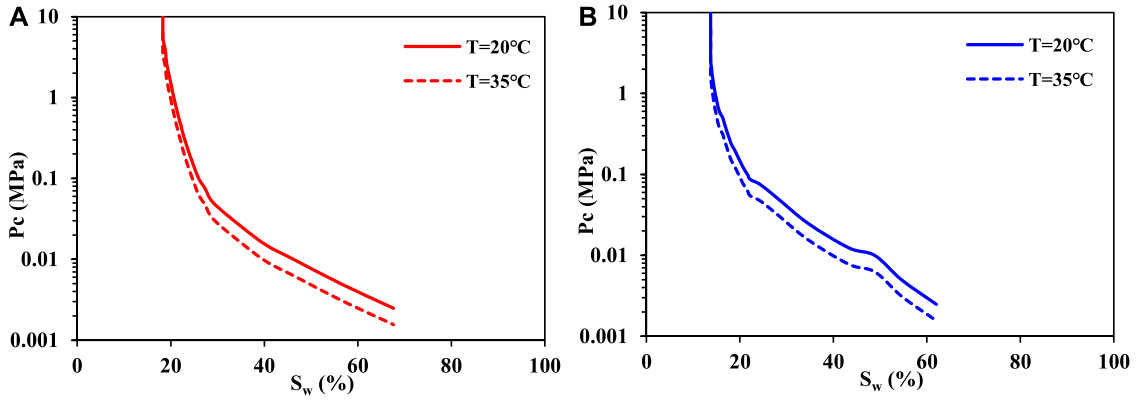

FIGURE 5 | Estimated capillary pressure of two cores for the oil–water system. **(A)** Sample 1. **(B)** Sample 2

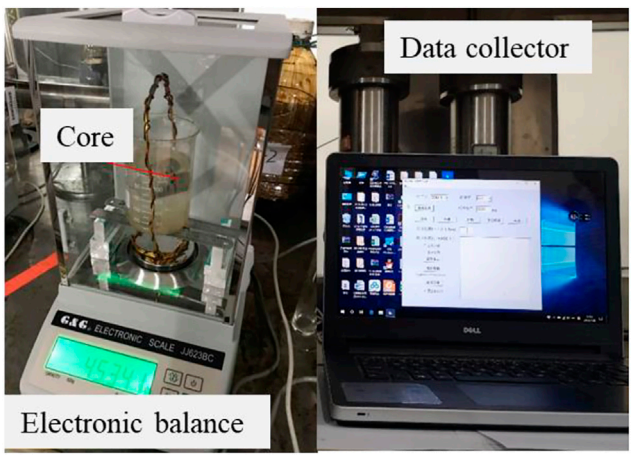

FIGURE 6 | Picture of spontaneous imbibition experiments.

of water increases the water saturation of the cores, which leads to a decrease in the capillary pressure. Moreover, the experimental data are managed by the method, that is, the Y-coordinate is plotted as the imbibed mass m, while the X-coordinate is plotted as the square root of time $t^{1/2}$, as shown in **Figure 7B**. The results show that m has a linear relationship with $t^{1/2}$. This finding may help to determine the relative permeability of the imbibition process.

Relative Permeability

By neglecting the gravity effect, a mathematical model for immiscible, incompressible, and isothermal two-phase flow is obtained by combining the Darcy flow and continuity equation (Ren et al., 2016; Alyafei and Blunt, 2018) as follows:

$$v_t \frac{\partial f_r(S_w)}{\partial x} + \frac{\partial}{\partial x}\left[D_r(S_w)\frac{\partial S_w}{\partial x}\right] + \phi\frac{\partial S_w}{\partial t} = 0, \tag{1}$$

where v_t is the total velocity, $f_r(S_w)$ is the fractional flow function, and $D_r(S_w)$ is the capillary dispersion coefficient.

The fractional flow function can be expressed as follows:

$$f_r(S_w) = \frac{K_{rw}/\mu_w}{K_{rw}/\mu_w + K_{ro}/\mu_o}, \tag{2}$$

where K_{rw} and K_{ro} are the water relative permeability and oil relative permeability, respectively; μ_w and μ_o are the water viscosity and oil viscosity, respectively.

The capillary dispersion coefficient can be expressed as follows:

$$D_r(S_w) = -K\frac{K_{rw}K_{ro}}{\mu_w K_{ro} + \mu_o K_{rw}}\frac{\partial P_c(S_w)}{\partial S_w}. \tag{3}$$

For spontaneous imbibition, the initial condition is given as follows:

$$S_w(x, t=0) = S_i. \tag{4}$$

The boundary condition for spontaneous imbibition is given as follows:

$$S_w(x=0, t) = S_0, \tag{5}$$

$$S_w(x=\infty, t) = S_0. \tag{6}$$

Based on the experimental results in **Section 3.2**, imbibed mass m has a linear relationship with the square root of time $t^{1/2}$. Correspondingly, the imbibed rate is also in proportion to the $t^{1/2}$, which can be written as follows (Ren et al., 2016):

$$v_w(0, t) = At^{-0.5}, \tag{7}$$

where A is an imbibition constant.

Furthermore, capillary fractional flow $F(S_w)$ is defined as the ratio of water flux in the core to the condition at the inlet.

$$v_w(x, t) = v_w(0, t)F(S_w). \tag{8}$$

Based on **Eqs 1**–**8**, the water saturation profile for spontaneous imbibition can be given with the semi-analytic form, as follows:

$$x(S_w, t) = \frac{2A}{\phi}F'(S_w)t^{1/2}, \tag{9}$$

$$A^2 = \frac{\phi}{2}\left(\int_{S_i}^{S_o}\frac{(S_w - S_i)D(S_w)}{F(S_w)}dS_w\right), \tag{10}$$

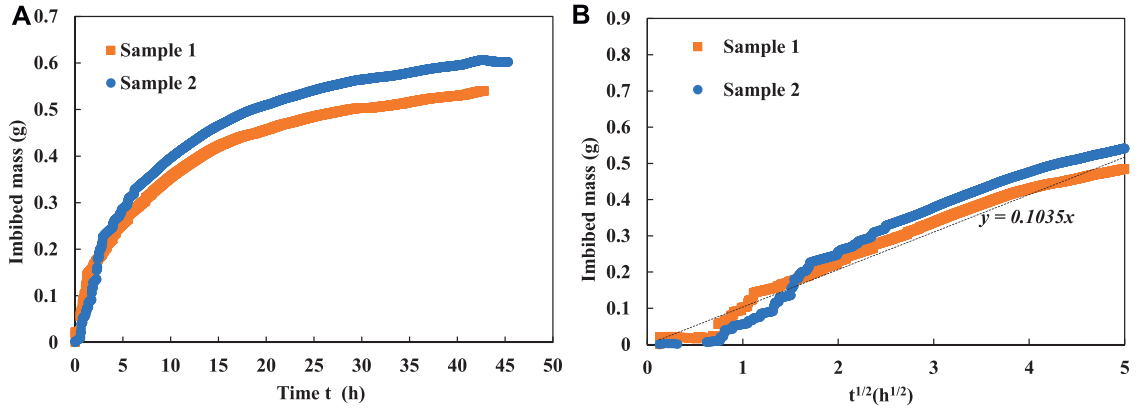

FIGURE 7 | Results of imbibition experiments. **(A)** m~t. **(B)** m~$t^{1/2}$.

$$F(S_w) = 1 - \left(\int_{S_w}^{S_o} \frac{(\beta - S_w)D(\beta)}{F(\beta)} d\beta \right) \Big/ \left(\int_{S_i}^{S_o} \frac{(S_w - S_i)D(S_w)}{F(S_w)} dS_w \right), \tag{11}$$

$$F'(S_w) = \left(\int_{S_w}^{S_o} \frac{D(\beta)}{F(\beta)} d\beta \right) \Big/ \left(\int_{S_i}^{S_o} \frac{(S_w - S_i)D(S_w)}{F(S_w)} dS_w \right). \tag{12}$$

Based on **Eq. 9**, the imbibition mass can be given as follows:

$$m = \rho_w C\phi \int_{S_{wc}}^{S_{max}} x(S_w, t) dS_w = \rho_w C\phi \int_{S_{wc}}^{S_{max}} \frac{2A}{\phi} F'(S_w) dS_w \cdot t^{1/2}. \tag{13}$$

Therefore, the slope between m and $t^{1/2}$ is given as follows:

$$L = \rho_w C\phi \int_{S_{wc}}^{S_{max}} \frac{2A}{\phi} F'(S_w) dS_w. \tag{14}$$

According to **Eqs 10–14**, we can know that besides the physical properties of core samples and fluids, the capillary dispersion coefficient and relative permeability are the key factors to determine the imbibition results. The capillary pressure is shown in **Figure 5**, and the relative permeability curve can be determined as the function of normalized water saturation.

$$K_{rw} = (S^*)^{1/2} \left[1 - \left(1 - S^{*1/\lambda} \right)^{\lambda} \right]^2, \tag{15}$$

$$K_{rg} = (1 - S^*)^{1/2} \left(1 - S^{*1/\lambda} \right)^{2\lambda}, \tag{16}$$

$$S^* = \frac{S_w - S_{wc}}{1 - S_{wc} - S_{or}}. \tag{17}$$

Based on **Eqs 14–17**, parameter λ can be obtained by the slope between m and $t^{1/2}$ in our experiments. Moreover, the relative permeability curve can be estimated, and the results are shown in **Figure 8**. The results provide the basic seepage parameters for our numerical simulations.

Meanwhile, some uncertainties during this process should be noted: 1) as shown in **Figure 2B**, the measured PSD curves demonstrated that the pore dimension of samples ranges from several nanometers to several micrometers. Non-Darcy flow has been widely acknowledged in such a small space because of its remarkable surface effects (Feng et al., 2018b; Feng et al., 2019). 2) Microfractures induced by the imbibed water could also influence the imbibition process. 3) Some special phenomena (e.g., electric double layer, electro-viscosity, and osmotic pressure) induced by the ion in the formation fluids increase the complexity of multiphase flow (Feng et al., 2018a). This would be our future work.

4 NUMERICAL SIMULATION AND FIELD APPLICATION

In this section, well A in the Chang 6 reservoir is taken to perform the numerical simulation. The Chang 6 reservoir is located in the

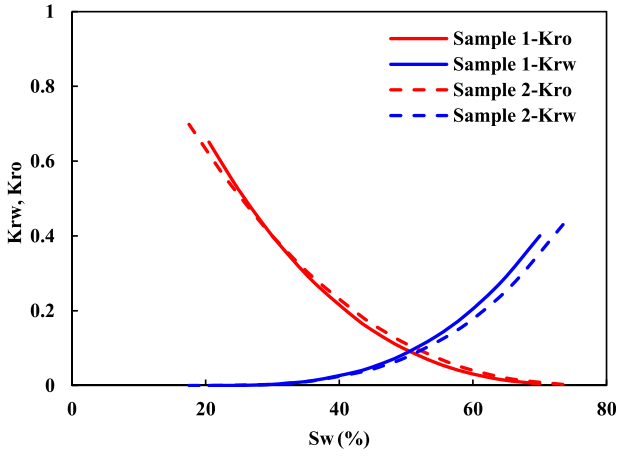

FIGURE 8 | Estimated relative permeability curves of two samples.

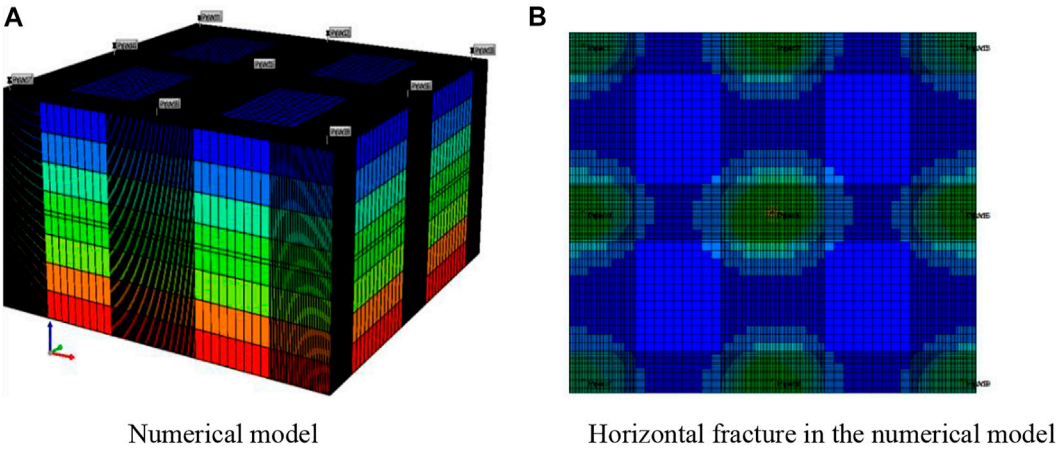

FIGURE 9 | Diagram of the reservoir numerical model. **(A)** Numerical model. **(B)** Horizontal fracture in the numerical model.

eastern region of the Yanchang oil field. The buried depth is in the range of 500–700 m. The average porosity is only 7–9%, and the average permeability is 0.3–0.5 mD. Based on the geological analysis and production practice, it is confirmed that the fractures in this area are extended in the horizontal direction. Based on the multiphase flow characteristics in **Section 3**, we performed a series of simulations to evaluate the effect of water huff-n-puff on the well production with further considering the horizontal fracture and imbibition effect.

4 1 Model Establishment

The black oil model in CMG is adopted to simulate the water huff-n-puff in well A. The grid size is 43 × 43 × 9 (**Figure 9**). In the vertical direction, the reservoir is divided into nine layers, among which the fifth layer is the fracturing one. The depth of the first layer is set as 500 m. In the horizontal direction, the grid size is 7 m × 7 m. In order to describe the elliptically horizontal fracture and improve the computational accuracy, the local mesh encryption method is employed to set the grid near the well point. The sizes in this area are set as 1 m × 1 m. Therefore, the total grid number is 145 × 193 × 9. In the well pattern design, a nine-point pattern is adopted in this block, and all the well points are located in the center of the elliptic horizontal fracture. Based on the monitoring results in the field, the long axis and short axis of elliptically horizontal fracture are respectively assumed to be 35 and 25 m. The aperture and permeability of fracture are set to 0.5 cm and 300 mD, respectively. In terms of the seepage parameters, the relative permeability in **Section 3.3** and capillary pressure at the reservoir temperature in **Section 3.1** are adopted to describe the fluids flow in the matrix, while the diagonal line phase permeability curve is adopted to model the fluids flow in the fractures. In this simulation, the stress sensitivity of fractures is not included because of the shallow buried depth (500–700 m) and low reservoir pressure (4.5 MPa). Other reservoir parameters are shown in **Table 2**.

TABLE 2 | Reservoir parameters and production parameters.

Parameter	Value	Parameter	Value
Depth of the top layer	500 m	Initial water saturation	30%
Reservoir pressure	4.5 MPa	Oil density	0.83 g cm^{-3}
Reservoir temperature	35°C	Water density	1 g cm^{-3}
Matrix permeability	0.5 mD	Oil viscosity	4.67 mPa s
Matrix porosity	10%	Water viscosity	0.8 mPa s

4 2 Sensitivities Analysis

Combined with the research status and field practice, a series of numerical simulations were performed to choose the optimal parameters in one cycle, that is, the injection rate, injected volume, and soak time. Then based on these optimal parameters, well performance with multiple cycles of huff and puff is analyzed.

4.2.1Effect of Injected Rate

With a constant injected water volume (300 m^3) and constant soak time (30 days), three cases, that is, 5 m^3/d, 10 m^3/d, and 15 m^3/d, are simulated to investigate the effect of the injected rate on the well performance. Meanwhile, depletion production is regarded as the reference. Considering the actual case in the practice field, water huff-n-puff is adopted after a year of depletion production, and the simulated time lasts for 400 days with a constant bottom pressure at 1 MPa. As shown in **Figure 10**, compared with the depletion production, water huff-n-puff can significantly enhance the well production. Moreover, as the injection rate increases, the time for one cycle becomes shorter and the cumulative oil production is higher. Considering the economic benefits and limitations of field injection equipment, 10 m^3/d is the optimal injected rate. On the other hand, there is no difference in water production for the three cases, indicating that after soaking for 30 days, the distribution of oil and water reached a steady state. Thus, the injected water rate has little influence on water production.

4.2.2Injected Volume

With a constant injected water rate (10 m^3/d) and constant soak time (30 days), four cases, that is, 100 m^3, 150 m^3, 300 m^3, and

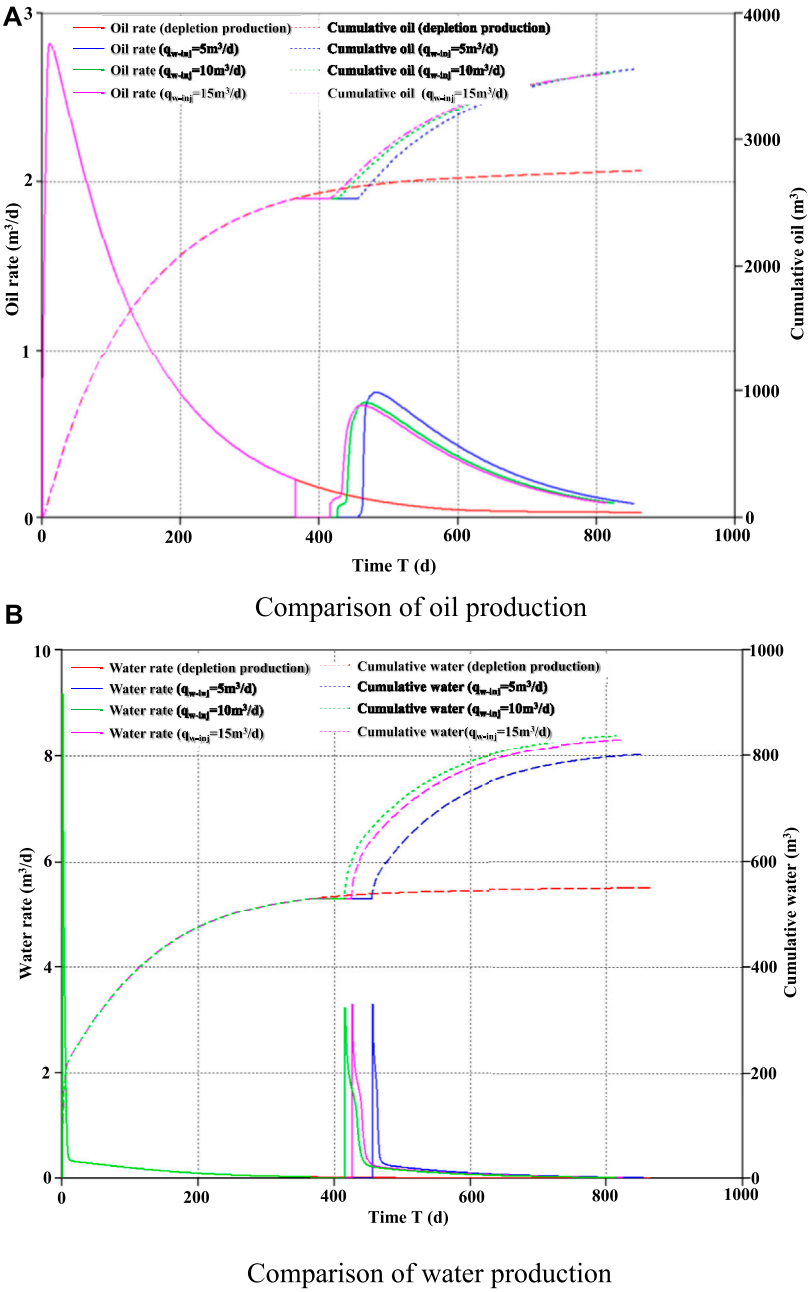

FIGURE 10 | Comparison of oil and water production with different injection rates. **(A)** Comparison of oil production. **(B)** Comparison of water production.

500 m^3, are simulated to investigate the effect of injected volume on the well performance. The production system and the reference are consistent with the case in **Section 4.2.1**. As shown in **Figure 11**, the simulated results showed that the increase of injected water volume can enhance the production of oil. When the injected volume is small (100 and 150 m^3), the well production rapidly reaches its peak once the well is reopened. This is because during the soak period, the injected water is totally imbibed to the depth of the reservoir, and the oil in the fracture and near-well zone can be outputted directly. Correspondingly, the daily water production curves have also proved this mechanism.

In terms of cumulative production, cumulative oil production increases with the increase of injection volume. With a constant injected rate, the larger the injected volume is, the longer the time for one cycle will be. After the well is reopened, within 150 days, the highest cumulative oil production is obtained with the case of 500 m^3 injected water. While for a longer production time, 300 m^3 is the optimal one. In terms of water production, when the injection rate is 500 m^3, it takes a longer time for the daily water production to drop

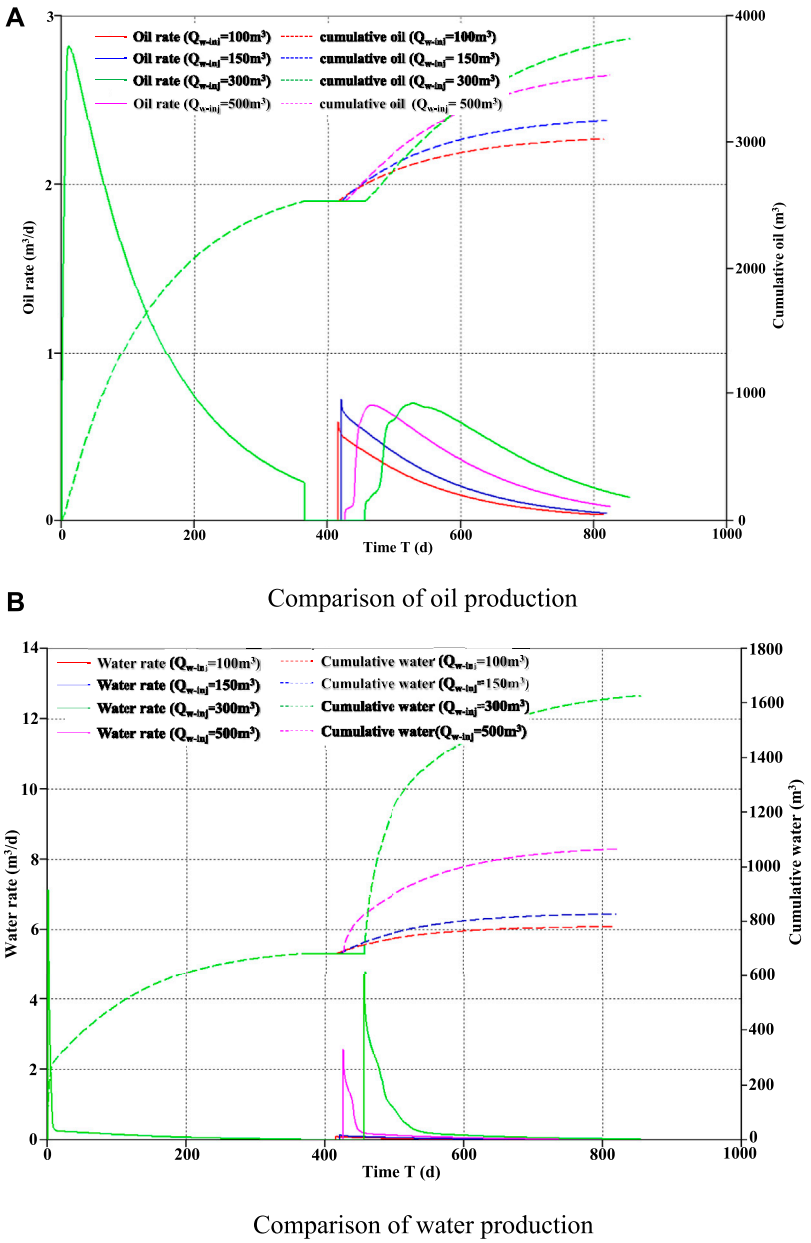

FIGURE 11 | Comparison of oil and water production with different injection volumes. **(A)** Comparison of oil production. **(B)** Comparison of water production.

to the normal level, indicating that some injection water is ineffective, which neither has a contribution to the supplement of formation energy nor enhances the exchange between crude oil and injected water. Therefore, 300 m^3 is the optimal injected volume for well A.

4.2.3Soak Time

Soak time is the key parameter to determine the redistribution of oil and water. With a constant injected water rate (10 m^3/d) and injected volume (300 m^3 day), four cases, that is, 10, 30, 50, and 70 days, are simulated to investigate the effect of soak time on well performance. As illustrated in **Figure 12A**, our results suggest that the soak time has an insignificant influence on the cumulative oil production. As illustrated in **Figure 12B**, due to the imbibition effect between injected water and crude oil, the cumulative water production decreases with the increase of soak time, and the reduction is sensitive with the soak time ranging from 10 to 30 days. However, when the soak time is over 50 days, the variation of cumulative water production is very small. In terms of the comprehensive improvement of the production level, including supplementation of formation pressure and economic benefits, 30 days is the optimal soak time for well A.

4.2.4Number of Cycles

At the field application, water huff-n-puff is usually put into practice for several cycles. With a constant water injection rate

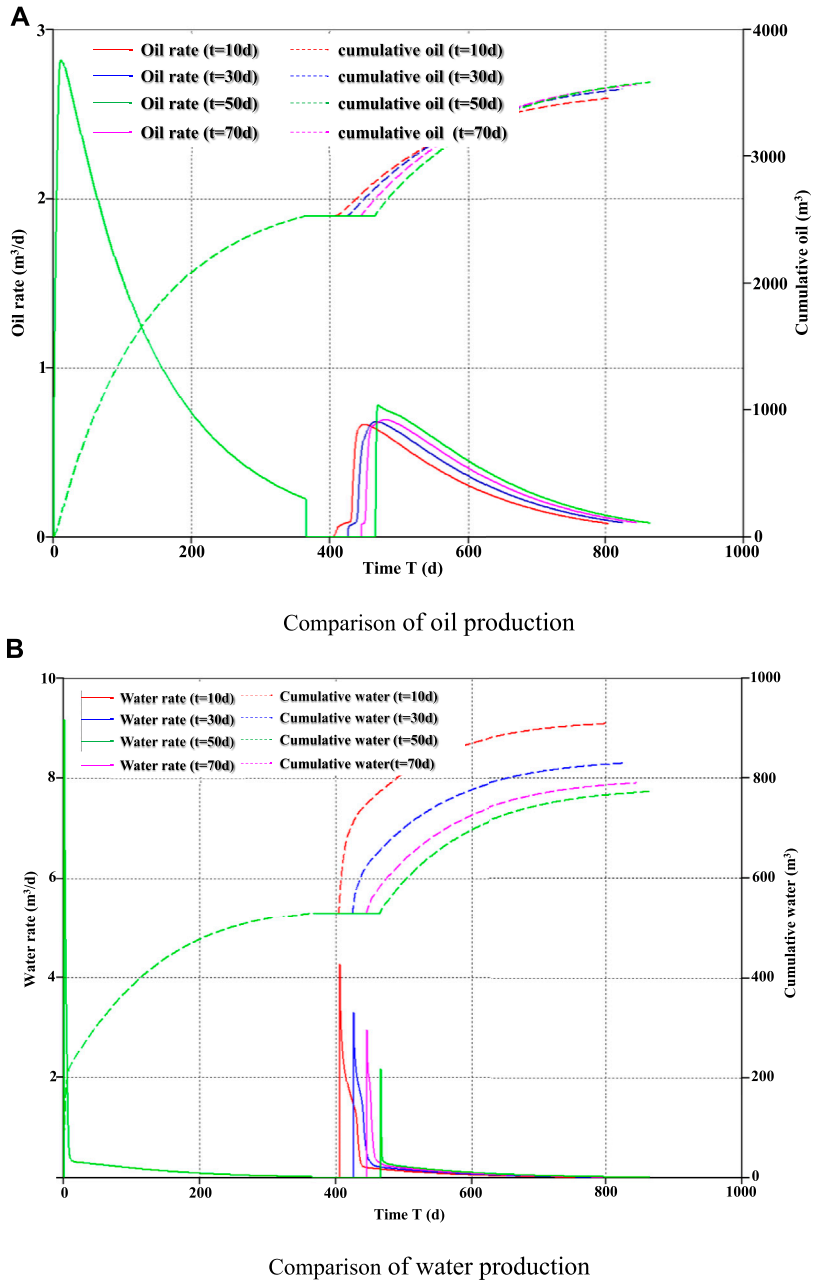

FIGURE 12 | Comparison of oil and water production with different soak time. **(A)** Comparison of oil production. **(B)** Comparison of water production.

(10 m^3/d) and total injected volume (900 m^3), three cases, that is, one cycle, two cycles and three cycles, are simulated to investigate the effect of multiple cycles on the well production. It should be noted that one cycle includes huff, soak, and puff stages. In each cycle, the soak time is assumed to be 30 days. The simulated results are demonstrated in **Figure 13**. As shown in **Figure 13A**, for the case of one cycle, the oil production gradually decreases after reopening the well, while for the case of two cycles and three cycles, the oil production can maintain stability for a longer period of time. Meanwhile, the variation of cycle numbers is found to have little influence on the cumulative oil production. As shown in **Figure 13B**, we observed that the cumulative water production decreases as the cycle numbers increases, which indicates that more water is imbibed into the depth of the reservoirs and acts as a supplement to the formation energy. Therefore, increasing the number of cycles is not only beneficial to the fluids exchange but also helpful to enhance the formation pressure, which can help achieve the best development effect.

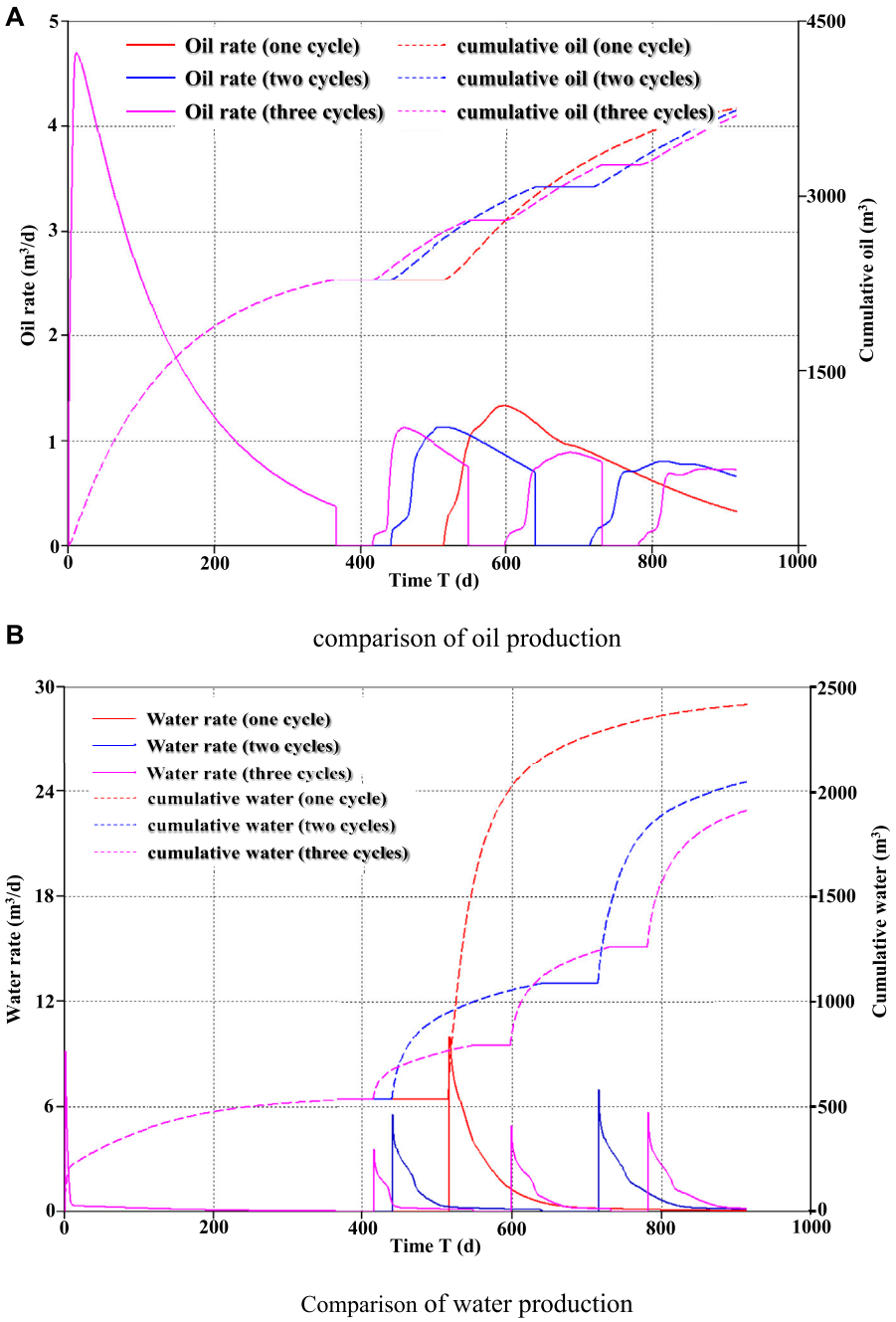

FIGURE 13 | Comparison of oil and water production with different cycles. **(A)** Comparison of oil production. **(B)** Comparison of water production

5 CONCLUSION

In this study, we first introduced the water huff-n-puff process in a low-permeability oil reservoir with horizontal fractures and described the multiphase flow characteristics during the huff, soak, and puff stages. Then combined with a series of experiments, a comprehensive method was used to determine the key flow parameters, that is, capillary pressure and relative permeability. Finally, using the Chang 6 reservoir as an example, a series of numerical simulations were conducted to demonstrate the effect of water huff-n-puff on the well performance in this field. Based on our studies, following conclusions can be drawn:

1) The mechanism of water huff-n-puff for low-permeability reservoirs with horizontal fractures is revealed. Based on the migration of fluids, water huff-n-puff can be divided into huff, soak, and puff stages. During the shut-in period, the fluid

exchange between crude oil in the matrix and water in the fractures occurs in the radial direction and the vertical direction.
2) The framework for relative permeability from the spontaneous imbibition experiments is estimated. Spontaneous imbibition experiments demonstrate the linear relationship between imbibition mass and the square root of time. Coupling this finding and capillary pressure into the two-phase flow theory, relative permeability can be properly determined.
3) Water huff-n-puff parameters for a well in the Chang 6 reservoir are optimized considering the horizontal fractures and imbibition effect. The results show that oil production is mainly influenced by the injection volume and the injection speed, while water production is mainly determined by the well shut-in time. The optimal injection volume, injection rate, and well shut-in time are 300 m^3, 10 m^3/d, and 30 days, respectively. Moreover, the increase in the cycle number is not only beneficial to the fluids exchange but also helpful to enhance the formation pressure. Both of them can accelerate the development of low-permeability oil reservoirs.

DATA AVAILABILITY STATEMENT

The raw data supporting the conclusion of this article will be made available by the authors, without undue reservation.

AUTHOR CONTRIBUTIONS

XM contributed to conceptualization, methodology, and writing—original draft. SH helped with methodology, writing—review and editing, and supervision. HZ assisted with methodology and validation. FG contributed to conceptualization and methodology. YG helped with software. XL assisted with funding acquisition and supervision.

ACKNOWLEDGMENTS

We acknowledge the support of the National Natural Science Foundation Projects of China (51874319).

REFERENCES

Alyafei, N., and Blunt, M. J. (2018). Estimation of Relative Permeability and Capillary Pressure from Mass Imbibition Experiments. *Adv. Water Resour.* 115, 88–94. doi:10.1016/j.advwatres.2018.03.003

Feng, D., Bakhshian, S., WuSong, K. Z., Song, Z., Ren, B., Li, J., et al. (2021). Wettability Effects on Phase Behavior and Interfacial Tension in Shale Nanopores. *Fuel* 290, 119983. doi:10.1016/j.fuel.2020.119983

Feng, D., Li, X., Wang, X., Li, J., Sun, F., Sun, Z., et al. (2018a). Water Adsorption and its Impact on the Pore Structure Characteristics of Shale clay. *Appl. Clay Sci.* 155, 126–138. doi:10.1016/j.clay.2018.01.017

Feng, D., Li, X., WangLiZhang, X. J. X., Li, J., and Zhang, X. (2018b). Capillary Filling under Nanoconfinement: the Relationship between Effective Viscosity and Water-wall Interactions. *Int. J. Heat Mass Transfer* 118, 900–910. doi:10.1016/j.ijheatmasstransfer.2017.11.049

Feng, D., Wu, K., Wang, X., Li, J., and Li, X. (2019). Modeling the Confined Fluid Flow in Micro-nanoporous media under Geological Temperature and Pressure. *Int. J. Heat Mass Transfer* 145 (145), 118758. doi:10.1016/j.ijheatmasstransfer.2019.118758

Fisher, K., and Warpinski, N. (2012). Hydraulic-Fracture-Height Growth: Real Data. *SPE Prod. operations* 27 (01), 8–19. doi:10.2118/145949-pa

Gao, S., Yang, Y., Liao, G., Xiong, W., Liu, H., Shen, R., et al. (2022). Experimental Research on Inter-fracture Asynchronous Injection-Production Cycle for a Horizontal Well in a Tight Oil Reservoir. *J. Pet. Sci. Eng.* 208, 109647. doi:10.1016/j.petrol.2021.109647

Graham, J. W., and Richardson, J. G. (1959). Theory and Application of Imbibition Phenomena in Recovery of Oil. *Trans. AIME* 216, 377–381. doi:10.2118/1143-g

Han, B., Cui, G., Wang, Y., Zhang, J., Zhai, Z., Shi, Y., et al. (2021). Effect of Fracture Network on Water Injection Huff-Puff for Volume Stimulation Horizontal wells in Tight Oil Reservoir: Field Test and Numerical Simulation Study. *J. Pet. Sci. Eng.* 207, 109106. doi:10.1016/j.petrol.2021.109106

Hartsock, J. H., and Warren, J. E. (1961). The Effect of Horizontal Hydraulic Fracturing on Well Performance. *J. Petrol. Technol.* 13, 1050–1056. doi:10.2118/61-pa

Held, R. J., and Celia, M. A. (2001). Modeling Support of Functional Relationships between Capillary Pressure, Saturation, Interfacial Area and Common Lines. *Adv. Water Resour.* 24, 325–343. doi:10.1016/s0309-1708(00)00060-9

Huang, L., Ning, Z., Lin, H., Zhou, W., Wang, L., Zou, J., et al. (2021b). High-pressure Sorption of Methane, Ethane, and Their Mixtures on Shales from Sichuan Basin, China. *Energy Fuels* 35 (5), 3989–3999. doi:10.1021/acs.energyfuels.0c04205

Huang, L., Zhou, W., XuWang, H. Lu., Wang, L., Zou, J., and Zhou, Q. (2021a). Dynamic Fluid States in Organic-Inorganic Nanocomposite: Implications for Shale Gas Recovery and CO2 Sequestration. *Chem. Eng. J.* 411, 128423. doi:10.1016/j.cej.2021.128423

Li, Z., Qu, X., Liu, W., Lei, Q., Sun, H., and He, Y. (2015). Development Modes of Triassic Yanchang Formation Chang 7 Member Tight Oil in Ordos Basin, NW China. *Petrol. Explor. Dev.* 42 (2), 217–221. doi:10.1016/s1876-3804(15)30011-2

Liu, L., Liu, Y., Yao, J., and Huang, Z. (2020). Mechanistic Study of Cyclic Water Injection to Enhance Oil Recovery in Tight Reservoirs with Fracture Deformation Hysteresis. *Fuel* 271, 117677. doi:10.1016/j.fuel.2020.117677

Rangel-German, E. R., and Kovscek, A. R. (2004). "Microvisual Analysis of Matrix-Fracture Interaction," in SPE International Petroleum Conference in Mexico. doi:10.2118/92133-ms

Rao, X., Zhao, H., and Deng, Q. (2020). Artificial-neural-network (ANN) Based Proxy Model for Performances Forecast and Inverse Project Design of Water Huff-N-Puff Technology. *J. Pet. Sci. Eng.* 195, 107851. doi:10.1016/j.petrol.2020.107851

Ren, W., Li, G., Tian, S., Sheng, M., and Geng, L. (2016). Analytical Modelling of Hysteretic Constitutive Relations Governing Spontaneous Imbibition of Fracturing Fluid in Shale. *J. Nat. Gas Sci. Eng.* 34, 925–933. doi:10.1016/j.jngse.2016.07.050

Sun, K., Liu, H., Wang, J., Wei, X., Ma, L., Kang, Z., et al. (2022). Three-dimensional Physical Simulation of Water Huff-N-Puff in a Tight Oil Reservoir with Stimulated Reservoir Volume. *J. Pet. Sci. Eng.* 208, 109212. doi:10.1016/j.petrol.2021.109212

Takahashi, S., and Kovscek, A. R. (2010). Spontaneous Countercurrent Imbibition and Forced Displacement Characteristics of Low-Permeability, Siliceous Shale Rocks. *J. Pet. Sci. Eng.* 71 (1-2), 47. doi:10.1016/j.petrol.2010.01.003

Tavassoli, Z., Zimmerman, R. W., and Blunt, M. J. (2005). Analysis on Counter-current Imbibition with Gravity in Weakly Water-Wet Systems. *J. Pet. Sci. Eng.* 48 (1–2), 94–104. doi:10.1016/j.petrol.2005.04.003

Wang, D., Cheng, L., Cao, R., Jia, P., Fang, S., Rao, X., et al. (2019). The Effects of the Boundary Layer and Fracture Networks on the Water Huff-N-Puff Process of Tight Oil Reservoirs. *J. Pet. Sci. Eng.* 176, 466–480. doi:10.1016/j.petrol.2019.01.065

Wang, X., Peng, X., Zhang, S., Du, Z., and Zeng, F. (2018). Characteristics of Oil Distributions in Forced and Spontaneous Imbibition of Tight Oil Reservoir. *Fuel* 224, 280–288. doi:10.1016/j.fuel.2018.03.104

Wang, Y., Liu, H., Guo, M., Shen, X., Han, B., and Zhou, Y. (2021b). Image Recognition Model Based on Deep Learning for Remaining Oil Recognition from Visualization experiment. *Fuel* 291, 120216. doi:10.1016/j.fuel.2021.120216

Wang, Y., Liu, H., and Zhou, Y. (2021a). Development of a Deep Learning-Based Model for the Entire Production Process of Steam-Assisted Gravity Drainage (SAGD). *Fuel* 287, 119565. doi:10.1016/j.fuel.2020.119565

Wilsey, L. E., and Bearden, W. G. (1954). Reservoir Fracturing - A Method of Oil Recovery from Extremely Low Permeability Formations. *J. Petrol. Technol.* 6 (08), 21–27. doi:10.2118/317-g

Conflict of Interest: Authors HZ, FG, and YG were employed by the company Yanchang Oilfield Co. Ltd.

The remaining authors declare that the research was conducted in the absence of any commercial or financial relationships that could be construed as a potential conflict of interest.

Publisher's Note: All claims expressed in this article are solely those of the authors and do not necessarily represent those of their affiliated organizations, or those of the publisher, the editors, and the reviewers. Any product that may be evaluated in this article, or claim that may be made by its manufacturer, is not guaranteed or endorsed by the publisher.

frontiers in Earth Science

ORIGINAL RESEARCH
published: 03 March 2022
doi: 10.3389/feart.2022.841456

The Fractured Model Study of Low-Permeability Reservoir in Xinli Oil Field

Yongchao Xue[*†], *Longjun Wang, Xiaoliang Zhao and Hua Tian*

School of Petroleum Engineering, China University of Petroleum (Beijing), Changping, Beijing

With the development of the petroleum industry, the importance of low-permeability reservoirs becomes clear. The fracture, which serves as the notable characteristic of a low-permeability reservoir, controls the flow system of reservoir fluid and restrains the development effect. Finding ways to recognize the fracture by using the normal data and building the fracture 3-D model are the important and difficult points of low-permeability development. According to this problem, the authors use a helpful probe. First, from similar outcrop and drilling core study of the fractured original model, the knowledge base of the fracture was built. Second, based on the analysis of the principle of dual-later log identification fracture, the core calibration was used to make logging, and using dual-later log, the fracture in wells was recognized. Third, based on the analysis of the principle of the fractal kriging method, the inter-well fractures were predicted. Finally, the 3-D model of fracture was built with fractural random simulation. The result shows that the 3-D model is in accordance with the fact of the development. So, the method is correct.

Keywords: prototype model, low permeability, fractural kriging, fracture, 3D model

OPEN ACCESS

Edited by:
Wenhui Song,
China University of Petroleum, Huadong, China

Reviewed by:
Jianhui Han,
Chengdu University of Technology, China
Hongqi Liu,
Southwest Petroleum University, China

***Correspondence:**
Yongchao Xue
xyc75@cup.edu.cn

[†]***ORCID ID:***
Yingchao Xue
orcid.org/0000-0003-1903-7519

Specialty section:
This article was submitted to Economic Geology, a section of the journal Frontiers in Earth Science

Received: *22 December 2021*
Accepted: *03 February 2022*
Published: *03 March 2022*

Citation:
Xue Y, Wang L, Zhao X and Tian H (2022) The Fractured Model Study of Low-Permeability Reservoir in Xinli Oil Field. Front. Earth Sci. 10:841456. doi: 10.3389/feart.2022.841456

INTRODUCTION

Oil and gas in tight and low-permeability reservoirs is an important replacement resource and development field in China (Ding et al., 2015; Sun et al., 2019). Tight and low-permeability reservoirs have poor physical properties and strong heterogeneity. Natural fractures generally develop under the action of multistage structural deformation (Wu et al., 2021a). Natural fracture characterization methods include natural fracture description methods and prediction methods, among which natural fracture characterization methods include qualitative and quantitative description methods, which can be divided into 1) geological methods, including field similar outcrops, core observation, thin slices, scanning electron microscope, CT layer analysis and scanning technology, and core MRI scanning image analysis technology (Xiong et al., 2019; Liu et al., 2020; Wu et al., 2021b; Jia et al., 2021; Rao et al., 2022); 2) well logging methods, including special logging and conventional logging methods (Tang et al., 2012; Zhao et al., 2012; Wu et al., 2021c); 3) reservoir engineering methods, including well test analysis, pressure analysis, tracer analysis, water injection dynamic analysis, and microseismic monitoring (Clarkson and Qanbari, 2015; Fang et al., 2017; Jia et al., 2017; Chen et al., 2019; Li et al., 2020). The prediction methods of natural fractures mainly include the following: 1) The geological data method predicts fractures, mainly based on the geological data such as cores, logging, and seismic data of the oil field to predict the development of fractures. Core analysis is the most accurate and intuitive way to reflect the development of underground fractures. Due to the high cost of coring, core data are generally scarce. Imaging logging uses high-resolution two-dimensional images to display fracture information, but imaging

logging costs are relatively high, and imaging logging implemented in actual production is limited. Using conventional logging data to accurately identify and predict fractures in the entire well section requires maximum use of drilling core and imaging logging data to calibrate conventional logging data. At present, the main technologies for predicting fractures through seismic methods include coherence analysis technology, tracking technology, seismic inversion technology, and shear wave splitting technology (Wang et al., 2014; Su et al., 2017; Teng and Li, 2019). 2) The numerical simulation method is used to predict fractures. Based on geological knowledge, the distribution law of the fractures is studied theoretically by establishing a mathematical model. The numerical simulation method is based on certain geological knowledge and establishes a mathematical model to analyze and predict the fractures theoretically. Numerical simulation methods mainly include finite element tectonic stress field numerical simulation method, rock fracture method, curvature method, energy method, and statistical method (Li et al., 2013; Wang et al., 2013; Ju et al., 2014; Dong et al., 2018). 3) Other qualitative methods are used to predict fractures, that is, based on the relationship between fracture development and structure and lithology, to qualitatively understand the distribution characteristics of fractures. Qualitative methods to predict fractures are mainly based on the relationship between fracture development and structure and lithology, to qualitatively understand fractures and distribution characteristics. Predecessors believed through analysis that fractures are more likely to develop in high structural positions and near faults. Rocks with more brittle components are more likely to develop fractures than rocks with less brittle components (Ju et al., 2013; Liu et al., 2017). 4) The non-linear theory method predicts fractures. Non-linear theoretical methods are mainly a series of technical methods emerging in the 1990s, mainly including fractal theory, gray relation theory, backpropagation neural network, and other methods (Gong et al., 2012; Wang et al., 2015; Dong et al., 2016).

After years of fracture research, although great progress has been made in the characterization of reservoir natural fractures, the current research on 3-D geological modeling of reservoir fractures is still relatively weak, which cannot meet further needs of tight and low-permeability oil and gas exploration and development.

GEOLOGICAL CONDITION OF XINLI OIL FIELD

Xinli oil field is located on the westernmost Xinli anticline in the central depression of the Songliao Basin, Fuyu-Xinmu uplift zone. It is a dome anticline complicated by faults, with two groups of normal faults in the NNW direction and NNE direction. The Fuyu reservoir is of meandering river facies, mainly composed of fine sandstone, siltstone, and largely siltstone. The average porosity of the matrix reservoir is 12.8%, and the average permeability is 2.5×10^{-3} μm^2. Xinli oil field was discovered by exploration in 1973, opened a production experimental area in 1980, and carried out a comprehensive infill adjustment stage from 1997 to 1999. At present, the oil field has entered the stage of ultrahigh water cut development. Exploration indicates that there are large amounts of high-angle fractures in a shaft of the oil field. Unclear understanding of fracture characteristics and distribution seriously constrains the highly efficient oil field development.

FRACTURED ORIGINAL MODEL

The original fracture model is mainly studied by fracture investigation in similar outcrop areas and core fracture observations.

Study of Similar Crop

From a study of a similar crop in the research area, we find the following characteristics of fractures (**Table 1**) (**Figure 1**).

1) There are four groups of high-angle fractures (nearly EW, SN, NW, and NE direction). The group of fractures in nearly SN direction is developed earlier than the other three groups. Fractures in nearly EW direction are main fractures. NW and NE direction fractures show as conjugate shear fractures of the nearly SN direction fractures.
2) Fractures in the study area are mainly high-angle fractures, and 80% of the fractures are with angles larger than 70°.
3) Fracture density in the study area is mainly affected by lithology and tectonic stress. The measured data show that there are 14.6 fractures per meter in fine sandstone, 10.4 per meter in siltstone, and 3.8 fractures per meter in pelitic siltstone. The density of fractures in nearly EW direction is dramatically larger than that of fractures in nearly SN direction.
4) Length of tectonic fissures in similar outcrops ranges in a large scope from few centimeters to tens of meters. Fracture aperture also varies widely. Fractures in nearly EW direction have largest apertures up to several centimeters, followed by fractures in nearly NE and NW direction, and fractures in nearly SN direction have apertures of only a few millimeters. This is affected by the orientation of principal stress (nearly EW direction) in the area.
5) Fractures in nearly SN direction are commonly filled with calcite, while those in nearly EW direction have fewer fillings.

Study of Drilling Cores

From the observation of drilling cores of Xinli oil field, we get the following results (**Figure 2A**):

1) Fuyang reservoir in Xinli oil field develops multiple groups of fractures with different angles, aperture, and cutting depth. For example, the core drilled from the well section 1,359.5–1,359.85 m of Xin 318 shows groups of fractures and their spatial relationships.
2) Statistics of core fracture density indicate that there are 0.23 fractures per meter in sandstone, 0.1 in pelitic siltstone barrier, and 0.88 fractures per meter in calcareous sandstone at the bottom of the reservoir.
3) Core fracture aperture ranges in a large scope from few micrometers to millimeters and is filled with calcium or argillite (**Figure 2B**).

TABLE 1 | Strike distribution characteristics of similar outcrop fractures in the target reservoir.

Trend	Amount	Trend feature		Inclination (°)	
		Average trend (°)	Frequency	Inclination range	Average inclination
SN	70	4.5	31.1	72–86	78.5
EW	95	86	42.2	65–87	83.5
NE	32	43	14.2	67–76	75.3
NW	28	316	12.4	65–74	74.6

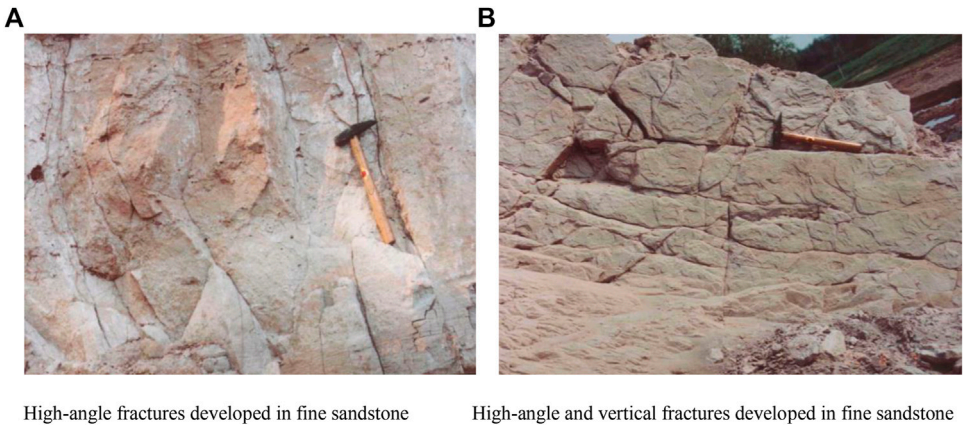

FIGURE 1 | Fracture inclination observed by similar outcrops. **(A)** High-angle fractures developed in fine sandstone. **(B)** High-angle and vertical fractures developed in fine sandstone.

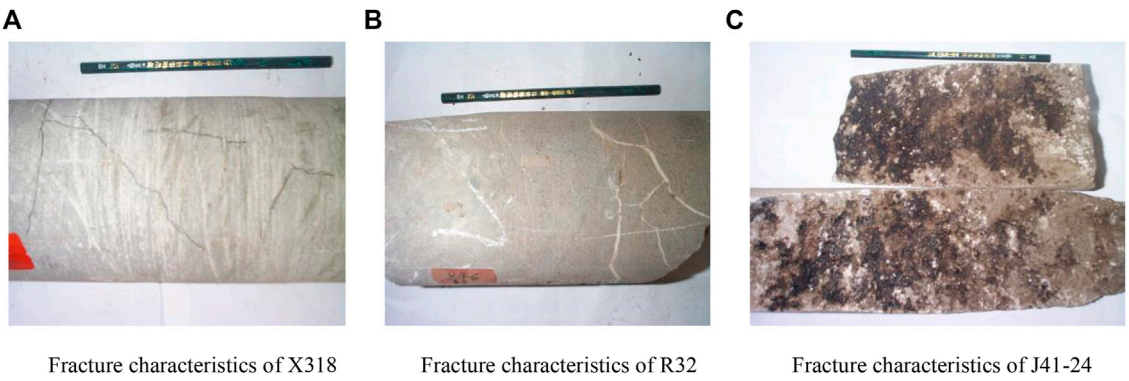

FIGURE 2 | Observation of typical fracture characteristics in the target reservoir core. **(A)** Fracture characteristics of X318. **(B)** Fracture characteristics of R32. **(C)** Fracture characteristics of J41-24.

4) The study area has a good oil-bearing ability, which benefits from the developed fractures (**Figure 2C**).

PRINCIPLE OF FRACTURE DETECTION BY WELL LOGS

Using logging methods to detect fractures is mainly based on the fact that fractures and matrices have different geophysical characteristics. Therefore, when fractures develop in the formation, different logging responses may be caused. Based on these response characteristics, fractures can be identified and analyzed.

Acoustic Logging Curve

The study area is mainly based on compensated acoustic logging, and the detected longitudinal wave head waves are more sensitive to horizontal fractures and low-angle fractures, and cycle jumps and abnormal high-value characteristics of acoustic waves may occur in the fracture section. However, the fractures in this area are dominated by high-angle fractures. At the same time, the

length of the fractures observed by the core is basically between 20 and 30 cm. Therefore, there are no obvious acoustic anomalies and cycle skipping characteristics in the sonic logging section of the fracture development section.

Radioactive Logging

Density logging, natural gamma, neutron, and other radioactive logging have a certain response to fractures. In the fracture section, it is characterized by low density, high neutron porosity, and low gamma. Due to the changes in stratum lithology and radiation intensity in the target area, these curves are irregular in the fracture section and have no response to the fracture.

Well Diameter and Well Temperature Logging

The hole diameter is also a method to identify fractures. When drilling into fracture-developed zones, it will generally cause diameter expansion or well wall collapse. Well temperature logging is also a means of identifying fractures. Usually, mud invades and the formation temperature gradually decreases, which causes a local temperature drop in the well and a negative well temperature anomaly. In the logging series in this area, there are no caliper and temperature logging curves, so these curves cannot be used to identify fractures.

Principle of Resistivity Tools to Identify Fractures

Theoretical study (Quillan, 1973; Philippe and Roger, 1990; Jian and Li, 2001) indicates that when fractures developed in low-permeability reservoirs, the anisotropy coefficient of electrical resistivity can be given as follows:

$$\lambda = \sqrt{\frac{R_b}{R_f}} = \sqrt{\frac{\sigma_f}{\sigma_b}} = \sqrt{\frac{2 + \eta(1 + \cos^2\theta)}{2 + 2\eta\sin^2\theta}}, \quad (1)$$

where

$$\eta = \frac{\phi_f \sigma_f}{\sigma_b}, \quad (2)$$

where λ is the anisotropy coefficient of electrical resistivity, dimensionless; η is the additional conductivity coefficient of fractures, dimensionless; R_b and R_f are the resistivity of fluids in bedrock and fractures, respectively, Ω m; σ_b and σ_f are the conductivity of fluids in bedrock and fractures, respectively, S/m; θ is the fracture angle, °; and φ_f is the fracture porosity, %.

From **Eq. 1** and **Eq. 2** we can see that η is a good indicator of the additional conductivity coefficient of fracture. The larger the η is, the stronger the anisotropy of electrical resistivity will be.

Eq. 2 can be rewritten as follows:

$$\eta = \frac{\phi_f \sigma_f}{\sigma_b} = \frac{\phi_f}{R_f} R_b. \quad (3)$$

According to **Eq. 3**, we know that η is only associated with R_b when fractures are fixed. The larger the R_b is, the larger the η and the stronger the anisotropy of electrical resistivity will be. Therefore, preferable fracture identification results can be obtained with resistivity tools if the electrical resistivity of bedrock is large.

Resistivity Method to Identify Fractures

Both theory and practice indicate that the electrical resistivity of a fractured reservoir is lower than that of a normal reservoir. From **Figure 3** which is the fracture identification result of well Ji 10–17, we know that there is a high-angle fracture with few fillings in oil-immersed fine sandstone in section 1,176.00–1,176.50 m. The characteristic of a dual-later log is as follows: deep and shallow resistivities of sections where fractures developed are about 18 Ω m and 16 Ω m, respectively, while those of the near sections without fractures are larger than 35 Ω m; difference on a dual later log of fracture sections changes from normal value 5 Ω m–10 Ω m to 2 Ω m–3 Ω m, even 0 Ω m locally. The characteristic of a micro log is as follows: micro-resistivity of sections with fractures is lower than 7 Ω m, while that of the near sections without fracture is higher than 10 Ω m; difference on a micro-log of fracture sections changes from 4 Ω m–10 Ω m for normal sections to 1 Ω m–3 Ω m, and even 0 Ω m locally.

FRACTURE IDENTIFICATION METHOD

Plate Method to Identify Fractures

According to the logging response characteristics of fractures, based on selecting the best response curve of fractures, the double lateral and its amplitude difference and the microelectrode and its amplitude difference are used to make plates (**Figure 4**, **Figure 5**, **Figure 6**). There is a clear difference between the fracture and non-fracture sections on the chart. The resistivity of the fracture sections is generally low, and they are concentrated in the lower left of the chart. **Table 2** is the statistical data table of the fracture identification resistivity lower limit, the positive judgment rate of the microelectrode system and its amplitude difference, the double-lateral curve, and its amplitude difference determined by each interpretation plate. It can be seen from the table that the standards for identifying fractures by the difference between the bilateral lateral amplitude and the microelectrode amplitude are both no more than 5 Ω m, and the correct rate of the two cross-platforms for identifying fractures is as high as 94%; the standards for micro-gradient and micro-potential identification of fractures are, respectively, as follows: if greater than 8 Ω m and no greater than 12 Ω m, the correct rate of the two intersecting plates to identify fractures is 91%; the standard for identifying fractures in shallow and deep lateral directions is not greater than 28 Ω m and not greater than 30 Ω m in the shallow side. The correct rate of fractures identified by the cross-directional and double-lateral amplitude difference plates was 89%, and the correct rate of the fractures by the deep-lateral and double-lateral amplitude difference cross plates was 90%. The quantitative identification of fractures using these standard plates is accurate and credible.

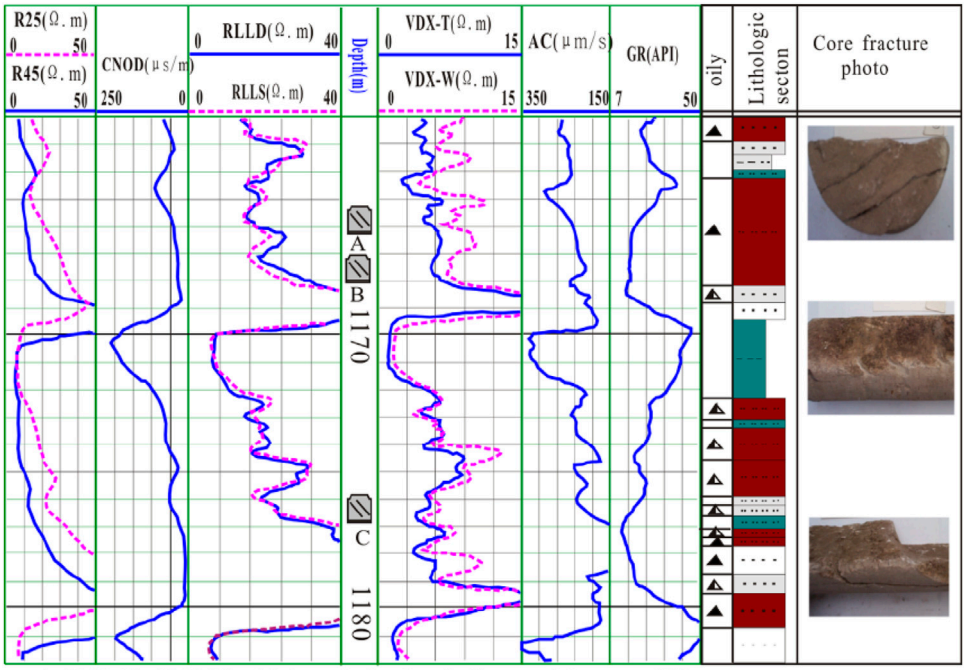

FIGURE 3 | Lithology electric fracture response analysis of Well Ji10-17.

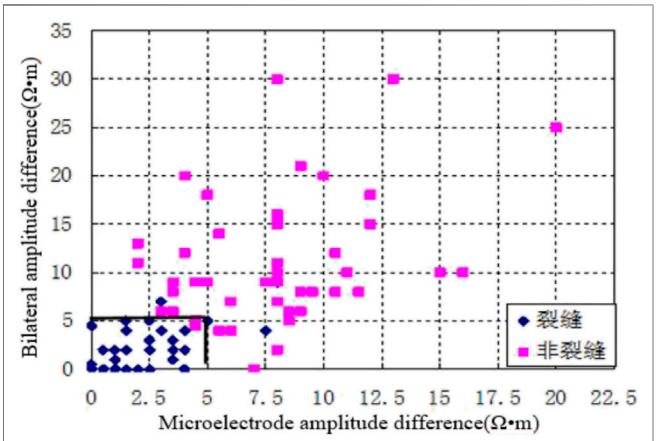

FIGURE 4 | Intersection chart of bilateral lateral amplitude difference and microelectrode amplitude.

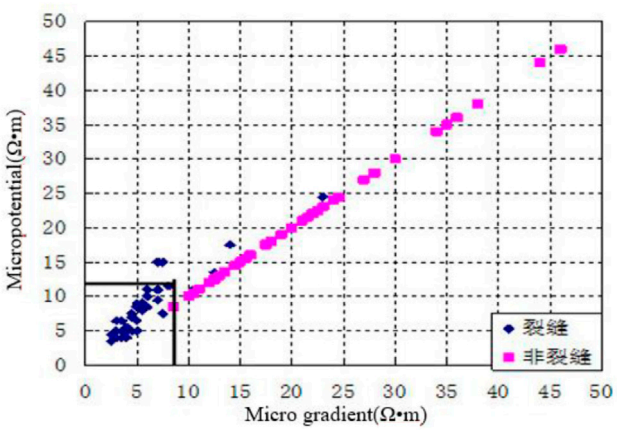

FIGURE 5 | Intersection diagram of micro-gradient and micro-potential.

Discriminant Analysis Method to Identify Fractures

Discriminant analysis is an analysis method to find the discriminant function based on the variable values that indicate the characteristics of things and their categories and to classify things with unknown categories according to the discriminant function.

Although all the aforementioned multiple logging curves respond to fractures, they do not have the same effect. To retain the main characteristic curves and eliminate the secondary characteristic curves, the discriminant function tends to be simplified, and the stepwise judgment analysis method is adopted.

The selected 85 samples are divided into two parts, of which 1 to 55 samples are used to establish the discriminant function, and the 56 to 85 samples are used to test the reliability of the discriminant function.

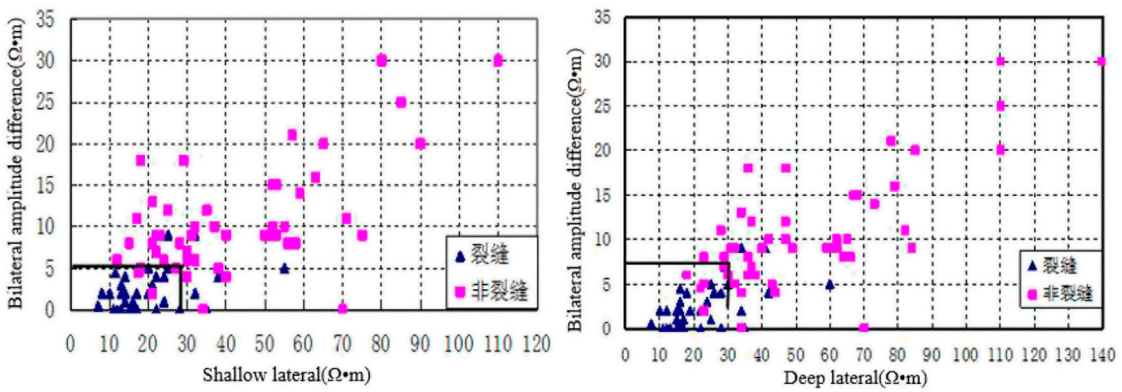

FIGURE 6 | Shallow deep lateral and bilateral lateral amplitude difference intersection chart.

TABLE 2 | Standards for fractures in the plate method.

Rendezvous plate type	Bilateral amplitude difference and microelectrode amplitude difference		Micro-gradient and micro-potential		Shallow lateral and bilateral lateral amplitude difference (%)		Deep lateral and bilateral amplitude difference (%)	
	Bilateral amplitude difference	Microelectrode amplitude difference	Micro-gradient	Micro-potential	Shallow lateral	Bilateral amplitude difference	Deep lateral	Bilateral amplitude difference
Fracture value range/(Ω·m)	≤5	≤5	≤8	≤12	≤28	≤5	≤30	≤5
Positive judgment rate	94%		91%		89		90	

Using the stepwise discriminant analysis procedure, the core calibration results are processed, and through the introduction and removal of several variables, several logging curves that play a major role in fracture discrimination are finally selected. Here, the dual lateral direction and its amplitude difference and micro-scale are mainly used. The electrode and its amplitude difference are used as the discriminant function:

$$y_1 = -0.0593(X_1) + 0.1202(X_2) - 0.1087(X_3) + 0.0249(X_4) + 0.0295(X_5) - 0.1622(X_6) - 0.6349, \quad (4)$$

$$y_2 = -0.2237(X_1) + 0.3123(X_2) - 0.0248(X_3) + 0.0428(X_4) + 0.0202(X_5) - 0.0749(X_6) - 3.4353, \quad (5)$$

where X_1 is the micro-gradient logging value, Ω m; X_2 is the micro-potential logging value, Ω m; X_3 is the microelectrode system amplitude difference, Ω m; X_4 is the shallow lateral logging value, Ω m; X_5 is the deep lateral logging value, Ω m; X_6 is the double-lateral logging amplitude difference, Ω m; and y_1 and y_2 are the fracture and non-fracture discriminant function values, respectively.

Using the discriminant function established by samples 1 to 55, the accuracy of the discriminant function is nearly 92.7%, and only four samples are judged wrong. The positive judgment rate of the inspection samples 56 to 85 is 90%, and there are three samples wrong. The accuracy of the discriminant function is relatively high.

Neural Network Pattern Recognition

This fracture study uses the BP network to predict. The BP network realizes forward mapping by weights. For a multilayer network with hidden units added between the input and output, when there is an error in the output, the error of the output layer unit is propagated back to the input layer by layer to "apportion" to each layer unit, to obtain the reference error of each layer unit. To adjust the corresponding connection rights, the cycle continues until the error of the output layer unit meets the requirements.

The characteristic parameters of the samples that have identified fractures and non-fractures are input into the computer to form a training set for the network to learn, to obtain the classification knowledge of fractures and non-fractures, and then use the classification knowledge to identify the samples to be discriminated, and the network will, according to the learned knowledge, judge whether the sample has fractured. Samples from 1 to 55 are still used to establish the discriminant function, and samples from 56 to 85 are used to test the reliability of the discriminant function.

The trained network is used to judge the learning samples, and the positive judgment rate is 96%, while the trained network has a positive judgment rate of 93% for the known samples to be judged, which proves the reliability of the network.

TABLE 3 | Comparative analysis of discriminant errors of various research methods.

	Research methods	Positive judgment rate, %
Picture	Intersection of microelectrode amplitude difference and bilateral lateral amplitude difference	94
Version	Intersection of micro-potential and micro-gradient	91
Law	Shallow lateral and bilateral lateral amplitude difference intersect	89
	Intersection of deep lateral and bilateral amplitude differences	90
Discriminant analysis	Learning sample back-judgment	92
	Identification of known samples to be judged	90
Neural networks	Learning sample back-judgment	96
	Identification of known samples to be judged	93

Discrimination Error Analysis of Various Research Methods

According to **Table 3** that among all the methods, the intersection method of microelectrode amplitude difference and bilateral amplitude difference has the highest positive judgment rate; the lowest positive judgment rate is the shallow lateral and bilateral amplitude difference intersection pattern method.

Inter-Well Fracture Prediction and Development of 3-D Model

Principle of Fractural Kriging Method

Theoretical bases of the fractural kriging method are fractional Brownian motion and the geostatistical method. Fractional Brownian motion is a Gaussian process with an average value of 0 and variance $E[X(t)]^2 = |t|^{2H}$, where H is the Hurst index, ranging from 0 to 1. One distinctive feature of the Gaussian process is that the increment of $X(t)$ with the parameter H has statistical self-similarity. The relationship between H and fractal dimension D is $D = d + 1\text{-}H$, where d is the topological dimension. This helps to fractional Brownian motion from the time domain to the spatial domain. Suppose there are two points at a distance of h in the reservoir with parameters $z(x)$ and $z\ (x + h)$, respectively. If the parameters have fractal features and meet fractional Brownian motion (Barnsley, 1986; Barton and La Pointe, 1995; Cello, 1997; Malek and Maryam, 2010), then

$$E\{[z(x+h) - z(x)]^2\} = V_H h^H. \tag{6}$$

This formula is highly similar to the variation function in geostatistics, that is,

$$2\gamma(h) = E\left\{ [z(x+h) - z(x)]^2 \right\} = V_H h^H. \tag{7}$$

Suppose the linear estimate $z^*(x)$ is the linear combination of several given points, kriging equations are follows:

$$\begin{cases} \sum_{j=1}^{n} \beta_j \gamma(x_i, x_j) + \mu = \gamma(x_i, x) \\ \sum_{i}^{n} \beta_i = 1,\ i = 1, \cdots, n \end{cases}, \tag{8}$$

where μ is the Lagrange multiplier and β_i is the weight coefficient. When there are only two vertical wells at a distance of h, the previous equations can be written as follows:

$$\begin{cases} \beta_2 \gamma(0,h) + \mu = \gamma(0,x) \\ \beta_1 \gamma(h,0) + \mu = \gamma(h,x) \\ \beta_1 + \beta_2 = 1 \end{cases}. \tag{9}$$

By substituting $\gamma(x_i, x_j) = \frac{V_H h^{2H}}{2}$ and $\{\beta_1, \beta_2\}$ into **Eq. 9**, we obtain the estimate of $z(x)$ as follows:

$$z^*(x) = \beta_1 z(0) + \beta_2 z(h), \tag{10}$$

where $\beta_1 = (1-\omega)/2$, $\beta_2 = (1+\omega)/2$, $\omega = (\frac{x}{h})^{2H} - (1-\frac{x}{h})^{2H}$ $z(0)$ is the parameter of the first well, and $z(h)$ the second well. **Eq. 10** is the fractal kriging equation, by which the parameter of any point can be obtained.

Inter-Well Fractures Prediction

If all the parameters provided by logging information are distributed vertically, then how to predict the laterally distributed fracture parameters? Hardy's research suggests that vertical fractal dimensions are nearly equal to lateral fractal dimensions, so the parameters provided by logging can also be used to predict inter-well fractures. Fractal dimensions of fracture are generally obtained by using the "box-counting method". **Figure 7** is the prediction result of the distribution of the fracture of the study area, from which we know that if fracture fractal dimensions of two wells are close, then the characteristic of the fractures, genetic mechanism, and fracture properties would also be close, and the inter-well continuity will be good; on the contrary, if fracture fractal dimensions of two wells have great difference from each other, then the characteristics of the fractures, genetic mechanism, and fracture properties will also be highly different, and the inter-well continuity will be bad.

Develop Dynamic Data to Verify the Reliability of Fracture Prediction Between Wells

A demonstration tracer test was conducted in the J25-4 well group, and the distance between the J25-4 well and the J25-6 well was 200 m. The tracer was injected into Well J25-4, and the peak of the tracer quantity was displayed in Well J25-6 after 3 days. For reservoirs with good reservoir quality in this area, the peak detection time of tracer quantity is more than 60 days. Such a fast tracer shows that it can be determined that it is due to the existence of high permeability fractures.

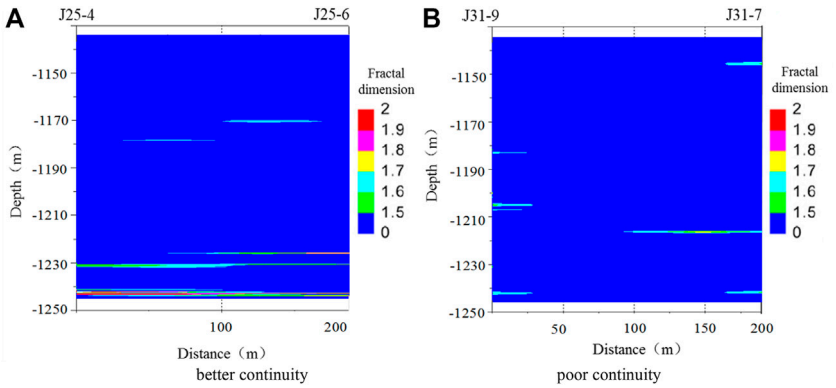

FIGURE 7 | Predicting map of fracture distribution in Xinli oil field. **(A)** Better continuity. **(B)** Poor continuity.

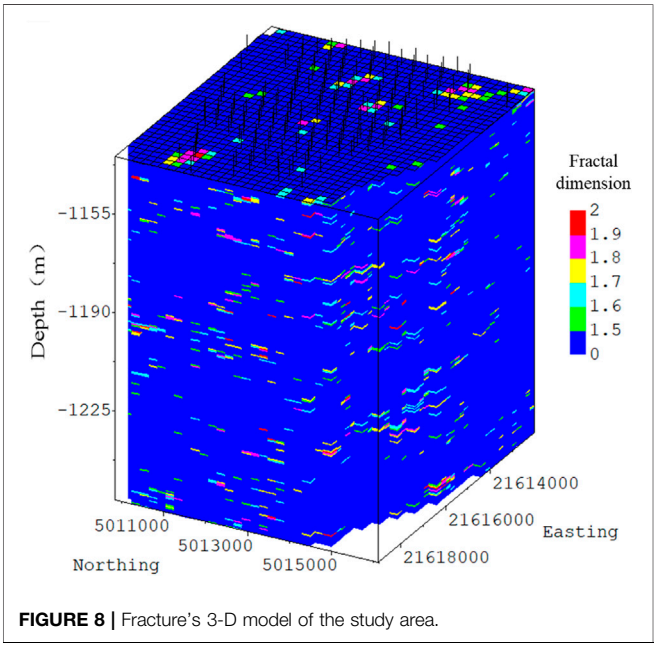

FIGURE 8 | Fracture's 3-D model of the study area.

Tracer testing was also carried out in the J31-9 well group, and the distance between the J31-9 well and the J31-7 well was 200 m. The tracer was injected into Well J31-9, and the tracer display was seen in Well J31-7 only 55 days later, indicating that there is no fracture communication between Well J31-9 and Well J31-7.

Development of the 3-D Model

Figure 8 is the fracture 3-D model of the study area developed with the fractal stochastic method based on the study of the fractured original model. From the figure, we can see that fracture density in the local area is large and inter-well continuity is good. This is consistent with the actual development of the study area, which has a higher production in the early stage and is severely flooded later. All of these show that the developed model is precise enough.

CONCLUSION

1. Synthesize similar outcrops and drilling cores, explore the fracture development characteristics of the target reservoir, and establish a prototype model of the target reservoir.
2. Using the fracture described by the core and scaling it to the logging curve, and it is found that among all logging curves of the target reservoir, only the resistivity logging curve has a good response to the fracture.
3. The fusion of multiple methods carried out the quantitative identification of the fractures at the target reservoir well points, and the application of dynamic data to verify the reliability of the identified fractures.
4. Applying the fractal theory to predict the development characteristics of inter-well fractures in the target reservoir, and establishing a three-dimensional fracture distribution model.

DATA AVAILABILITY STATEMENT

The raw data supporting the conclusion of this article will be made available by the authors, without undue reservation.

AUTHOR CONTRIBUTIONS

YX: thesis ideas and three-dimensional fracture model. LW: data collation, data analysis, calibration model, and writing the first draft of the manuscript. XZ: investigation of fracture identification methods, collection of core fracture photos of Xinli oil field, and the trend of target oil fracture count. HT: investigation of the principle of logging method and translation of the first draft of the manuscript.

ACKNOWLEDGMENTS

We acknowledge that this partially funded by the Strategic Cooperation Technology Projects of CNPC and CUPB (No.ZLZX2020-02–04). We would further like to acknowledge financial support of the National Natural Science Foundation of China (No. U1762210).

REFERENCES

Barnsley, M. F. (1986). Fractal Function and Interpolation[J]. *Constructive Proximaton* 29 (2), 303–329. doi:10.1007/bf01893434

Barton, C. C., and La Pointe, P. R. (1995). *Fractals in the Earth sciences[M]*. New York: Plenum Press, 1–88.

Cello, G. (1997). Fractal Analysis of a Quaternary Fault Array in the central Apennines, Italy. *J. of Structural Geology.* 19 (7), 945–953. doi:10.1016/s0191-8141(97)00024-2

Chen, Z., Liao, X., and Chu, H. (2019). A Boundary Element Model for Falloff Testing in Unconventional Reservoirs by Considering Natural Fractures. *Eng. Anal. Boundary Elem.* 108, 71–81. doi:10.1016/j.enganabound.2019.08.005

Clarkson, C. R., and Qanbari, F. (2015). An Approximate Semi-analytical Two-phase Forecasting Method for Multi-Fractured Tight Light-Oil wells with Complex Fracture Geometry[J]. *J. Can. Pet. Technology* 54 (6), 489–508. doi:10.2118/178665-pa

Ding, W. L., Wang, X. H., Hu, Q. J., Yin, S., Cao, X. Y., Liu, J. J., et al. (2015). Research Progress of Fractures in Tight sandstone Reservoirs. *Earth Sci. Prog.* 30 (7), 737–750

Dong, F. J., Lu, X. F., Liu, M. Y., and Rao, X. J. (2016). Correlation Analysis of Micro-geological Factors and Micro-fracture Development Degree Based on gray Correlation [J]. *Geology. Exploration* 52 (5), 950–955. doi:10.13712/j.cnki.dzykt.2016.05.017

Dong, S. Q., Zeng, L. B., and Cao, R. (2018). Discrete Fracture Network Modeling Method and Realization Constrained by Fracture Density. *Geol. Rev.* 64 (5), 1302–1314. doi:10.16509/j.georeview.2018.05.020

Fang, S., Cheng, L., and Ayala, L. F. (2017). A Coupled Boundary Element and Finite Element Method for the Analysis of Flow through Fractured Porous media. *J. Pet. Sci. Eng.* 152, 375–390. doi:10.1016/j.petrol.2017.02.020

Gong, L., Zeng, L. B., Miao, F. B., Wang, Z. S., Wei, Y., Zu, K. W., et al. (2012). Application of Fractal Geometry Method in the Description of the Complex Fracture System. *J. Hunan Univ. Sci. Technology (Natural Sci. Edition)* 27 (4), 6–10. doi:10.13712/j.cnki.dzykt.2016.05.017

Jia, P., Cheng, L., Clarkson, C. R., and Williams-Kovacs, J. D. (2017). Flow Behavior Analysis of Two-phase (Gas/water) Flowback and Early-Time Production from Hydraulically-Fractured Shale Gas wells Using a Hybrid Numerical/analytical Model. *Int. J. of Coal Geology.* 182, 14–31. doi:10.1016/j.coal.2017.09.001

Jia, P., Ma, M., Cao, C., Cheng, L. S., Yin, H. F., Li, Z., et al. (2021). Capturing Dynamic Behavior of Propped and Unpropped Fractures during Flowback and Early-Time Production of Shale Gas wells Using a Novel Flow-Geomechanics Coupled Model. *J. Pet. Sci. Eng.* 208, 109412. doi:10.1016/j.petrol.2021.109412

Jian, Q., and Li, S. J. (2001). An Interpretation Method for Identifying and Evaluating Fractured Sand Oil Reservoirs in Deep Zone in Bohai Gulf Using Dual Laterolog Responses[J]. *WLT* 25 (4), 282–286. doi:10.16489/j.issn.1004-1338.2001.04.009

Ju, W., Hou, G. T., Feng, S. B., Zhao, S. B., Zhang, J. T., You, Y., et al. (2014). Quantitative Prediction of Structural Fractures in Chang 63 Reservoir of Yanchang Formation in Qingcheng-Heshui Area, Ordos Basin. *Frontier Earth Sci.* 221 (6), 310–320. doi:10.13745/j.esf.2014.06.030

Ju, W., Hou, G. T., Huang, S. Y., and Reng, K. X. (2013). Prediction of Structural Fracture Distribution in sandstone of Lower Jurassic Ahe Formation in Yinan-Tuzi Area, Kuqa Depression. *Tectonics and mineralization* 37 (4), 592–602. doi:10.16539/j.ddgzyckx.2013.04.002

Li, C., Zhao, L., Liu, B., and Sun, M. (2020). Origin, Distribution, and Implications on Production of Bedding-Parallel Fractures: A Case from the Carboniferous KT-I Formation in the NT Oilfield, Precaspian Basin, Kazakhstan. *J. Pet. Sci. Eng.* 196, 107655. doi:10.1016/j.petrol.2020.107655

Li, Z. J., Zhang, Y., and Dou, Y. (2013). Prediction of Fractures in Tight sandstone Reservoirs by Curvature Method. *J. Southwest Pet. Univ. (Natural Sci. Edition)* 35 (6), 57–63. https://kns.cnki.net/kns8/manage/FileToText.

Liu, H., Rao, X., and Xiong, H. (2020). Evaluation of CO2 Sequestration Capacity in Complex-Boundary-Shape Shale Gas Reservoirs Using Projection-Based Embedded Discrete Fracture Model (pEDFM). *Fuel* 277, 118201. doi:10.1016/j.fuel.2020.118201

Liu, J. J., Wu, M. Y., Song, R., et al. (2017). Research on Modeling Method of Multi-Scale Fractures in Low Permeability Reservoirs. *J. Southwest Pet. Univ. (Natural Sci. Edition)* 39 (4), 90–103.

Malek, A., and Maryam, Y. (2010). Image Fusion Algorithms for Color and gray Level Images Based on LCLS Method and Novel Artificial Neural Network. *Neurocomputing* 73 (4-6), 937–943. doi:10.1016/j.neucom.2009.09.002

Philippe, A. P., and Roger, N. A. (1990) Situ Measurements of Electrical Resistivity, Formation Anisotropy and Tectonic Context[C]. SPWLA 31st Annual Logging Symposium. Louisiana: Lafayette, 24–27.

Quillan, H. (1973). Small Scale Fracture Density in Asmari Formation of Southwest Iran and its Relation to Bed Thickness and Structural Setting. *AAPG Bull.* 57 (4), 2367–2385. doi:10.1306/83d9131c-16c7-11d7-8645000102c1865d

Rao, X., Xin, L., He, Y., Fang, X., Gong, R., Wang, F., et al. (2022). Numerical Simulation of Two-phase Heat and Mass Transfer in Fractured Reservoirs Based on Projection-Based Embedded Discrete Fracture Model (pEDFM). *J. Pet. Sci. Eng.* 208, 109323. doi:10.1016/j.petrol.2021.109323

Su, H., Lei, Z. D., Zhang, D. D., Li, J. C., Zhang, Z. R., Ju, B. S., et al. (2017). Dynamic and Static Comprehensive Prediction Method of Natural Fractures in Fractured Reservoirs[J]. *Pet. exploration Dev.* 44 (6), 919–929. doi:10.1016/s1876-3804(17)30109-x

Sun, L. D., Zhou, C. N., Jia, A. L., et al. (2019). Characteristics and Direction of Tight Oil and Gas Development in China. *Pet. Exploration Development* 46 (6), 1015–1026. doi:10.1016/s1876-3804(19)60264-8

Tang, X. M., Tang, L. B., and Feng, Y. (2012). Fracture Characteristics of Shale Oil Reservoirs in the Triassic Yanchang Formation in the Ordos Basin and Conventional Logging Identification Methods. *J. Pet. Nat. Gas* 34 (6), 95–99. https://kns.cnki.net/kns8/manage/FileToText.

Teng, B., and Li, H. A. (2019). Pressure-transient Behavior of Partially Penetrating Inclined Fractures with a Finite Conductivity[J]. *SPE J.* 24 (2), 811–833. doi:10.2118/194189-pa

Wang, G. C., Zhang, C. G., Tang, J., Zhu, L., Ju, D. H., Cao, J. N., et al. (2015). Application of Fractal Dimension in Identifying Deep-Seated Tight sandstone Fractures[J]. *J. Yangtze Univ. (Self Sci. Edition)* 12 (8), 33–36. doi:10.16772/j.cnki.1673-1409.2015.08.008

Wang, H. Q., Yang, W. Y., Xie, C. H., Zheng, D. M., Wang, H. L., Zhang, X. M., et al. (2014). Azimuth Anisotropy Analysis of Different Seismic Attributes and Fracture Prediction. *Pet. Geophys. exploration* 49 (5), 925–931. doi:10.13810/j.cnki.issn.1000-7210.2014.05.043

Wang, J., Li, Y. D., and Gan, L. D. (2013). Fracture Characterization Method Based on Ant Body Anisotropy. *Pet. Geophys. prospecting* 48 (5), 763–769. doi:10.13810/j.cnki.issn.1000-7210.2013.05.022

Wu, H., Ma, D., and Spearing, A. J. S. (2021). Fracture Phenomena and Mechanisms of Brittle Rock with Different Numbers of Openings under Uniaxial Loading. *Geomechanics Eng.* 25 (6), 481–493. doi:10.12989/gae.2021.25.6.481

Wu, Y., Cheng, L., Killough, J., Huang, S., Fang, S., Jia, P., et al. (2021). Integrated Characterization of the Fracture Network in Fractured Shale Gas Reservoirs-Stochastic Fracture Modeling, Simulation and Assisted History Matching. *J. Pet. Sci. Eng.* 205, 108886. doi:10.1016/j.petrol.2021.108886

Wu, Y., Cheng, L., Ma, L., Huang, S., Fang, S., Killough, J., et al. (2021). A Transient Two-phase Flow Model for Production Prediction of Tight Gas wells with Fracturing Fluid-Induced Formation Damage. *J. Pet. Sci. Eng.* 199, 108351. doi:10.1016/j.petrol.2021.108351

Xiong, H., Devegowda, D., and Huang, L. (2019). EOR Solvent-Oil Interaction in Clay-Hosted Pores: Insights from Molecular Dynamics Simulations. *Fuel* 249, 233–251. doi:10.1016/j.fuel.2019.03.104

Zhao, J. L., Gong, Z. W., Li, G., Feng, C. Y., Bai, X, Hong, Y., et al. (2012). A Review and Perspective of Identifying and Evaluating the Logging Technology of Fractured Carbonate Reservoir. *Prog. Geophys.* 27 (2), 543–547. doi:10.6038/j.issn.1004-2903.2012.02.017

Conflict of Interest: The authors declare that the research was conducted in the absence of any commercial or financial relationships that could be construed as a potential conflict of interest.

frontiers in Earth Science

ORIGINAL RESEARCH
published: 11 March 2022
doi: 10.3389/feart.2022.852381

Investigating the Impacts of Nonuniform Proppant Distribution and Fracture Closure on Well Performance in Shale Gas Reservoirs

Qiang Zhang[1], *Xia Yan*[2]*, *Xiaoyu Wang*[2]*, *Gaocheng Feng*[1], *Weiying Yao*[1], *Yanjun Yin*[1] *and Kai Zhang*[2]

[1]CNOOC EnerTech-Drilling and Production Co., Tianjin, China, [2]School of Petroleum Engineering, China University of Petroleum (East China), Qingdao, China

The nonuniform distribution of proppant in hydraulic fractures is an essential factor determining the accuracy of well performance evaluation in shale gas reservoirs. In particular, unpropped and propped parts hold distinct closure behavior. To study the impacts of distinct closure behavior between unpropped and propped parts in fracture on gas production, we combine the proppant transport simulation and the 3D hydromechanical coupling simulation. This study quantitatively indicates the significant effects of nonuniform proppant distribution and fracture closure on well performance in shale gas reservoirs. By comparing the well performances with three kinds of typical proppant distribution at the same injection volume, the distribution accumulating near the wellbore is recommended as it can reduce the impact of unpropped fracture and exploit more gas. In addition, the cases with higher natural fracture permeability are found to have less difference in the well performance with different proppant coverages. Therefore, the impacts of nonuniform proppant distribution and fracture closure on well performance in shale gas reservoirs should be investigated comprehensively.

Keywords: nonuniform proppant distribution, fracture closure, hydromechanical coupling, shale gas, numerical simulation

OPEN ACCESS

Edited by:
Jianlin Zhao,
ETH Zürich, Switzerland

Reviewed by:
Yanlong Li,
Qingdao Institute of Marine Geology (QIMG), China
Qi ZHANG,
Hong Kong Polytechnic University, Hong Kong, SAR China

***Correspondence:**
Xia Yan
jsyanxia1989@163.com
Xiaoyu Wang
wxyupc@126.com

Specialty section:
This article was submitted to Economic Geology, a section of the journal Frontiers in Earth Science

Received: *11 January 2022*
Accepted: *14 February 2022*
Published: *11 March 2022*

Citation:
Zhang Q, Yan X, Wang X, Feng G, Yao W, Yin Y and Zhang K (2022) Investigating the Impacts of Nonuniform Proppant Distribution and Fracture Closure on Well Performance in Shale Gas Reservoirs. Front. Earth Sci. 10:852381. doi: 10.3389/feart.2022.852381

INTRODUCTION

Hydraulic fracturing has been a key technology for the economic exploitation of shale resources (Longlong, 2014; Yang et al., 2015; Song et al., 2016; Moghadasi et al., 2019; Yan, 2021). During the treatments of hydraulic fracturing, a great deal of slickwater and proppants is pumped to form hydraulic fractures in the shale formation. Within these hydraulic fractures, the proppant distribution is usually nonuniform, and the unpropped and propped parts hold distinct closure behavior (Li et al., 2020; Manchanda, 2020; Li and Voskov, 2021). Meanwhile, the distinct closure behavior conversely results in different stress-related conductivity for the propped and unpropped regions, which has a great effect on gas transport (Shen et al., 2019; Liu, 2020; Yan et al., 2020). Therefore, the nonuniform proppant distribution and fracture closure should be considered for accurately evaluating the well performance in shale gas reservoirs.

Placement of injected proppant in the fracture is one of the key factors determining fracture flow capacity after hydraulic fracturing (Liu, 2020; Yan et al., 2020). The mechanism of multiphase flow with proppant is relatively complex and needs to be further studied. Limitation of the formation

environment makes direct monitoring of fracturing slurry flow impossible. Currently, a series of lab-scale experimental models built by transparent glass plates have been applied to search rules of sanding patterns (Tong and Mohanty, 2016; Ray, 2017; Tong et al., 2018). This kind of laboratory-based research and analysis is difficult to be directly applied to oilfield scale prediction, and thus numerical simulation becomes a feasible choice. In addition, the type of Lagrangian-based simulation always processes particles or particle clusters into a single tracking object, which requires a huge amount of calculation and is very challenging to achieve large-scale simulation such as the so-called DDPM(Hu et al., 2018), CFD-DEM (Zeng et al., 2016; Zhang et al., 2017; Wang et al., 2019; Zhu et al., 2019; Zhu et al., 2020), and MP-PIC methods (Zeng et al., 2019; Mao et al., 2021). On the contrary, the Eulerian-based scheme is thought to be more efficient which treats the particle phase as one of the continuous phases. For example, many study results of proppant distribution in long fracture by the two-fluid model (TFM) (Han, 2016; Huang, 2017; Wen et al., 2020) have been reported. To simulate the proppant flow in a fracture of 100 m long and 20 m high, the Eulerian granular model is used.

A number of reported studies, which investigated the impacts of proppant distribution and fracture closure on the well performance in shale gas reservoirs, are summarized as follows: Sierra et al.(Sierra et al., 2014) and Cipolla et al. (Cipolla et al., 2009; Cipolla et al., 2010) investigated the effects of the high-conductivity arch, unpropped fracture conductivity, and proppant distribution on gas production; however, they did not consider the fracture closure. Lee et al. (Lee et al., 2016) proposed the numerical model incorporating fracture closure to study the influence of proppant distribution in fracture on cumulative gas production. Liu et al.(Liu et al., 2018; Liu et al., 2019) studied the effects of fracture closure and proppant distribution on water flowback and gas production by using geomechanical simulation and flow simulation separately. Mao et al. (Mao et al., 2021) developed a MP-PIC-EDFM coupling system to evaluate the impact of proppant pumping schedules on gas production. However, their study is mainly focused on the fluid flow aspect, and the geomechanical effects have not been considered in detail. Zhou et al. (Zhou et al., 2019) and Zheng et al. (Zheng, 2019; Zheng et al., 2020) conducted the hydromechanical coupling simulations to study the impacts of proppant distribution and closure of fracture on cumulative gas production, while they ignored the displacement discontinuity at hydraulic fractures, which is significant for the stress change around these fractures. Due to the geomechanical effects being considered by using the over-simplification method in these studies, Yan et al. (Yan et al., 2020) developed a fully coupled geomechanics and gas transport model, in which the displacement discontinuity was simulated by using the stabilized extended finite element method, to investigate the impacts of partially supported fracture closure on well performance in shale gas reservoirs. However, the nonuniform proppant distribution is artificial in their study. In this study, the proppant transport simulation will be carried out to provide a more reliable nonuniform proppant distribution, and then the influence of proppant distribution patterns and fracture closure on well performance will be studied by using the fully coupled geomechanics and gas transport model.

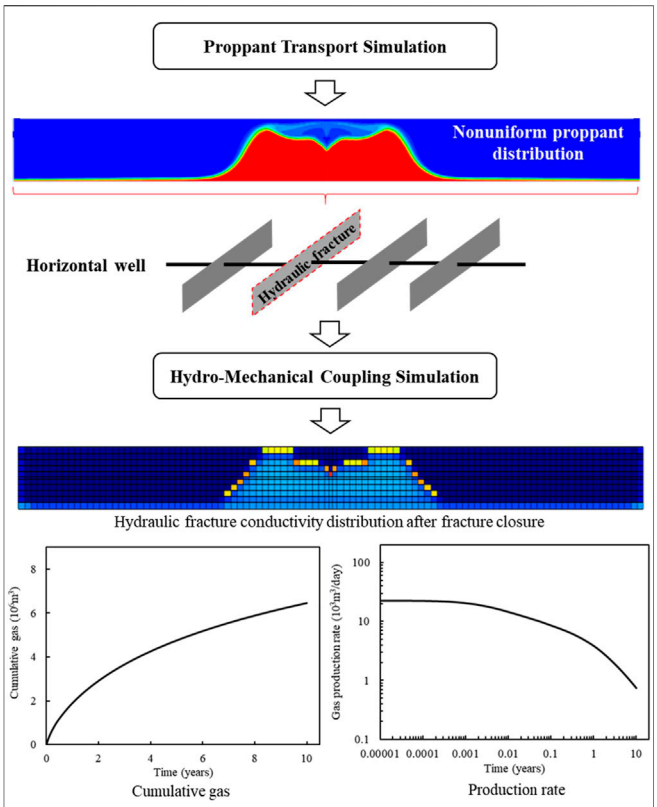

FIGURE 1 | Schematic workflow for studying the impacts of heterogenous proppant distribution and fracture closure on shale gas production.

This article is structured as follows: the numerical models for proppant transport and gas production are illustrated in **Section 2**; the impacts of proppant distribution patterns and fracture closure on gas production performance are analyzed in **Section 3**; in **Section 4**, some conclusions are provided.

METHODOLOGY

The schematic workflow for studying the impacts of nonuniform proppant distribution and fracture closure on shale gas production includes two procedures: proppant transport simulation and hydromechanical coupling simulation, as shown in **Figure 1**. First, we use the Eulerian granular model (Han, 2016) (EGM) to simulate the proppant transport and obtain its nonuniform distribution in hydraulic fractures. Then, we conduct the hydromechanical coupling simulation to

find the impacts of fracture closure and nonuniform proppant displacement on well performance in a 3D shale reservoir.

Proppant Transport Simulation

The proppant transport simulations are conducted based on the EGM, and the main model details are described as follows: the main phase in the EGM is the fluid phase and shares the same single pressure as the other solid phase. All the phases are treated as continuous, and the phase volume fraction is used to distinguish the computational region taken by various phases.

The mass conservation equation can be written as (Han, 2016):

$$\frac{\partial}{\partial t}\left(\alpha_q\rho_q\right)+\nabla\cdot\left(\alpha_q\rho_q\overrightarrow{V_q}\right)=\sum_{p=1}^{n}\left(\dot{m}_{pq}-\dot{m}_{qp}\right), \tag{1}$$

where p and q are the subscripts for representing different phases, α is the volume fraction, $\vec{V}$ indicates velocity, ρ is the density, and $\dot{m}_{pq}$ and $\dot{m}_{qp}$ denote the mass transfer between phases. The following two equations (Han, 2016) are used to compute the momentum balance of the fluid phase and solid phase, respectively:

$$\begin{aligned}&\frac{\partial}{\partial t}\left(\alpha_q\rho_q\overrightarrow{V_q}\right)+\nabla\cdot\left(\alpha_q\rho_q\overrightarrow{V_q}\overrightarrow{V_q}\right)\\&=-\alpha_q\nabla p+\nabla\cdot\bar{\bar{\tau}}_q+\alpha_q\rho_q\vec{g}+\sum_{p=1}^{n}\left[K_{pq}\left(\overrightarrow{V_p}-\overrightarrow{V_q}\right)+\dot{m}_{pq}\vec{V}_{pq}\right.\\&\left.-\dot{m}_{qp}\vec{V}_{qp}\right]+\left(\vec{F}_q+\vec{F}_{lift,q}+\vec{F}_{wl,q}+\vec{F}_{vm,q}+\vec{F}_{td,q}\right);\end{aligned} \tag{2}$$

$$\begin{aligned}&\frac{\partial}{\partial t}\left(\alpha_q\mu_q\vec{V}_s\right)+\nabla\cdot\left(\alpha_s\rho_s\vec{V}_s\vec{V}_s\right)=-\alpha_s\nabla p+\nabla\cdot\bar{\bar{\tau}}_s+\alpha_s\rho_s\vec{g}\\&+\sum_{p=1}^{N}\left[K_{ls}\left(\vec{V}_l-\vec{V}_s\right)+\dot{m}_{ls}\vec{V}_{ls}-\dot{m}_{sl}\vec{V}_{sl}\right]-\nabla p_s+\left(\vec{F}_q+\vec{F}_{lift,q}\right.\\&\left.+\vec{F}_{wl,q}+\vec{F}_{td,q}\right),\end{aligned} \tag{3}$$

where K indicates the coefficient used to calculate interphase momentum exchange; $\vec{F}$ with a subscript means different kinds of forces, such as $\vec{F}_q$, $\vec{F}_{lift,q}$, $\vec{F}_{td,q}$, $\vec{F}_{wl,q}$, and $\vec{F}_{vm,q}$ representing the external body force, lift force, turbulent dispersion force, wall lubrication force, and virtual mass force, respectively; $\bar{\bar{\tau}}_q$ is the stress–strain tensor; and p_s is solid phase's pressure.

Please note that the mass conservation and momentum balance equations of each phase are solved separately and then coupled with the mass and momentum exchange coefficients (Han, 2016). The numerical simulations are conducted by using ANSYS Fluent software. The reliability and accuracy of EGM have been verified by comparing it with experimental results in our previously published work (Wang, 2021). The proppant distribution results obtained by numerical simulation agree well with experimental results in the work of Tong, S. et al. (Tong and Mohanty, 2016).

Hydromechanical Coupling Simulation

Figure 2 shows the schematic of a typical shale gas reservoir, which consists of two sections. The darker section indicates the stimulated reservoir volume (SRV) including hydraulic fractures and natural fractures, while the other section outside the SRV contains few fractures. Therefore, the hybrid model (Yan, 2018; Yan et al., 2018) consisting of the embedded discrete fracture model, multiple porosity model, and single porosity model (Yan et al., 2016; Yan et al., 2019) will be used to evaluate the gas well performance.

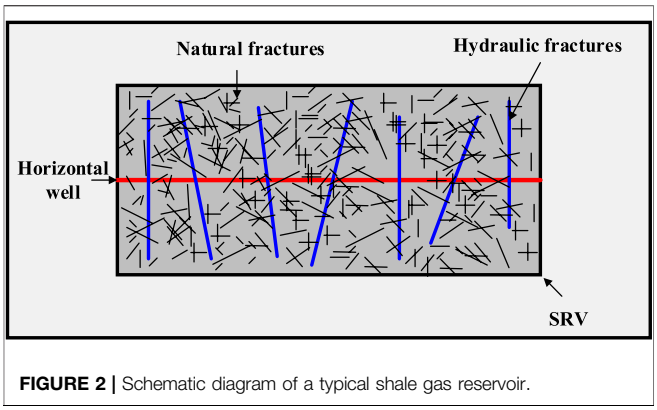

FIGURE 2 | Schematic diagram of a typical shale gas reservoir.

To reduce the simulation complexity and clearly investigate the effects of nonuniform proppant distribution and fracture closure on gas production, the single-phase gas model considering adsorption/desorption and Klinkenberg effects is applied to describe the gas transport in shale reservoirs (Yan et al., 2020), and its mass conservation equation is

$$\begin{aligned}&\frac{\partial}{\partial t}\int_{\Omega}\left[\phi\rho_{\mathrm{g}}+(1-\phi)m\right]\mathrm{d}\Omega+\int_{\Gamma}\left[-\rho_{\mathrm{g}}\frac{k}{\mu}\left(1+\frac{b}{p}\right)\left(\nabla p-\rho_{\mathrm{g}}\mathrm{g}\nabla D\right)\right]\\&\cdot\boldsymbol{n}\mathrm{d}\Gamma=\int_{\Omega}q\mathrm{d}\Omega,\end{aligned} \tag{4}$$

where ϕ is the Lagrange porosity, in which the influences of fluid pressure and effective stress on pore deformation are fully considered (Yan, 2018), ρ_{g} represents gas density, m denotes the adsorption/desorption term, which is only for the shale matrix and could be calculated with the Langmuir's isotherm (Langmuir, 1917), k indicates the absolute permeability, μ represents gas viscosity, b is the Klinkenberg coefficient incorporating gas-slippage effect (Wu et al., 2014), p indicates gas pressure; g and D represent gravity acceleration and depth, respectively, $\boldsymbol{n}$ is the normal vector of boundary Γ, and q is the sink/source term on domain Ω.

The quasi-static geomechanics model (Shao, 2021; Zhang, 2021; Zhang et al., 2021) considering displacement discontinuity is used to describe the reservoir deformation and fracture closure, and its governing equation is

$$\nabla\cdot\sigma+\boldsymbol{b}=0, \tag{5}$$

where $\boldsymbol{b}$ indicates the body force vector, and with the sign convention (i.e., negative for compression and positive for tension), the total stress tensor $\boldsymbol{\sigma}$ of the hybrid model is written as (Yan et al., 2020):

$$\sigma=\begin{cases}\boldsymbol{C}\varepsilon-\alpha p\mathbf{I}, & \text{outside the SRV}\\ \boldsymbol{C}_{\mathrm{up}}\varepsilon+\sum_l K_{\mathrm{dr}}b_l p_l\mathbf{I}, & \text{in the SRV}\end{cases}, \tag{6}$$

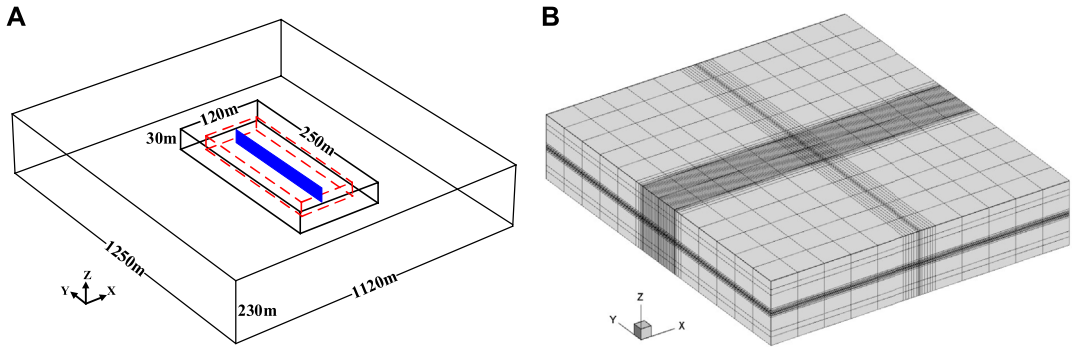

FIGURE 3 | Schematic diagram of the 3D reservoir model **(A)** and its geometry discretization **(B)**.

TABLE 1 | Model parameters used in shale gas production simulation.

Name	Value
SRV region size (red dashed line), m	80 × 200×20
Half-length and height of hydraulic fracture, m	100.0, 20.0
Fracture spacing and initial aperture of natural fracture, m	1.0, 5.0E-6
Initial permeabilities of matrix, natural fracture, and hydraulic fracture, mD	2.0E-5, 0.01, 1.0E4
Initial porosities of matrix, natural fracture, and hydraulic fracture	0.05, 1.0, 0.5
Minimum hydraulic aperture of unpropped fracture, m	6.0E-6
Volume fractions of matrix sub-gridblocks	0.15, 0.21, 0.38, 0.26
Young's modulus of matrix and natural fracture, GPa	40.0, 0.05
Poisson's ratios of matrix and natural fracture	0.2, 0.2
Intrinsic solid grain bulk modulus, GPa	400.0
Langmuir pressure, MPa	4.0
Langmuir volume, m^3/kg	0.018
Initial pressure and bottomhole pressure, MPa	25.0, 10.0
Reservoir temperature, K	343.15
Rock density, kg/m^3	2,850
Well radius, m	0.1

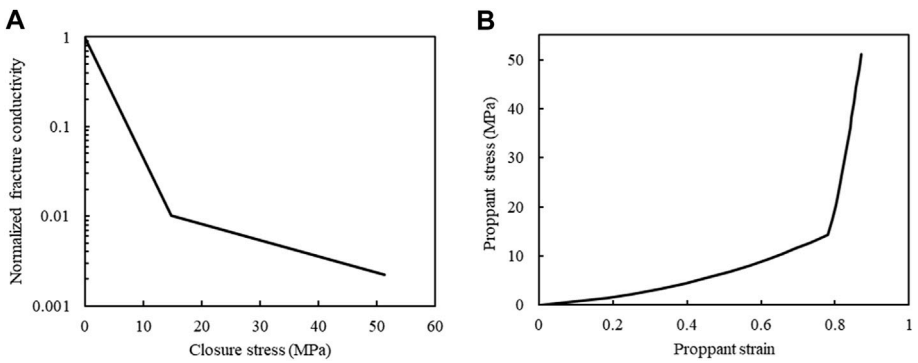

FIGURE 4 | Stress-dependent normalized fracture conductivity **(A)** and the nonlinear stress–strain for proppant compression **(B)** (Yan et al., 2020).

where $\boldsymbol{C}$ and α denote the elasticity tensor and Biot coefficient for single porosity model, respectively, $\mathbf{I}$ indicates the unit tensor, $\boldsymbol{C}_{\mathrm{up}}$, K_{dr}, and b_l denote the upscaled elasticity tensor, drained bulk modulus, and the coupling parameter for the multiple porosity model (Yan, 2018). The small deformation assumption is adopted here, and thus the strain tensor $\boldsymbol{\varepsilon}$ can be written as:

$$\varepsilon = \frac{1}{2}\left(\nabla \boldsymbol{u} + \nabla^{\mathrm{T}} \boldsymbol{u}\right), \tag{7}$$

where $\boldsymbol{u}$ indicates the displacement vector, ∇ is a gradient operator, and superscript T indicates transpose.

The flow and geomechanics boundary conditions are

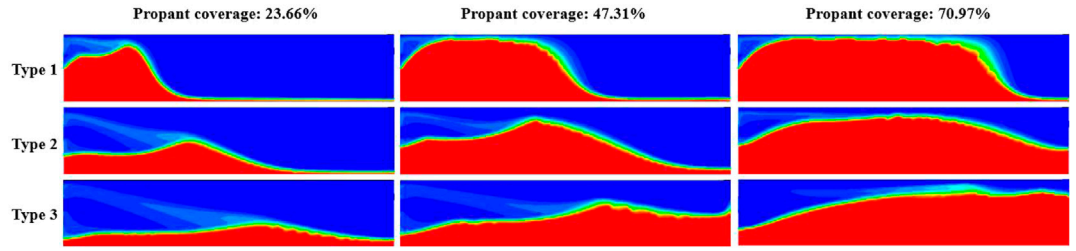

FIGURE 5 | Proppant distributions with different injection volumes, and the half-profiles are shown due to symmetry.

$$\begin{aligned} &\boldsymbol{v}\cdot\boldsymbol{n}_q=\bar{\boldsymbol{q}}\ \text{ on }\Gamma_q,\ p=\bar{p}\ \text{on}\ \Gamma_p;\\ &\sigma\cdot\boldsymbol{n}_t=\bar{\boldsymbol{t}}\ \text{ on }\Gamma_t,\ \boldsymbol{u}=\bar{\boldsymbol{u}}\ \text{on}\ \Gamma_u;\\ &\sigma\cdot\boldsymbol{n}_{\mathrm{HF}}=-\left(p_{\mathrm{HF}}+p_s\right)\cdot\boldsymbol{n}_{\mathrm{HF}}\ \text{on}\ \Gamma_{\mathrm{HF}}, \end{aligned} \tag{8}$$

where $\boldsymbol{v}$ indicates the gas flow rate; $\bar{\boldsymbol{q}}$ and $\bar{p}$ are the prescribed rate and pressure on the Neumann flow boundary Γ_q and Dirichlet flow boundary Γ_p, respectively; $\bar{\boldsymbol{t}}$ and $\bar{\boldsymbol{u}}$ are the prescribed traction and displacement on the Neumann geomechanics boundary Γ_t and Dirichlet geomechanics boundary Γ_u, respectively; p_{HF} and p_s represent gas pressure and effective stress acting on the inner fracture boundary Γ_{HF}; and $\boldsymbol{n}_q$, $\boldsymbol{n}_t$, and $\boldsymbol{n}_{\mathrm{HF}}$ indicate the unit normal vectors to Γ_q, Γ_t, and Γ_{HF}, respectively. The effective stress equation for propped fracture closure is (Yan et al., 2020)

$$p_s=\begin{cases} f_s(\varepsilon_s), & \varepsilon_s>0\\ 0, & \varepsilon_s\le 0 \end{cases}, \tag{9}$$

where f_s denotes the general stress–strain relationship of proppant compression, and ε_s is the proppant normal strain. On the other hand, the effective stress equation for unpropped fracture closure is (Yan et al., 2020)

$$p_s=\begin{cases} -E_n d_{\mathrm{HF}}, & d_{\mathrm{HF}}<0\\ 0, & d_{\mathrm{HF}}\ge 0 \end{cases}, \tag{10}$$

where d_{HF} indicates current fracture aperture, and E_n is the normal penalty parameter. Note that **Eq. (10)** permits a small interpenetration for fracture faces because its value is infinitesimal.

As the properties of matrix and fractures are affected by reservoir deformation, the matrix's dynamic permeabilities (k_m), hydraulic fractures (k_{HF}), and natural fractures (k_f) are adopted here:

$$k_m=k_{m0}\left(\frac{\phi_m}{\phi_{m0}}\right)^3\left(\frac{1-\phi_{m0}}{1-\phi_m}\right)^2; \tag{11}$$

$$k_f=k_{f0}\left(1+\frac{K_{dr}}{K_f}\varepsilon_v\right)^3\left(1+\varepsilon_v\right)^{-2}; \tag{12}$$

$$k_{\mathrm{HF}}=\begin{cases} f_k(p_s), & \text{proppedpart}\\ \left(\max\left(d_{HF},d_{HF\,\min}\right)\right)^2/12, & \text{unproppedpart} \end{cases}, \tag{13}$$

where subscripts m, f, HF, and 0 represent matrix, natural fracture, hydraulic fracture, and initial state, respectively; K_f is the drained bulk modulus for natural fracture; ε_v indicates volumetric strain; f_k denotes the general relationship between effective stress and proppant permeability; and d_{HFmin} indicates the minimum hydraulic aperture of unpropped fracture.

The developed fully coupled gas transport and geomechanics model can be solved by using our in-house hydromechanical coupling simulator. In this simulator, the flow and geomechanics models are discretized through the stabilized extended finite element method and the finite volume method. The coupled model is solved utilizing a sequential implicit method. The detailed numerical procedure and model verification can be found in our previous studies (Yan, 2018; Yan et al., 2018; Yan et al., 2019; Yan et al., 2020).

RESULTS AND DISCUSSION

In this section, some numerical examples will be carried out to research the impacts of nonuniform proppant displacement and fracture closure on gas production performance. In the proppant transport simulation, the fixed time step (i.e., 1 s) is adopted to ensure that the moving distance of material in each step is the size of one or two grids, while the variable time step is used in the hydromechanical coupling simulation. We first set the initial time step and max time step, and then the time step would be reduced multiply, if the convergence solution cannot be obtained with the current time step. Conversely, if the convergence solution is obtained with the current time step, the next time step would be increased in multiples or kept the same. In addition, the time step cannot be over the max time step. In the following examples, the initial time step and max time step are 1 s and 100 days, respectively.

To reduce the computational costs, we only simulate one stage within a shale reservoir in 3D (**Figure 3A**). A horizontal well as well as the proppant injector is set at the hydraulic fracture center.

TABLE 2 | Parameters used for proppant transport simulations.

Name	Value
Fracturing fluid density, kg/m^3	1,000.0
Proppant density, kg/m^3	2,650.0
Proppant radius, μm	400.0
Volume fraction of proppant	0.1
Injection rate, m^3/min	1.2E-4
Fracturing fluid viscosity for Type 1, mPa·s	1.0
Fracturing fluid viscosity for Type 2, mPa·s	5.0
Fracturing fluid viscosity for Type 3, mPa·s	10.0

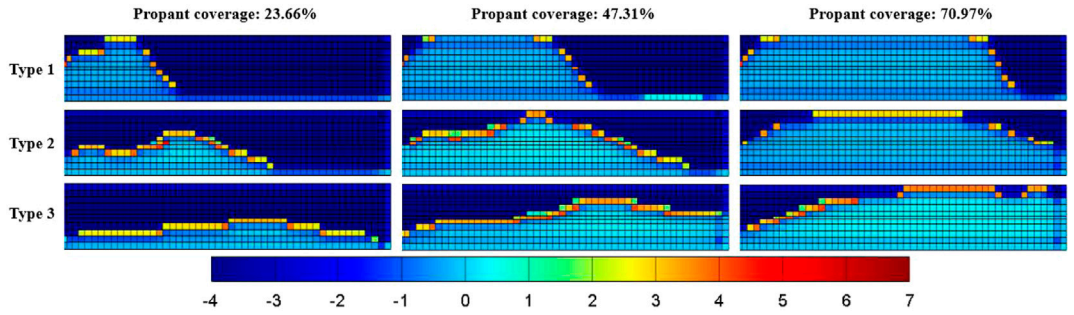

FIGURE 6 | Comparison of the conductivity map after 10 years between cases with various proppant distributions, lg (k_{HF}·d_{HF}/md-m).

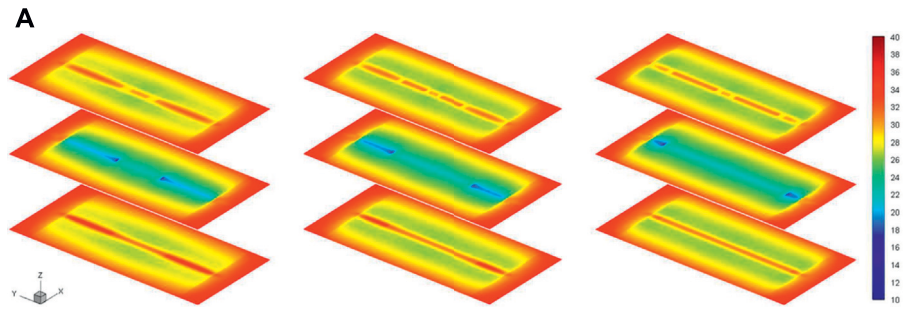

Type 1 with propant coverage: 23.66% (left), 47.31% (middle), and 70.97% (right), MPa.

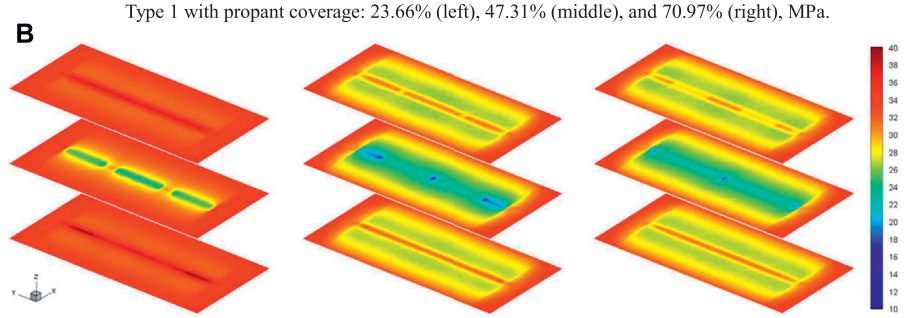

Type 2 with propant coverage: 23.66% (left), 47.31% (middle), and 70.97% (right), MPa.

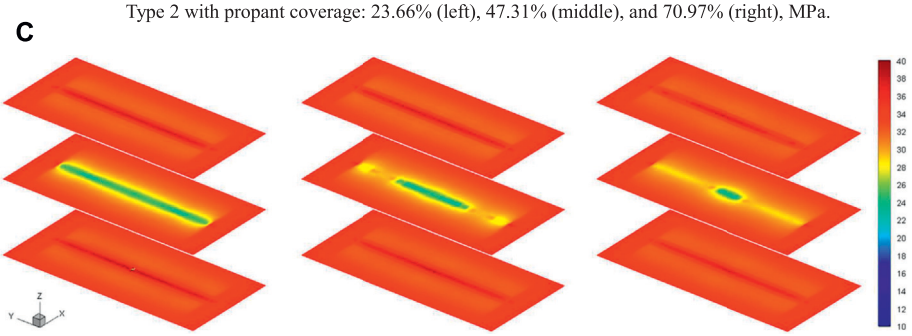

Type 3 with propant coverage: 23.66% (left), 47.31% (middle), and 70.97% (right), MPa.

FIGURE 7 | Comparison of σ_{xx} distribution after 10 years between cases with various proppant distributions. The profiles are shown in three layers (top, middle, and bottom), and the *z* length is shown nine times of the actual size for clarity. **(A)** Type 1 with proppant coverage: 23.66% (left), 47.31% (middle), and 70.97% (right), MPa. **(B)** Type 2 with proppant coverage: 23.66% (left), 47.31% (middle), and 70.97% (right), MPa. **(C)** Type 3 with proppant coverage: 23.66% (left), 47.31% (middle), and 70.97% (right), MPa.

The outer flow boundary is closed. The two stresses (35 MPa and 40 MPa) in the horizontal direction and the overburden stress (30 MPa) are applied on the back, right, and top boundaries, respectively. In addition, the roller constraint is applied to the other boundaries. **Table 1** gives the model parameters, and the stress-dependent normalized fracture conductivity and the

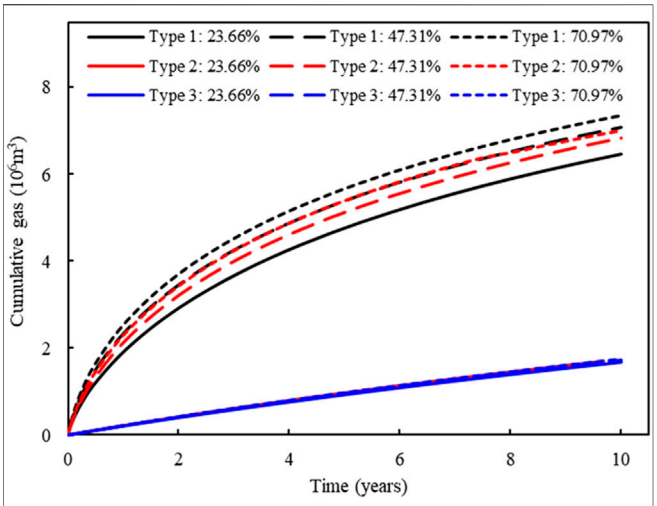

FIGURE 8 | Comparison of cumulative gas after 10 years between cases with various proppant displacements.

stress–strain curve for proppant compression are presented in **Figure 4**. The geometry discretization of this model is plotted in **Figure 3B**. Note that the surrounding formation is impermeable, and it is used to accurately consider geomechanical effects.

As concluded in our previous research (Wang, 2021), various proppant distributions can be obtained for different pumping schemes. For example, the proppant distributions are adjusted by controlling the fracturing fluid viscosity in this work. It should be noted that a similar effect can be achieved by altering other injection conditions. Overall, three representative distribution types are selected from a series of cases: proppants accumulate near the wellbore (Type 1), proppants transport to the location away from the wellbore (Type 2), and proppants screen out in fracture tip (Type 3), as shown in **Figure 5**. With the same injection volumes, which distribution would have the best gas production is a valuable question. At first, we mimic the fracturing treatment with high pressure fluid (42 MPa) within hydraulic fracture to obtain its initial aperture distribution. Then, the proppant transport simulation is conducted to form the proppant distribution within the hydraulic fracture, and the simulation parameters are summarized in **Table 2**.

The proppant distributions with different injection volumes (proppant coverage, the ratio of the propped fracture area to the total fracture area) are shown in **Figure 5**. The comparisons of conductivity distribution, σ_{xx} distribution (only the reservoir part), and cumulative gas among various cases after 10 years are compared in **Figures 6–8**, respectively. First, we can find that the conductivity of the supported fracture area is significantly higher than that of the unpropped part, while the highest conductivity is located at the interface between propped and unpropped parts because there is a

TABLE 3 | Cumulative gas for different cases after 10 years.

	Cumulative gas, 10^6m^3								
	Type 1			Type 2			Type 3		
	23.66%	47.31%	70.97%	23.66%	47.31%	70.97%	23.66%	47.31%	70.97%
0.018 md-m	6.47	7.07	7.35	1.75	6.85	7.00	1.69	1.73	1.76
0.090 md-m	6.65	7.15	7.37	3.77	6.93	7.06	3.64	3.76	3.81
0.180 md-m	6.79	7.21	7.38	4.86	7.00	7.11	4.72	4.90	4.92

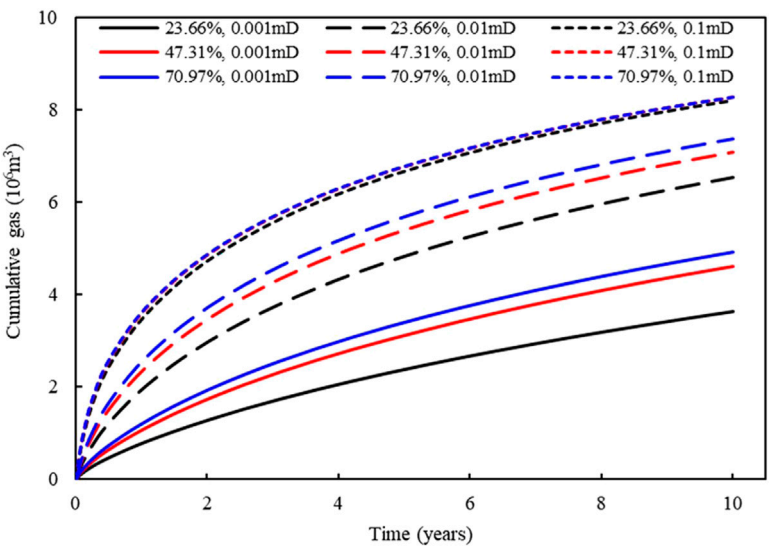

FIGURE 9 | Comparison of cumulative gas between different cases after 10 years.

high conductivity arch at the interface as the result of different closure behaviors for propped and unpropped parts. We can also find that σ_{xx} around the part supported by the proppant is higher than that of the unpropped area. Because the part supported by the proppant is stiffer than the unpropped part, which can resist higher closing. From **Figure 8**, it can be concluded that Type 1 has the best gas production as its cumulative gas is the highest for all injection volumes. On the contrary, Type 3 has the worst gas production because the wellbore cannot be effectively supported in this type. Another interesting observation is that σ_{xx} of the reservoir part decreases as the cumulative gas increases. Because when pressure decreases in the reservoir part, the region outside of the reservoir part suffers higher stress to support the boundary force.

In addition, to illustrate the sensitivity of gas production to the conductivity of unpropped fracture, three conductivities (0.018-m, 0.090-m, and 0.180-m) are applied for unpropped fracture. **Table 3** lists the cumulative gas for different cases after 10 years. It indicates that gas production correlates positively with the conductivity of unpropped fracture, especially the gas production of the distribution type, in which the wellbore cannot be effectively supported, is the most affected. As the conductivity of unpropped fracture is usually low and difficult to improve, the completion design should strive to form Type 1 proppant distribution to reduce the impact of unpropped fracture and exploit more gas with the same proppant injection volume.

Last, we study the influence of proppant coverage for Type 1 on gas production under different natural fracture permeability (0.001 mD, 0.01 mD, and 0.1 mD). **Figure 9** shows the comparison of cumulative gas between different cases after 10 years. We can see that cumulative gas increases as the proppant covered coverage increases under different natural fracture permeability; however, the increase of cumulative gas caused by covered coverage increasing is negligible when natural fracture permeability is high enough. Therefore, the proppant covered coverage in the hydraulic fracture can be appropriately reduced by increasing natural fracture permeability.

CONCLUSION

In this work, the gas production in shale reservoirs considering nonuniform proppant distribution and fracture closure is studied by combing proppant transport simulation and hydromechanical coupling simulation. Specifically, we use the EGM to simulate the proppant transport and obtain its nonuniform distribution in hydraulic fractures, and then we conduct the hydromechanical coupling simulation to simulate the impacts of nonuniform proppant distribution and fracture closure on gas production performance in a 3D shale reservoir. The following insights are obtained: 1) the nonuniform proppant distribution and fracture closure have a significant influence on gas production performance; 2) Type 1 proppant distribution is recommended as it can reduce the impact of unpropped fracture and exploit more gas with the same proppant injection volume; 3) higher natural fracture permeability leads to less impact of proppant coverage on gas production. Therefore, the nonuniform proppant distribution and fracture closure should be considered for accurately evaluating the well performance in shale gas reservoirs. As there is no limit to fracture number and fracture pattern in the proposed method, the large-scale implementation with a complex fracture pattern will be realized in our future study.

DATA AVAILABILITY STATEMENT

The raw data supporting the conclusion of this article will be made available by the authors, without undue reservation.

AUTHOR CONTRIBUTIONS

XY and XW: conceptualization; QZ, XY, and XW: methodology; QZ: software; XY and QZ: validation; GF: formal analysis; WY: investigation; YY: resources; QZ: data curation; XY and QZ: writing—original draft preparation; KZ: writing—review and editing; QZ: visualization; XY: supervision; WY: project administration; YY: funding acquisition. All authors have read and agreed to the published version of the manuscript.

FUNDING

This work was supported by the National Natural Science Foundation of China (52004321 and 52034010), Natural Science Foundation of Shandong Province, China (ZR2020QE116), and Fundamental Research Funds for the Central Universities (20CX06025A, 21CX06031A, and YCX2021033).

REFERENCES

Cipolla, C. L. L., Warpinski, N. R. R., Mayerhofer, M. J. J., Lolon, E. P. P., and Vincent, M. C. C. (2010). The Relationship between Fracture Complexity, Reservoir Properties, and Fracture-Treatment Design. *SPE Prod. Operations* 25 (04), 438–452. doi:10.2118/115769-pa

Cipolla, C., Lolon, E., and Mayerhofer, M. (2009). "The Effect of Proppant Distribution and Un-propped Fracture Con-Ductivity on Well Performance in Unconventional Gas Reservoirs," in SPE Hydraulic Fracturing Technology Conference, The Woodlands, Texas, January 19–21, 2009 (SPE), 119368. doi:10.2118/119368-ms

Han, J. (2016). "Numerical Study of Proppant Transport in Complex Fracture Geometry," in SPE Low Perm Symposium, Denver, Colorado, USA, May 5–6, 2016 (Society of Petroleum Engineers). doi:10.2118/180243-ms

Hu, X., Wu, K., Li, G., Tang, J., and Shen, Z. (2018). Effect of Proppant Addition Schedule on the Proppant Distribution in a Straight Fracture for Slickwater Treatment. *J. Pet. Sci. Eng.* 167, 110–119. doi:10.1016/j.petrol.2018.03.081

Huang, X. (2017). "Numerical Study of wall Roughness Effect on Proppant Transport in Complex Fracture Geometry," in SPE Middle East Oil & Gas Show and Conference, Manama, Kingdom of Bahrain, March 6–9, 2017 (Society of Petroleum Engineers). doi:10.2118/183818-ms

Langmuir, I. (1917). The Constitution and Fundamental Properties of Solids and Liquids. *J. Franklin Inst.* 183 (1), 102–105. doi:10.1016/s0016-0032(17)90938-x

Lee, T., Park, D., Shin, C., Jeong, D., and Choe, J. (2016). Efficient Production Estimation for a Hydraulic Fractured Well Considering Fracture Closure and Proppant Placement Effects. *Energy Exploration & Exploitation* 34 (4), 643–658. doi:10.1177/0144598716650066

Li, L., and Voskov, D. (2021). A Novel Hybrid Model for Multiphase Flow in Complex Multi-Scale Fractured Systems. *J. Pet. Sci. Eng.* 203, 108657. doi:10.1016/j.petrol.2021.108657

Li, Y., Cheng, Y., Yan, C., Song, L., Liu, H., Tian, W., et al. (2020). Mechanical Study on the Wellbore Stability of Horizontal wells in Natural Gas Hydrate Reservoirs. *J. Nat. Gas Sci. Eng.* 79, 103359. doi:10.1016/j.jngse.2020.103359

Liu, L. (2020). Efficient Coupled Multiphase-Flow and Geomechanics Modeling of Well Performance and Stress Evolution in Shale-Gas Reservoirs Considering Dynamic Fracture Properties. *SPE J.*, 25 1523–1542. doi:10.2118/200496-PA

Liu, Y., Leung, J. Y., and Chalaturnyk, R., (2018). Geomechanical Simulation of Partially Propped Fracture Closure and its Implication for Water Flowback and Gas Production. *SPE Reservoir Eval. Eng.* 21 (02). 273–290. doi:10.2118/189454-pa

Liu, Y., Leung, J. Y., Chalaturnyk, R. J., and Virues, C. J. (2019). New Insights on Mechanisms Controlling Fracturing-Fluid Distribution and Their Effects on Well Performance in Shale-Gas Reservoirs. *SPE Prod. Operations* 34 (03), 564–585. doi:10.2118/185043-pa

Longlong, L. (2014). Productivity Calculation and Distribution of Staged Multi-Cluster Fractured Horizontal wells. *Pet. Exploration Dev.* 41 (4). 504–508. doi:10.1016/S1876-3804(14)60058-6

Manchanda, R. (2020). Integrating Reservoir Geomechanics with Multiple Fracture Propagation and Proppant Placement. *SPE J.* 25, 662–691. doi:10.2118/199366-pa

Mao, S., Siddhamshetty, P., Zhang, Z., Yu, W., Chun, T., Kwon, J. S.-I., et al. (2021). Impact of Proppant Pumping Schedule on Well Production for Slickwater Fracturing. *SPE J.* 26 (01), 342–358. doi:10.2118/204235-pa

Moghadasi, R., Rostami, A., and Hemmati-Sarapardeh, A. (2019). Application of Nanofluids for Treating Fines Migration during Hydraulic Fracturing: Experimental Study and Mechanistic Understanding. *Adv. Geo-energy Res.* 3 (2), 198–206. doi:10.26804/ager.2019.02.09

Ray, B. (2017). "An Investigation into Proppant Dynamics in Hydraulic Fracturing," in SPE hydraulic fracturing technology conference and exhibition, The Woodlands, Texas, USA, January 24–26, 2017 (Society of Petroleum Engineers).

Shao, J. (2021). Effects of the Borehole Drainage for Roof Aquifer on Local Stress in Underground Mining. *Geomechanics Eng.* 24 (5), 479–490. 10.12989/gae.2021.24.5.479.

Shen, W., Li, X., Cihan, A., Lu, X., and Liu, X. (2019). Experimental and Numerical Simulation of Water Adsorption and Diffusion in Shale Gas Reservoir Rocks. *Adv. Geo-energy Res.* 3 (2), 165–174. doi:10.26804/ager.2019.02.06

Sierra, L., Sahai, R. R., and Mayerhofer, M. J. (2014). "Quantification of Proppant Distribution Effect on Well Productivity and Recovery Factor of Hydraulically Fractured Unconventional Reservoirs," in SPE/CSUR Unconventional Resources Conference–Canada, Canada, Calgary, Alberta, Canada, eptember 30–October 2, 2014 (Society of Petroleum Engineers). doi:10.2118/171594-ms

Song, W., Yao, J., Li, Y., Sun, H., Zhang, L., Yang, Y., et al. (2016). Apparent Gas Permeability in an Organic-Rich Shale Reservoir. *Fuel* 181, 973–984. doi:10.1016/j.fuel.2016.05.011

Tong, S., and Mohanty, K. K. (2016). Proppant Transport Study in Fractures with Intersections. *Fuel* 181, 463–477. doi:10.1016/j.fuel.2016.04.144

Tong, S., Singh, R., and Mohanty, K. K. (2018). A Visualization Study of Proppant Transport in Foam Fracturing Fluids. *J. Nat. Gas Sci. Eng.* 52, 235–247. doi:10.1016/j.jngse.2018.01.030

Wang, X. (2021). Numerical Analysis of Gas Production Laws Considering Heterogeneous Proppant Distribution. *J. Nat. Gas Sci. Eng.* 95, 104211. doi:10.1016/j.jngse.2021.104211

Wang, X., Yao, J., Gong, L., Sun, H., Yang, Y., Zhang, L., et al. (2019). Numerical Simulations of Proppant Deposition and Transport Characteristics in Hydraulic Fractures and Fracture Networks. *J. Pet. Sci. Eng.* 183, 106401. doi:10.1016/j.petrol.2019.106401

Wen, H., Yang, R., Huang, Z., Zheng, Y., Wu, X., and Hu, X. (2020). Numerical Simulation of Proppant Transport in Liquid Nitrogen Fracturing. *J. Nat. Gas Sci. Eng.* 84, 103657. doi:10.1016/j.jngse.2020.103657

Wu, Y.-S., Li, J., Ding, D.-Y., Wang, C., and Di, Y. (2014). A Generalized Framework Model for the Simulation of Gas Production in Unconventional Gas Reservoirs. *SPE J.* 19 (05). 845–857, doi:10.2118/163609-pa

Yan, X. (2018). An Efficient Numerical Hybrid Model for Multiphase Flow in Deformable Fractured-Shale Reservoirs. *SPE J.* 23 (04), 1412–1437. doi:10.2118/191122-pa

Yan, X. (2021). Hierarchical Modeling of Hydromechanical Coupling in Fractured Shale Gas Reservoirs with Multiple Porosity Scales. *Energy & Fuels* 35, 5758–5776. doi:10.1021/acs.energyfuels.0c03757

Yan, X., Huang, Z., Yao, J., Li, Y., and Fan, D. (2016). An Efficient Embedded Discrete Fracture Model Based on Mimetic Finite Difference Method. *J. Pet. Sci. Eng.* 145, 11–21. doi:10.1016/j.petrol.2016.03.013

Yan, X., Huang, Z., Yao, J., Li, Y., Fan, D., and Zhang, K. (2018). An Efficient Hydro-Mechanical Model for Coupled Multi-Porosity and Discrete Fracture Porous media. *Comput. Mech.* 62 (5), 943–962. doi:10.1007/s00466-018-1541-5

Yan, X., Huang, Z., Yao, J., Zhang, Z., Liu, P., Li, Y., et al. (2019). Numerical Simulation of Hydro-Mechanical Coupling in Fractured Vuggy Porous media Using the Equivalent Continuum Model and Embedded Discrete Fracture Model. *Adv. Water Resour.* 126, 137–154. doi:10.1016/j.advwatres.2019.02.013

Yan, X., Huang, Z., Zhang, Q., Fan, D., and Yao, J. (2020). Numerical Investigation of the Effect of Partially Propped Fracture Closure on Gas Production in Fractured Shale Reservoirs. *Energies* 13 (20), 5339. doi:10.3390/en13205339

Yang, Y., Yao, J., Wang, C., Gao, Y., Zhang, Q., An, S., et al. (2015). New Pore Space Characterization Method of Shale Matrix Formation by Considering Organic and Inorganic Pores. *J. Nat. Gas Sci. Eng.* 27, 496–503. doi:10.1016/j.jngse.2015.08.017

Zeng, J., Li, H., and Zhang, D. (2016). Numerical Simulation of Proppant Transport in Hydraulic Fracture with the Upscaling CFD-DEM Method. *J. Nat. Gas Sci. Eng.* 33, 264–277. doi:10.1016/j.jngse.2016.05.030

Zeng, J., Li, H., and Zhang, D. (2019). Numerical Simulation of Proppant Transport in Propagating Fractures with the Multi-phase Particle-In-Cell Method. *Fuel* 245, 316–335. doi:10.1016/j.fuel.2019.02.056

Zhang, G., Gutierrez, M., and Li, M. (2017). A Coupled CFD-DEM Approach to Model Particle-Fluid Mixture Transport between Two Parallel Plates to Improve Understanding of Proppant Micromechanics in Hydraulic Fractures. *Powder Tech.* 308, 235–248. doi:10.1016/j.powtec.2016.11.055

Zhang, Q. (2021). Strip Load on Transversely Isotropic Elastic Double Porosity media with strong Permeability Contrast. *Adv. Geo-energy Res.* 5 (4), 353–364. doi:10.46690/ager.2021.04.02

Zhang, Q., Yan, X., and Shao, J. (2021). Fluid Flow through Anisotropic and Deformable Double Porosity media with Ultra-low Matrix Permeability: A Continuum Framework. *J. Pet. Sci. Eng.* 200, 108349. doi:10.1016/j.petrol.2021.108349

Zheng, S., Manchanda, R., and Sharma, M. M. (2020). Modeling Fracture Closure with Proppant Settling and Embedment during Shut-In and Production. *SPE Drilling & Completion* 35, 668–683. doi:10.2118/201205-pa

Zheng, S. (2019). "Simulating Production from Complex Fracture Networks: Impact of Geomechanics and Closure of Propped/Unpropped Fractures," in Unconventional Resources Technology Conference, Denver, Colorado, July 22–24, 2019 (SPE), 2019. doi:10.15530/urtec-2019-21

Zhou, L., Shen, Z., Wang, J., Li, H., and Lu, Y. (2019). Numerical Investigating the Effect of Nonuniform Proppant Distribution and Unpropped Fractures on Well Performance in a Tight Reservoir. *J. Pet. Sci. Eng.* 177, 634–649. doi:10.1016/j.petrol.2019.02.086

Zhu, G., Kou, J., Yao, B., Wu, Y.-s., Yao, J., and Sun, S. (2019). Thermodynamically Consistent Modelling of Two-phase Flows with Moving Contact Line and Soluble Surfactants. *J. Fluid Mech.* 879, 327–359. doi:10.1017/jfm.2019.664

Zhu, G., Kou, J., Yao, J., Li, A., and Sun, S. (2020). A Phase-Field Moving Contact Line Model with Soluble Surfactants. *J. Comput. Phys.* 405, 109170. doi:10.1016/j.jcp.2019.109170

Conflict of Interest: Authors QZ, GF, WY, and YY are employed by CNOOC EnerTech-Drilling and Production Co.

The remaining authors declare that the research was conducted in the absence of any commercial or financial relationships that could be construed as a potential conflict of interest.

Advantages of publishing in Frontiers

OPEN ACCESS
Articles are free to read for greatest visibility and readership

FAST PUBLICATION
Around 90 days from submission to decision

HIGH QUALITY PEER-REVIEW
Rigorous, collaborative, and constructive peer-review

TRANSPARENT PEER-REVIEW
Editors and reviewers acknowledged by name on published articles

Frontiers
Avenue du Tribunal-Fédéral 34
1005 Lausanne | Switzerland

Visit us: www.frontiersin.org
Contact us: frontiersin.org/about/contact

REPRODUCIBILITY OF RESEARCH
Support open data and methods to enhance research reproducibility

DIGITAL PUBLISHING
Articles designed for optimal readership across devices

FOLLOW US
@frontiersin

IMPACT METRICS
Advanced article metrics track visibility across digital media

EXTENSIVE PROMOTION
Marketing and promotion of impactful research

LOOP RESEARCH NETWORK
Our network increases your article's readership